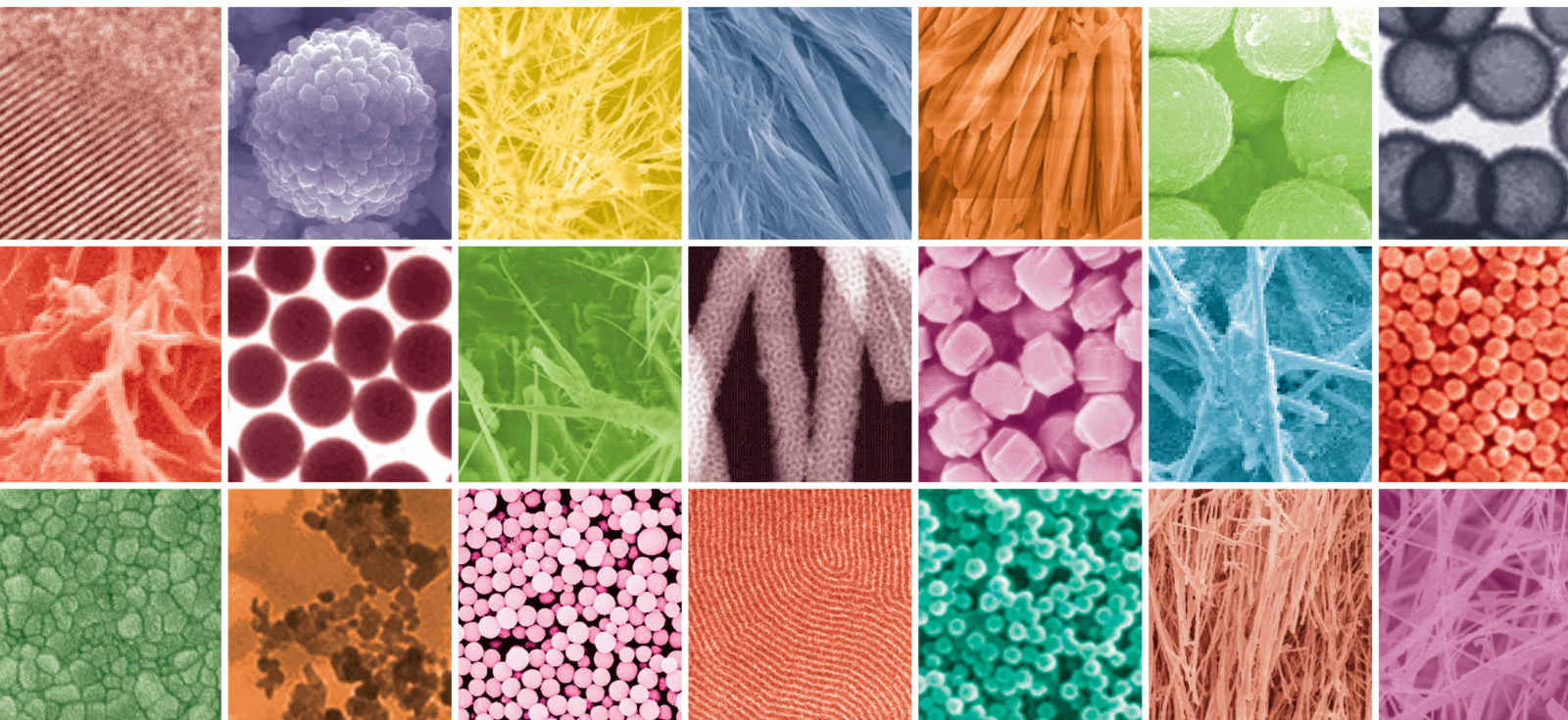


Environmental Applications of Nanomaterials

Lead Guest Editor: Karthikeyan Sathasivam

Guest Editors: Rathinam Raja and Sabariswaran Kandasamy





Environmental Applications of Nanomaterials

Journal of Nanomaterials

Environmental Applications of Nanomaterials

Lead Guest Editor: Karthikeyan Sathasivam

Guest Editors: Rathinam Raja and Sabariswaran
Kandasamy






Copyright © 2023 Hindawi Limited. All rights reserved.

This is a special issue published in "Journal of Nanomaterials." All articles are open access articles distributed under the Creative Commons Attribution License, which permits unrestricted use, distribution, and reproduction in any medium, provided the original work is properly cited.




Chief Editor

Stefano Bellucci , Italy

















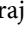
















Associate Editors

Ilaria Armentano, Italy
Stefano Bellucci , Italy
Paulo Cesar Morais , Brazil
William Yu , USA

Academic Editors

Buzuayehu Abebe, Ethiopia
Domenico Acierno , Italy
Sergio-Miguel Acuña-Nelson , Chile
Katerina Aifantis, USA
Omer Alawi , Malaysia
Nageh K. Allam , USA
Muhammad Wahab Amjad , USA
Martin Andersson, Sweden
Hassan Azzazy , Egypt
Ümit Ağbulut , Turkey
Vincenzo Baglio , Italy
Lavinia Balan , France
Nasser Barakat , Egypt
Thierry Baron , France
Carlos Gregorio Barreras-Urbina, Mexico
Andrew R. Barron , USA
Enrico Bergamaschi , Italy
Sergio Bietti , Italy
Raghvendra A. Bohara, India
Mohamed Bououdina , Saudi Arabia
Victor M. Castaño , Mexico
Albano Cavaleiro , Portugal
Kondareddy Cherukula , USA
Shafiul Chowdhury, USA
Yu-Lun Chueh , Taiwan
Elisabetta Comini , Italy
David Cornu, France
Miguel A. Correa-Duarte , Spain
P. Davide Cozzoli , Italy
Anuja Datta , India
Loretta L. Del Mercato, Italy
Yong Ding , USA
Kaliannan Durairaj , Republic of Korea
Ana Espinosa , France
Claude Estournès , France
Giuliana Faggio , Italy
Andrea Falqui , Saudi Arabia

Matteo Ferroni , Italy
Chong Leong Gan , Taiwan
Siddhartha Ghosh, Singapore
Filippo Giubileo , Italy
Iaroslav Gnilitzkiy, Ukraine
Hassanien Gomaa , Egypt
Fabien Grasset , Japan
Jean M. Greneche, France
Kimberly Hamad-Schifferli, USA
Simo-Pekka Hannula, Finland
Michael Harris , USA
Hadi Hashemi Gahruei , Iran
Yasuhiko Hayashi , Japan
Michael Z. Hu , USA
Zhengwei Huang , China
Zafar Iqbal, USA
Balachandran Jeyadevan , Japan
Xin Ju , China
Antonios Kelarakis , United Kingdom
Mohan Kumar Kesarla Kesarla , Mexico
Ali Khorsand Zak , Iran
Avvaru Praveen Kumar , Ethiopia
Prashant Kumar , United Kingdom
Jui-Yang Lai , Taiwan
Saravanan Lakshmanan, India
Meiyong Liao , Japan
Shijun Liao , China
Silvia Licocchia , Italy
Zainovia Lockman, Malaysia
Jim Low , Australia
Rajesh Kumar Manavalan , Russia
Yingji Mao , China
Ivan Marri , Italy
Laura Martinez Maestro , United Kingdom
Sanjay R. Mathur, Germany
Tony McNally, United Kingdom
Pier Gianni Medaglia , Italy
Paul Munroe, Australia
Jae-Min Myoung, Republic of Korea
Rajesh R. Naik, USA
Albert Nasibulin , Russia
Ngoc Thinh Nguyen , Vietnam
Hai Nguyen Tran , Vietnam
Hiromasa Nishikiori , Japan

Sherine Obare , USA
Abdelwahab Omri , Canada
Dillip K. Panda, USA
Sakthivel Pandurengan , India
Dr. Asisa Kumar Panigrahy, India
Mazeyar Parvinzadeh Gashti , Canada
Edward A. Payzant , USA
Alessandro Pegoretti , Italy
Oscar Perales-Pérez, Puerto Rico
Anand Babu Perumal , China
Suresh Perumal , India
Thathan Premkumar , Republic of Korea
Helena Prima-García, Spain
Alexander Pyatenko, Japan
Xiaoliang Qi , China
Haisheng Qian , China
Baskaran Rangasamy , Zambia
Soumyendu Roy , India
Fedlu Kedir Sabir , Ethiopia
Lucien Saviot , France
Shu Seki , Japan
Senthil Kumaran Selvaraj , India
Donglu Shi , USA
Muhammad Hussnain Siddique , Pakistan
Bhanu P. Singh , India
Jagpreet Singh , India
Jagpreet Singh, India
Surinder Singh, USA
Thangjam Ibomcha Singh , Republic of Korea
Korea
Vidya Nand Singh, India
Vladimir Sivakov, Germany
Tushar Sonar, Russia
Pingan Song , Australia
Adolfo Speghini , Italy
Kishore Sridharan , India
Marinella Striccoli , Italy
Andreas Stylianou , Cyprus
Fengqiang Sun , China
Ashok K. Sundramoorthy , India
Bo Tan, Canada
Leander Tapfer , Italy
Dr. T. Sathish Thanikodi , India
Arun Thirumurugan , Chile
Roshan Thotagamuge , Sri Lanka

Valeri P. Tolstoy , Russia
Muhammet S. Toprak , Sweden
Achim Trampert, Germany
Tamer Uyar , USA
Cristian Vacacela Gomez , Ecuador
Luca Valentini, Italy
Viet Van Pham , Vietnam
Antonio Vassallo , Italy
Ester Vazquez , Spain
Ajayan Vinu, Australia
Ruibing Wang , Macau
Magnus Willander , Sweden
Guosong Wu, China
Ping Xiao, United Kingdom
Zhi Li Xiao , USA
Yingchao Yang , USA
Hui Yao , China
Dong Kee Yi , Republic of Korea
Jianbo Yin , China
Hesham MH Zakaly , Russia
Michele Zappalorto , Italy
Mauro Zarrelli , Italy
Osman Ahmed Zeleke, Ethiopia
Wenhui Zeng , USA
Renyun Zhang , Sweden

Contents

Retracted: Nanometal-Based Magnesium Oxide Nanoparticle with *C. vulgaris* Algae Biodiesel in Diesel Engine

Journal of Nanomaterials

Retraction (1 page), Article ID 9861247, Volume 2023 (2023)

Retracted: Structural and Optical Properties of CdSe/CdTe Core-Shell Quantum Dots

Journal of Nanomaterials

Retraction (1 page), Article ID 9854379, Volume 2023 (2023)

Retracted: Evaluation of Physicothermal Properties of Silicone Oil Dispersed with Multiwalled Carbon Nanotubes and Data Prediction Using ANN

Journal of Nanomaterials

Retraction (1 page), Article ID 9813208, Volume 2023 (2023)

Retracted: Experimental Investigation of Spirulina Microalgae Biodiesel with Metal Nanoadditive on Single-Cylinder Diesel Engine

Journal of Nanomaterials

Retraction (1 page), Article ID 9756721, Volume 2023 (2023)

Retracted: Newly Synthesized Micro-Nano Transition Metal Complexes of Hexadecanoic Acid as Anti-Microbial Agents: Synthesis, Characterization, and Biological Investigations

Journal of Nanomaterials

Retraction (1 page), Article ID 9896201, Volume 2023 (2023)

Retracted: Wire Electrical Discharge Machining (WEDM) of Hybrid Composites (Al-Si12/B₄C/Fly Ash)

Journal of Nanomaterials

Retraction (1 page), Article ID 9865132, Volume 2023 (2023)

Retracted: Analysis of Ethanol to Reduce Solid Particle Pollution in SI Engines

Journal of Nanomaterials

Retraction (1 page), Article ID 9863702, Volume 2023 (2023)

Retracted: Environmental Emission Analysis of Biodiesel with Al₂O₃ Nanometal Additives as Fuel in a Diesel Engine

Journal of Nanomaterials

Retraction (1 page), Article ID 9850407, Volume 2023 (2023)

Retracted: Emission Measurement Analysis of Sapodilla Seed Oil Blending Fueled IC Engine

Journal of Nanomaterials

Retraction (1 page), Article ID 9837905, Volume 2023 (2023)

Retracted: Eco-Friendly Synthesis of Multishaped Crystalline Silver Nanoparticles Using Hill Garlic Extract and Their Potential Application as an Antifungal Agent

Journal of Nanomaterials

Retraction (1 page), Article ID 9827203, Volume 2023 (2023)

Retracted: Chlorella protothecoides Algae Oil and Its Mixes with Lower and Higher Alcohols and Al₂O₃ Metal Nanoadditives for Reduction of Pollution in a CI Engine

Journal of Nanomaterials

Retraction (1 page), Article ID 9820567, Volume 2023 (2023)

Retracted: Tribological Behavior and Surface Characterization of Gray Cast Iron-EN31 Steel under Lubricated Sliding Conditions

Journal of Nanomaterials

Retraction (1 page), Article ID 9817636, Volume 2023 (2023)

Retracted: Experimental Study on Surface Roughness and Flank Wear in Turning of Nimonic C263 under Dry Cutting Conditions

Journal of Nanomaterials

Retraction (1 page), Article ID 9789243, Volume 2023 (2023)

Retracted: Evaluation of Physicothermal Properties of Solar Thermic Fluids Dispersed with Multiwalled Carbon Nanotubes and Prediction of Data Using Artificial Neural Networks

Journal of Nanomaterials

Retraction (1 page), Article ID 9785712, Volume 2023 (2023)

Retracted: Preparation of Ti Material Supported SBA-15 Functionalized with Sulfonic Acid Environmental Friendly Catalyst: Application for Esterification Process

Journal of Nanomaterials








Retraction (1 page), Article ID 9782719, Volume 2023 (2023)

Retracted: Analysis of Environmental Emission Neat Diesel-Biodiesel-Algae Oil-Nanometal Additives in Compression Ignition Engines

Journal of Nanomaterials







Retraction (1 page), Article ID 9761672, Volume 2023 (2023)

Environmental Effect of Zinc Oxide Metal Nano Additives in Microalgae Biodiesel in Diesel Engine

M. Subbulakshmi , S. Srujana , ArifSenolSener , Mohammad A. Al Zubi , Ravi Kumar , Shanthi Natarajan , and Tewodros Derese Gidebo 

Research Article (6 pages), Article ID 1051117, Volume 2023 (2023)

[Retracted] Nanometal-Based Magnesium Oxide Nanoparticle with C. vulgaris Algae Biodiesel in Diesel Engine

J. Arunprasad , Alla Naveen Krishna , Dharavathu Radha , Mandeep Singh , Raviteja Surakasi , and Tewodros Derese Gidebo 









Research Article (9 pages), Article ID 1688505, Volume 2022 (2022)

Contents







[Retracted] Analysis of Environmental Emission Neat Diesel-Biodiesel–Algae Oil-Nanometal Additives in Compression Ignition Engines

Raviteja Surakasi , Mohd Yunus Khan , Arif Senol Sener , Tushar Choudhary , Sumantha Bhattacharya , Piyush Singhal , Bharat Singh , and Velivela Lakshmikanth Chowdary 
Research Article (7 pages), Article ID 3660233, Volume 2022 (2022)









[Retracted] Chlorella protothecoides Algae Oil and Its Mixes with Lower and Higher Alcohols and Al₂O₃ Metal Nanoadditives for Reduction of Pollution in a CI Engine

Gayatri Vaidya , Pravin P. Patil , Arif Senol SENER , Navale Sainath Ramnath , Bharat Singh , Raviteja Surakasi , Srujana Sripathi , and Tsegaye Alemayehu Atiso 
Research Article (6 pages), Article ID 9658212, Volume 2022 (2022)








[Retracted] Preparation of Ti Material Supported SBA-15 Functionalized with Sulfonic Acid Environmental Friendly Catalyst: Application for Esterification Process

Raju Kalakuntala , Mallaiah Mekala , Suman Chirra , Venkatathri Narayanan , Vighneswara Rao Kakara , and Srinath Suranani 
Research Article (8 pages), Article ID 6712464, Volume 2022 (2022)






[Retracted] Eco-Friendly Synthesis of Multishaped Crystalline Silver Nanoparticles Using Hill Garlic Extract and Their Potential Application as an Antifungal Agent

V. Uma Maheshwari Nallal , M. Razia , Ozlem Ates Duru , G. Ramalingam , Sasikala Chinnappan , Murugesan Chandrasekaran , R. M. Gengan , Woo Jin Chung, Soon Woong Chang, and Balasubramani Ravindran 
Research Article (7 pages), Article ID 7613210, Volume 2022 (2022)


[Retracted] Structural and Optical Properties of CdSe/CdTe Core-Shell Quantum Dots

G. Ramalingam , C. Ragupathi, Baskaran Rangasamy , I. Colak , V. Vetrivelan , Neda Poudineh , Balasubramani Ravindran , Soon Woong Chang, and Robert M. Gengan 
Research Article (7 pages), Article ID 6316716, Volume 2022 (2022)

[Retracted] Experimental Investigation of Spirulina Microalgae Biodiesel with Metal Nanoadditive on Single-Cylinder Diesel Engine

J. Arunprasad , Arif Senol Sener , R. Thirugnanasambantham , T. Elango , and T. Bothichandar 
Research Article (7 pages), Article ID 4701610, Volume 2022 (2022)

[Retracted] Newly Synthesized Micro-Nano Transition Metal Complexes of Hexadecanoic Acid as Anti-Microbial Agents: Synthesis, Characterization, and Biological Investigations








Kavitha Govindarajan, Vijayarohini Parasuraman, Parasuraman Perumalswamy Sekar, Ilhami Colak, and Balkew Zewge Hailemeskel 
Research Article (10 pages), Article ID 1678894, Volume 2022 (2022)

[Retracted] Evaluation of Physicothermal Properties of Solar Thermic Fluids Dispersed with Multiwalled Carbon Nanotubes and Prediction of Data Using Artificial Neural Networks

K. Ch. Sekhar , Raviteja Surakasi , Ilhan Garip , S. Srujana , V. V. Prasanna Kumar , and Naziya Begum 





Research Article (13 pages), Article ID 7306189, Volume 2021 (2021)

[Retracted] Evaluation of Physicothermal Properties of Silicone Oil Dispersed with Multiwalled Carbon Nanotubes and Data Prediction Using ANN

Raviteja Surakasi , K. Ch. Sekhar , Ekrem Yanmaz , G. Yuvaraj , Jayaprakash Venugopal , S. Srujana , and Naziya Begum 


Research Article (11 pages), Article ID 3444512, Volume 2021 (2021)

[Retracted] Wire Electrical Discharge Machining (WEDM) of Hybrid Composites (Al-Si12/B₄C/Fly Ash)

J. Udaya Prakash , P. Sivaprakasam , Ilhan Garip, S. Jebarose Juliyana, G. Elias , G. Kalusuraman , and Ilhami Colak

Research Article (10 pages), Article ID 2503673, Volume 2021 (2021)

[Retracted] Environmental Emission Analysis of Biodiesel with Al₂O₃ Nanometal Additives as Fuel in a Diesel Engine

Mohammad Ibrahim Al Mishlah Alghamdi, Ilhami Colak, Musaddak Maher Abdul Zahra, and T. Bothichandar 

Research Article (7 pages), Article ID 2544098, Volume 2021 (2021)

[Retracted] Tribological Behavior and Surface Characterization of Gray Cast Iron-EN31 Steel under Lubricated Sliding Conditions

S. Ananth , P. Sivaprakasam , J. Udaya Prakash , P. Maheandera Prabu , Varatharaju Perumal , and G. Kalusuraman 







Research Article (9 pages), Article ID 7725959, Volume 2021 (2021)

[Retracted] Experimental Study on Surface Roughness and Flank Wear in Turning of Nimonic C263 under Dry Cutting Conditions

J. Francis Xavier , B. Ravi, D. Jayabalakrishnan , Chakaravarthy Ezilarasan , V. Jayaseelan , and G. Elias 






Research Article (11 pages), Article ID 2054399, Volume 2021 (2021)

[Retracted] Analysis of Ethanol to Reduce Solid Particle Pollution in SI Engines

P. Sivaprakasam , P. Maheandera Prabu , M. Srinivasan , S. Balakrishnan , V. S. Karthikeyan , and M. Chithirai Pon Selvan 

Research Article (11 pages), Article ID 2726645, Volume 2021 (2021)

[Retracted] Emission Measurement Analysis of Sapodilla Seed Oil Blending Fueled IC Engine

P. Maheandera Prabu , P. Sivaprakasam , Varatharaju Perumal , Sung Chul Kim, P. Balasubramani , and S. Santosh Kumar 

Research Article (8 pages), Article ID 2385356, Volume 2021 (2021)

Retraction

Retracted: Nanometal-Based Magnesium Oxide Nanoparticle with *C. vulgaris* Algae Biodiesel in Diesel Engine

Journal of Nanomaterials

Received 10 October 2023; Accepted 10 October 2023; Published 11 October 2023

Copyright © 2023 Journal of Nanomaterials. This is an open access article distributed under the Creative Commons Attribution License, which permits unrestricted use, distribution, and reproduction in any medium, provided the original work is properly cited.

This article has been retracted by Hindawi following an investigation undertaken by the publisher [1]. This investigation has uncovered evidence of one or more of the following indicators of systematic manipulation of the publication process:

- (1) Discrepancies in scope
- (2) Discrepancies in the description of the research reported
- (3) Discrepancies between the availability of data and the research described
- (4) Inappropriate citations
- (5) Incoherent, meaningless and/or irrelevant content included in the article
- (6) Peer-review manipulation

The presence of these indicators undermines our confidence in the integrity of the article's content and we cannot, therefore, vouch for its reliability. Please note that this notice is intended solely to alert readers that the content of this article is unreliable. We have not investigated whether authors were aware of or involved in the systematic manipulation of the publication process.

Wiley and Hindawi regrets that the usual quality checks did not identify these issues before publication and have since put additional measures in place to safeguard research integrity.

We wish to credit our own Research Integrity and Research Publishing teams and anonymous and named external researchers and research integrity experts for contributing to this investigation.

The corresponding author, as the representative of all authors, has been given the opportunity to register their agreement or disagreement to this retraction. We have kept a record of any response received.

References

- [1] J. Arunprasad, A. N. Krishna, D. Radha, M. Singh, R. Surakasi, and T. D. Gidebo, "Nanometal-Based Magnesium Oxide Nanoparticle with *C. vulgaris* Algae Biodiesel in Diesel Engine," *Journal of Nanomaterials*, vol. 2022, Article ID 1688505, 9 pages, 2022.

Retraction

Retracted: Structural and Optical Properties of CdSe/CdTe Core-Shell Quantum Dots

Journal of Nanomaterials

Received 10 October 2023; Accepted 10 October 2023; Published 11 October 2023

Copyright © 2023 Journal of Nanomaterials. This is an open access article distributed under the Creative Commons Attribution License, which permits unrestricted use, distribution, and reproduction in any medium, provided the original work is properly cited.

This article has been retracted by Hindawi following an investigation undertaken by the publisher [1]. This investigation has uncovered evidence of one or more of the following indicators of systematic manipulation of the publication process:

- (1) Discrepancies in scope
- (2) Discrepancies in the description of the research reported
- (3) Discrepancies between the availability of data and the research described
- (4) Inappropriate citations
- (5) Incoherent, meaningless and/or irrelevant content included in the article
- (6) Peer-review manipulation

The presence of these indicators undermines our confidence in the integrity of the article's content and we cannot, therefore, vouch for its reliability. Please note that this notice is intended solely to alert readers that the content of this article is unreliable. We have not investigated whether authors were aware of or involved in the systematic manipulation of the publication process.

Wiley and Hindawi regrets that the usual quality checks did not identify these issues before publication and have since put additional measures in place to safeguard research integrity.

We wish to credit our own Research Integrity and Research Publishing teams and anonymous and named external researchers and research integrity experts for contributing to this investigation.

The corresponding author, as the representative of all authors, has been given the opportunity to register their agreement or disagreement to this retraction. We have kept a record of any response received.

References

- [1] G. Ramalingam, C. Ragupathi, B. Rangasamy et al., "Structural and Optical Properties of CdSe/CdTe Core-Shell Quantum Dots," *Journal of Nanomaterials*, vol. 2022, Article ID 6316716, 7 pages, 2022.

Retraction

Retracted: Evaluation of Physicothermal Properties of Silicone Oil Dispersed with Multiwalled Carbon Nanotubes and Data Prediction Using ANN

Journal of Nanomaterials

Received 10 October 2023; Accepted 10 October 2023; Published 11 October 2023

Copyright © 2023 Journal of Nanomaterials. This is an open access article distributed under the Creative Commons Attribution License, which permits unrestricted use, distribution, and reproduction in any medium, provided the original work is properly cited.

This article has been retracted by Hindawi following an investigation undertaken by the publisher [1]. This investigation has uncovered evidence of one or more of the following indicators of systematic manipulation of the publication process:

- (1) Discrepancies in scope
- (2) Discrepancies in the description of the research reported
- (3) Discrepancies between the availability of data and the research described
- (4) Inappropriate citations
- (5) Incoherent, meaningless and/or irrelevant content included in the article
- (6) Peer-review manipulation

The presence of these indicators undermines our confidence in the integrity of the article's content and we cannot, therefore, vouch for its reliability. Please note that this notice is intended solely to alert readers that the content of this article is unreliable. We have not investigated whether authors were aware of or involved in the systematic manipulation of the publication process.

Wiley and Hindawi regrets that the usual quality checks did not identify these issues before publication and have since put additional measures in place to safeguard research integrity.

We wish to credit our own Research Integrity and Research Publishing teams and anonymous and named external researchers and research integrity experts for contributing to this investigation.

The corresponding author, as the representative of all authors, has been given the opportunity to register their agreement or disagreement to this retraction. We have kept a record of any response received.

References

- [1] R. Surakasi, K. C. Sekhar, E. Yanmaz et al., "Evaluation of Physicothermal Properties of Silicone Oil Dispersed with Multiwalled Carbon Nanotubes and Data Prediction Using ANN," *Journal of Nanomaterials*, vol. 2021, Article ID 3444512, 11 pages, 2021.

Retraction

Retracted: Experimental Investigation of Spirulina Microalgae Biodiesel with Metal Nanoadditive on Single-Cylinder Diesel Engine

Journal of Nanomaterials

Received 10 October 2023; Accepted 10 October 2023; Published 11 October 2023

Copyright © 2023 Journal of Nanomaterials. This is an open access article distributed under the Creative Commons Attribution License, which permits unrestricted use, distribution, and reproduction in any medium, provided the original work is properly cited.

This article has been retracted by Hindawi following an investigation undertaken by the publisher [1]. This investigation has uncovered evidence of one or more of the following indicators of systematic manipulation of the publication process:

- (1) Discrepancies in scope
- (2) Discrepancies in the description of the research reported
- (3) Discrepancies between the availability of data and the research described
- (4) Inappropriate citations
- (5) Incoherent, meaningless and/or irrelevant content included in the article
- (6) Peer-review manipulation

The presence of these indicators undermines our confidence in the integrity of the article's content and we cannot, therefore, vouch for its reliability. Please note that this notice is intended solely to alert readers that the content of this article is unreliable. We have not investigated whether authors were aware of or involved in the systematic manipulation of the publication process.

Wiley and Hindawi regrets that the usual quality checks did not identify these issues before publication and have since put additional measures in place to safeguard research integrity.

We wish to credit our own Research Integrity and Research Publishing teams and anonymous and named external researchers and research integrity experts for contributing to this investigation.

The corresponding author, as the representative of all authors, has been given the opportunity to register their agreement or disagreement to this retraction. We have kept a record of any response received.

References

- [1] J. Arunprasad, A. S. Sener, R. Thirugnanasambantham, T. Elango, and T. Bothichandar, "Experimental Investigation of Spirulina Microalgae Biodiesel with Metal Nanoadditive on Single-Cylinder Diesel Engine," *Journal of Nanomaterials*, vol. 2022, Article ID 4701610, 7 pages, 2022.

Retraction

Retracted: Newly Synthesized Micro-Nano Transition Metal Complexes of Hexadecanoic Acid as Anti-Microbial Agents: Synthesis, Characterization, and Biological Investigations

Journal of Nanomaterials

Received 11 July 2023; Accepted 11 July 2023; Published 12 July 2023

Copyright © 2023 Journal of Nanomaterials. This is an open access article distributed under the Creative Commons Attribution License, which permits unrestricted use, distribution, and reproduction in any medium, provided the original work is properly cited.

This article has been retracted by Hindawi following an investigation undertaken by the publisher [1]. This investigation has uncovered evidence of one or more of the following indicators of systematic manipulation of the publication process:

- (1) Discrepancies in scope
- (2) Discrepancies in the description of the research reported
- (3) Discrepancies between the availability of data and the research described
- (4) Inappropriate citations
- (5) Incoherent, meaningless and/or irrelevant content included in the article
- (6) Peer-review manipulation

The presence of these indicators undermines our confidence in the integrity of the article's content and we cannot, therefore, vouch for its reliability. Please note that this notice is intended solely to alert readers that the content of this article is unreliable. We have not investigated whether authors were aware of or involved in the systematic manipulation of the publication process.

Wiley and Hindawi regrets that the usual quality checks did not identify these issues before publication and have since put additional measures in place to safeguard research integrity.

We wish to credit our own Research Integrity and Research Publishing teams and anonymous and named external researchers and research integrity experts for contributing to this investigation.

The corresponding author, as the representative of all authors, has been given the opportunity to register their

agreement or disagreement to this retraction. We have kept a record of any response received.

References

- [1] K. Govindarajan, V. Parasuraman, P. Perumalswamy Sekar, I. Colak, and B. Z. Hailemeskel, "Newly Synthesized Micro-Nano Transition Metal Complexes of Hexadecanoic Acid as Anti-Microbial Agents: Synthesis, Characterization, and Biological Investigations," *Journal of Nanomaterials*, vol. 2022, Article ID 1678894, 10 pages, 2022.

Retraction

Retracted: Wire Electrical Discharge Machining (WEDM) of Hybrid Composites (Al-Si12/B₄C/Fly Ash)

Journal of Nanomaterials

Received 11 July 2023; Accepted 11 July 2023; Published 12 July 2023

Copyright © 2023 Journal of Nanomaterials. This is an open access article distributed under the Creative Commons Attribution License, which permits unrestricted use, distribution, and reproduction in any medium, provided the original work is properly cited.

This article has been retracted by Hindawi following an investigation undertaken by the publisher [1]. This investigation has uncovered evidence of one or more of the following indicators of systematic manipulation of the publication process:

- (1) Discrepancies in scope
- (2) Discrepancies in the description of the research reported
- (3) Discrepancies between the availability of data and the research described
- (4) Inappropriate citations
- (5) Incoherent, meaningless and/or irrelevant content included in the article
- (6) Peer-review manipulation

The presence of these indicators undermines our confidence in the integrity of the article's content and we cannot, therefore, vouch for its reliability. Please note that this notice is intended solely to alert readers that the content of this article is unreliable. We have not investigated whether authors were aware of or involved in the systematic manipulation of the publication process.

Wiley and Hindawi regrets that the usual quality checks did not identify these issues before publication and have since put additional measures in place to safeguard research integrity.

We wish to credit our own Research Integrity and Research Publishing teams and anonymous and named external researchers and research integrity experts for contributing to this investigation.

The corresponding author, as the representative of all authors, has been given the opportunity to register their agreement or disagreement to this retraction. We have kept a record of any response received.

References

- [1] J. Udaya Prakash, P. Sivaprakasam, I. Garip et al., "Wire Electrical Discharge Machining (WEDM) of Hybrid Composites (Al-Si12/B₄C/Fly Ash)," *Journal of Nanomaterials*, vol. 2021, Article ID 2503673, 10 pages, 2021.

Retraction

Retracted: Analysis of Ethanol to Reduce Solid Particle Pollution in SI Engines

Journal of Nanomaterials

Received 11 July 2023; Accepted 11 July 2023; Published 12 July 2023

Copyright © 2023 Journal of Nanomaterials. This is an open access article distributed under the Creative Commons Attribution License, which permits unrestricted use, distribution, and reproduction in any medium, provided the original work is properly cited.

This article has been retracted by Hindawi following an investigation undertaken by the publisher [1]. This investigation has uncovered evidence of one or more of the following indicators of systematic manipulation of the publication process:

- (1) Discrepancies in scope
- (2) Discrepancies in the description of the research reported
- (3) Discrepancies between the availability of data and the research described
- (4) Inappropriate citations
- (5) Incoherent, meaningless and/or irrelevant content included in the article
- (6) Peer-review manipulation

The presence of these indicators undermines our confidence in the integrity of the article's content and we cannot, therefore, vouch for its reliability. Please note that this notice is intended solely to alert readers that the content of this article is unreliable. We have not investigated whether authors were aware of or involved in the systematic manipulation of the publication process.

Wiley and Hindawi regrets that the usual quality checks did not identify these issues before publication and have since put additional measures in place to safeguard research integrity.

We wish to credit our own Research Integrity and Research Publishing teams and anonymous and named external researchers and research integrity experts for contributing to this investigation.

The corresponding author, as the representative of all authors, has been given the opportunity to register their agreement or disagreement to this retraction. We have kept a record of any response received.

References

- [1] P. Sivaprakasam, P. M. Prabu, M. Srinivasan, S. Balakrishnan, V. S. Karthikeyan, and M. C. P. Selvan, "Analysis of Ethanol to Reduce Solid Particle Pollution in SI Engines," *Journal of Nanomaterials*, vol. 2021, Article ID 2726645, 11 pages, 2021.

Retraction

Retracted: Environmental Emission Analysis of Biodiesel with Al₂O₃ Nanometal Additives as Fuel in a Diesel Engine

Journal of Nanomaterials

Received 11 July 2023; Accepted 11 July 2023; Published 12 July 2023

Copyright © 2023 Journal of Nanomaterials. This is an open access article distributed under the Creative Commons Attribution License, which permits unrestricted use, distribution, and reproduction in any medium, provided the original work is properly cited.

This article has been retracted by Hindawi following an investigation undertaken by the publisher [1]. This investigation has uncovered evidence of one or more of the following indicators of systematic manipulation of the publication process:

- (1) Discrepancies in scope
- (2) Discrepancies in the description of the research reported
- (3) Discrepancies between the availability of data and the research described
- (4) Inappropriate citations
- (5) Incoherent, meaningless and/or irrelevant content included in the article
- (6) Peer-review manipulation

The presence of these indicators undermines our confidence in the integrity of the article's content and we cannot, therefore, vouch for its reliability. Please note that this notice is intended solely to alert readers that the content of this article is unreliable. We have not investigated whether authors were aware of or involved in the systematic manipulation of the publication process.

Wiley and Hindawi regrets that the usual quality checks did not identify these issues before publication and have since put additional measures in place to safeguard research integrity.

We wish to credit our own Research Integrity and Research Publishing teams and anonymous and named external researchers and research integrity experts for contributing to this investigation.

The corresponding author, as the representative of all authors, has been given the opportunity to register their agreement or disagreement to this retraction. We have kept a record of any response received.

References

- [1] M. I. A. M. Alghamdi, I. Colak, M. M. A. Zahra, and T. Bothichandar, "Environmental Emission Analysis of Biodiesel with Al₂O₃ Nanometal Additives as Fuel in a Diesel Engine," *Journal of Nanomaterials*, vol. 2021, Article ID 2544098, 7 pages, 2021.

Retraction

Retracted: Emission Measurement Analysis of Sapodilla Seed Oil Blending Fueled IC Engine

Journal of Nanomaterials

Received 11 July 2023; Accepted 11 July 2023; Published 12 July 2023

Copyright © 2023 Journal of Nanomaterials. This is an open access article distributed under the Creative Commons Attribution License, which permits unrestricted use, distribution, and reproduction in any medium, provided the original work is properly cited.

This article has been retracted by Hindawi following an investigation undertaken by the publisher [1]. This investigation has uncovered evidence of one or more of the following indicators of systematic manipulation of the publication process:

- (1) Discrepancies in scope
- (2) Discrepancies in the description of the research reported
- (3) Discrepancies between the availability of data and the research described
- (4) Inappropriate citations
- (5) Incoherent, meaningless and/or irrelevant content included in the article
- (6) Peer-review manipulation

The presence of these indicators undermines our confidence in the integrity of the article's content and we cannot, therefore, vouch for its reliability. Please note that this notice is intended solely to alert readers that the content of this article is unreliable. We have not investigated whether authors were aware of or involved in the systematic manipulation of the publication process.

Wiley and Hindawi regrets that the usual quality checks did not identify these issues before publication and have since put additional measures in place to safeguard research integrity.

We wish to credit our own Research Integrity and Research Publishing teams and anonymous and named external researchers and research integrity experts for contributing to this investigation.

The corresponding author, as the representative of all authors, has been given the opportunity to register their agreement or disagreement to this retraction. We have kept a record of any response received.

References

- [1] P. M. Prabu, P. Sivaprakasam, V. Perumal, S. C. Kim, P. Balasubramani, and S. S. Kumar, "Emission Measurement Analysis of Sapodilla Seed Oil Blending Fueled IC Engine," *Journal of Nanomaterials*, vol. 2021, Article ID 2385356, 8 pages, 2021.

Retraction

Retracted: Eco-Friendly Synthesis of Multishaped Crystalline Silver Nanoparticles Using Hill Garlic Extract and Their Potential Application as an Antifungal Agent

Journal of Nanomaterials

Received 11 July 2023; Accepted 11 July 2023; Published 12 July 2023

Copyright © 2023 Journal of Nanomaterials. This is an open access article distributed under the Creative Commons Attribution License, which permits unrestricted use, distribution, and reproduction in any medium, provided the original work is properly cited.

This article has been retracted by Hindawi following an investigation undertaken by the publisher [1]. This investigation has uncovered evidence of one or more of the following indicators of systematic manipulation of the publication process:

- (1) Discrepancies in scope
- (2) Discrepancies in the description of the research reported
- (3) Discrepancies between the availability of data and the research described
- (4) Inappropriate citations
- (5) Incoherent, meaningless and/or irrelevant content included in the article
- (6) Peer-review manipulation

The presence of these indicators undermines our confidence in the integrity of the article's content and we cannot, therefore, vouch for its reliability. Please note that this notice is intended solely to alert readers that the content of this article is unreliable. We have not investigated whether authors were aware of or involved in the systematic manipulation of the publication process.

Wiley and Hindawi regrets that the usual quality checks did not identify these issues before publication and have since put additional measures in place to safeguard research integrity.

We wish to credit our own Research Integrity and Research Publishing teams and anonymous and named external researchers and research integrity experts for contributing to this investigation.

The corresponding author, as the representative of all authors, has been given the opportunity to register their

agreement or disagreement to this retraction. We have kept a record of any response received.

References

- [1] V. U. M. Nallal, M. Razia, O. A. Duru et al., "Eco-Friendly Synthesis of Multishaped Crystalline Silver Nanoparticles Using Hill Garlic Extract and Their Potential Application as an Antifungal Agent," *Journal of Nanomaterials*, vol. 2022, Article ID 7613210, 7 pages, 2022.

Retraction

Retracted: *Chlorella protothecoides* Algae Oil and Its Mixes with Lower and Higher Alcohols and Al₂O₃ Metal Nanoadditives for Reduction of Pollution in a CI Engine

Journal of Nanomaterials

Received 11 July 2023; Accepted 11 July 2023; Published 12 July 2023

Copyright © 2023 Journal of Nanomaterials. This is an open access article distributed under the Creative Commons Attribution License, which permits unrestricted use, distribution, and reproduction in any medium, provided the original work is properly cited.

This article has been retracted by Hindawi following an investigation undertaken by the publisher [1]. This investigation has uncovered evidence of one or more of the following indicators of systematic manipulation of the publication process:

- (1) Discrepancies in scope
- (2) Discrepancies in the description of the research reported
- (3) Discrepancies between the availability of data and the research described
- (4) Inappropriate citations
- (5) Incoherent, meaningless and/or irrelevant content included in the article
- (6) Peer-review manipulation

The presence of these indicators undermines our confidence in the integrity of the article's content and we cannot, therefore, vouch for its reliability. Please note that this notice is intended solely to alert readers that the content of this article is unreliable. We have not investigated whether authors were aware of or involved in the systematic manipulation of the publication process.

Wiley and Hindawi regrets that the usual quality checks did not identify these issues before publication and have since put additional measures in place to safeguard research integrity.

We wish to credit our own Research Integrity and Research Publishing teams and anonymous and named external researchers and research integrity experts for contributing to this investigation.

The corresponding author, as the representative of all authors, has been given the opportunity to register their agreement or disagreement to this retraction. We have kept a record of any response received.

References

- [1] G. Vaidya, P. P. Patil, A. S. SENER et al., "Chlorella protothecoides Algae Oil and Its Mixes with Lower and Higher Alcohols and Al₂O₃ Metal Nanoadditives for Reduction of Pollution in a CI Engine," *Journal of Nanomaterials*, vol. 2022, Article ID 9658212, 6 pages, 2022.

Retraction

Retracted: Tribological Behavior and Surface Characterization of Gray Cast Iron-EN31 Steel under Lubricated Sliding Conditions

Journal of Nanomaterials

Received 11 July 2023; Accepted 11 July 2023; Published 12 July 2023

Copyright © 2023 Journal of Nanomaterials. This is an open access article distributed under the Creative Commons Attribution License, which permits unrestricted use, distribution, and reproduction in any medium, provided the original work is properly cited.

This article has been retracted by Hindawi following an investigation undertaken by the publisher [1]. This investigation has uncovered evidence of one or more of the following indicators of systematic manipulation of the publication process:

- (1) Discrepancies in scope
- (2) Discrepancies in the description of the research reported
- (3) Discrepancies between the availability of data and the research described
- (4) Inappropriate citations
- (5) Incoherent, meaningless and/or irrelevant content included in the article
- (6) Peer-review manipulation

The presence of these indicators undermines our confidence in the integrity of the article's content and we cannot, therefore, vouch for its reliability. Please note that this notice is intended solely to alert readers that the content of this article is unreliable. We have not investigated whether authors were aware of or involved in the systematic manipulation of the publication process.

Wiley and Hindawi regrets that the usual quality checks did not identify these issues before publication and have since put additional measures in place to safeguard research integrity.

We wish to credit our own Research Integrity and Research Publishing teams and anonymous and named external researchers and research integrity experts for contributing to this investigation.

The corresponding author, as the representative of all authors, has been given the opportunity to register their agreement or disagreement to this retraction. We have kept a record of any response received.

References

- [1] S. Ananth, P. Sivaprakasam, J. Udaya Prakash, P. Maheandera Prabu, V. Perumal, and G. Kalusuraman, "Tribological Behavior and Surface Characterization of Gray Cast Iron-EN31 Steel under Lubricated Sliding Conditions," *Journal of Nanomaterials*, vol. 2021, Article ID 7725959, 9 pages, 2021.

Retraction

Retracted: Experimental Study on Surface Roughness and Flank Wear in Turning of Nimonic C263 under Dry Cutting Conditions

Journal of Nanomaterials

Received 11 July 2023; Accepted 11 July 2023; Published 12 July 2023

Copyright © 2023 Journal of Nanomaterials. This is an open access article distributed under the Creative Commons Attribution License, which permits unrestricted use, distribution, and reproduction in any medium, provided the original work is properly cited.

This article has been retracted by Hindawi following an investigation undertaken by the publisher [1]. This investigation has uncovered evidence of one or more of the following indicators of systematic manipulation of the publication process:

- (1) Discrepancies in scope
- (2) Discrepancies in the description of the research reported
- (3) Discrepancies between the availability of data and the research described
- (4) Inappropriate citations
- (5) Incoherent, meaningless and/or irrelevant content included in the article
- (6) Peer-review manipulation

The presence of these indicators undermines our confidence in the integrity of the article's content and we cannot, therefore, vouch for its reliability. Please note that this notice is intended solely to alert readers that the content of this article is unreliable. We have not investigated whether authors were aware of or involved in the systematic manipulation of the publication process.

Wiley and Hindawi regrets that the usual quality checks did not identify these issues before publication and have since put additional measures in place to safeguard research integrity.

We wish to credit our own Research Integrity and Research Publishing teams and anonymous and named external researchers and research integrity experts for contributing to this investigation.

The corresponding author, as the representative of all authors, has been given the opportunity to register their agreement or disagreement to this retraction. We have kept a record of any response received.

References

- [1] J. F. Xavier, B. Ravi, D. Jayabalakrishnan, C. Ezilarasan, V. Jayaseelan, and G. Elias, "Experimental Study on Surface Roughness and Flank Wear in Turning of Nimonic C263 under Dry Cutting Conditions," *Journal of Nanomaterials*, vol. 2021, Article ID 2054399, 11 pages, 2021.

Retraction

Retracted: Evaluation of Physicothermal Properties of Solar Thermic Fluids Dispersed with Multiwalled Carbon Nanotubes and Prediction of Data Using Artificial Neural Networks

Journal of Nanomaterials

Received 11 July 2023; Accepted 11 July 2023; Published 12 July 2023

Copyright © 2023 Journal of Nanomaterials. This is an open access article distributed under the Creative Commons Attribution License, which permits unrestricted use, distribution, and reproduction in any medium, provided the original work is properly cited.

This article has been retracted by Hindawi following an investigation undertaken by the publisher [1]. This investigation has uncovered evidence of one or more of the following indicators of systematic manipulation of the publication process:

- (1) Discrepancies in scope
- (2) Discrepancies in the description of the research reported
- (3) Discrepancies between the availability of data and the research described
- (4) Inappropriate citations
- (5) Incoherent, meaningless and/or irrelevant content included in the article
- (6) Peer-review manipulation

The presence of these indicators undermines our confidence in the integrity of the article's content and we cannot, therefore, vouch for its reliability. Please note that this notice is intended solely to alert readers that the content of this article is unreliable. We have not investigated whether authors were aware of or involved in the systematic manipulation of the publication process.

Wiley and Hindawi regrets that the usual quality checks did not identify these issues before publication and have since put additional measures in place to safeguard research integrity.

We wish to credit our own Research Integrity and Research Publishing teams and anonymous and named external researchers and research integrity experts for contributing to this investigation.

The corresponding author, as the representative of all authors, has been given the opportunity to register their

agreement or disagreement to this retraction. We have kept a record of any response received.

References

- [1] K. C. Sekhar, R. Surakasi, I. Garip, S. Srujana, V. V. P. Kumar, and N. Begum, "Evaluation of Physicothermal Properties of Solar Thermic Fluids Dispersed with Multiwalled Carbon Nanotubes and Prediction of Data Using Artificial Neural Networks," *Journal of Nanomaterials*, vol. 2021, Article ID 7306189, 13 pages, 2021.

Retraction

Retracted: Preparation of Ti Material Supported SBA-15 Functionalized with Sulfonic Acid Environmental Friendly Catalyst: Application for Esterification Process

Journal of Nanomaterials

Received 11 July 2023; Accepted 11 July 2023; Published 12 July 2023

Copyright © 2023 Journal of Nanomaterials. This is an open access article distributed under the Creative Commons Attribution License, which permits unrestricted use, distribution, and reproduction in any medium, provided the original work is properly cited.

This article has been retracted by Hindawi following an investigation undertaken by the publisher [1]. This investigation has uncovered evidence of one or more of the following indicators of systematic manipulation of the publication process:

- (1) Discrepancies in scope
- (2) Discrepancies in the description of the research reported
- (3) Discrepancies between the availability of data and the research described
- (4) Inappropriate citations
- (5) Incoherent, meaningless and/or irrelevant content included in the article
- (6) Peer-review manipulation

The presence of these indicators undermines our confidence in the integrity of the article's content and we cannot, therefore, vouch for its reliability. Please note that this notice is intended solely to alert readers that the content of this article is unreliable. We have not investigated whether authors were aware of or involved in the systematic manipulation of the publication process.

Wiley and Hindawi regrets that the usual quality checks did not identify these issues before publication and have since put additional measures in place to safeguard research integrity.

We wish to credit our own Research Integrity and Research Publishing teams and anonymous and named external researchers and research integrity experts for contributing to this investigation.

The corresponding author, as the representative of all authors, has been given the opportunity to register their agreement or disagreement to this retraction. We have kept a record of any response received.

References

- [1] R. Kalakuntala, M. Mekala, S. Chirra, V. Narayanan, V. R. Kakara, and S. Suranani, "Preparation of Ti Material Supported SBA-15 Functionalized with Sulfonic Acid Environmental Friendly Catalyst: Application for Esterification Process," *Journal of Nanomaterials*, vol. 2022, Article ID 6712464, 8 pages, 2022.

Retraction

Retracted: Analysis of Environmental Emission Neat Diesel-Biodiesel–Algae Oil-Nanometal Additives in Compression Ignition Engines

Journal of Nanomaterials

Received 11 July 2023; Accepted 11 July 2023; Published 12 July 2023

Copyright © 2023 Journal of Nanomaterials. This is an open access article distributed under the Creative Commons Attribution License, which permits unrestricted use, distribution, and reproduction in any medium, provided the original work is properly cited.

This article has been retracted by Hindawi following an investigation undertaken by the publisher [1]. This investigation has uncovered evidence of one or more of the following indicators of systematic manipulation of the publication process:

- (1) Discrepancies in scope
- (2) Discrepancies in the description of the research reported
- (3) Discrepancies between the availability of data and the research described
- (4) Inappropriate citations
- (5) Incoherent, meaningless and/or irrelevant content included in the article
- (6) Peer-review manipulation

The presence of these indicators undermines our confidence in the integrity of the article's content and we cannot, therefore, vouch for its reliability. Please note that this notice is intended solely to alert readers that the content of this article is unreliable. We have not investigated whether authors were aware of or involved in the systematic manipulation of the publication process.

Wiley and Hindawi regrets that the usual quality checks did not identify these issues before publication and have since put additional measures in place to safeguard research integrity.

We wish to credit our own Research Integrity and Research Publishing teams and anonymous and named external researchers and research integrity experts for contributing to this investigation.

The corresponding author, as the representative of all authors, has been given the opportunity to register their

agreement or disagreement to this retraction. We have kept a record of any response received.

References

- [1] R. Surakasi, M. Y. Khan, A. S. Sener et al., "Analysis of Environmental Emission Neat Diesel-Biodiesel–Algae Oil-Nanometal Additives in Compression Ignition Engines," *Journal of Nanomaterials*, vol. 2022, Article ID 3660233, 7 pages, 2022.

Research Article

Environmental Effect of Zinc Oxide Metal Nano Additives in Microalgae Biodiesel in Diesel Engine

M. Subbulakshmi ¹, S. Srujana ², ArifSenolSener ³, Mohammad A. Al Zubi ⁴,
Ravi Kumar ⁵, Shanthi Natarajan ⁶, and Tewodros Derese Gidebo ⁷

¹Department of Microbiology, K.R. College of Arts & Science, K.R. Nagar, Kovilpatti, Tamil Nadu, India

²Department of Biotechnology, School of Sciences, Jain University, JC Road, Bengaluru 560027, India

³Department of Mechanical Engineering, Engineering and Architecture Faculty, Nisantasi University, Istanbul, Turkey

⁴Mechanical Engineering Department, Hijawi Faculty for Engineering Technology Yarmouk University, Irbid, Jordan 21163

⁵Department of Mechanical Engineering, BTKIT Dwarahat, Almora, Uttarakhand, India

⁶PG and Research, Department of Botany, Pachaiyappa's College, Affiliated to University of Madras, Chennai, 600030 Tamil Nadu, India

⁷Department of Mechanical Engineering, Wolaita Sodo University, Ethiopia

Correspondence should be addressed to Tewodros Derese Gidebo; teddyderese@gmail.com

Received 12 February 2022; Revised 13 March 2022; Accepted 17 March 2022; Published 17 February 2023

Academic Editor: Karthikeyan Sathasivam

Copyright © 2023 M. Subbulakshmi et al. This is an open access article distributed under the Creative Commons Attribution License, which permits unrestricted use, distribution, and reproduction in any medium, provided the original work is properly cited.

We investigated how to extract energy from algal oil and convert it to biodiesel by transesterification in this study. In addition to performing engine performance tests with varying quantities of fuel mixture, parameters such as power, hourly torque consumption, specific consumption, and emissions of dioxide and monoxide were evaluated as an alternate solution to the pollution problem caused by fossil fuels. A 5.2 kW diesel engine powered the engine. The production of algal oil-based biodiesel was carried out effectively. The algal oil extraction procedure resulted in the production of biodiesel, which was then blended with commercial diesel in the amounts of 20, 40, and 60%. The engine performance testing revealed no statistically significant difference between the power and torque delivered by the various commercial diesel blends. Both hourly and particular consumption showed an increase of 15% and 20%, respectively, regarding commercial diesel consumption. However, the most significant advantage is the reduction in pollutant emissions, as demonstrated by the reduction in carbon dioxide emissions by more than 20% in any mixture of commercial diesel and biodiesel when compared to commercial diesel.

1. Introduction

As a result of the increasing need for oil, biodiesel has emerged as a valuable source of energy and a viable alternative to the production of clean energy through the use of internal combustion engines, stoves, and other burners [1]. The growing use of biodiesel of the first generation in each country has occurred due to the introduction of policies that encourage the production and widespread use of this biofuel in the respective countries. In some countries, the growth of oil palm has been encouraged to manufacture biodiesel, which can be used to meet the demand for fuel in the crea-

tion of electricity [2]. In addition, it should be highlighted that first-generation biofuels have several drawbacks, including competition with crops for human consumption and the requirement of large amounts of water for their production. This results in a debate about food and fuels derived from these, which is a crucial point to consider when designing new policies in some countries. As a result, new alternatives and raw materials are being developed to address these issues; most of these initiatives are geared toward developing second-, third-, and fourth-generation biofuels derived from nonedible crops and other raw materials [3]. The manufacturing of biodiesel from these nonedible basic

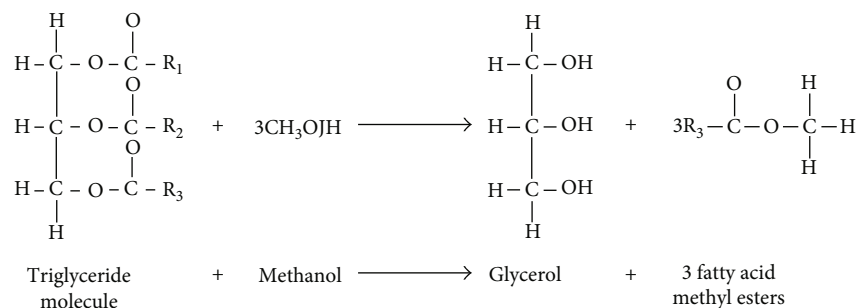


FIGURE 1: Transesterification process.



FIGURE 2: The separation of glycerol from biodiesel.



FIGURE 3: Biodiesel mixes in nanoparticles.

materials, as well as the use of this biodiesel, as a result, there is a disagreement over the food and fuel that can be gotten from these sources, which is an important matter to examine when new legislation is being drafted in some nations. Several authors from throughout the world have conducted substantial research into the performance of internal combustion engines [4]. A valuable review of the properties and performance of biodiesel derived from nonedible vegetable oils is available online. Numerous researchers looked examined raw materials such as rubber seed oil, cottonseed oil, jojoba oil, tobacco oil, flaxseed oil, and *Jatropha* as potential sources of raw materials, as well as other plants. For example, in some countries, the growth of oil palm has been promoted to manufacture biodiesel to meet the need for fuel in power generation [5]. In 2012, biodiesel from olive oil was created in one of these countries, the Philippines. In addition, it should be highlighted that first-generation biofuels have several drawbacks, including a rivalry with crops for human consumption and the high need for water during the cultivation process. As a result,

there is a dispute regarding food and energy obtained from them, which is essential to address when developing new legislation in various jurisdictions. It was demonstrated that it is possible to produce biodiesel from algae oil while adhering to international environmental regulations and norms [6]. The researchers used a similar approach to generate biodiesel using an integrated catalytic process that included a composite membrane and sodium methoxide. This group of researchers concluded that it was possible to create this biofuel under optimal conditions with 98.1% of the total transesterification conversion rate. It is an important area of research in which various authors have contributed to recent years, and the use of biodiesel as a source of energy in internal combustion engines is one of them. Most of the research that has been conducted in recent years, however, has focused on the performance of internal combustion engines utilized in the transportation industry [7].

2. Materials and Method

2.1. Biodiesel Production. According to the FAO, the process begins with extracting algae oil using heating operations that yield around 10 liters of oil. A sample of this oil is used for acidity analysis. When free fatty acids are present in a triglyceride, its acidity is indicated by its acid number (acidity number). It is necessary to titrate using potassium hydroxide, and the acidity is measured using an index known as the acid number. The acid number of the oil will be determined through this analysis; if it finds a value that is not greater than 5, it will be possible to work without problems; acidity index values greater than 5 are not recommended for the production of biodiesel due to the high acid number; however, the use of this is recommended for other products other than biodiesel production. For the acidity test, 5 grams of sample was weighed and diluted with 50 mL of ethyl alcohol neutralized at 50°C before being placed in an Erlenmeyer flask with a few drops of phenolphthalein and then titrated with potassium hydroxide solution 0.1 N [8]. Figure 1 shows the transesterification process.

Biodiesel is a mixture of monoalkyl esters of long-chain fatty acids derived from renewable lipids such as vegetable and animal oils and obtained by the transesterification process. The procedure consisted of pouring the ten liters of algae oil into a container; then, methanol 20% (v/v) was added about the amount of sample. The amount of catalyst was calculated by adding an excess depending on the acid

TABLE 1: Properties of different fuel blends.

S. no	Properties	Diesel (D100)	Algae methyl ester (B20)	B20+50 ppm of ZnO	B20+100 ppm of ZnO
1	Kinetic viscosity, cSt	5.6	6	6.12	6.18
2	Density, kg/m ³	890	888	893	896
3	Calorific value, MJ/kg	39.5	40	41	41.6
4	Flashpoint, °C	96	92	128	137
5	Fire point, °C	115	118	136	151

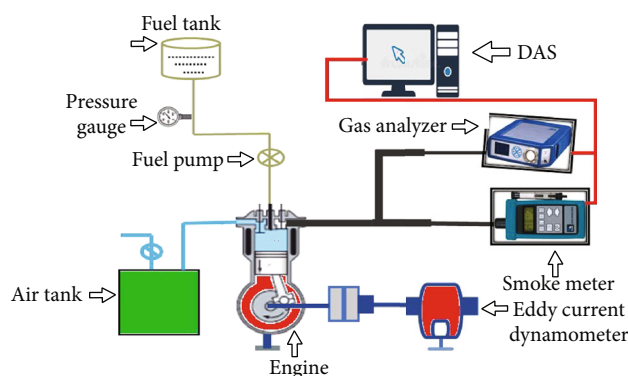


FIGURE 4: Experimental set-up.

number. KOH (potassium hydroxide) was taken as 8 grams. The catalyst was mixed with methanol (methoxide), the methoxide mixture was added to the sample, and the mixture was mixed at 50–60°C for approximately 2 hours. The glycerin was decanted and separated, and then, 3 to 4 washes with water (20–30% (v/v) depending on the yield of biodiesel) were carried out, followed by drying and filtering [9]. The separation of glycerol from biodiesel is shown in Figure 2.

2.2. Fuel Samples. Figure 3 shows photographs of the biodiesel mixes in nanoparticles. It was created by mixing 20% biodiesel and 80% diesel on a volumetric basis in a magnetic stirrer to create the *C. vulgaris* algal methyl ester blend (B20), which was then tested. As previously reported, ZnO nanoparticles were also disseminated into B20 fuel test samples at dose levels of 50 and 100 parts per million (ppm) using an ultrasonicator. This experiment employed B20, B20+50 ppm ZnO, and B20+100 ppm ZnO as the starting materials. To measure the qualities of these fuels, we used ASTM D 6751, a standard procedure for testing fuel parameters [10]. The properties of fuel blends are shown in Table 1.

2.3. Experimental Set-Up. The engine used for the experimental analysis was a one-cylinder four-stroke CI engine (Make: Kirloskar, TV1 model engine with overhead valves controlled by pushrods) with a water-cooled system, which was employed for the experiments. The engine can provide 5.2 kW of output power at 1500 rpm when operating at full load. The fuel injection pressure and timing were maintained at 23° before TDC and 210 bar, respectively, by the manufacturer's recommendations. The coolant was circulated through the water jackets in the cylinder, and the tem-

perature of the coolant was maintained at 80°C throughout the process. To measure the in-cylinder pressure, a piezoelectric transducer was flush-mounted on the cylinder head of the engine. The engine was equipped with an eddy current dynamometer, which measured torque. The experimental set-up is schematically depicted in Figure 4, which illustrates the schematic diagram. The engine specification is shown in Table 2.

3. Result Analysis

Statistically, general and mixed linear models were made using fuel type and load as factors with all the data. To analyze the assumption of errors with normal distribution, the normality was analyzed using the Shapiro-France test for each parameter of all the measured variables.

4. Performance Analysis

4.1. Power Test. Each type of fuel mixture is represented in Figure 5, with the power developed by the engine operating at a fixed speed of 3600 rpm and four variable loads increased by 25% for each type of fuel mixture being used as a baseline. The power developed by the mixture B20+100 ppm ZnO is being used as a reference. The power values for each type of mixture differ by an average of 0.01 kw, indicating that there is no significant change in this operational feature compared to the base power. Figure 5 depicts the results for each load applied to the engine and for each of the various blends. The power does not change about the power deemed to be the base (B20). In the same way, the power increases as the load increases, demonstrating the distinctive line that is commonly observed [11].

4.2. Torque Test. Figure 6 shows that the engine torque values are practically the same for each load group and each type of mixture, showing an increasing trend practically linear as the load increases. The figure shows that the types of fuel do not influence the result of the engine torque [1]. This corresponds to each load imposed on the engine, and its tendency is growing as the imposed load grows (B20+100 ppm ZnO), as shown by the trend line.

4.3. Consumption Test. The results of Figure 7 show that in commercial fuel, the hourly consumption is lower than the consumption with the mixtures almost in the entire range of load [12]. This increased consumption in the mixture of commercial fuel with algae biodiesel is due to a kind of compensation due to the lower calorific value of biodiesel compared to B20. Figure 7 shows the trend that the hourly

TABLE 2: Engine specification.

Engine type	Make Kirloskar 1 cylinder, 4 stroke water-cooled, diesel (computerized), modified to VCR engine
Model	TV1
Bore diameter	87.50 mm
Stroke	110.00 mm
Combustion principle	Compression ignition
Engine capacity	661 cc
Peak pressure	77.5 kg/cm ²
Power	5.2 kW at 1500 rpm
Dynamometer	Eddy current dynamometer cooled by water includes a loading unit
Airbox	Fabricated by MS including an orifice meter and U-tube manometer
Fuel tank	Maximum capacity of 15 liters including metering column
Piezoelectric sensor	Range 345 bar, including no noise cable
Encoder	1 degree resolution, 5500 RPM speed including TDC pulse
Data acquisition system	NI USB-6210, 250 kb/s, bit-16
Digital voltmeter	0-200 mV range mounted on panel
Temperature detector	RTD type, K-type thermocouple, and PT100
Load indicator	0-50 kg range, digital type
Load sensor	Strain gauge with 0-50 kg range
Direction of rotation	Clockwise (looking from flywheel end side)
Idle speed range	750 rpm to 2000 rpm
Min. running speed	1200 rpm
Fuel timing for the engine	23 ^o BTDC
Valve clearance	At inlet 0.18 mm
Valve clearance	At exhaust 0.20 mm
Bumping clearance	0.046 inch to 0.052 inch
BMEP at 1500 rpm	6.35 kg/cm ²
Lubricating oil pump	Gear type
Lub. oil pump	6.50 lit/min

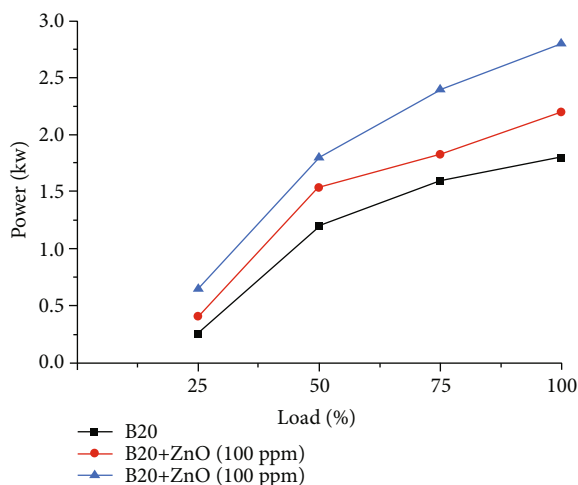


FIGURE 5: Variation of power vs. load.

consumption curve has with any of the mixtures used depending on the loads adjusting to the expected characteristic [13]. The minimum hourly consumption is given with a biodiesel mixture. The consumption is lower for all types of fuel.

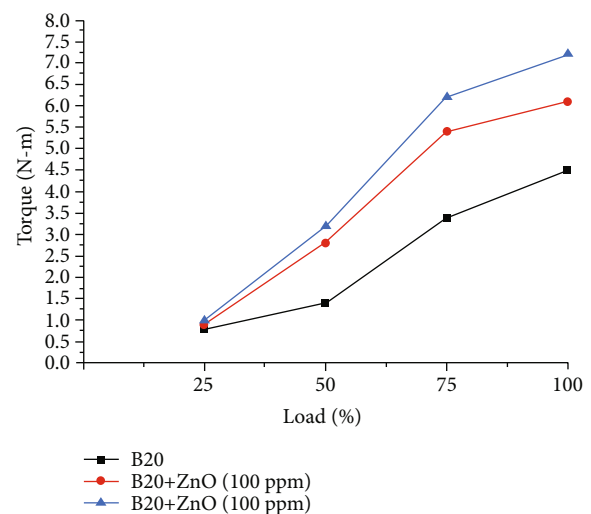


FIGURE 6: Variation of torque vs. load.

5. Emission Analysis

5.1. CO Emission Test. Figure 8 shows that the values of the emissions both in a low load or high load close to the

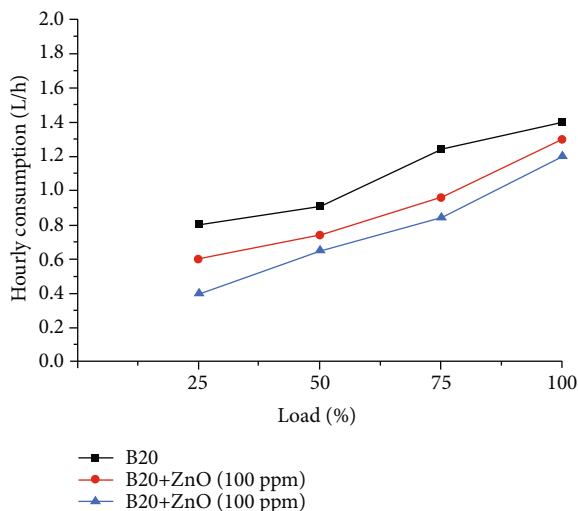


FIGURE 7: Variation of hourly consumption vs. load.

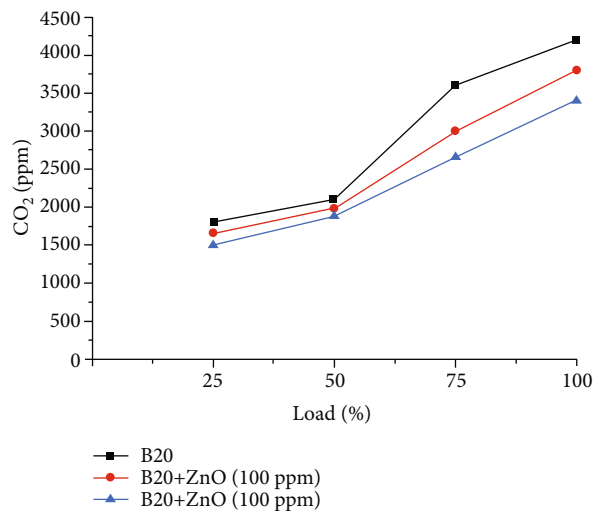
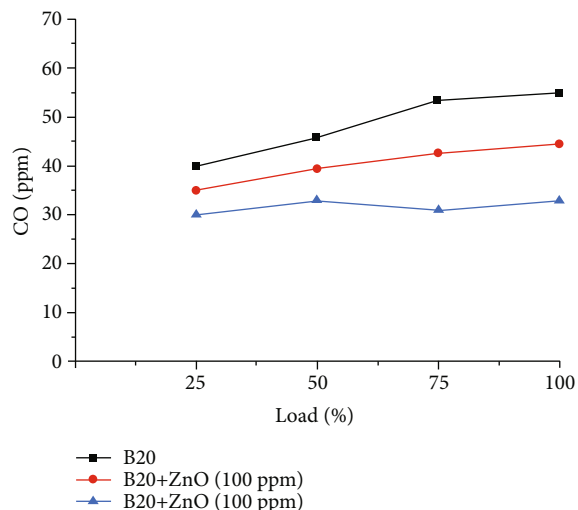
FIGURE 9: Variation of CO₂ vs. load.

FIGURE 8: Variation of CO vs. load.

maximum power increase its emission of CO [14]. According to the theory, the scarcity of oxygen produces an increase in CO. It means that the richness of the fuel is greater than the ratio of the fuel-air mixture [13]. In Figure 8, it can see that in the range of operation, the CO emission is lower for any mixture, also being the mixture with B20+100 ppm ZnO has lower emissions than B20 [15].

5.2. CO₂ Emission Test. From the data shown in Figure 9, it is observed that the emission of CO₂ increases proportionally to the increase in all loads. In the case of fuel mixed with algae biodiesel, these figures drop considerably reduction of 20% to 25% in CO₂ emissions in general [16]. In Figure 9, it can see that the CO₂ emission for each load to which it is subjected to the engine with B20. The highest proportion of CO₂ in general is for the mixture of B20 blend [17]. It can ensure that the mixture of B20+100 ppm ZnO considerably reduces this greenhouse gas emission.

6. Conclusion

Algae oil represents an important source of input to be used in biodiesel production due to a large amount of consumption at the national level and world. Biodiesel made from algal oil is a third- or fourth-generation renewable fuel that does not impact food security. Using algal oil as a biodiesel raw material discharges a lower rate of harmful gases into the atmosphere. The energy capacity of algae oil biodiesel is higher than that of commercial diesel. The mechanical effects of blended biodiesel with ZnO nano additives are similar to those of commercial diesel, increasing power, and reduced emission than B20.

Data Availability

The data used to support the findings of this study are included in the article.

Conflicts of Interest

The authors declare that they have no conflicts of interest regarding the publication of this paper.

References

- [1] Z. Chen, H. Chen, L. Wang, L. Geng, and K. Zeng, "Parametric study on effects of excess air/fuel ratio, spark timing, and methanol injection timing on combustion characteristics and performance of natural gas/methanol dual-fuel engine at low loads," *Energy Conversion and Management*, vol. 210, article 112742, 2020.
- [2] A. Khanra, S. Vasistha, and M. P. Rai, "Glycerol on lipid enhancement and FAME characterization in algae for raw material of biodiesel. International," *Journal of Renewable Energy Research*, vol. 7, no. 4, 2017.
- [3] S. Zighmi, S. Ladjel, M. B. Goudjil, and S. E. Bencheikh, "Renewable energy from the seaweed *Chlorella pyrenoidosa* cultivated in developed systems," *International Journal of Renewable Energy Research*, vol. 7, no. 1, 2017.

- [4] S. R. Hamed, M. G. Mahamoud, and B. Abo-el-khair, "Complementary production of biofuels by the green alga *Chlorella vulgaris*," *International Journal of Renewable Energy Research*, vol. 5, no. 3, 2015.
- [5] S. Raviteja, "Combustion characteristics of waste cooking oil bio diesel on four stroke diesel engine using additives," *Turkish Journal of Computer and Mathematics Education*, vol. 12, no. 13, 2021.
- [6] Y. Li, M. Jia, L. Xu, and X. S. Bai, "Multiple-objective optimization of methanol/diesel dual-fuel engine at low loads: a comparison of reactivity controlled compression ignition (RCCI) and direct dual fuel stratification (DDFS) strategies," *Fuel*, vol. 262, article 116673, 2020.
- [7] L. Ning, Q. Duan, Z. Chen et al., "A comparative study on the combustion and emissions of a non-road common rail diesel engine fueled with primary alcohol fuels (methanol, ethanol, and n-butanol)/diesel dual fuel," *Fuel*, vol. 266, article 117034, 2020.
- [8] A. P. Singh, N. Sharma, D. P. Satsangi, and A. K. Agarwal, "Effect of fuel injection pressure and premixed ratio on mineral diesel-methanol fueled reactivity controlled compression ignition mode combustion engine," *Journal of Energy Resources Technology*, vol. 142, no. 12, article 122301, 2020.
- [9] R. Surakasi, M. Y. Khan, A. S. Sener et al., "Analysis of environmental emission neat diesel-biodiesel-algae oil-nanometal additives in compression ignition engines," *Journal of Nanomaterials*, vol. 2022, Article ID 3660233, 7 pages, 2022.
- [10] T. Blumberg, G. Tsatsaronis, and T. Morosuk, "On the economics of methanol production from natural gas," *Fuel*, vol. 256, article 115824, 2019.
- [11] C. Chen, A. Yao, C. Yao et al., "Study of the characteristics of PM and the correlation of soot and smoke opacity on the diesel methanol dual fuel engine," *Applied Thermal Engineering*, vol. 148, pp. 391–403, 2019.
- [12] C. Gong, Z. Li, Y. Chen, J. Liu, F. Liu, and Y. Han, "Influence of ignition timing on combustion and emissions of a spark-ignition methanol engine with added hydrogen under lean-burn conditions," *Fuel*, vol. 235, pp. 227–238, 2019.
- [13] Z. Li, Y. Wang, H. Geng et al., "Parametric study of a diesel engine fueled with directly injected methanol and pilot diesel," *Fuel*, vol. 256, article 115882, 2019.
- [14] G. Vaidya, P. P. Patil, A. S. Sener et al., "Chlorella protothecoides algae oil and its mixes with lower and higher alcohols and Al_2O_3 metal nanoadditives for reduction of pollution in a CI engine," *Journal of Nanomaterials*, vol. 2022, Article ID 9658212, 6 pages, 2022.
- [15] L. Ning, Q. Duan, H. Kou, and K. Zeng, "Parametric study on effects of methanol injection timing and methanol substitution percentage on combustion and emissions of methanol/diesel dual-fuel direct injection engine at full load," *Fuel*, vol. 279, article 118424, 2020.
- [16] M. Sairam, S. Raviteja, Y. S. Ratnakar, and V. V. Prasanna Kumar, *Performance Evaluation and Emission Characteristics of Organic Sunflower Oil Biodiesel Using Additives*, Design Engineering, 2021.
- [17] H. Venu and V. Madhavan, "Influence of diethyl ether (DEE) addition in ethanol-biodiesel-diesel (EBD) and methanol-biodiesel-diesel (MBD) blends in a diesel engine," *Fuel*, vol. 189, pp. 377–390, 2017.

Retraction

Retracted: Nanometal-Based Magnesium Oxide Nanoparticle with *C. vulgaris* Algae Biodiesel in Diesel Engine

Journal of Nanomaterials

Received 10 October 2023; Accepted 10 October 2023; Published 11 October 2023

Copyright © 2023 Journal of Nanomaterials. This is an open access article distributed under the Creative Commons Attribution License, which permits unrestricted use, distribution, and reproduction in any medium, provided the original work is properly cited.

This article has been retracted by Hindawi following an investigation undertaken by the publisher [1]. This investigation has uncovered evidence of one or more of the following indicators of systematic manipulation of the publication process:

- (1) Discrepancies in scope
- (2) Discrepancies in the description of the research reported
- (3) Discrepancies between the availability of data and the research described
- (4) Inappropriate citations
- (5) Incoherent, meaningless and/or irrelevant content included in the article
- (6) Peer-review manipulation

The presence of these indicators undermines our confidence in the integrity of the article's content and we cannot, therefore, vouch for its reliability. Please note that this notice is intended solely to alert readers that the content of this article is unreliable. We have not investigated whether authors were aware of or involved in the systematic manipulation of the publication process.

Wiley and Hindawi regrets that the usual quality checks did not identify these issues before publication and have since put additional measures in place to safeguard research integrity.

We wish to credit our own Research Integrity and Research Publishing teams and anonymous and named external researchers and research integrity experts for contributing to this investigation.

The corresponding author, as the representative of all authors, has been given the opportunity to register their agreement or disagreement to this retraction. We have kept a record of any response received.

References

- [1] J. Arunprasad, A. N. Krishna, D. Radha, M. Singh, R. Surakasi, and T. D. Gidebo, "Nanometal-Based Magnesium Oxide Nanoparticle with *C. vulgaris* Algae Biodiesel in Diesel Engine," *Journal of Nanomaterials*, vol. 2022, Article ID 1688505, 9 pages, 2022.

Research Article

Nanometal-Based Magnesium Oxide Nanoparticle with *C. vulgaris* Algae Biodiesel in Diesel Engine

J. Arunprasad ¹, Alla Naveen Krishna ², Dharavathu Radha ³, Mandeep Singh ⁴,
Raviteja Surakasi ⁵ and Tewodros Derese Gidebo ⁶

¹Department of Mechanical Engineering, Dhanalakshmi Srinivasan Engineering College, Perambalur, India

²Department of Mechanical Engineering, Institute of Aeronautical Engineering, Hyderabad, Telangana, India

³Department of Computer Science and Engineering, Raghu Engineering College, Visakhapatnam, Andhra Pradesh, India

⁴School of Mechanical and Mechatronic Engineering, Faculty of Engineering and Information Technology, University of Technology Sydney, 15 Broadway Ultimo, 2007 Sydney, New South Wales, Australia

⁵Department of Mechanical Engineering, Lendi Institute of Engineering and Technology, Jonnada, Vizianagaram, Andhra Pradesh, India

⁶Department of Mechanical Engineering, Wolaita Sodo University, Ethiopia

Correspondence should be addressed to Tewodros Derese Gidebo; teddyderese@gmail.com

Received 9 February 2022; Revised 20 February 2022; Accepted 10 March 2022; Published 24 March 2022

Academic Editor: Karthikeyan Sathasivam

Copyright © 2022 J. Arunprasad et al. This is an open access article distributed under the Creative Commons Attribution License, which permits unrestricted use, distribution, and reproduction in any medium, provided the original work is properly cited.

Many researchers are interested in biofuels because it is environmentally friendly and potentially reduce global warming. Incorporating nanoparticles into biodiesel has increased its performance and emission characteristics. The current study examines the influence of magnesium oxide nanoadditions on the performance and emissions of a diesel engine that runs on *C. vulgaris* algae biodiesel. The transesterification process produced methyl ester from *C. vulgaris* algae biodiesel. The morphology of nanoadditives was studied using scanning electron microscopy, transmission electron microscopy, and energy-dispersive X-ray spectroscopy. The fuel sample consisted of biodiesel blends with and without magnesium oxide nanoadditives. The fuel properties of the prepared *C. vulgaris* methyl ester were found to conform with the ASTM standards. The experimental results were determined by running a single-cylinder four-stroke diesel engine at different load conditions. When compared to B20, a B20 blend containing 100 ppm magnesium oxide nanoparticles enhanced brake thermal efficiency while reducing specific fuel consumption, according to the research. When MgO nanoparticles were introduced to B20, engine emissions of HC, CO, and smoke were decreased.

1. Introduction

Depleting fossil fuels, rising fuel consumption, uncertainty in fuel price, and serious environmental concerns have prompted us to research alternative fuels for compression ignition engines [1]. Biodiesel is a feasible alternative fuel for diesel engines compared to other fuels. Biodiesel is an oxygenated fuel that is biodegradable, non-toxic, and environmentally friendly [2]. Many studies have shown that biodiesel is made from various seeds. Blending, pyrolysis, microemulsion, and transesterification have all been suggested as processes for producing biodiesel.

Transesterification is the most powerful biodiesel production technology due to its high conversion rate. Biodiesel has a higher viscosity than diesel; using biodiesel alone in current diesel engines will be challenging. As a result, it is preferable to mix biodiesel with diesel to get the required blend properties for present diesel engines. Biodiesel appears to have significant drawbacks, including a low heating value, high density, and higher viscosity. It affects fuel atomization in the combustion chamber, lowering the combustion pressure and temperature [3]. To improve biodiesel's performance and emission characteristics as fuel to CI engines, various researchers promoted the usage of nanoparticles as

additives. They resulted in better performance and emission characteristics due to high surface reactivity. Maximum of the studies on nanoparticle additive on the fuel has collective consent that metal additives at nanoscale improved catalytic action during combustion progression, which stimulates and promotes complete combustion [4]. They assessed the performance and emission characteristics of mahua biodiesel that included copper oxide nanoparticles. The CuO blended fuel improved BTE by 2.2% while decreasing BSFC marginally. In addition, CuO nanoadditive blended fuel decreases hydrocarbon, carbon monoxide, and smoke emissions by 5.34, 32, and 12.6%, respectively [5]. They discovered that adding silver oxide nanoparticles to BD100 increased BTE and reduced BSFC in diesel engines. When BD100+ Ag₂O (10 ppm) was utilized to replace BD100, CO, HC, NO_x, and smoke emissions were decreased by 16.47%, 14.21%, 6.66%, and 8.34%, respectively [6]. Compared to a blend without copper oxide, the pongamia methyl ester with copper oxide blends reduces HC, CO, NO_x, and smoke. Brake thermal efficiency increased by 4.01% during the same period, while specific fuel consumption decreased by 1% [7]. The performance and emission characteristics of mahua methyl ester blends with aluminum oxide nanoparticles were investigated in this study. According to the findings, aluminum oxide nanoparticles incorporated in biodiesel have a significant advantage over mineral diesel in brake thermal efficiency [8]. Mahua oil blended with nanoadditions emits less CO, HC, NO_x, and smoke than standard fuel. According to a literature survey, only a few tests have been undertaken in single-cylinder compression ignition engines using algal biodiesel with nanoadditions. Magnesium oxide nanoadditives are incorporated in varying amounts in *C. vulgaris* algae biodiesel in this study (50 ppm and 100 ppm). The prepared fuel blends' performance and emission characteristics were examined using the CI engine, and the results were compared to B20.

2. Materials and Method

2.1. Biofuel from Microalgae. Microalgae have a less complex structure, comparatively faster growth rate, higher photosynthetic rates, and high oil contents that make them unique over first-generation biofuel feedstock. As algae can be cultivated in shallow water, pond, and bioreactor, it could help in saving the agricultural land to cultivate more food crops. The main reason for selecting *C. vulgaris* algae is that these photosynthetic microalgae are available as fresh water and marine algae growing in normal climatic conditions. It is a great source of biomass, and the methyl ester extracted from it is seen as a promising alternative to fossil fuel. The high lipid content in the algae makes it suitable for the extraction of methyl ester and its use as an alternate fuel.

2.2. *Chlorella vulgaris* Algae Biodiesel. *C. vulgaris* is a prominent source of attraction for biodiesel production since it contains hydrocarbons in 40-75% of its dry mass. *C. vulgaris* can survive in various kinds of environments. *C. vulgaris* can grow in various conditions, including calm freshwater with low nutrient content.



FIGURE 1: After the transesterification process of *C. vulgaris* methyl ester.

2.3. Transesterification of *C. vulgaris* Algae Biodiesel. The transesterification method is used to reduce the viscosity of *Chlorella vulgaris* oil. The 5.3 grams of NaOH and 300 ml of methanol are blended to avoid methanol evaporation in a closed container. The raw *C. vulgaris* oil is next heated to 40°C with continual uniform stirring. Every 30 minutes, a burette is filled with NaOH and methanol, which is subsequently blended with raw *C. vulgaris* oil. In addition, the temperature should be between 50 and 60°C. This temperature may be measured using a thermometer. A container containing a mixture of raw *C. vulgaris* oil, methanol, and NaOH is taken, and the combination is thoroughly mixed using a stirrer. The combination is heated using a heating instrument, and the mixture's temperature is recorded. With raw *C. vulgaris* oil, a combination of methanol and NaOH is placed in a container and left to settle for 10 hours. Figure 1 depicts the transesterification of *C. vulgaris* biodiesel. At the end of 10 hours, the ester and glycerol are separated. Figure 2 depicts the chemical process of transesterification.

2.4. Nanoparticle Characterization. The interaction of the high-energy electron beam with the sample enables the scanning electron microscope to obtain information on the topography, morphology, and composition of solids. The detector in SEM observes X-rays, backscattered electrons, and secondary electrons and converts them into a signal to produce a final image. EDX is one of the standard analytic surface techniques used for an unknown sample's elemental detection and composition. EDX technique is generally associated with the SEM instrument. Sometimes, EDX is also used to work in combination with the transmission electron microscope and scanning transmission electron microscope. The X-rays of different wavelengths emitted by the specimen atoms are energy-specific and carry information about a particular atom. The position of the peak in the histogram plot represents the energy correlated with the concerned element, and the area under the peak provides information about the number of atoms irradiated in the

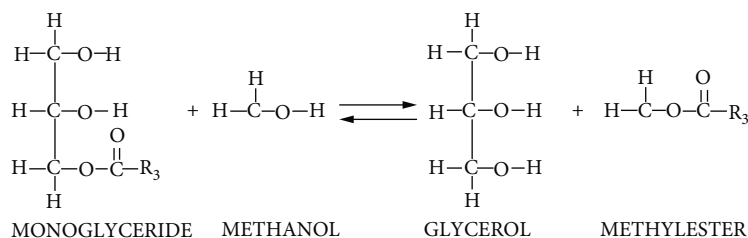


FIGURE 2: The chemical reaction in transesterification.



FIGURE 3: Biodiesel with nanoadditive blends.

selected area. The crystalline structure, particle shape, and elemental composition of MgO were investigated morphologically using a JEOL-JSM-IT 200 scanning electron microscope armed with only an Energy-Dispersive X-ray analyzer. The sample was accelerated between 0.5 and 30 kV. The nanoparticle pictures were acquired using a JEOL JEM-1200EX transmission electron microscope.

2.5. Fuel Samples. Figure 3 depicts photographic views of the various biodiesel blends. The *C. vulgaris* algae methyl ester blend (B20) was produced using a magnetic stirrer by blending 20% biodiesel and 80% diesel on a volumetric basis. Furthermore, using an ultrasonicator, MgO nanoparticles were disseminated into B20 fuel test samples at dose levels of 50 and 100 ppm. B20, B20 + 50 ppm MgO, and B20 + 100 ppm MgO were used in this experiment. Table 1. Properties of these fuels are measured using ASTM D 6751, which is a prescribed method for testing fuel properties.

2.6. Experimental Set-Up. The test rig used for experimental analysis was a one-cylinder four-stroke CI engine (Make: Kirloskar, TV1 model engine with over-head valves controlled by pushrods) with a water-cooled system. The engine can deliver an output power of 5.2 kW at 1500 rpm at full load. The fuel injection pressure and timing were kept at 23° before TDC and 210 bar as recommended by the manufacturer. The coolant was circulated through the water jackets in the cylinder, and the coolant temperature was maintained at 80°C. A piezoelectric transducer was flush-mounted on the cylinder head to measure the in-cylinder pressure. Eddy current dynamometer was fitted to the engine to measure torque. Figure 4 shows the schematic diagram of the experimental set-up.

3. Results and Discussion

3.1. Scanning Electron Microscope. Figure 5 shows an SEM image of magnesium oxide nanoparticles. These findings indicate that particles with flat surfaces were approximately spherical. In certain instances, the particles were found to be evenly dispersed, and in others, they were discovered to be consolidated. The black color in the particles represents the carbon concentration with some oxygen distributed among them. Overall, the distribution of particles is found to be homogeneous. It demonstrates the existence of roughly spherical nanoparticles varying in size from 20 to 38 nm.

3.2. Energy-Dispersive X-Ray Analyzer. The EDX spectrum was used to analyze components quantitatively and qualitatively. The EDX analysis of magnesium oxide nanoparticle samples revealed Mg and O component peaks compared to other elements, as shown in Figure 6. The structure of the remaining elements is relatively insignificant. The elements notified in magnesium oxide nanoparticles are magnesium, oxygen, iron sulfide, silicon dioxide, and sodium. On a weight basis, about 50.74% of oxygen, 45.36% of magnesium, 3.24% of silicon dioxide, and 0.66% of sodium were recorded.

3.3. Transmission Electron Microscope. The transmission electron microscope examination can also elucidate the processed magnesium oxide size, structure, and composition. TEM is an essential technique to extract a clear understanding of particle size distribution and nanoparticle size. After interactions, the electrons transmitted and pass through the nanoparticles provide an image or spectra on the imaging screen. Figure 7 TEM image represents that the magnesium oxide formed takes on unusual forms, with diameters ranging from 9.24 to 14.94 nm.

3.4. Brake Specific Fuel Consumption. Brake-specific fuel consumption is the engine's fuel consumption per unit power generated per unit time and is expressed in kg/kWh. The change in specific fuel consumption as a function of load is seen in Figure 8 for all blends. As the load on the engine increments, the BSFC values decrease. The SFC values for B20, B20 + 50 ppm MgO, and B20 + 100 ppm MgO fuel blends are 0.45 kg/kWh, 0.41 kg/kWh, and 0.38 kg/kWh, respectively. The presence of MgO nanoparticles provides further oxidation and stimulates complete combustion, and hence it results in the reduction of BSFC at a constant speed. This was mainly because of the higher

TABLE 1: Properties of different fuel blends.

S. no	Properties	C. vulgaris methyl ester (B20)	B20 + 50 ppm of MgO	B20 + 100 ppm of MgO
1	Kinetic viscosity cSt	6.01	6.19	6.21
2	Density kg/m ³	886	891	893
3	Calorific value MJ/kg	39.14	40.23	40.52
4	Flash point °C	91	126	135
5	Fire point °C	116	134	149

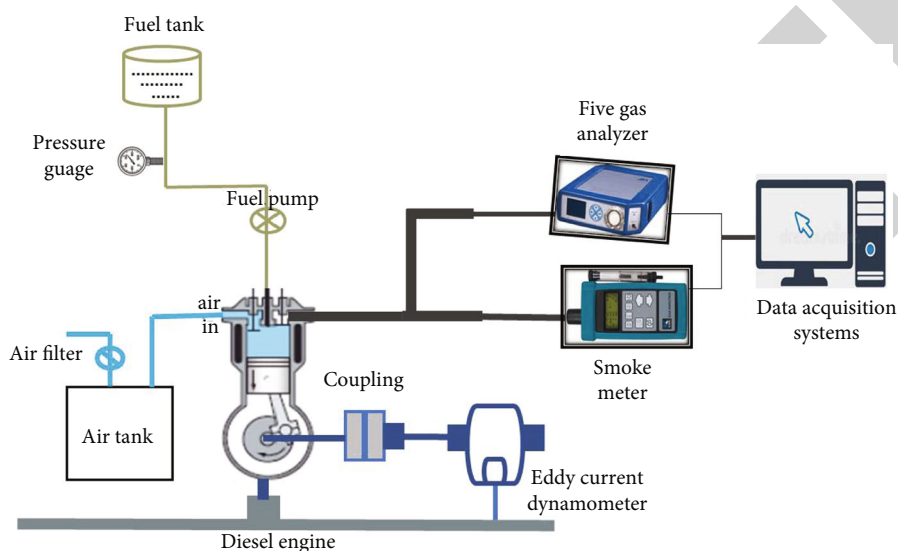


FIGURE 4: Experimental set-up.

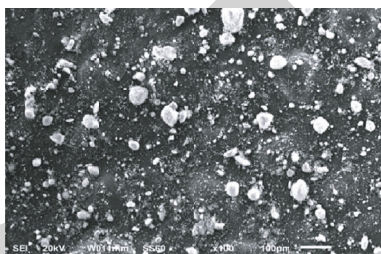


FIGURE 5: SEM image of MgO.

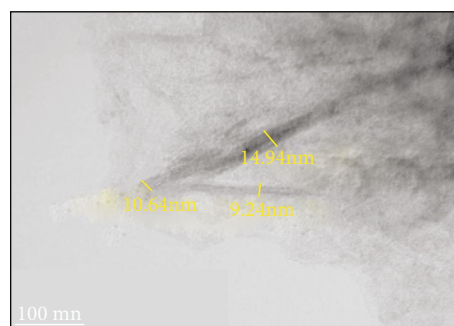


FIGURE 7: TEM image of MgO.

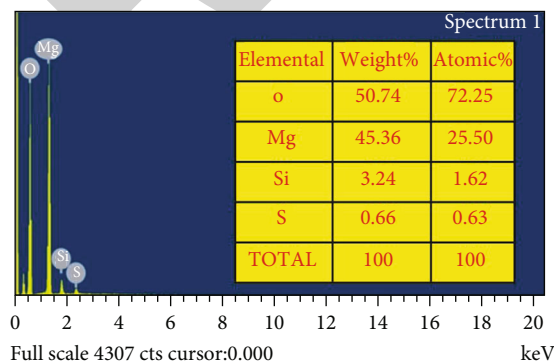


FIGURE 6: EDX image of MgO.

oxygen content in magnesium oxide nanoadditives, which promotes further combustion and decreases the combustion chamber's fuel-rich region. These results concur with previous research on biodiesel and nano-additives [9].

3.5. Brake Thermal Efficiency. BTE of the engine is the ratio of fuel energy to mechanical energy. Fuel energy depends on many parameters such as fuel blend types, carbon and hydrogen atoms present, cetane number, heating value, and specific gravity. Figure 9 shows the changes in BTE for a variety of blended fuels under different engine loads. The brake thermal efficiency for B20, B20 + 50 ppm MgO, and B20 + 100 ppm MgO fuel blends are 24.9%, 25.8%, and 27.3%, respectively.

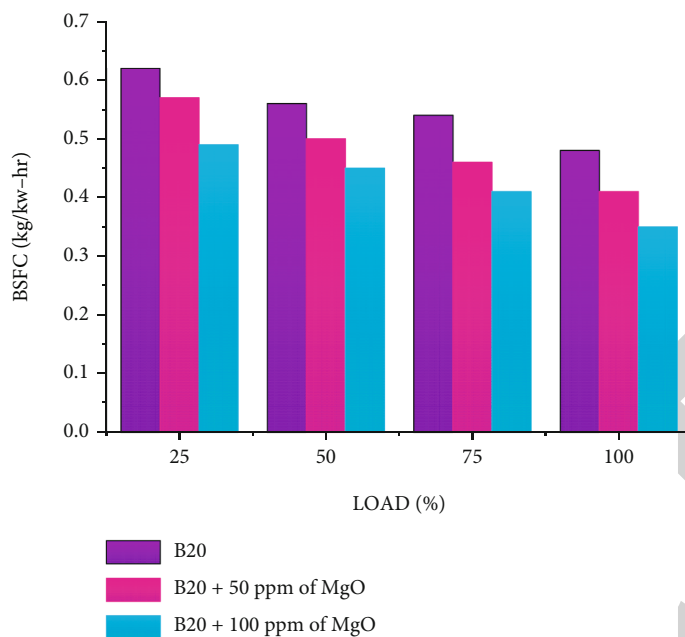


FIGURE 8: Brake specific fuel consumption vs. load.

B20 + 100 ppm MgO blend increased brake thermal efficiency by 2.4% compared to B20. The inclusion of biodiesel reduces the ignition delay, resulting in longer combustion durations. This is due to a decrease in indicated power, peak in-cylinder pressure, and rate of pressure increase, resulting in decreased biodiesel BTE. The inclusion of magnesium oxide nanoparticles, which improve oxidation, heat release rate, and in-cylinder pressure, is primarily responsible for the increased brake thermal efficiency. Nanoparticles in biodiesel blends have a larger surface area to volume ratio than B20, allowing for more combustion within the combustion chamber. Similar outcomes were obtained in the presence of nanoparticles [10].

3.6. Emission of Carbon Monoxide. CO emission occurred due to partial oxidation of carbon in the fuel. The absence of fuel-borne oxygen in diesel's molecular structure might lead to the production of CO emissions. Due to low flame temperature, fuel combustion with insufficient oxygen leads to increased CO.

Figure 10 depicts the fluctuation of CO emissions with load for all fuel samples. As the engine load incremented, the engine CO emissions generally decreased. Carbon monoxide emissions varied the minimum at low load and the maximum at high load. The CO emissions at maximum load conditions were 0.063%, 0.059%, and 0.051% for B20, B20 + 50 ppm MgO, and B20 + 100 ppm MgO, respectively. Adding 100 ppm of MgO nanoparticles to the B20 reduces CO emissions by 19.02% compared to the B20 at full load. MgO nanoadditive blended fuels have a more incredible oxygen content, allowing for complete combustion. The complete combustion process reduces the CO emission [11, 12].

3.7. Hydrocarbon Emission. Incomplete combustion of fossil fuels in an engine, be it petrol or diesel, which are hydrocarbons, has become the primary sources of emissions of hydrocarbons, and it is expressed in terms of ppm. Figure 11 depicts the variance in HC emissions as a different load function for all the samples. For all test fuels, increasing load function showed higher HC emission. The HC emission of B20 + 100 ppm MgO is 27.9% lower than that of B20. The magnesium oxide nanoparticle improves the combustion process within the combustion chamber by enhancing the ignition delay time, increasing the efficiency of the fuel explosion cycle, and boosting the rate of heat escape during fuel combustion. It was concluded that adding magnesium oxide nanoparticles to biodiesel blends decreased hydrocarbon emissions [13, 14].

3.8. Smoke Emission. This was due to a higher amount of fuel with the increasing load, which resulted in rich mixture formation and incomplete combustion. The quantity of unburned hydrocarbons produces ample reasons for smoke emission. Under full load engine conditions, Figure 12 displays the HC emission results for all test fuels. The smoke opacity percentage for B20, B20 + 50 ppm of MgO, and B20 + 100 ppm of MgO test fuels were 28.2%, 26.4%, and 24.5%, respectively. The maximum reduction in smoke opacity is obtained for B20 + 100 ppm of MgO. Compared to B20, the smoke emission of the B20 + 100 ppm MgO blend was reduced by 3.7% at full load. Magnesium oxide nanoparticles accelerate evaporation, and material oxidation ensures complete combustion. The catalytic activity of nanoparticles in biodiesel blends enhanced further oxidation of soot particles, resulting in more reduction of smoke emissions than biodiesel blends without additives [15, 16].

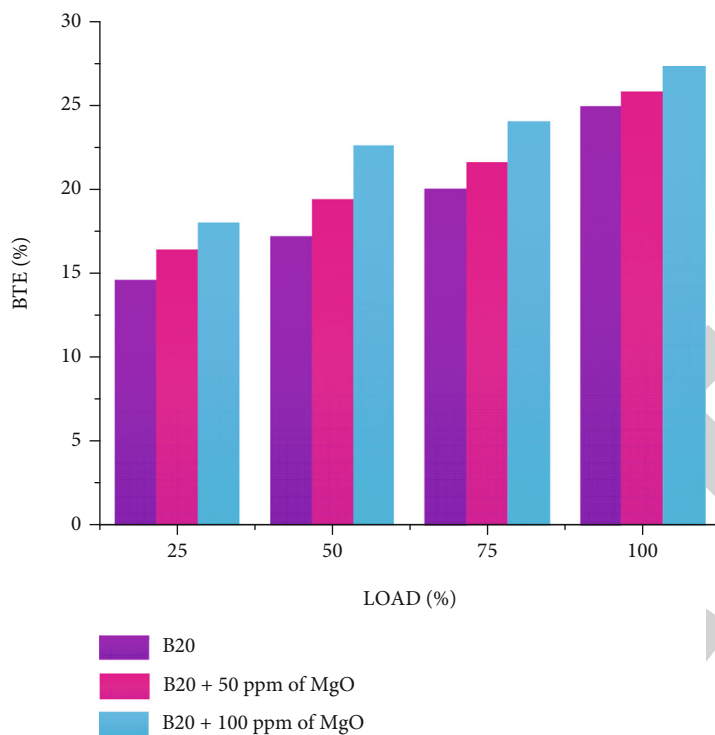


FIGURE 9: Brake thermal efficiency vs. load.

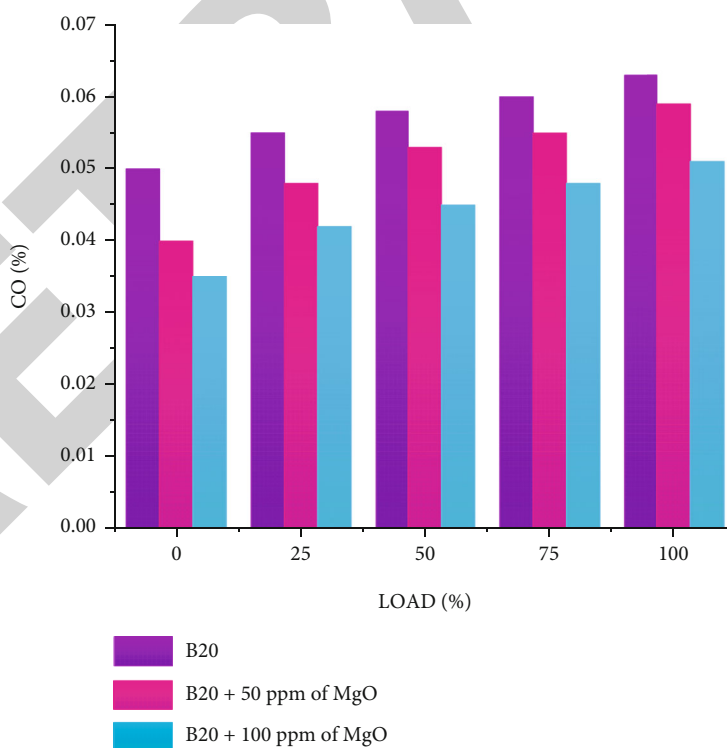


FIGURE 10: Carbon monoxide vs. load.

3.9. *Nitrogen Oxide Emission.* The emission of oxides of nitrogen takes place from an internal combustion engine when nitrogen present in the air combines with oxygen. This occurs at a high temperature in the engine cylinder. The var-

iation of NO_x formation versus different engine load is shown in Figure 13, for B20, B20 + 50 ppm MgO, and B20 + 100 ppm MgO. The combustion temperature of B20 + 50 ppm of MgO and B20 + 100 ppm of MgO blends

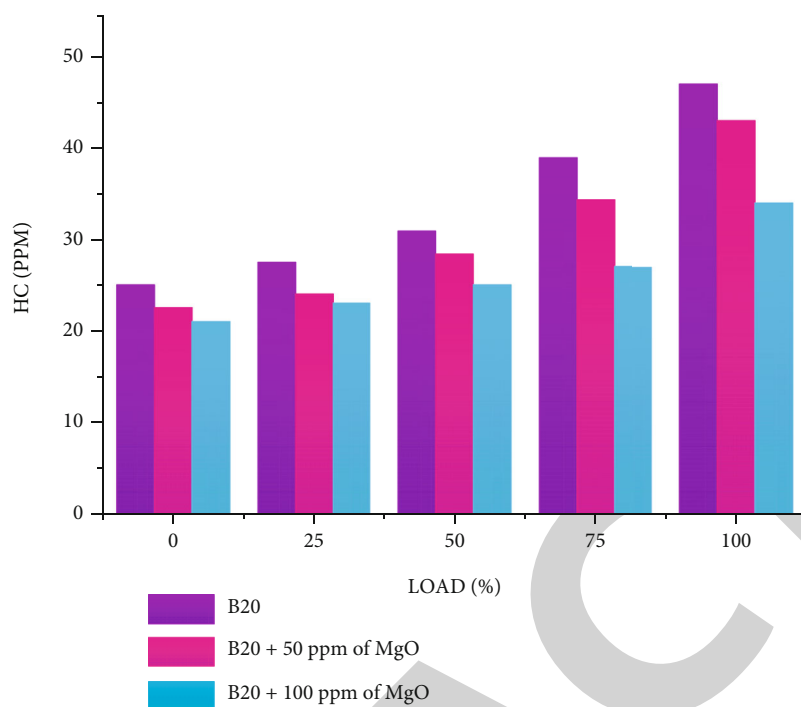


FIGURE 11: Hydrocarbon emission vs. load.

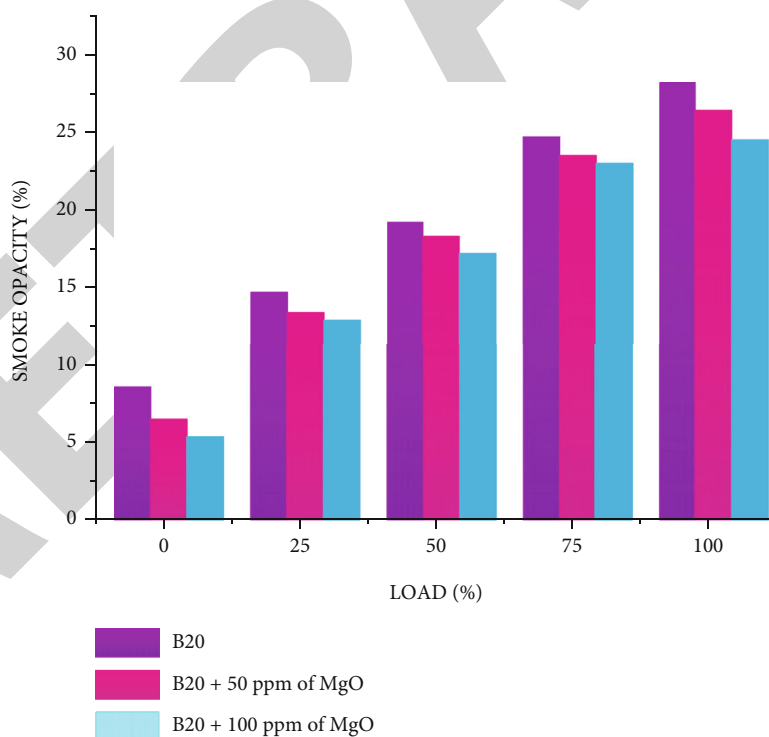


FIGURE 12: Smoke emission vs. load.

substantially increased due to an increase in O_2 , resulting in a high combustion temperature in the cylinder. The B20 + 100 ppm MgO blend emits more NO_x than the B20 blend. This could be due to the presence of oxygen in nanoadditions, causing biodiesel blends with additives to burn

entirely than B20. For biodiesel blends with additives, this raises the maximum temperature within the cylinder. Because of the nitrogen oxidation processes in the engine cylinder, biodiesel with additives releases more NO_x [17, 18].

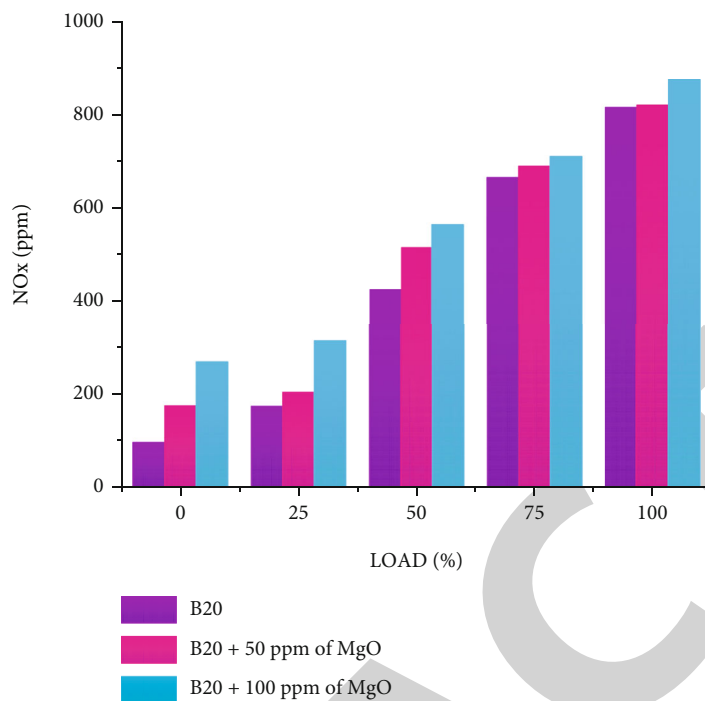


FIGURE 13: Nitrogen oxide emission vs. load.

4. Conclusion

The performance and emission characteristics of MgO nanoparticle incorporated *C. vulgaris* fuel were investigated using a single-cylinder diesel engine under different load conditions. The properties were determined following ASTM D6751 standards. Because of its enhanced combustion properties, the MgO nanoparticle impregnated *C. vulgaris* fuel improved engine performance. In addition, the MgO mixed fuel resulted in lower levels of HC, CO, and smoke emissions. The following conclusions were drawn based on the experimental results. Due to its higher density, viscosity, and lower calorific value, the B20 test fuel had a 15.8% increase in BSFC compared to B20 + 100 ppm of MgO. Compared with B20, brake thermal efficiency increases of 1.9% and 2.4% are obtained for B20 + 50 ppm MgO and B20 + 100 ppm MgO. Carbon monoxide emissions for B20 + 50 ppm MgO and B20 + 100 ppm MgO are reduced by 13.5% and 19.04%, respectively, compared to B20. CO emissions were reduced when the nanoparticle concentration was increased. Hydrocarbon emissions are reduced by 12.81% and 27.9% for B20 + 50 ppm MgO and B20 + 100 ppm MgO, respectively, compared to B20. The MgO nanoadditives added to biodiesel-diesel blends resulted in better combustion. The MgO nanoparticle blended fuel has lower HC emissions when compared with B20. Compared to B20, smoke emissions for B20 + 50 ppm MgO and B20 + 100 ppm MgO are reduced by 1.9% and 3.7%, respectively. When the concentration of nanoparticles was raised, smoke emissions were lowered. The higher oxygen content in B20 + 100 ppm of MgO fuel blend leads to higher combustion temperature, resulting in higher NO_x emission.

Data Availability

The data used to support the findings of this study are included in the article.

Conflicts of Interest

The authors declare that they have no conflicts of interest regarding the publication of this paper.

References

- [1] A. Sharma, Y. Singh, N. Kumar Singh, A. Singla, H. Chyuan Ong, and W. H. Chen, "Effective utilization of tobacco (*Nicotiana tabacum*) for biodiesel production and its application on diesel engine using response surface methodology approach," *Fuel*, vol. 273, article 117793, 2020.
- [2] W. N. Maawa, R. Mamat, G. Najafi, and L. P. H. De Goeij, "Performance, combustion, and emission characteristics of a CI engine fueled with emulsified diesel-biodiesel blends at different water contents," *Fuel*, vol. 267, article 117265, 2020.
- [3] E. Sadeghinezhad, S. N. Kazi, A. Badarudin, C. S. Oon, M. N. M. Zubir, and M. A. Mehrli, "Comprehensive review of biodiesel as alternative fuel for compression ignition engines," *Renewable and Sustainable Energy Reviews*, vol. 28, pp. 410–424, 2013.
- [4] A. Kadarohman, Hernani, F. Khoerunisa, and R. M. Astuti, "A Potential study on clove oil, eugenol and eugenyl acetate as diesel fuel bio-additives and their performance on one cylinder engine," *Transport*, vol. 25, no. 1, pp. 66–76, 2010.
- [5] S. Raviteja, "Combustion characteristics of waste cooking oil bio diesel on four stroke diesel engine using additives," *Turkish*

Retraction

Retracted: Analysis of Environmental Emission Neat Diesel-Biodiesel–Algae Oil-Nanometal Additives in Compression Ignition Engines

Journal of Nanomaterials

Received 11 July 2023; Accepted 11 July 2023; Published 12 July 2023

Copyright © 2023 Journal of Nanomaterials. This is an open access article distributed under the Creative Commons Attribution License, which permits unrestricted use, distribution, and reproduction in any medium, provided the original work is properly cited.

This article has been retracted by Hindawi following an investigation undertaken by the publisher [1]. This investigation has uncovered evidence of one or more of the following indicators of systematic manipulation of the publication process:

- (1) Discrepancies in scope
- (2) Discrepancies in the description of the research reported
- (3) Discrepancies between the availability of data and the research described
- (4) Inappropriate citations
- (5) Incoherent, meaningless and/or irrelevant content included in the article
- (6) Peer-review manipulation

The presence of these indicators undermines our confidence in the integrity of the article's content and we cannot, therefore, vouch for its reliability. Please note that this notice is intended solely to alert readers that the content of this article is unreliable. We have not investigated whether authors were aware of or involved in the systematic manipulation of the publication process.

Wiley and Hindawi regrets that the usual quality checks did not identify these issues before publication and have since put additional measures in place to safeguard research integrity.

We wish to credit our own Research Integrity and Research Publishing teams and anonymous and named external researchers and research integrity experts for contributing to this investigation.

The corresponding author, as the representative of all authors, has been given the opportunity to register their

agreement or disagreement to this retraction. We have kept a record of any response received.

References

- [1] R. Surakasi, M. Y. Khan, A. S. Sener et al., "Analysis of Environmental Emission Neat Diesel-Biodiesel–Algae Oil-Nanometal Additives in Compression Ignition Engines," *Journal of Nanomaterials*, vol. 2022, Article ID 3660233, 7 pages, 2022.

Research Article

Analysis of Environmental Emission Neat Diesel-Biodiesel–Algae Oil-Nanometal Additives in Compression Ignition Engines

Raviteja Surakasi ¹, Mohd Yunus Khan ², Arif Senol Sener ³, Tushar Choudhary ⁴,
Sumantha Bhattacharya ⁵, Piyush Singhal ⁶, Bharat Singh ⁶,
and Velivela Lakshmikanth Chowdary ⁷

¹Department of Mechanical Engineering, Lendi Institute of Engineering and Technology, Vizianagaram, Andhra Pradesh, India

²Department of Mechanical Engineering, National Institute of Technical Teachers Training and Research, Chandigarh, India

³Department of Mechanical Engineering, Engineering and Architecture Faculty, Nisantasi University, Istanbul, Turkey

⁴Department of Mechanical Engineering, PDPM Indian Institute of Information Technology Design and Manufacturing, Jabalpur, Madhya Pradesh, India

⁵Department of Textile Technology, MAKAUT, West Bengal, India

⁶Department of Mechanical Engineering, GLA University Mathura, Mathura, Uttar Pradesh, India

⁷Department of Mechanical Engineering, Wolaita Sodo University, Ethiopia

Correspondence should be addressed to Velivela Lakshmikanth Chowdary; lucky.19862@gmail.com

Received 31 January 2022; Revised 13 February 2022; Accepted 15 February 2022; Published 28 February 2022

Academic Editor: Karthikeyan Sathasivam

Copyright © 2022 Raviteja Surakasi et al. This is an open access article distributed under the Creative Commons Attribution License, which permits unrestricted use, distribution, and reproduction in any medium, provided the original work is properly cited.

The production of biodiesel as an alternative fuel and its use as a mixture and other additives are presented. In the present research work, additive blends with diesel biodiesel from algae oil are physically characterised and an analysis of pollutant emissions is carried out when used in an ignition engine by compression. The measurement of pollutant emissions is carried out through a combined emission analyzer adapted to a system of valves attached to the experimental facility. The properties of each mixture with the polluting emissions are compared with that of the reference diesel. It was found that each of the properties improves compared to that of diesel, reducing most emissions in the use of mixtures with biodiesel.

1. Introduction

Natural resources such as oil, natural gas, and coal have a wide range of applications in science and technology; these resources and their derivatives are widely utilised in power plants, boilers, and some car engines to meet people's demands worldwide. On the other side, the rapid growth of humanity has increased energy demand, which is predicted to increase by 50% by 2040 compared to current levels. This has resulted in a faster depletion of these nonrenewable resources, which are the study of renewable energies which aim to ensure energy security in some form [1]. The energy resources from oil, natural gas, and coal are not sustainable to meet energy demand. The fields identified are dwindling, and there are environmental constraints for

their exploration and development and geopolitical issues. It leads to possible oil and gas reserves and gas becoming scarcer and the exploitation of more restrictive carbon regulations. The increasing industrialization, the motorization of the world, and climate changes have resulted in the hunt for alternative fuels that may be generated using raw materials available in any country. The world's vehicle fleet is powered by gasoline and diesel, which pollute the environment due to their polluting emissions, so bioenergetics such as biomass, biogas, primary alcohols, vegetable oils, animal oils, and biodiesel have been studied. Although the fuels above are part of the solution to the challenge of being environmentally friendly, advantages and disadvantages in their use must be examined in each of them. It is crucial to note that some of the fuels mentioned above can be used directly. Still,

others must be treated or formulated so that their qualities are comparable to those of the conventional fuel being replaced. Biodiesel and bioethanol are the most widely used biofuels in the world [2]. It is critical to have a clean fuel that does not pollute like traditional diesel and is also nontoxic as it can be used as a mixture with diesel to improve the mechanical efficiency of the engines. High lubricating properties and improved thermal efficiency due to a high compression ratio decreased fuel consumption, reduced sulphur dioxide emissions, and increased engine operating safety due to its high flash point [3]. The massive accumulation of tyre waste, a result of the number of vehicles that exist all over the world, causes us to look at another medium problem environmental, uncontrolled disposal and nonbiodegradability of tyres, which leads to the need for careful action regarding recycling of tyres used to solve this problem. The waste refinery entails thermochemical processes to produce fuels, materials, and chemicals from wastes such as tyres, plastics, sludge, and other wastes due to their chemical composition and carbon and hydrogen richness. They constitute a possible source for the manufacture of fuels. The performance of biofuels and diesel engine emissions is increasingly being studied globally [4]. Because biodiesel is clean, energy-efficient, and highly biodegradable and has strong lubricating properties, it has been explored extensively. Improving diesel fuel's physical and chemical qualities is important to use 100% biodiesel cleanly. Biodiesel as a fuel alternative can only be utilised in compression ignition engines, provided it meets the worldwide standard biodiesel criteria. Chains of unsaturated fatty acids and the double bond in the parent molecule reacting with oxygen during combustion and storage cause the fuel to become acidic, creating a rubber and insoluble silt that can clog filters. Biodiesel's thermophysical properties influence its performance, combustion, and emission characteristics. The viscosity, density, cetane number, calorific value, flashpoints and ignition, cloud point, and pour point of biodiesel are important parameters to consider. According to several types of research, its properties are dependent on fatty acid concentration and chemical composition [5]. So, before utilising biodiesel in a diesel engine with compression ignition, it must meet the ASTM D6751 and EN 14214 criteria. The physicochemical qualities of the fuel used in an engine are vital in determining performance and emissions: injection pressure, compression ratio, ignition delay, air-fuel ratio, and chamber turbulence. Combustion and other factors directly affect compression ignition performance. The most common ternary mixture studied is ethanol-biodiesel-diesel. According to the high latent heat of vaporisation and lower combustion temperature, ternary fuel mixing yields reduced NO_x , smoke, and higher HC and CO emissions. Increasing the quantity of ethanol in blended fuels reduced the peak smoke emission peaks. The ethanol in biodiesel/diesel blends is ideal for lowering NO_x emissions. The binary biodiesel-diesel mixture reduced particle concentration and mass emission. Adding ethanol in biodiesel mixtures results in higher fuel consumption and CO and HC emissions, but decreased NO_x emissions [6]. This research examines the physicochemical properties of binary

and ternary mixes and their environmental pollution emissions. In a compression ignition engine, each fuel is characterised by its harmful emissions of NO_x , CO, CO_2 , HC, and PM.

2. Polluting Emissions

The study of harmful emissions from engines is currently very important because of the high degree of pollution they create as a factor. It has been changed into the main axis while developing a machine due to the strict rules that have been set today for environmental protection and mitigation. Within the pollutants of a diesel engine, this research finds nitrogen oxide, unburned hydrocarbons, carbon monoxide, dioxide carbon, and particulate matter [5]. When oxygen and nitrogen are combined at high temperatures, these gases are formed: nitrogen monoxide, nitrogen dioxide, nitrous oxide, dinitrogen trioxide, and dinitrogen pentoxide are the principal nitrogen oxides that occur in combustion chambers and have a significant influence on the environment and human health due to their toxicity. Fuel that has not been properly burned when it departs the engine's internal combustion chamber through the exhaust is known as unburned hydrocarbons. Because of the low concentration of HC in the exhaust gas, the typical unit of measurement is parts per million (ppm). Carbon dioxide is another name for carbonaceous anhydride and carbonaceous gas (II). Despite its critical relevance for all living things as the primary carbon source, carbon dioxide is significant. The use of fossil fuels has resulted in a rapid increase in carbon dioxide content in the atmosphere, resulting in global warming [6]. They are a collection of small solid entities or liquid droplets scattered in the atmosphere due to anthropogenic or natural activities. Many microscopic soot particles are created mostly caused by the incomplete burning of fossil fuels and coal. It is critical to emphasise that particulate matter does not all have the same physical and chemical properties; it varies in size, shape, and chemical makeup.

3. Experimental Installation

The diagram of each of the engine components is shown in Figure 1. The experimental installation consists of a diesel engine, a mass flow sensor, an IR rpm sensor, a data acquisition and control system, and an analyzer of gases. The diesel engine in the installation is a 4-cylinder engine, 5.9 L, 180 HP @2500 rpm 6BTA model, which is shown in Figure 1. For engine, rpm control has a metal gear servo motor model RB-330 MG and an infrared sensor model E18-D80NK for rpm. It has a control system in the LabVIEW software through which it is activated and speeds up and slows down the engine as required. The gas analyzer that the experimental installation has is a gas analyzer combined with gases. The analyzer consists of basic equipment, gas analyzer and opacimeter in a high-quality plastic housing with an integrated display unit and keyboard, a grating measuring probe of 600 mm steel, 2000 mm probe hose, one LAN interface with LAN cable (RJ 45), a power supply 110 V-230 V, 50/60 Hz, a transparent hose for condensate separation with



FIGURE 1: Experimental setup with engine and analyzer.

the receiver, one main filter, point filter zero and condensate filter, an electrochemical O_2 sensor, trigger clamps for MET 6.4 for the inductive recording of the number of revolutions in ignition cables, and measurement value software for continuous measurement.

4. Experimental Protocol

Experimental protocol for measuring polluting emissions: once the physicochemical characterisation of the established mixtures has been carried out; the polluting emissions are measured. The medicines are injected into the Cummins 4 cylinder engine, model 6BTA 5.9 L, 180 HP using the combined gas analyzer MET. The equipment's method is to pass an infrared light through a gas cell and measure each gas's energy absorbed with chemical gas sensors. The MAHA Emission and Viewer software communicates via an Ethernet connection to the analyzer. Through this software, tests are carried out of tightness and the zero adjustment required when starting the measurements and controlling the beginning and end of the test. Similarly, the MAHA Emission Viewer software monitors the test since its interface allows you to view sizes in real time. It is important to highlight that all the tests are carried out under the same conditions for the same period where the engine runs empty without any load. Five trials are performed on the test bench for each experimental trial to verify repeatability in the sampling. Then, averages are obtained, minimum value and maximum value to be graphed later. In each test, the exhaust gases CO_2 , CO, NO_x , HC, and PM are measured and monitored oxygen, rpm, and oil temperature. Verification of equipment connection and operation of the LabVIEW user interface: once the experimentation starts in the laboratory of the SCR begins by verifying that all the equipment of the installation necessary for the measurement is connected and

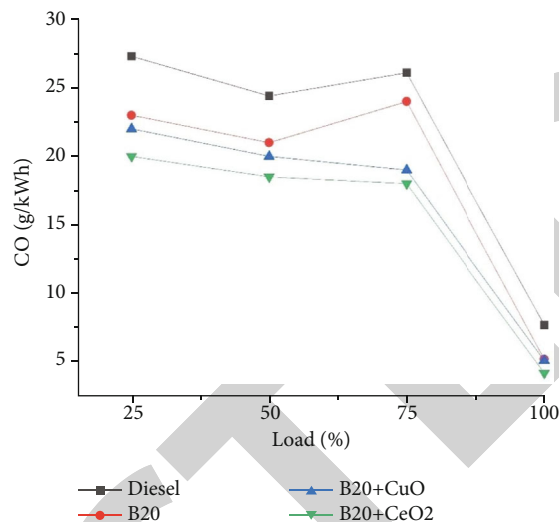


FIGURE 2: Variation of CO with load.

working correctly. The computer is turned on, and in the LabVIEW program, the file test 14 is opened, where the engine control interface will appear. It is important to emphasise that you must check that the signal module box is turned on before running the program. The gas analyzer is then connected to its wiring network to prepare for the start of trials.

5. Result and Discussion

This section shows the results of the polluting emissions of each of the mixtures of the importance of CO, CO_2 , HC, NO_x , and PM. The results obtained from the present investigation are shown below. A comparison is made with the properties of the reference diesel. The polluting emissions measured in the present investigation for defined mixtures are CO, CO_2 , NO_x , HC, and PM. Five measurements were made during a time of 1 minute for each of the mixtures from which a weighted average and said value are the published ones. The analyzer used performs simultaneously measuring each one of the reported emissions. The engine was operated in all tests at 1000 rpm without load; the power and the specific fuel consumption are not measured in the experiment. It is important to mention that the oil temperature was monitored in each of the measurements to take them at the same temperature, in the range of 86 to 88°C.

5.1. CO Emissions. The formation of carbon monoxide depends on the oxygen content and the combustion temperature so that combustion with a supply of inadequate oxygen results in the production of carbon monoxide. Figure 2 represents the raw values of CO emission from pure diesel and other blending fuels [7]. The CO values are for mixtures B20+CeO₂100ppm, B20+CuO100ppm, B20, and D100 at 1000 rpm. Figure 2 shows how the combination of biodiesel and nanoparticle affects slightly polluting emissions. In the case of biodiesel, the trend line shows that adding biodiesel to diesel causes CO to decrease which coincides with the literature where they report that carbon

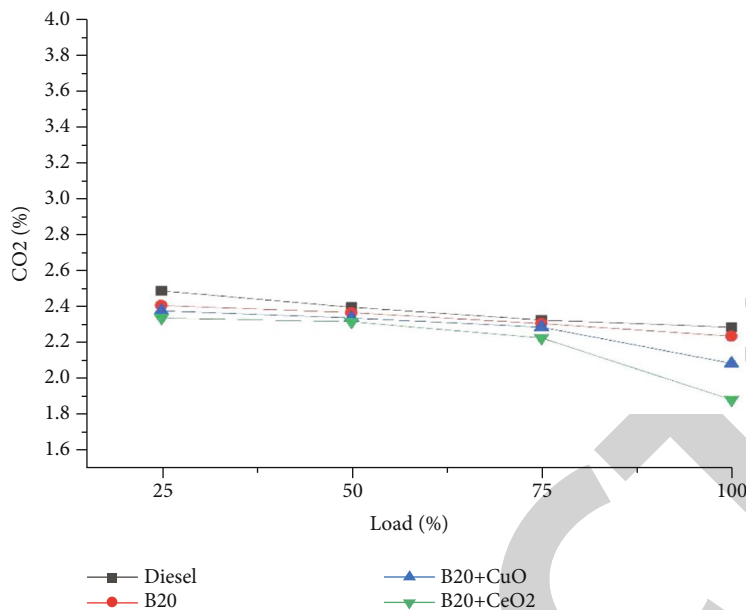


FIGURE 3: Variation of CO₂ with load.

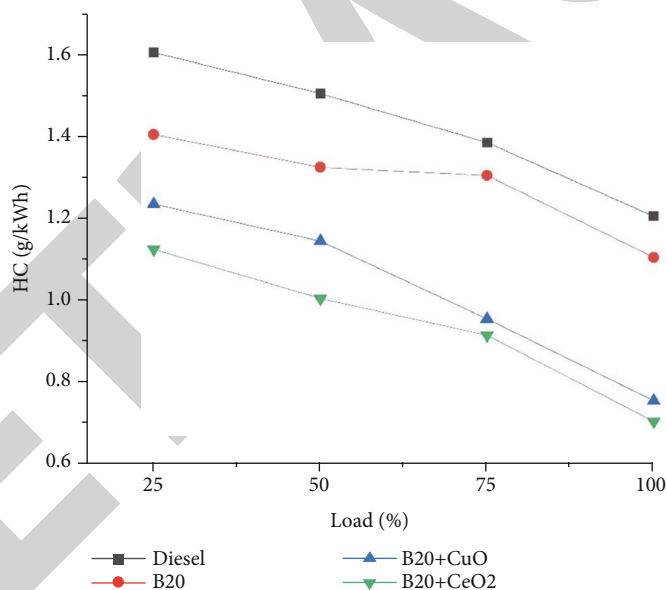


FIGURE 4: Variation of HC with load.

monoxide emissions of carbon blend with biodiesel are lower due to the presence of extra oxygen in biodiesel molecules. It is observed that as the percentage of algae oil is increased, the value of monoxide is closer to the diesel value. Light oil is a naphthenic fluid composed of carbons and hydrogens like diesel and is not an oxygenated compound like biodiesel [8].

5.2. CO₂ Emission. The CO₂ emission is the result of the complete combustion of the fuel. Figure 2 represents the raw values of CO₂ emission of pure diesel and other blending fuels. The carbon dioxide values are for mixtures B20 +CeO₂100ppm, B20+CuO100ppm, B20, and D100 at

1000 rpm. It is seen in Figure 3 that the importance of carbon dioxide that emits the combination with biodiesel participation is within the same rank [9]. In the case of algae oil, as its percentage of participation increases, the amount of CO₂ decreases, possibly due to less complete combustion with increasing percentage. However, if you compare the reference diesel and all the mixtures, when 100 ppm of algae oil is added, values are below the value of the diesel; these are the mixtures that emit the less amount of carbon dioxide. Figure 3 shows the dimensionless values concerning diesel from reference, where it is observed that for B20 +CeO₂100ppm and B20+CuO100ppm of biodiesel, the addition of nanoparticles does have a great impact [10].

5.3. HC Emissions. HC emissions occur when a rich mixture is delivered to the cylinder. The cross does not burn completely, which can be reduced by delaying the ignition associated with fuels with a higher cetane number [11]. Figure 4 shows the effects of test fuels on HC emissions. The highest HC emission is obtained for pure diesel, B20, B20+CeO₂100ppm, and B20+CuO100ppm. The lowest HC emission for mixtures is obtained for B20+CeO₂100ppm; this value is less than that for diesel, due to which its naphthenic characteristics need more energy to break its bonds and have complete combustion. For mixtures with biodiesel, the opposite occurs. Due to the oxygen content, the explosion of this is more complete. For all varieties, the same effect occurs as in the mixtures of a decrease in HC for nanoparticle mixtures. The addition of nanoparticles has the same impact when comparing the diesel mixture. There is no noticeable variation when adding one or the other; however, all combinations decrease the amount of HC [12–14].

5.4. Nitrogen Oxides. The emissions of nitrogen oxides in combustion result from the combustion temperature in the cylinder, which if it is approximately higher than 1600°C, the nitrogen molecules begin to participate in the reaction and, therefore, produce NO_x [15]. The variation of the emissions of nitrogen oxides concerning 1000 rpm for all test fuels is presented in Figure 5. In the nanoparticle mixture, slight increases in NO_x emissions are compared with B20+CeO₂100ppm, B20+CuO100ppm, B20, and diesel. This is a consequence of the high content of oxygen in biodiesel which causes higher NO_x emission rates; as the amount of participation of these nanoadditives increases, the oxides of nitrogen increase [16, 17]. Figure 5 shows that the number of nitrogen oxides was lower for all ternary mixtures evaluated for the same engine speed. It is observed in the graph of dimensionless values for the ternary mixtures that the emission of NO_x has a very particular trend by increasing the percentage of nanoadditives for each quantity of biodiesel in the mix, which can be attributed to the fact that the additive would be accelerating the ignition time of the diesel and reducing the amount of mixture in the combustion premixed resulting in NO_x reduction. It is important to mention that the formation of NO_x is not only a function of the temperature of combustion, factors such as the geometry of the piston and the fuel play a vital role in their formation [18].

5.5. Particulate Matter (PM). The amount of particulate matter emitted into the atmosphere is a consequence of a combination of parameters such as engine speed, load, strategy of injection, combustion process, and ultimately the after-treatment system. Particles are considered any material in the exhaust gases in a liquid or solid state under approximately ambient conditions [19]. Figure 6 shows the particulate matter for the mixtures, managing to observe that, compared to the reference diesel, the PM emissions for all the mixtures decrease in speed conditions of 1000 rpm on the engine—the PM concentration of the mixtures B20+CeO₂100ppm, B20+CuO100ppm, B20, and diesel [20]. As the percentage of nanoparticle concentration of particulate

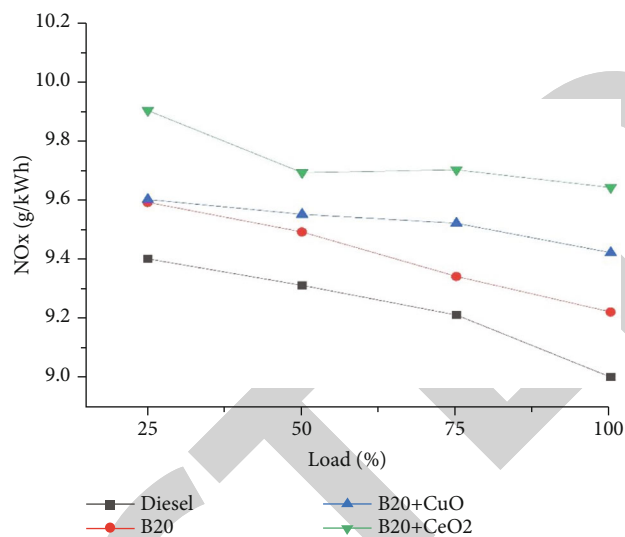


FIGURE 5: Variation of NO_x with load.

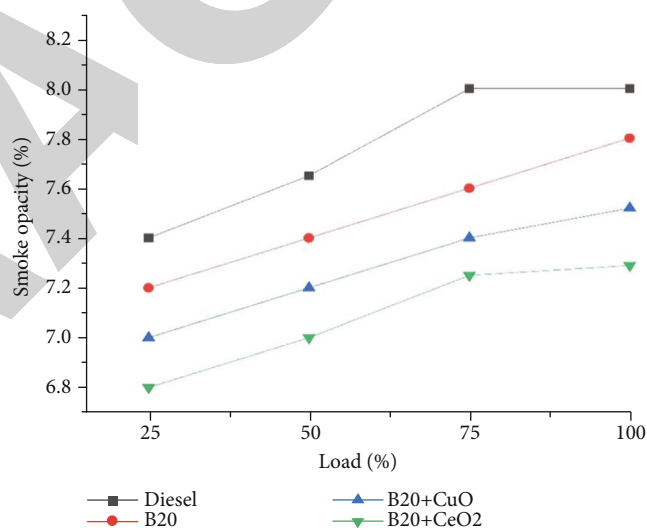


FIGURE 6: Variation of NO_x with load.

material rises, the mixture with higher PM is diesel [21]. As seen in Figure 6, as the mixtures increase, the PM concentration does not significantly impact. However, the particulate material for mixtures with biodiesel decreases with more oxygen molecules. However, more studies should be done to carry out a deeper discussion of the behaviour found. In the same way, it was observed that the nitrogen oxides decreased as an effect of the addition of nanoparticles, which would cause a decrease in the particulate matter possibly caused by a shorter duration of the combustion and the increase of the oxygen concentration in the mixture of air and fuel or also due to complete combustion [22, 23].

6. Conclusions

This study is aimed at analyzing polluting emissions from mixtures between B20+CeO₂100ppm, B20+CuO100ppm,

B20, and diesel to evaluate its use in compression ignition engines. Pollutant emissions from mixtures: the CO emitted by pure diesel is higher than that by all mixtures with biodiesel and nanoadditive blends. CO₂ emissions from blends with biodiesel are lower compared to those from pure diesel fuel. In the medicines, the diesel had a greater effect on the emission of CO, although adding biodiesel mixture with nanoadditives, due to its content of oxygen, decreases the percentage of CO. All the mixtures studied in this investigation showed that their HC emissions are lower compared to the pure fuel diesel. NO_x emissions for blends with biodiesel with nanoadditives are higher than those of diesel due to their oxygen content. The particulate matter for all the mixtures evaluated in this study is below the reference diesel. The mixtures with the highest particulate matter emitted mixtures with higher concentrations of biodiesel, which was of a maximum of 20% for this study. In the varieties, as biodiesel content was increased, NO_x emissions increased while PM emissions decreased, as mentioned in the literature.

Data Availability

The data used to support the findings of this study are included in the article.

Conflicts of Interest

The authors declare that they have no conflicts of interest regarding the publication of this paper.

References

- [1] P. Zhang, X. Su, C. Yi, H. Chen, H. Xu, and L. Geng, "Spray, atomization and combustion characteristics of oxygenated fuels in a constant volume bomb: a review," *Journal of Traffic and Transportation Engineering*, vol. 7, no. 3, pp. 282–297, 2020.
- [2] K. Velmurugan and A. P. Sathiyagnanam, "Impact of antioxidants on NO_x emissions from a mango seed biodiesel powered DI diesel engine," *Alexandria Engineering Journal*, vol. 55, no. 1, pp. 715–722, 2016.
- [3] V. Perumal and M. Ilangkumaran, "Experimental analysis of operating characteristics of a direct injection diesel engine fuelled with cleome viscosa biodiesel," *Fuel*, vol. 224, pp. 379–387, 2018.
- [4] A. Khanra, S. Vasistha, and M. P. Rai, "Glycerol on lipid enhancement and FAME characterization in algae for raw material of biodiesel," *International Journal of Renewable Energy Research*, vol. 7, no. 4, 2017.
- [5] S. Zighmi, S. Ladjel, M. B. Goudjil, and S. E. Bencheikh, "Renewable energy from the seaweed *Chlorella pyrenoidosa* cultivated in developed systems," *International Journal of Renewable Energy Research*, vol. 7, no. 1, 2017.
- [6] A. El-Khair, B. El-Sayed, G. M. Manal, and R. Shima, "Hamed Complementary production of biofuels by the green alga *Chlorella vulgaris*," *International Journal of Renewable Energy Research*, vol. 5, no. 3, 2015.
- [7] A. Purandaradas, T. Silambarasan, K. Murugan et al., "Development and quantification of biodiesel production from chicken feather meal as a cost-effective feedstock by using green technology," *Biochemistry and Biophysics Reports*, vol. 14, pp. 133–139, 2018.
- [8] G. Vaidya, P. P. Patil, A. S. SENER et al., "Chlorella protothecoides algae oil and its mixes with lower and higher alcohols and Al₂O₃ metal nanoadditives for reduction of pollution in a CI Engine," *Journal of Nanomaterials*, vol. 2022, Article ID 9658212, 6 pages, 2022.
- [9] S. Tripathi and K. A. Subramanian, "Experimental investigation of utilization of soya soap stock based acid oil biodiesel in an automotive compression ignition engine," *Applied Energy*, vol. 198, pp. 332–346, 2017.
- [10] P. Verma, G. Dwivedi, A. K. Shukla, A. Kumar, and A. K. Behura, "Ionic liquids as green bio-lubricant additives," in *Industrial Applications of Green Solvents: Vol. II*, Inamuddin, R. Mobin, and A. M. Asiri, Eds., pp. 224–248, Materials Research Forum LLC, Millersville, 2019.
- [11] H. E. Saleh and M. Y. E. Selim, "Improving the performance and emission characteristics of a diesel engine fueled by joboba methyl ester-diesel-ethanol ternary blends," *Fuel*, vol. 207, pp. 690–701, 2017.
- [12] S. Raviteja, "Combustion characteristics of waste cooking oil bio diesel on four stroke diesel engine using additives," *Turkish Journal of Computer and Mathematics Education (TURCOMAT)*, vol. 12, no. 13, 2021.
- [13] N. Acharya, P. Nanda, S. Panda, and S. Acharya, "Analysis of properties and estimation of optimum blending ratio of blended mahua biodiesel," *Engineering Science and Technology, an International Journal*, vol. 20, no. 2, pp. 511–517, 2017.
- [14] D. R. Raviteja, "Investigation of performance and emission on a single cylinder di-die sel engine with a catalytic converter using bio-diesel," *International Journal of Modern Agriculture*, vol. 10, no. 2, pp. 3465–3475, 2021.
- [15] A. K. Agarwal, A. Dhar, J. G. Gupta et al., "Effect of fuel injection pressure and injection timing of Karanja biodiesel blends on fuel spray, engine performance, emissions and combustion characteristics," *Energy Conversion and Management*, vol. 91, pp. 302–314, 2015.
- [16] A. Zare, T. A. Bodisco, P. Verma et al., "Emissions and performance with diesel and waste lubricating oil: a fundamental study into cold start operation with a special focus on particle number size distribution," *Energy Conversion and Management*, vol. 209, p. 112604, 2020.
- [17] S. Raviteja, Y. S. Ratnakar, V. V. Prasanna Kumar, and M. Sairam, *Performance evaluation and emission characteristics of organic sunflower oil biodiesel using additives*, Design Engineering, 2021, <http://thedesigengineering.com/index.php/DE/article/view/5439>.
- [18] A. K. Agarwal, A. Shrivastava, and R. K. Prasad, "Evaluation of toxic potential of particulates emitted from jatropha biodiesel fuelled engine," *Renewable Energy*, vol. 99, pp. 564–572, 2016.
- [19] S. H. Al-lwayzy and T. Yusaf, "Diesel engine performance and exhaust gas emissions using microalgae *Chlorella protothecoides* biodiesel," *Renewable Energy*, vol. 101, pp. 690–701, 2017.
- [20] H. Chen, J. He, and X. Zhong, "Engine combustion and emission fuelled with natural gas: a review," *Journal of the Energy Institute*, vol. 92, no. 4, pp. 1123–1136, 2019.
- [21] G. Dwivedi, S. Pillai, and A. K. Shukla, "Study of performance and emissions of engines fueled by biofuels and its blends," *Journal of Traffic and Transportation Engineering*, vol. 8, no. 4, pp. 510–533, 2019.

Retraction

Retracted: *Chlorella protothecoides* Algae Oil and Its Mixes with Lower and Higher Alcohols and Al₂O₃ Metal Nanoadditives for Reduction of Pollution in a CI Engine

Journal of Nanomaterials

Received 11 July 2023; Accepted 11 July 2023; Published 12 July 2023

Copyright © 2023 Journal of Nanomaterials. This is an open access article distributed under the Creative Commons Attribution License, which permits unrestricted use, distribution, and reproduction in any medium, provided the original work is properly cited.

This article has been retracted by Hindawi following an investigation undertaken by the publisher [1]. This investigation has uncovered evidence of one or more of the following indicators of systematic manipulation of the publication process:

- (1) Discrepancies in scope
- (2) Discrepancies in the description of the research reported
- (3) Discrepancies between the availability of data and the research described
- (4) Inappropriate citations
- (5) Incoherent, meaningless and/or irrelevant content included in the article
- (6) Peer-review manipulation

The presence of these indicators undermines our confidence in the integrity of the article's content and we cannot, therefore, vouch for its reliability. Please note that this notice is intended solely to alert readers that the content of this article is unreliable. We have not investigated whether authors were aware of or involved in the systematic manipulation of the publication process.

Wiley and Hindawi regrets that the usual quality checks did not identify these issues before publication and have since put additional measures in place to safeguard research integrity.

We wish to credit our own Research Integrity and Research Publishing teams and anonymous and named external researchers and research integrity experts for contributing to this investigation.

The corresponding author, as the representative of all authors, has been given the opportunity to register their agreement or disagreement to this retraction. We have kept a record of any response received.

References

- [1] G. Vaidya, P. P. Patil, A. S. SENER et al., "Chlorella protothecoides Algae Oil and Its Mixes with Lower and Higher Alcohols and Al₂O₃ Metal Nanoadditives for Reduction of Pollution in a CI Engine," *Journal of Nanomaterials*, vol. 2022, Article ID 9658212, 6 pages, 2022.

Research Article

Chlorella protothecoides Algae Oil and Its Mixes with Lower and Higher Alcohols and Al₂O₃ Metal Nanoadditives for Reduction of Pollution in a CI Engine

Gayatri Vaidya ¹, Pravin P. Patil ², Arif Senol SENER ³, Navale Sainath Ramnath ⁴,
Bharat Singh ⁵, Raviteja Surakasi ⁶, Srujana Sripathi ⁷,
and Tsegaye Alemayehu Atiso ⁸

¹Department of studies in Food Technology, Davangere University, Davangere, Karnataka, India

²Mechanical engineering department, Graphic Era Deemed to be University Dehradun, Uttarakhand, India

³Department of Mechanical Engineering, Engineering and Architecture Faculty, Nisantasi University, Istanbul, Turkey

⁴Department of Physics, SN Art's, DJ Malpani Commerce and BN Sarda Science College, Sangamner, Maharashtra, India

⁵Department of Mechanical Engineering, GLA University Mathura, Mathura, India

⁶Department of Mechanical Engineering, Lendi institute of engineering and Technology, Jonnada, Vizianagaram, Andhrapradesh, India

⁷Department of Biotechnology, Center for post graduate studies, Jain University, Jayanagar, 9th Block, Bengaluru, 560011 Karnataka, India

⁸Department of Mechanical Engineering, Wolaitasodo university, Wolaita Sodo, SNNPR, Ethiopia

Correspondence should be addressed to Tsegaye Alemayehu Atiso; tsegayealemayehusj@gmail.com

Received 1 January 2022; Revised 22 January 2022; Accepted 25 January 2022; Published 15 February 2022

Academic Editor: Karthikeyan Sathasivam

Copyright © 2022 Gayatri Vaidya et al. This is an open access article distributed under the Creative Commons Attribution License, which permits unrestricted use, distribution, and reproduction in any medium, provided the original work is properly cited.

Numerous Algae oils with low and medium viscosity were investigated as fuel for CI engines. However, high viscous algae oil has not been explored in detail as a replacement for diesel in CI engines due to operational problems and poor performance characteristics. Esterification of neat algae oil to obtain its biodiesel is a complex process. The biodiesel obtained also has viscosity nearly five times more than diesel viscosity. Hence, research efforts on CI engines using algae oil methyl ester are lacking, particularly in combustion characteristics. This work focuses on utilizing algae oil as a fuel in CI engines. Algae oil has more affinity for alcohols due to a higher percentage of ricinoleic acid which aids in forming a homogeneous mixture. Alcohols with better fuel properties improve the combustion capability of algae oils with low and medium viscosity. However, not much research has been carried out in alcohols with very high viscous algae oil. Hence, in this work, higher and lower-order alcohols were blended with algae oil in their neat form and their biodiesel with Al₂O₃ nanoadditives for performance improvement.

1. Introduction

Extensive research has been carried out worldwide in compression ignition (CI) engines using algae oils with low and medium viscosities, particularly nonedible algae oils. Biodiesel obtained from nonedible sources is a viable option in CI engines for commercial applications. Compared to mineral diesel, biodiesel has many advantages such as biodegradability, safer storage, better lubricity, low toxicity, and environ-

ment friendly [1]. Algae oils with low to medium viscosity can be modified to obtain the properties equivalent to diesel by a suitable chemical process. However, high viscous algae oils such as *Chlorella protothecoides* oil cannot be esterified easily to obtain biodiesel. They require a complicated transesterification process and cannot match the diesel viscosity. As a result, not much experimental research was carried out using high viscous nonedible algae oil for diesel engine applications. In particular, the combustion behavior of heavy

viscous oils either in raw form or biodiesel is not available in the literature [2].

The present work focuses on this direction by investigating neat *C. Protothecoides* oil (CPO) with higher and lower-order alcohols as a fuel substitute for CI engines. Numerous nonedible vegetable oils with low and medium viscosity were investigated for CI engines. However, high viscous nonedible vegetable oil such as algae oil has not been explored in detail as a replacement for diesel in CI engines due to operational problems and poor performance characteristics [3]. Esterification of neat *C. Protothecoides* oil to obtain biodiesel is complex. The biodiesel obtained also has viscosity nearly five times of diesel viscosity. Hence, research efforts on CI engines using neat *C. Protothecoides* oil or its methyl ester are lacking, particularly in combustion characteristics. This work utilizes *C. Protothecoides* oil as a fuel in CI engines. *C. Protothecoides* oil has more affinity for alcohols due to a higher percentage of ricinoleic acid which aids in forming a homogeneous mixture [4].

Alcohols with better fuel properties improve the combustion capability of vegetable oils with low and medium viscosity [5, 6]. However, not much research has been carried out in alcohols with very high viscous *C. Protothecoides* oil. Hence, in this work, higher and lower-order alcohols were blended with *C. Protothecoides* oil in its neat form and its biodiesel for performance improvement. A literature survey was done on the following methods to improve the performance of a CI engine operating on vegetable oil or its biodiesel. It evaluated the use of canola biodiesel (COME) and diesel blends in a CI engine on the performance and emission behavior. COME was blended with diesel in proportion on a volume basis [7].

It was observed that pour point and cetane number of biodiesel were better, while density, viscosity, and calorific value were poor compared to diesel. They observed that engine power output was reduced with biodiesel and diesel blends. Based on the experimental results, they concluded that 25% blend of COME with diesel would be the best alternative to diesel, based on emission and performance parameters. It was performed as experiments in a CI engine at a rated speed of 1500 rpm with diesel-ethanol and biodiesel-ethanol blend as fuel. Ethanol was blended by volume with both diesel and biodiesel to assess the performance parameters of a CI engine in comparison with diesel and biodiesel [8]. They observed that in comparison to the biodiesel-ethanol blend, the diesel-ethanol blend produced higher indicated thermal efficiency and showed mean effective pressure. Both the parameters increased with ethanol proportion in the blend. Ignition delay was longer with higher ethanol concentration in the blend, and the delay period was longer with biodiesel-ethanol blend compared to diesel-ethanol blend. Also, the combustion duration for ethanol blended with biodiesel was higher than diesel. NO_x and HC emissions were higher and increased with ethanol proportion. They observed that CO emission increased proportionally to ethanol concentration with diesel and biodiesel blends. The objectives of the present research work are to improve the combustion, emission, and performance of very high viscous algae oil

with lower and higher-order alcohol and Al_2O_3 nanoadditives fueled compression ignition engines [9].

2. Experimental Setup

The test engine was a four-stroke single-cylinder CI engine with a water-cooled and direct fuel injection system. It developed a maximum rated output of 3.5 kW at 1500 rpm with maximum load condition. The engine made was Kirloskar, a TV1 model engine with over-head valves controlled by push rods. The fuel injection timing and pressure were maintained 23° before TDC and 200 bar as recommended by the manufacturer. The engine coolant was circulated through the water jackets in the cylinder, and the temperature of the coolant was maintained at 80°C. A pressure transducer (piezoelectric) was fitted on the cylinder head to measure in-cylinder pressure. The engine was loaded by coupling it with an eddy current dynamometer.

Tests were conducted in four load conditions, namely, 25, 50, 75, and 100% of maximum brake power. Engine performance parameters like speed, load, exhaust temperature, fuel consumption, and emissions like smoke, hydrocarbon, carbon monoxide, and NO were measured at all load conditions. This experimental study tested the following fuels: diesel, CPO, CPO with lower/higher-order alcohol, and CPOAl_2O_3 nanoadditives. The size of the nanoadditives is less than 100 nm. The experiments were conducted at a constant speed of 1500 rpm. The tests were conducted after the engine attained a stable condition. The fuel injection pressure was set at 200 bar. The engine output was varied in steps from 25% to 100% loading under the single fuel mode. The DAQ system recorded pressure crank angle data of hundred consecutive cycles. This data was analyzed to interpret the variation in average pressure at the corresponding crank angle. The first phase of the test was conducted to compare the emission and performance behavior of the base fuels such as diesel, CPO, CPO with lower/higher-order alcohol, and CPOAl_2O_3 nanoadditives with variable load at the rated speed of 1500 rpm. The emission and performance behavior of the engine with ternary blends of diesel, ethanol, and hexagonal and Al_2O_3 nanoadditives were studied.

3. Result and Discussion

3.1. Engine Operation with Ternary Fuel Blends of NCO, Diesel, and Ethanol. In this phase of research work, the proportion of diesel fuel is maintained constant at 20% for all the blends. Binary fuel blend of CPO and diesel is blended with ethanol, hexagonal, and Al_2O_3 in different proportions [10]. Experiments were conducted with the following three ternary fuel blends: (i) neat algae oil 80% and hexagonal 20% by volume (PCO80 + Hex20); (ii) neat algae oil 100% (PCO 100%) and (iii) neat algae oil biodiesel (PCOME 100%); and (iv) neat algae oil 80% and ethanol 20% by volume (PCO80 + Eth20) and neat algae oil 100% with 100 ppm Al_2O_3 (PCO100% + 100 ppm Al_2O_3).

Figure 1 shows the BTE variation with BP for various test fuels. CPO + Hex has a BTE of 33%, whereas CPO has a BTE of 22%. CPO has a significantly lower BTE [11]. More

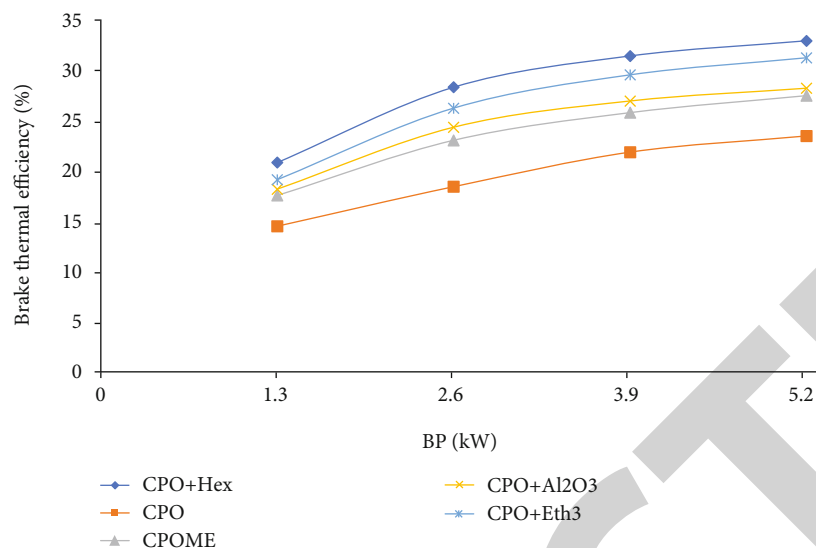


FIGURE 1: BTE with BP at full load.

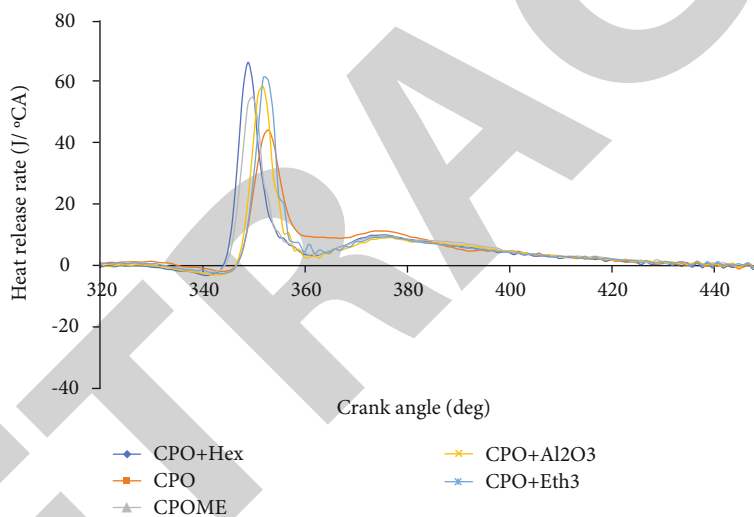


FIGURE 2: HRR with the crank angle at full load.

energy is released during the diffusion phase, resulting in more heat energy squandered in the exhaust. CPO + Eth, on the other hand, has a BTE of 31.25%, which is similar to CPO + Hex (33%). Ethanol was combined with PCO and diesel to increase CPO combustion. Blending improves atomization and the creation of air-fuel mixtures [12].

Figure 2 shows the HRR with an appropriate crank angle for various fuels at full load. CPO + Hex has a maximum HRR of 67 J/°CA at 100% load, whereas CPO has a maximum HRR of 45 J/°CA. Because hexagonal has a reduced viscosity and a high flame speed, ethanol addition in ternary fuel blends results in a significant increase in premixed combustion [13]. For CPO, it can be seen that primary combustion occurred during the diffusion phase. HRR for the optimal CPO + Eth combination is 62 J/°CA. This blend's premixed combustion is more similar to CPO + Hex. Compared to CPO and other trifuel blends,

this leads to higher BTE, higher peak pressure, and reduced smoke emission [14].

Figure 3 shows the in-cylinder pressure related to the crank angle at full load for several test fuels. Because of the reduced HRR and poor combustion with CPO, the peak pressure is limited to 61 bar, which is lower than with CPO + Hex (70 bar). Adding ethanol to CPO raises the peak pressure for CPO + Eth (66 bar), bringing it closer to that of CPO + Hex. Ignition delay is more significant, and oxygenated hexagonal is stored during the delay time, giving the injected fuel more oxygen to burn, resulting in a quicker HRR and higher peak pressure [15].

Figure 4 shows the fluctuation of ignition delay (ID) with BP. The ID of CPO and CPO + Hex at full load is 14°CA and 9°CA, respectively. Because of its low volatility, CPO has a higher ID than CPO + Hex. This contributes to incorrect air-fuel mixture creation and poor atomization, which

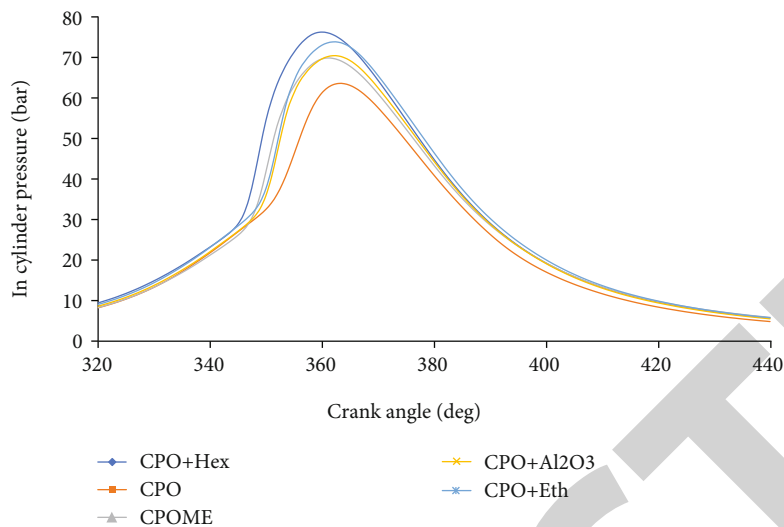


FIGURE 3: In-cylinder pressure with CA at full load.

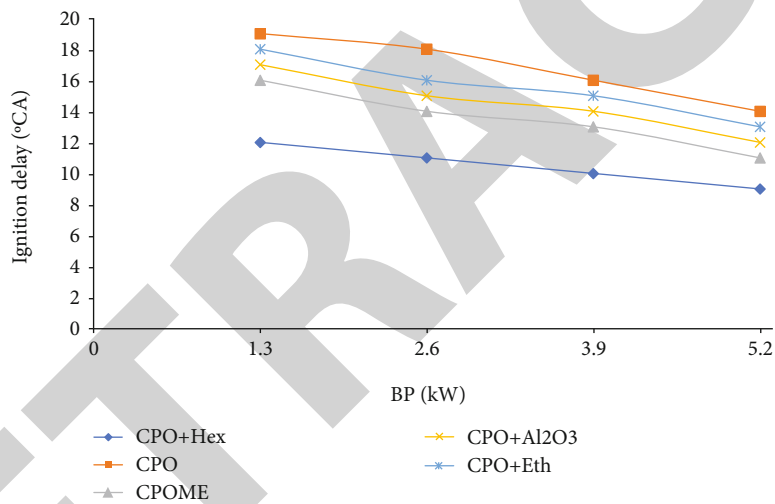


FIGURE 4: Ignition delay with BP at full load.

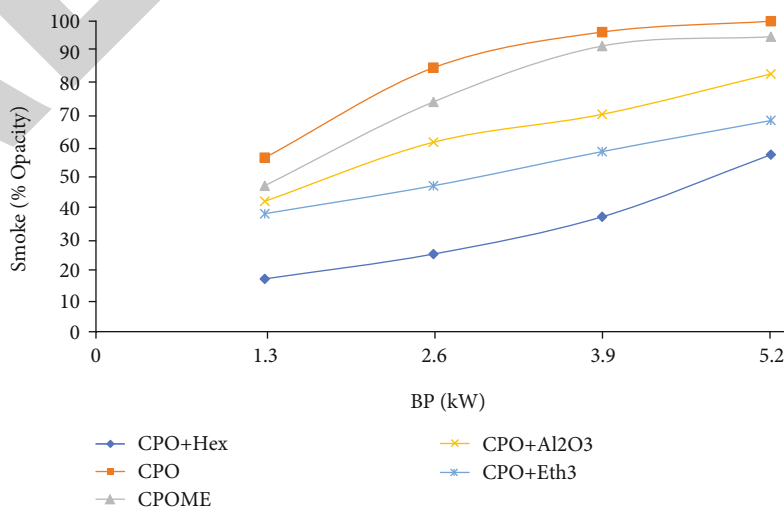


FIGURE 5: Smoke emission variation with BP at full load.

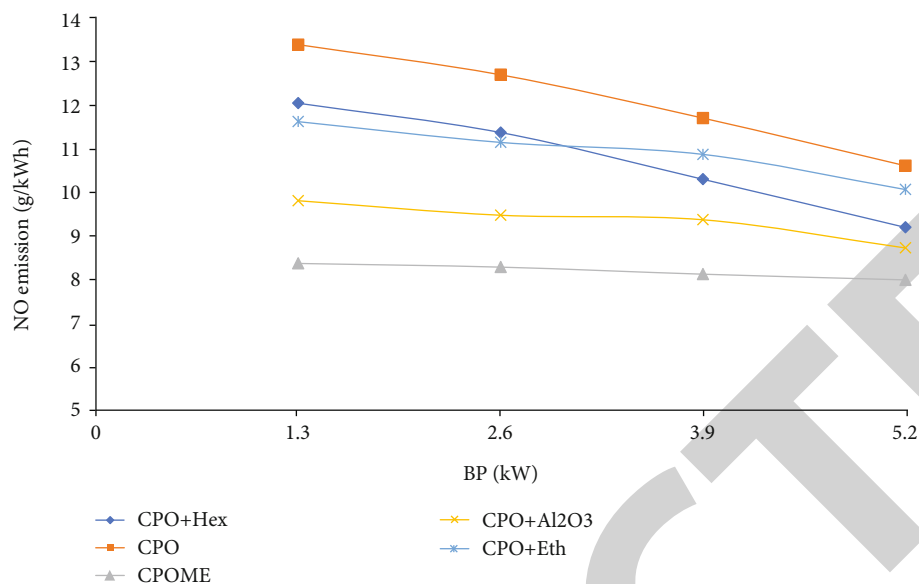


FIGURE 6: NO emission variation with BP at full load.

increases ignition delay. Hexagonal blending reduces viscosity while increasing volatility, resulting in better atomization, vaporization, and air-fuel mixing [16]. The ignition delay for the optimal CPO + Eth blend is 12°CA.

Figure 5 shows the variance in smoke emission with BP for several test fuels. The smoke opacity of CPO operation approaches 100% at full load; however, smoke emission lowers with ternary fuel blend of diesel, CPO, and ethanol [17]. Ternary fuel mixes have low density and viscosity, resulting in improved combustion. Ternary mixture with high ethanol concentration emits less smoke for CPO + Eth optimal blend is 69% opacity due to the blend's improved volatility. CPO + Hex emits smoke with a 58% opacity.

Figure 6 illustrates the variance in NO emission with BP for several test fuels. In comparison to CPO + Hex, CPO emits extremely little NO. Because of incorrect air-fuel mixture preparation, combustion is lower with CPO premixed. As a result, less heat is generated, resulting in a lower in-cylinder temperature and lower NO emissions [17]. At full load, CPO and CPO + Hex release NO emissions of 5.3 g/kWh and 8.2 g/kWh, respectively. The addition of hexagonal improves the premixed combustion phase for tri-fuel blends because hexagonal has a greater flame velocity, which raises the in-cylinder temperature, favouring NO production significantly [18, 19]. The NO emission for the CPO + Eth optimal blend at full load is 7.6 g/kWh.

4. Conclusion

In summary, NCO was successfully used in a CI engine after running the engine at full load for 15 minutes with diesel. However, in the current study, CPO demonstrates relatively poor combustion behavior compared to CPO + Hex. This is evidenced by a longer ignition delay, a lower HRR, a longer combustion duration, and so on. CPO has significantly superior combustion, performance, and emission behavior.

The strategies examined to improve the performance and combustion of CI engines were ternary fuel mixing of CPO, hexagonal, ethanol, and Al₂O₃ blending with NCO as the primary fuel. Among the approaches investigated, CI engine running with CPO + Hex is the best, comparable to diesel operation.

Data Availability

The data used to support the findings of this study are included within the article.

Conflicts of Interest

The authors declare that they have no conflicts of interest.

References

- [1] A. T. Hoang, "Critical review on the characteristics of performance, combustion and emissions of PCCI engine controlled by early injection strategy based on narrow-angle direct injection (NADI)," in *Energy Sources, Part A: Recovery, Utilization, and Environmental Effects*, pp. 1–15, Taylor & Francis, 2020.
- [2] Y. Liu, S. Wu, H. Zhang, and R. Xiao, "Preparation of carbonyl precursors for long-chain oxygenated fuels from cellulose ethanolysis catalyzed by metal oxides," *Fuel Processing Technology*, vol. 206, article 106468, 2020.
- [3] N. Chacko and T. Jeyaseelan, "Comparative evaluation of graphene oxide and graphene nanoplatelets as fuel additives on the combustion and emission characteristics of a diesel engine fuelled with diesel and biodiesel blend," *Fuel Processing Technology*, vol. 204, article 106406, 2020.
- [4] K. S. Thangavelu and M. Arthanarisamy, "Experimental investigation on engine performance, emission, and combustion characteristics of a DI CI engine using tyre pyrolysis oil and diesel blends doped with nanoparticles," *Environmental Progress & Sustainable Energy*, vol. 39, no. 2, article e13321, 2020.

Retraction

Retracted: Preparation of Ti Material Supported SBA-15 Functionalized with Sulfonic Acid Environmental Friendly Catalyst: Application for Esterification Process

Journal of Nanomaterials

Received 11 July 2023; Accepted 11 July 2023; Published 12 July 2023

Copyright © 2023 Journal of Nanomaterials. This is an open access article distributed under the Creative Commons Attribution License, which permits unrestricted use, distribution, and reproduction in any medium, provided the original work is properly cited.

This article has been retracted by Hindawi following an investigation undertaken by the publisher [1]. This investigation has uncovered evidence of one or more of the following indicators of systematic manipulation of the publication process:

- (1) Discrepancies in scope
- (2) Discrepancies in the description of the research reported
- (3) Discrepancies between the availability of data and the research described
- (4) Inappropriate citations
- (5) Incoherent, meaningless and/or irrelevant content included in the article
- (6) Peer-review manipulation

The presence of these indicators undermines our confidence in the integrity of the article's content and we cannot, therefore, vouch for its reliability. Please note that this notice is intended solely to alert readers that the content of this article is unreliable. We have not investigated whether authors were aware of or involved in the systematic manipulation of the publication process.

Wiley and Hindawi regrets that the usual quality checks did not identify these issues before publication and have since put additional measures in place to safeguard research integrity.

We wish to credit our own Research Integrity and Research Publishing teams and anonymous and named external researchers and research integrity experts for contributing to this investigation.






The corresponding author, as the representative of all authors, has been given the opportunity to register their agreement or disagreement to this retraction. We have kept a record of any response received.

References

- [1] R. Kalakuntala, M. Mekala, S. Chirra, V. Narayanan, V. R. Kakara, and S. Suranani, "Preparation of Ti Material Supported SBA-15 Functionalized with Sulfonic Acid Environmental Friendly Catalyst: Application for Esterification Process," *Journal of Nanomaterials*, vol. 2022, Article ID 6712464, 8 pages, 2022.

Research Article

Preparation of Ti Material Supported SBA-15 Functionalized with Sulfonic Acid Environmental Friendly Catalyst: Application for Esterification Process

Raju Kalakuntala ¹, Mallaiah Mekala ², Suman Chirra ³, Venkatathri Narayanan ³,
Vighneswara Rao Kakara ⁴, and Srinath Suranani ¹

¹Department of Chemical Engineering, National Institute of Technology, Warangal 506004, India

²Department of Chemical Engineering, B V Raju Institute of Technology, Narsapur, 502313, India

³Department of Chemistry, National Institute of Technology, Warangal 506004, India

⁴Department of Chemical Engineering, Wollega University, Shambu Campus, Ethiopia

Correspondence should be addressed to Vighneswara Rao Kakara; vignesh.che@gmail.com

Received 23 December 2021; Revised 10 January 2022; Accepted 26 January 2022; Published 9 February 2022

Academic Editor: Karthikeyan Sathasivam

Copyright © 2022 Raju Kalakuntala et al. This is an open access article distributed under the Creative Commons Attribution License, which permits unrestricted use, distribution, and reproduction in any medium, provided the original work is properly cited.

Kinetics of catalytic esterification between propionic acid and n-butanol has been studied in a batch reactor by using a Ti-supported SBA-15 catalyst with sulfonic acid. The synthesized catalyst is used to test the efficacy of catalyst for esterification reaction. The SBA-15 acidity is tied to incorporation of Ti and $-SO_3H$ groups through and the use of Si/Ti with Si/S molar ratios. The results are mesoporous materials with a typical hexagonal structure of the Ti SBA-15 and wide areas and high pore diameters that are operated with sulfonic groups. The addition of SBA to Ti leads mainly to catalytic materials with Bronsted and Lewis acid sites. Ti SBA-15 is the most effective catalyst for sulfonic acid, with the highest consents of Lewis acid sites and deactivation resistance and low hydrophilicity. The effect of temperature, catalyst amount, and molar ratio on reaction kinetics has been studied. The conversion of propionic acid is found to be 91% at 115°C at a 2:1 ratio of n-butanol to propionic acid molars with 2% of sulfonic acid supported Ti SBA-15. The Eley-Rideal kinetic model is used to fit the experimental data. The activation energy and kinetic factor are found to be 29.63 kJ mol⁻¹ and k_0 0.549 L² g⁻¹ mol⁻¹, respectively.

1. Introduction

Catalysis was first introduced as part of the growth of industrial technology in the 1960s, with a focus on refinery and petrochemical operations. Catalysis has advanced at a rapid rate over the last two decades, and it is now recognized as a multi-disciplinary discipline requiring synergistic interactions among a diverse spectrum of professionals, including materials, electrical, and mechanical engineers, physicists, biologists, and physicians. Catalysis provides and develops new, efficient, and cost-effective strategies and tools, as a leading technology toward a sustainable future and a clean environment, thereby improving people's quality of life [1].

In a multitude of goods, carboxylic acid esters are essential, from fragrances to biofuels. The latter would be of specific importance because of increasing crude oil prices and environmental issues. There are several hybrid routes for the production of organic esters [2]. The widely used technique for ester synthesis is an esterification reaction between carboxylic acids and alcohol. The reaction could be performed conventionally in batch reactors in a liquid state using powerful liquid nutrient acids like H₂SO₄, HI, and HCl as the catalyst [3, 4]. However, the handling strategy needs extra measures of catalyst removal and segregation with the substrate being disposed of salts, which usually adds to the processing cost. Alternatively, it is easy to separate strong catalysts from response products that can be used for various reaction cycles in most instances [4]. Furthermore, strong catalysts are used more readily in



ongoing processing activities, enhancing the ester manufacturing economy. For these reasons, the development of strong acid catalysts for esterification applications is of considerable concern [5]. The mathematical model and response mechanism for alkene esterification using homogeneous catalysts were well documented during a protonated methyl ester which was assaulted by a molecule of nucleophile alcohol, resulting in ester and water. With strong acid precursors containing mainly Bronsted acid clusters, esterification reaction could be expected with an analogous process to the homogeneous regime that mediates conversion [6, 7]. The results were uncertain in the literature on a basic strong acid-catalyzed esterification reaction. Two processes were suggested mainly for the esterification of heterogeneous catalysts. One is a single site mechanism, and the other one is a double site mechanism. Acetic acid esterification reaction with methanol by using SAC-13 was carried out with Bronsted acid sites as a single-site system. It is a gas stage with a range of temperatures of 90–140°C or within a condensed stage with temperature of 660°C, based on mainly the outcomes of studies with pyridine poisoning. An Eley-Rideal kinetic equation was developed to predict the experimental results with an accuracy of 8% for 1-octanol and hexanoic acid esterification utilizing zeolite and SAC-13 as catalysts [8].

The objective of the present research is the preparation and characterizations of an environmental catalyst for the esterification of propionic acid after the integration of Ti and sulfonic groups in SBA-15. The kinetics studies at different parameters have been carried out to find the conversion of propionic acid under various parameters. The Eley-Rideal model fitted with experimental data.

2. Experimental

2.1. Catalyst Preparation. Pluronic P123 is a discreet, linear substitute, triblock copolymer made up of polyethylene oxide (PEO) and polypropylene oxide (PPO). In an experiment 5 g of triblock copolymer (i.e., P123), structured mesoporous components such as SBA-15 are used as a backbone to be dispersed into distilled water of 116.25 g, and 29.13 g hydrochloric acid is inputted into the solution. Final 11 g of tetra-ethyl-ortho-silicate as a drug additive of silica was applied to tetraisopropoxide titanium (Si/Ti = 100) during steady 24-hour temperature mixing. The resulting slurry was accompanied by N-butanol and washed with distilled water. The material dried at 110°C for 12 hours and then calcined at 500°C for 8 hours [9].

2.2. Characterization. The pattern in the Ultima IV diffractometer is the powder X-ray diffraction (XRD). The following statistical figures are obtained within the range of 0.1–5° with a phase of 0.008° and a scanning speed of 0.5° per minute, using the nonfiltered Cu K α radiation source, in the form of a $T = 0.54178 \text{ \AA}$ with 30 mA and 40 kV. TESCAN and VEGA 3 LMU, Australia, used for surface morphology study a scanning electron microscope (SEM). The photos of the samples were analysed with a 200 kv acceleration voltage using a tool JEOL Australia. Sample pores and surface area are specified in liquid nitrogen (77 K) and the

Chinese surface inspection system, Quanta Chrome Nova-1000, and also the de Boert map, BET, and pore size. Samples were obtained at 1:10 KBr room temperature with 10 scans from FTIR, PerkinElmer, Spectrum 100, USA. A Fourier transform spectra registered the samples [10]. On Evolution 300 Thermo Science, the sample spectrum was recorded with UV-visible spectrometer, USA, and BaSO₄ as reference, diffuse UV-visible spectrum (UV-Vis-DRS).

2.3. Reaction Kinetics Study. The reactor was filled with one mole of propionic acid and one mole of n-butanol. The heat input is supplied by rotating the heating knob to a desired temperature. The stirrer is adjusted to 480 rpm to mix the catalyst with reactants. When there is no temperature, the recalculated amount of catalyst is transferred into the reaction mixture. This time onwards the actual reaction time counted. The samples have been withdrawn in the regular intervals and analysed for propionic acid conversion by titration with standard NaOH solution. The reaction is continued till there is no change in the concentration of propionic acid concentration with time. This indicates the reaction reached chemical equilibrium.

3. Results and Discussions

The synthesized sulfonic acid-functionalized Ti SBA-15 catalyst is analysed for its characterization and used for kinetic investigations for reaction temperature of 85°C to 115°C, catalyst loading of 1 wt% to 3 wt%, and mole ratio of acid to alcohol 1:1 to 1:4.

3.1. Transmission Electron Micrograph Analysis (TEM). Figure 1 shows Ti-supported SBA-15 functionalized with sulfonic acid, revealing a hexagonally well-organized mesoporous catalyst with severe parallel channels, close to porous configuration. Ti-supported SBA-15 functionalized with sulfonic acid; TEM images functionalized with sulfonic acid [11]. In the long-range mesoporous ordering determined as opposed to the Ti-supported SBA-15 functionalized with sulfonic acid, there were uniform morphologies of the macrostructure of silica materials sulfonated.

3.2. Diffuse Reflectance Ultraviolet-Visible Spectroscopic Analysis. The Ti-supported SBA-15 functionalized with sulfonic acid spectrum of UV-Vis-DRS is shown in Figure 2. Two large peaks of ~210–230 nm and 330–350 nm were observed confined to the presence and integration of the tetrahedral environment and the homogeneous distribution of Ti ions in the Ti-supported SBA-15 functionalized with sulfonic acid matrix [12].

3.3. Fourier Transform Infrared Spectroscopic Analysis (FTIR). Figure 3 displays the Ti-supported SBA-15 functionalized with sulfonic acid composite FTIR spectrum of sulfonic acid. The 1088 cm⁻¹ peak suggests the Si-O-Si bond in a Ti SBA-15 fused sulfonated binding. The vibrations of Si-O-Si symmetrically stretching were 802 cm⁻¹ and 466 cm⁻¹, respectively. Due to Ti-O-infrastructure Si's vibration, peaks 910 and 960 cm⁻¹ resulted, which means that Ti is strongly indicated in the SBA-15 matrix [13]. The exact

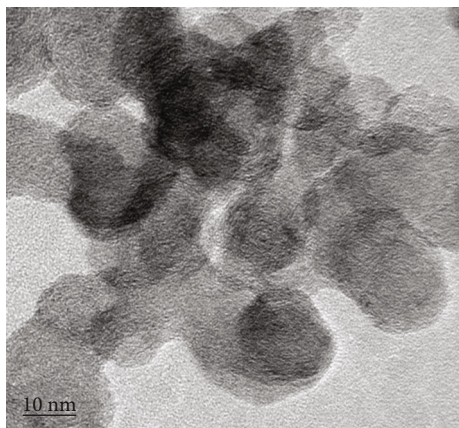


FIGURE 1: TEM images of Ti-supported SBA-15 functionalized with sulfonic acid.

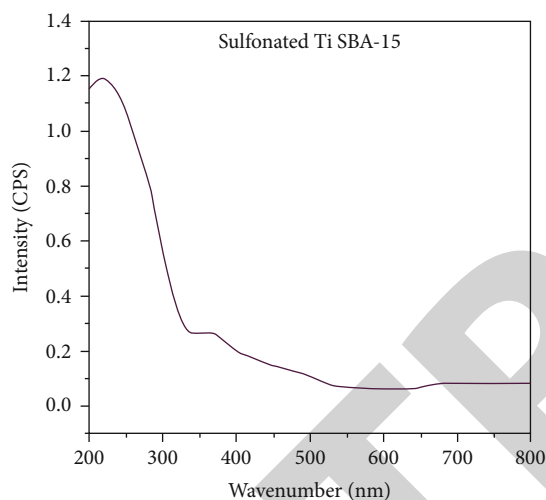


FIGURE 2: Ti-supported SBA-15 functionalized with sulfonic acid UV-Vis-DRS study.

location of the pictures was found to contribute both to the chemical composition and the calibration and resolution of the instrument used in the studies. In the Ti-supported SBA-15 functionalized with sulfonic acid catalyst, the maximum strength of the band is 960 cm^{-1} . Due to hydrogen interaction, breaks between the silanol groups and the water molecules adsorbed were seen at 1630 and 3400 cm^{-1} (SI-OH). The peaks of 1052 and 1140 cm^{-1} confirm that the functional groups $-\text{SO}_4\text{H}$ have symmetrical and asymmetrical vibrations.

3.4. Powder X-Ray Diffraction (XRD). Synthesized sulfonic acid pattern of powder X-ray diffraction (XRD) composites functionalized by Ti-supported SBA-15 shown in Figure 4. In the X-ray diffraction study, two weak peaks and a strong, extreme peak were noted [14]. The weak peaks found by 2θ were 1.4 and 1.7 , and the sharp peak by 2θ was 0.8 , which specify the periodicity of the high structures as a result of higher condensation between the silanol and titanium groups.

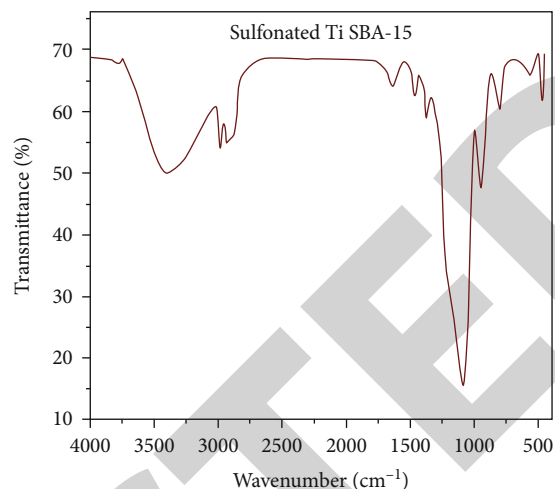


FIGURE 3: FT-IR analysis of Ti-supported SBA-15 functionalized with sulfonic acid.

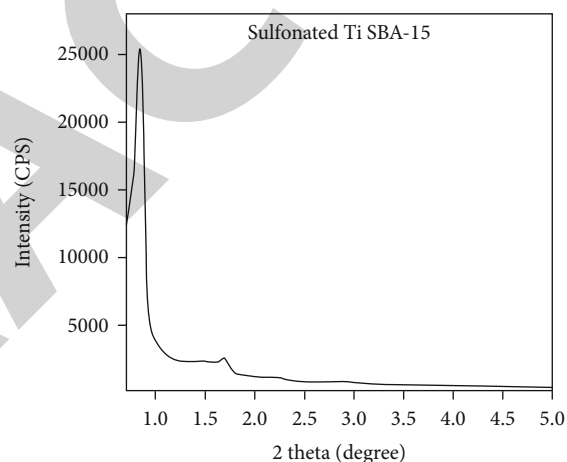


FIGURE 4: Small-angle XRD pattern of Ti-supported SBA-15 functionalized with sulfonic acid.

3.5. Thermogravimetry/Differential Thermal Analysis. Figures 5 and 6 display the Ti-supported SBA-15 functionalized with sulfonic acid materials from the TG-DTA analysis of sulfonic acid. It explains preliminary weight loss from 0°C to 300°C (4.31%) by loss in mesoporous composite of water adsorbed and ethanol molecules [15]. Therefore, the decomposition of the pattern that is trapped within the Ti-supported SBA-15 functionalized with sulfonic acid and its remainder shown to be steep weight loss between 350°C and 600°C is 29.86% to 58.75%.

The DTA plot proposed that the patterns of the mesoporous material should be heated. A weight loss of initial 0°C to 300°C of 0°C is observed in the data track of the sulfonic acid functionalized composite Ti-SBA-15 (4.06%). A further weight loss in sulfonic acid pores of Ti-SBA-15 (42.89%) was found to be 52.3% due to the oxidative decomposition of obstructed patterns, and residual mass was 52.3%. A large exothermic peak at 308.7°C has been reported. The Ti-supported SBA-15 functionalized with sulfonic acid composite has no weight loss observed in $500\text{--}700^\circ\text{C}$. These Ti-

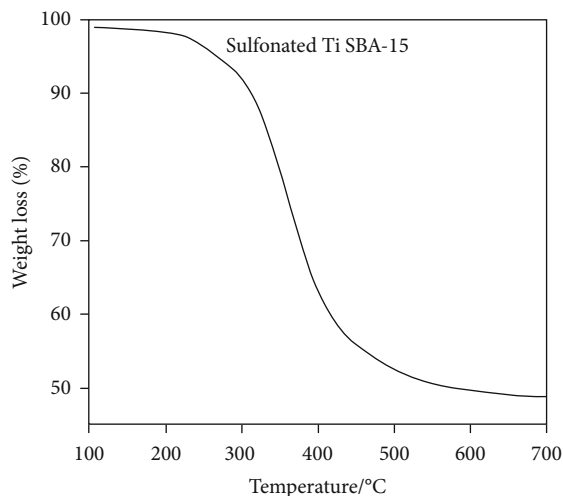


FIGURE 5: TGA analysis of Ti-supported SBA-15 functionalized with sulfonic acid.

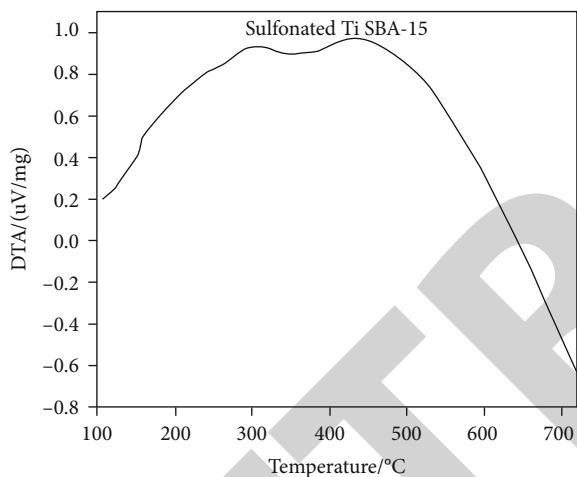


FIGURE 6: DTA analysis of Ti-supported SBA-15 functionalized with sulfonic acid.

SBA-15 composites with sulfonic acid function are also thermally stable up to 700°C.

3.6. N_2 Adsorption-Desorption Studies. Information on the surface area, the pores of composites Ti-supported SBA-15 functionalized with sulfonic acid have been provided through adsorption isothermal studies and is shown in Figure 7. Subsequently, it was noted that the silicon composites were shown to indicate their mesoporosity as the type IV nitrogen isotherms with the deposal H1 hysteresis loop [16]. The distribution of mesoporous sizes extends when the Ti is incorporated in the SBA-15 framework. These results have been validated using the distribution curve for pore size. The results show that when the Ti was integrated into the SBA-15 functionalized with sulfonic acid framework, the consistency of the mesoporous size distribution has declined. It was also noted that the pore volume, surface area, pore diameter, and also peak intensities were decreased sharply with increased incorporation of Ti into the SBA-15 functionalized with sulfonic

acid samples [17]. This could be due to the blocking by titanium-based mesoporous canals. In order to define the texture properties of the mesoporous catalysts, the BJH pore size distribution approach and the BET surface analysis are employed in Table 1.

4. Catalytic Performance (Sulfonic Acid Functionalized Ti SBA-15)

4.1. Effect of Reactant Molar Ratio. The mole ratio of propionic acid with n-butanol varied from 1:1 to 1:4 at a temperature of 115°C and a speed of 240 rpm for conversion of propionic acid with Ti-supported SBA-15 functionalized with sulfonic acid [18]. The conversion of propionic acid as function of molar ratio is shown in Figure 8. The propionic acid conversion increases as the molar ratio increases due to excess n-butanol. From the figure, it could be observed as 79.90%.

4.2. Effect of Temperature. The effect temperature on the conversion of propionic acid at 2% by wt catalyst loading and at 1:1 mole ratio is shown in Figure 9. The conversion of propionic acid is increased as temperature increases. Higher the temperatures, the time required to reach equilibrium is lesser [19]. It shows that the reaction is kinetically controlled.

4.3. Effect of Catalyst Amount. The effect of catalyst amount on the propionic acid conversion kinetics is shown in Figure 10 at a temperature of and mole ratio of 1:1. The experiments employ separate catalyst concentrations of 1, 2, and 3 wt%. The conversion of propionic acid increases as the catalyst loading increases [20]. When the catalyst quantity increased in the reaction mixture, the reaction rate increases due to availability of H^+ ions which in turn provide more catalyst surface area. The experiments were conducted for 4 runs with the same catalyst. The propionic acid conversion is the same under 1% error.

4.4. The Ti-Supported SBA-15 Functionalized with Sulfonic Acid for the Kinetic Analysis. The initial reaction rate of propionic acid with n-butanol has been carried out under different catalyst loadings ($r_{A0} = \Delta C_{A0}/\Delta t$) for this catalyst [21]. The general kinetic expression for the catalyzed heterogeneous esterification reaction can be written as

$$-r_A = \frac{k_f w_{\text{cat}} (C_A C_B - (C_R C_w / K_{eq}))}{(1 + K_A C_A + K_B C_B + K_E C_E + K_w C_w)^n}, \quad (2)$$

where r_A is the reaction rate and (w_{cat}) is the catalyst weight on dry basis. A, B, E, and W represent propionic acid, n-butanol, butyl propionate, and water. K is the adsorption constant, K_e is the equilibrium constant, and k_f is the forward reaction rate constant. In equation (2), when $n = 0$, it is a PH model; when $n = 1$, it is ER model; and when $n = 2$, it is a LHHW model.

As can be seen in Figure 11, the starting reaction rate instead of the plated one is a linear feature, which means the adsorption of propionic acid on the Ti-supported

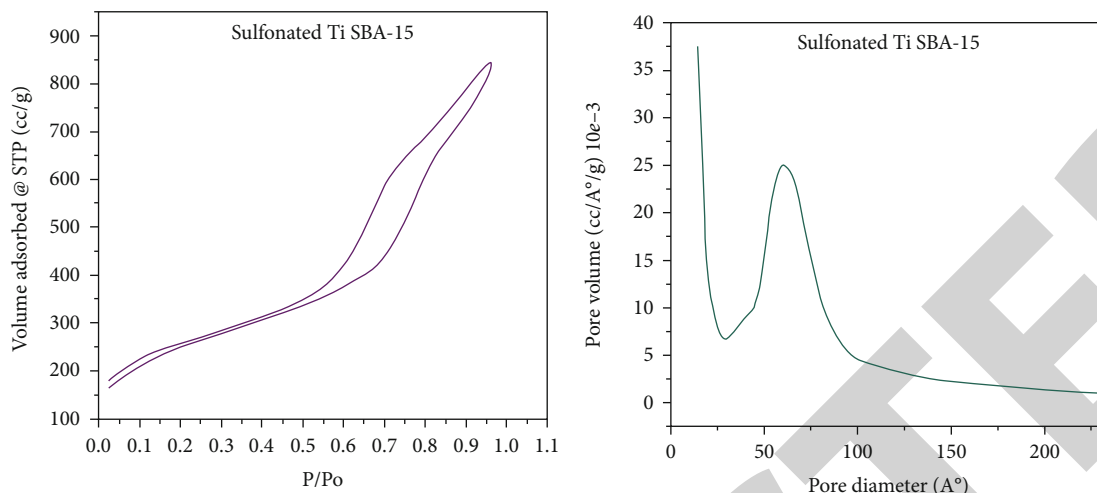


FIGURE 7: Ti-supported SBA-15 functionalized with sulfonic acid with N_2 adsorption/desorption isotherms, pore diameter, and pore volume distribution.

TABLE 1: BET-isothermic adsorption and porosity data.

Mesoporous material	Pore volume (cc/g)	Average pore diameter (\AA)	Surface area (m^2/g)
Ti-supported SBA-15 functionalized with sulfonic acid	1.02	31.78	457

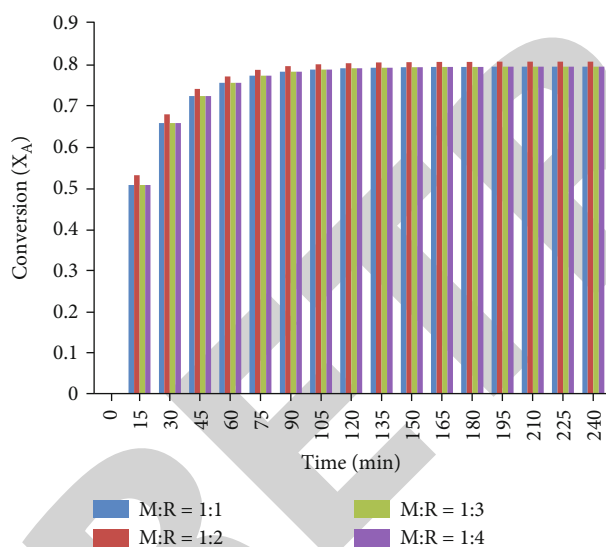


FIGURE 8: Conversion versus time for different molar ratios. Other conditions are catalyst loading: 2%, temperature: 115°C , and speed: 240 rpm.

SBA-15 functionalized with sulfonic acid catalyst surface is not possible, and at the same time, the initial rate of reaction increases in line with n-butanol concentrations. Therefore, we can infer that at low concentrations of n-butanol, it adsorbed n-butanol extremely low and almost continuously increases the concentration. This study concludes that the reaction mechanism is defined in the Eley-Rideal model, i.e., reaction between adsorbed butanol molecules and propionic acid molecules in the bulk solution. In the single site, only one reactant is adsorbed on

the catalyst and the remaining reactant is in the bulk reaction. In the double site, two reactants are at the catalyst surface and reaction proceed at this place and formed products desorbed from the catalyst surface. The literature found the solvent (dioxane) and ester adsorption to be insignificant. The rate determination step is to specifically take the stoichiometric and corresponding reaction rate as the Eley-Rideal (ER) model of a surface-reaction equation. After excluding terms of adsorption of acid and ester, ER form can be written as

$$-r_A = \frac{k_f w_{\text{cat}} (C_A C_B - (C_R C_w / K_{eq}))}{(1 + K_B C_B + K_w C_w)} \quad (3)$$

The Arrhenius law expresses the dependence of temperature on reaction rate as given in the following.

Equation (3) behavior is used for speed expression rather than concentration, because the predictions of models adapted to the measured film data result in improved prediction [22]. Relocation of equation (4) can be described as equation for the initial reaction rate without a product present, shown in

$$\frac{C_{A0} C_{B0}}{-r_{A0}} = \frac{1}{(k_f w_{\text{cat}})} + \frac{K_B}{k_f w_{\text{cat}}} C_{B0} \quad (4)$$

Figure 12 shows the plot of $C_{A0} C_{B0} / -r_{A0}$ versus C_{B0} results in a direct slope line $K_B / k_f w_{\text{cat}}$ and intercept $1/k_f w_{\text{cat}}$ as shown in the figure.

Slopes and intercepts in these figures indicate the constants in rates and adsorption constants k_f , K_B , K_w , and their estimated values at three temperatures as shown in Table 2.

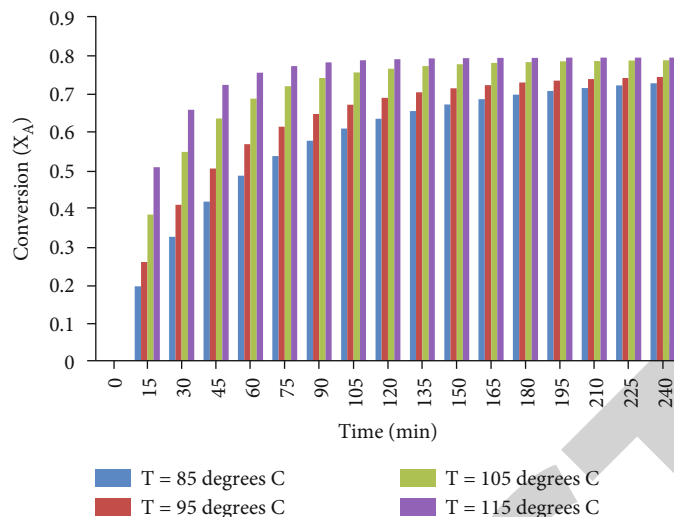


FIGURE 9: Conversion versus time for different temperatures. Other conditions are catalyst loading: 2%, mole ratio: 1 : 1, and speed: 240 rpm.

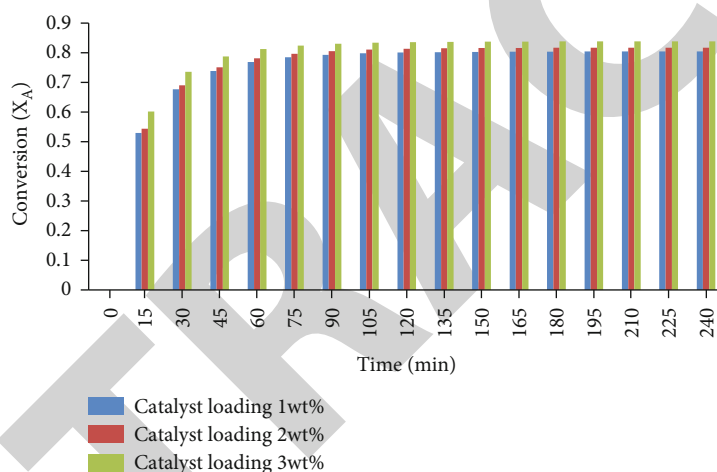


FIGURE 10: Conversion vs. time (min) for different catalyst loadings. Other conditions are mole ratio: 1 : 1, temperature: 115°C, and speed: 240 rpm.

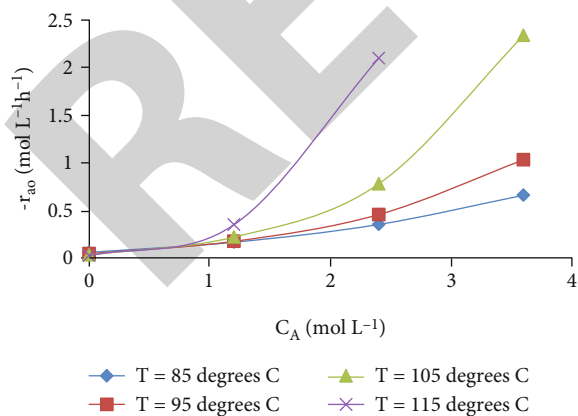


FIGURE 11: The effect on the initial reaction rate of ($-r_{A0}$) at different temperatures on the charging of catalyst.

4.5. *Activation Energy and Rate Constants.* The Arrhenius law expresses the dependence of temperature on reaction rate as given in the following:

$$k_i = k_i^0 \exp(-E_i/RT), \quad (5)$$

where k_f is the activation energy for forward reaction and k_{i0} is the frequency factor [23]. Equation (5), a plot of $\ln K_F$, $\ln K_B$, and $\ln K_W$ versus $1/T$ plot, lists a slope straight of (E/R) and, as shown in Figure 13, $\ln k_{i0}$ intercept opposed to $1/T$. In the presence of sulfonic acid functionalized Ti SBA-15, the activation energy was found to be 39.5 kJ mol⁻¹. The adsorption constants as function of temperature have arrived from Figure 13 as given in equations (7)–(9).

$$K_F (\text{L}^2 \text{g}^{-1} \text{mol}^{-1} \text{h}^{-1}) = \exp^{(232-1109/T)}, \quad (6)$$

$$K_B (\text{L mol}^{-1}) = \exp^{(3125/T-17.83)}, \quad (7)$$

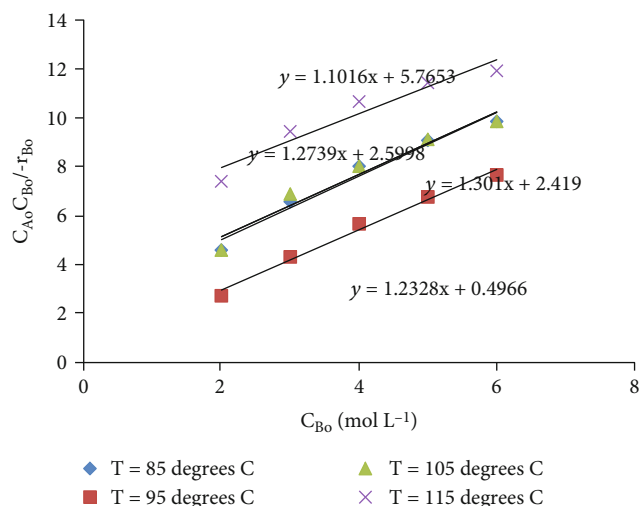


FIGURE 12: $C_{A_0} C_{B_0} / -r_{A_0}$ versus C_{B_0} at different temperatures.

TABLE 2: Kinetics and adsorption constants.

Temperature (°C)	$k_f / L^2 mol^{-1} h^{-1}$	$K_B / L mol^{-1}$	$K_W / L mol^{-1}$
85	0.78×10^{-4}	0.18	0.19
95	0.81×10^{-4}	0.20	0.49
105	0.78×10^{-4}	0.19	0.51
115	0.90×10^{-4}	0.09	0.56

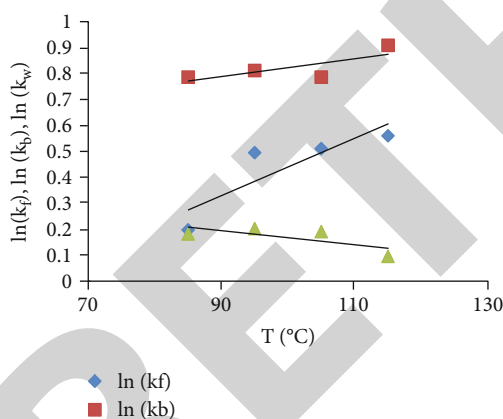


FIGURE 13: Arrhenius plot for $\ln K_b$, $\ln k_f$, and $\ln K_w$ vs. T .

$$K_w (L mol^{-1}) = \exp^{(4856/T - 54.9)}. \quad (8)$$

4.6. *Model Prediction.* Model predictions with ER model have been compared with experimental results as shown in Figure 14, for esterification of propionic acid with butanol over an entire range of expected parameters [24].

The following equation (9) is used to determine the experimental reaction rate for different time steps for various acid conversions.

$$-r_{A,\text{experimental}} = \frac{\Delta C_A}{\Delta t} = C_{A_0} \frac{\Delta X}{\Delta t}. \quad (9)$$

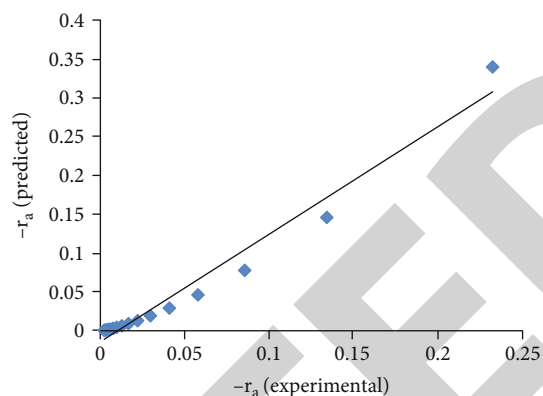


FIGURE 14: Parity plot for rate of reaction from experimental data and model prediction.

Figure 14 shows the parity plot between the experimental value and the calculated values. It can be observed that the findings fall within ± 5 percent error.

5. Conclusions

SBA-15, Ti, and $-SO_3H$ were successfully incorporated with a sol-gel process. It is found that final Ti-and-S contents were less than anticipated in samples. Moreover, the presence of sulphur decreases titanium's inclusion in the SBA-15. Propionic acid reaction kinetics with n-butanol has been investigated with this catalyst. Experimental results indicate that the reaction is kinetic controlled instead of mass transfer controlled. Eley-Rideal (ER) was developed based on an adsorption analysis to interpret kinetic data. The kinetic model was well prepared with experimental results. The EA 29.63 kJ/mol activation energy and kinetic factor k_0 0.549 L²/g-mol-h were found.

Data Availability

No data were used to support this study.

Conflicts of Interest

The authors declare that they have no conflicts of interest regarding the publication of this paper.

References

- [1] I. V. Yentekakis and F. Dong, "Grand challenges for catalytic remediation in environmental and energy applications toward a cleaner and sustainable future," *Frontiers in Environmental Chemistry*, vol. 1, pp. 1–14, 2020.
- [2] A. Chakrabarti and M. M. Sharma, "Cationic ion exchange resins as catalyst," *L' Azione sanitaria*, vol. 20, no. 1-2, pp. 1–45, 1993.
- [3] V. H. Agreda, L. R. Partin, and W. H. Heiss, "High purity methyl acetate via reactive distillation," *Chemical Engineering Progress*, vol. 86, no. 2, pp. 40–46, 1990.
- [4] R. Ronnback, T. Sami, A. Vuori et al., "Development of a kinetic model for the esterification of acetic acid with

Retraction

Retracted: Eco-Friendly Synthesis of Multishaped Crystalline Silver Nanoparticles Using Hill Garlic Extract and Their Potential Application as an Antifungal Agent

Journal of Nanomaterials

Received 11 July 2023; Accepted 11 July 2023; Published 12 July 2023

Copyright © 2023 Journal of Nanomaterials. This is an open access article distributed under the Creative Commons Attribution License, which permits unrestricted use, distribution, and reproduction in any medium, provided the original work is properly cited.

This article has been retracted by Hindawi following an investigation undertaken by the publisher [1]. This investigation has uncovered evidence of one or more of the following indicators of systematic manipulation of the publication process:

- (1) Discrepancies in scope
- (2) Discrepancies in the description of the research reported
- (3) Discrepancies between the availability of data and the research described
- (4) Inappropriate citations
- (5) Incoherent, meaningless and/or irrelevant content included in the article
- (6) Peer-review manipulation

The presence of these indicators undermines our confidence in the integrity of the article's content and we cannot, therefore, vouch for its reliability. Please note that this notice is intended solely to alert readers that the content of this article is unreliable. We have not investigated whether authors were aware of or involved in the systematic manipulation of the publication process.

Wiley and Hindawi regrets that the usual quality checks did not identify these issues before publication and have since put additional measures in place to safeguard research integrity.

We wish to credit our own Research Integrity and Research Publishing teams and anonymous and named external researchers and research integrity experts for contributing to this investigation.

The corresponding author, as the representative of all authors, has been given the opportunity to register their











agreement or disagreement to this retraction. We have kept a record of any response received.

References

- [1] V. U. M. Nallal, M. Razia, O. A. Duru et al., "Eco-Friendly Synthesis of Multishaped Crystalline Silver Nanoparticles Using Hill Garlic Extract and Their Potential Application as an Antifungal Agent," *Journal of Nanomaterials*, vol. 2022, Article ID 7613210, 7 pages, 2022.

Research Article

Eco-Friendly Synthesis of Multishaped Crystalline Silver Nanoparticles Using Hill Garlic Extract and Their Potential Application as an Antifungal Agent

V. Uma Maheshwari Nallal ¹, M. Razia ¹, Ozlem Ates Duru ², G. Ramalingam ³,
Sasikala Chinnappan ⁴, Murugesan Chandrasekaran ⁵, R. M. Gengan ⁶,
Woo Jin Chung ⁷, Soon Woong Chang ⁷ and Balasubramani Ravindran ⁷

¹Department of Biotechnology, Mother Teresa Women's University, Kodaikanal, 624101 Tamilnadu, India

²Department of Nutrition and Dietetics, School of Health Sciences, Nisantasi University, Turkey

³Department of Nanoscience and Technology, Science Campus, Alagappa University, Karaikudi, 630003 Tamil Nadu, India

⁴Department of Pharmaceutical Biology, Faculty of Pharmaceutical Sciences, UCSI University Kuala Lumpur (South Wing), No. 1, Jalan Menara Gading, UCSI Heights 56000 Cheras, Kuala Lumpur, Malaysia

⁵Department of Food Science and Biotechnology, Sejong University, Seoul, Republic of Korea

⁶Department of Chemistry, Faculty of Applied Sciences, Durban University of Technology, Durban 4001, South Africa

⁷Department of Environmental Energy and Engineering, Kyonggi University Yeongtong-Gu, Suwon, Gyeonggi-Do 16227, Republic of Korea

Correspondence should be addressed to M. Razia; razia581@gmail.com and R. M. Gengan; genganrm@gmail.com

Received 11 November 2021; Revised 14 December 2021; Accepted 27 December 2021; Published 29 January 2022

Academic Editor: Karthikeyan Sathasivam

Copyright © 2022 V. Uma Maheshwari Nallal et al. This is an open access article distributed under the Creative Commons Attribution License, which permits unrestricted use, distribution, and reproduction in any medium, provided the original work is properly cited.

Antimicrobial resistance is a global health challenge, and the large loads of biocides dumped into the environment augment the spread of antifungal resistance and environmental contamination. Therefore, eco-friendly antifungal agents must be developed to combat antibiotic resistance and to reduce environmental contamination. In the present investigation, *Allium sativum* (Hill garlic-Malai Poundu) extract was used as a green resource to achieve silver nanoparticle (AgNP) production. AgNPs were characterized by various spectral and microscopic analyses. In vitro free radical scavenging assays were instigated to determine the antioxidant capacity of the AgNPs, and the antifungal activity was assessed using Agar well-diffusion assay against pathogenic fungal strains. The mean particle size of the AgNPs was calculated as 35.1 nm with face-centered cubic (FCC) structure. AgNPs exhibited free radical scavenging activity against 2,2-diphenyl-1-picrylhydrazyl (DPPH), 2,2-azino-bis (3-ethylbenzotiazolin)-6-sulfonic acid (ABTS), and hydrogen peroxide (H₂O₂) radicals. Scavenging of DPPH radicals by AgNPs was impressive, and an IC₅₀ value of 6.3 ± 0.4 µg/ml was obtained in this assay. Among the tested *Candida* strains, the order of the least susceptibility on exposure to AgNPs synthesized using Hill garlic extract was as follows: *C. glabrata* ≤ *C. tropicalis* ≤ *C. parapsilosis* ≤ *C. krusei* ≤ *C. albicans*. The study highlights the synthesis of environment-friendly nanoparticles using Hill garlic extract with enhanced antifungal properties.

1. Introduction

The discovery of antibiotics has been a milestone in contemporary medicine. However, the extensive consumption of antibiotics has provoked the emergence of antimicrobial resistance (AMR) which in turn has become a global health

challenge [1]. Antibiotic pollution has a crucial impact on the environment apart from being a health care crisis. The overuse and misuse of antibiotics have increased the load of biocides that are being discarded into the surroundings as environmental contaminants. At a daily basis, antimicrobial agents are being disseminated into land and water

resources by pharmaceutical industries, hospitals, poultry, and livestock [2, 3]. The presence of antibiotic residues in the environment elevates the pressure on the bacteria to develop AMR through horizontal gene transfer of antibiotic resistance genes [4]. Antibiotic pollution also has a negative effect on developmental and behavioural characteristics of human and animal population. Similarly, aquatic animals are exposed to a higher dose of antibiotic residues that leads to bioaccumulation and chronic toxicity. Malformations including defects in head and body ratio and pericardial edema were identified in *Xenopus tropicalis* on tetracycline exposure [5]. The removal of pathogens from biomedical wastes has also become a meticulous process since biomedical wastes do not degrade easily in the environment. This can have a significant impact on wildlife and human beings and enhance antimicrobial resistance [6]. However, eco-friendly antimicrobial agents can be developed by the amalgamation of eco-friendly antifungal agents and modern technologies to combat multidrug-resistant microbes.

The current advancements in nanotechnology proffer new dimensions to develop unique nanoparticles (NPs) with enhanced antimicrobial properties. NPs not only act as antimicrobial agents but can also act as efficient carriers of herbal formulations and drugs [7]. Different scopes of nanomaterials and NPs have been explored to reveal their antimicrobial property; however, metallic nanoparticles such as silver and gold NPs have gained wide-spread attention due to their distinctive properties [8]. NPs are considered favourable agents in combating microorganisms due to their stability, solubility, feasibility, biocompatibility, and targeted drug release. The chief advantage of NPs over other conventional antibiotics is their small size and large surface area proportion [9]. AgNPs are considered the most effective antimicrobial agents in spite of the reasonable bactericidal effects exhibited by other NPs such as iron oxide, copper oxide, gold, and titanium oxide NPs [10–12]. The mechanism of action of NPs against microorganisms varies from that of the standard antibiotics. NPs interact directly with the cell of the microbes and inhibit the biofilm formation. They can also trigger the innate and adaptive immunity of the hosts. They can kill the microbes by initiating the generation of reactive oxygen species and effectively interact with the DNA and proteins of the pathogen [13]. Nevertheless, NPs can be promising candidates to target multidrug-resistant microbes.

Green resource employed synthesis of nanoparticles has several benefits that are not offered by other routes NP synthesis. It is highly feasible, robust, and biocompatible and can be used to produce stable and nontoxic NPs [8]. Diverse plant parts have been engaged in the production of green NPs and evaluated for their antimicrobial properties. For example, NPs synthesized from whole plant extract of *Leonurus japonicus* showed antimicrobial potential against *Pseudomonas aeruginosa*, *Enterobacter cloacae*, and *Escherichia coli* [14]. AgNPs synthesized using below the ground portion of the plant *Polygala tenuifolia* possessed antibacterial activity [15], whereas *Artemisia capillaris*-mediated AgNPs inhibited the growth of gram positive (+) and gram negative (-) bacteria [16]. Results of Jalal et al. [17] revealed

that AgNPs synthesized using *Syzygium cumini* seed extract conferred antifungal potential against *C. albicans* and four other *Candida* species by suppressing the biofilm and germ tube formation. NPs synthesized using *Allium sativum* extract possessed biocidal property against *P. aeruginosa* and antifungal activity against *C. albicans* [18]. This showed that plant extract-mediated NPs synthesized in an eco-friendly approach can combat microbes efficiently. Further, the use of garlic extracts in NP synthesis and evaluation of their antifungal property against multiple *Candida* strains is limited. Therefore, the current study was carried out to green synthesize AgNPs using Kodaikanal Hill garlic (Malai Pooundu) extract and evaluate their antifungal property against pathogenic *Candida* strains.

2. Experimental Details

2.1. Preparation of Plant Extract. Hill garlic was purchased from a Hill garlic cultivating farm at high altitudes of Kodaikanal Hills (Poombarai village). Garlic sample was processed by removing the skin and cleaned using distilled water. The garlic pods were chopped into small pieces and crushed using a mortar and pestle. Double distilled water was added in measured amounts to obtain the extract with 1 mg/1 ml concentration.

2.2. Biosynthesis of AgNPs. 0.025 l of Hill garlic extract was added to 0.495 l of the substrate (AgNO_3) prepared at a concentration of 1 mM. Later, the solution was centrifuged at 12,000 rpm and the resultant pellet was thoroughly washed using deionized water to remove unreacted substances. The pellets were air-dried and used for experiments [19].

2.3. Characterization of AgNPs. Reduction of silver ions was monitored at regular intervals with by an Ultra-Violet visible (UV-Vis) spectrophotometer (Shimadzu). To identify the functional groups, FTIR analysis was executed using a Perkin Elmer spectrum 100 N Fourier Transform Infrared (FTIR) (4000 to 500 cm^{-1}) spectrometer. XRD (X-ray diffractometer) analysis was performed to identify the particle nature of the AgNPs (X^3 Pert Pro PXRD). Identification of charge and assessment of stability was determined using a Malvern instruments Ltd. Zeta potential analyzer, and the AgNP shapes were recorded using a Joel/Jem 2100 High Resolution-Transmission Electron Microscopy instrument.

2.4. In Vitro Free Radical Scavenging Activity of AgNPs. DPPH free radical inhibiting assay was done by adding 0.5 ml of 0.1 mM DPPH dissolved in methanol to various concentrations of AgNPs. The solution was mixed well and kept in the dark for 30 min at room temperature. Measurements were recorded at 517 nm and DPPH in methanol served as blank. For ABTS radical scavenging assay, ABTS was prepared and stored for 16 hours in the dark. To 1 ml of AgNPs, preprepared ABTS was added, and the values were observed at 734 nm. In order to evaluate the H_2O_2 radical scavenging activity, 43 mM H_2O_2 was dissolved using phosphate buffer and 4 ml of this solution was mixed with calculated amounts of AgNPs. The optical density values

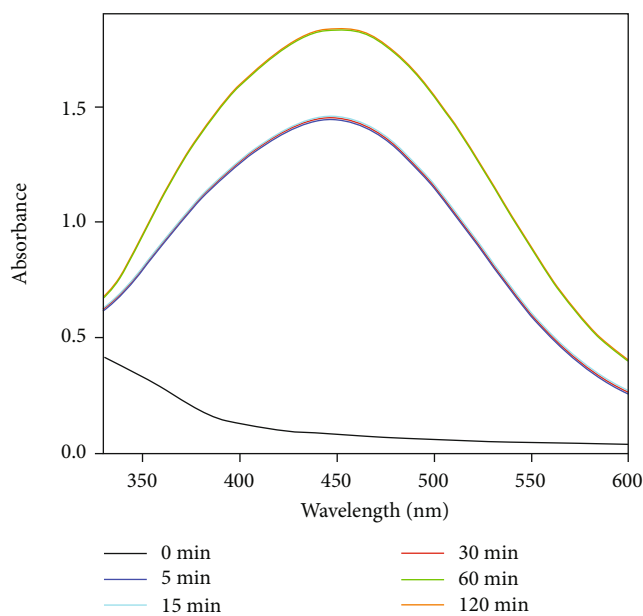


FIGURE 1: UV-visible absorption spectrum of AgNPs.

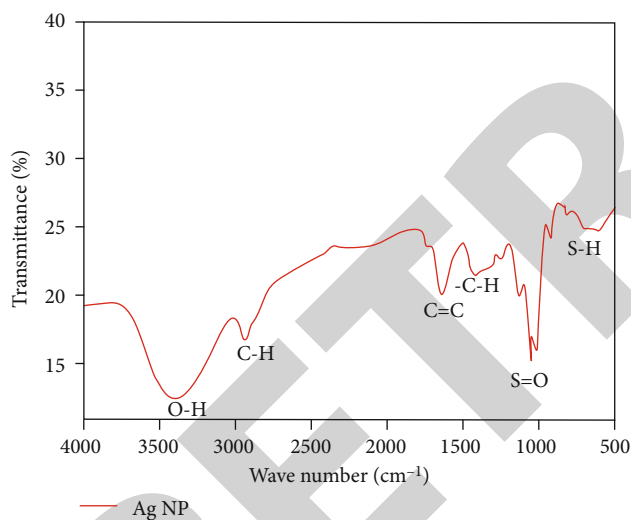


FIGURE 2: FT-IR spectrum of AgNPs.

were noted at 230 nm and compared to the values of standard (ascorbic acid) [20].

2.5. In Vitro Antifungal Activity of AgNPs. The potency of the AgNPs to inhibit pathogenic fungal strains was evaluated by agar well-diffusion assay. *C. tropicalis*, *C. albicans*, *C. glabrata*, *C. krusei* and *C. parapsilosis* were acquired from “Microbial Type Culture Collection and Gene Bank.” The organisms were swabbed across the fungal medium, and 6 mm wells were cut. To the wells, various concentrations of AgNPs were added. The antifungal agent amphotericin B which belongs to the polyene class of antifungals was employed as the standard, and distilled water served as negative control. The plates were kept at 37°C, and the inhibition was measured post 24 h [21].

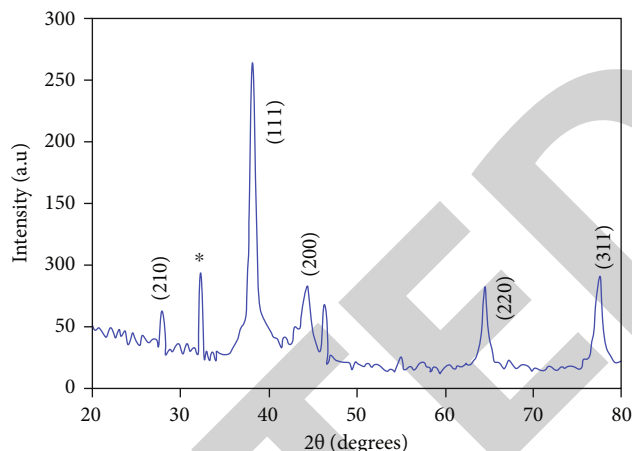


FIGURE 3: XRD pattern of AgNPs.

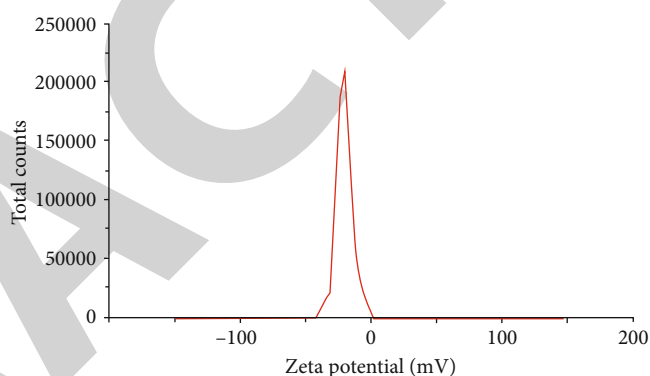


FIGURE 4: Zeta potential spectrum of AgNPs.

2.6. Statistical Analysis. In vitro assays were performed in triplicates and expressed as mean \pm standard deviation. Origin lab software was used for data analysis.

3. Results and Discussion

3.1. Synthesis. AgNPs were obtained in a biodirected and facile approach using Hill garlic extract. AgNPs were synthesized previously by Vijayakumar et al. [22] using garlic cloves produced from Karaikudi Market; AgNPs were successfully synthesized by using 100 mg/ml concentration of garlic extract. Here, synthesis of AgNPs was feasible at a concentration of 1 mg/ml by using silver nitrate as the precursor material. The data revealed that Hill garlic extract had multiple functions in the synthesis of AgNPs which includes reduction, capping, and stabilization through organic compounds. Silver ions are greatly reduced into AgNPs based on the bioactive plant metabolites and enzymes [23].

3.2. Characterization. The transformation of silver ions into AgNPs on exposure to Hill garlic extract could be monitored by the change of color in the solution from pallid yellow to brown on the completion of the reduction reaction. The absorption spectra of the AgNPs recorded using a UV-visible spectrophotometer are shown in Figure 1. The absorbance was monitored immediately after the exposure of the

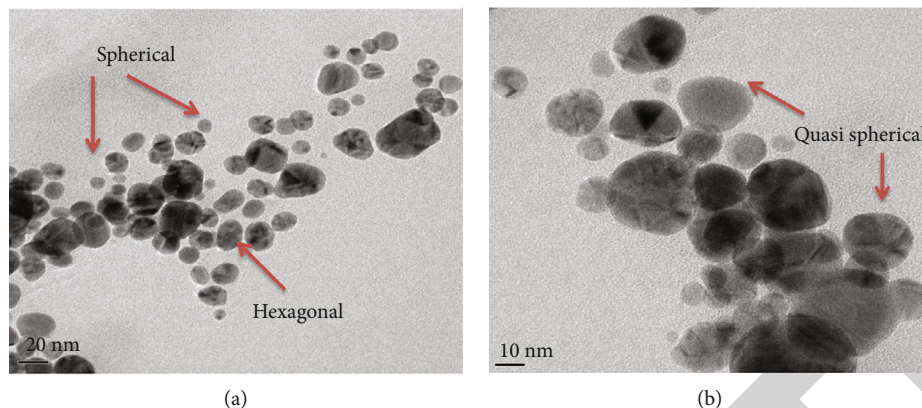


FIGURE 5: TEM micrograph of AgNPs at (a) 20 nm and (b) 10 nm.

extract up to 120 min. The absorbance spectra gradually increased with the increase in time. AgNPs showed a strong absorbance peak at 446 nm, and there was no variance in the absorption spectra after 48 hours. The FTIR spectrum (Figure 2) represents the moieties of the AgNPs that are responsible for its characteristic chemical reactions. Peaks were recorded at 3438, 1632, 1416, 1075, and 624 cm^{-1} wave number. The broad peak at 3438 cm^{-1} paralleled to O-H vibrations and peak at 1632 cm^{-1} designated the occurrence of phenols. Peaks at 1416 cm^{-1} and 1075 cm^{-1} represented the amine and alkane groups in the AgNPs. The presence of sulfur groups was correlated to 624 cm^{-1} wave number. Spectral studies using UV-visible spectrophotometer and FTIR spectrophotometer exposed the optical properties and functional groups present in the AgNPs. The identification of sulfur groups in the FTIR spectrum supports the role of organosulfur compounds present in the Hill garlic extract in the reduction process. The synergistic activity of Allicin (Garlic Organosulfur compound) and AgNPs has been proved to be effective against Methicillin-resistant *Staphylococcus aureus* [24]. Similarly, another organosulfur compound, diallyl disulfide, was loaded into spherical AuNPs (Gold nanoparticles), and their toxic effect on colorectal adenocarcinoma cells (HT-29) cells was evaluated. Diallyl disulfide loaded gold nanoparticles exhibited potential cytotoxic effects against HT-29 and are assumed to have future possibilities as nanocatalysts and nanocarriers [25].

The XRD pattern with diffraction peaks for the synthesized AgNPs is presented in Figure 3. The crystalline features of the synthesized AgNPs were witnessed in the PXRD analysis. The diffraction peaks (Bragg's reflection) at 38.42°, 44.36°, 64.40°, and 77.49° corresponded to the typical silver lattice planes (111), (200), (220), and (311). The diffraction peaks suggest that the biodirected AgNPs were face-centered cubic (FCC) crystals, indicating the presence of one full atom on the six centers of the cubic crystal and a fraction of an atom in each corner. The XRD data was parallel to the JCPDS No: 04-0783. The XRD pattern depicted the FCC nature of the AgNP crystals; according to Shetty et al. [26], in a FCC crystal, the higher intensity of (111) plane can enhance the antimicrobial activity of the AgNPs. In Figure 3, it was witnessed that the AgNPs synthesized using Hill garlic extract showed higher intensity of (111)



FIGURE 6: SAED pattern of AgNPs.

plane and could plausibly have enhanced antimicrobial potential.

Zeta potential analysis (Figure 4) reflected the charge and stability of the AgNPs; it was observed that the nanoparticles possessed negative charge (-23.3 mV) and were moderately stable. The zeta potential measurements were helpful in identifying the stability and charge based on electrophoretic mobility of the nanoparticles. Our results (-23.3 mV) were in comparable to the results obtained on using garlic extract to synthesize AgNPs in a previous study that showed a zeta potential value of -26.1 mV [22].

The size and shape of the nanoparticles were examined using HR-TEM technique and are shown in Figure 5. HR-TEM micrographs showed that the particles were predominantly spherical shaped, whereas quasispherical and hexagonal particles were also observed. The size of the particles was within the range of 20.3 nm to 60.5 nm. The mean size was measured as 35.1 nm. Ring patterns were observed in SAED analysis (Figure 6); the crystalline nature as predicted in the XRD analysis matched with the results of the SAED pattern obtained for the AgNPs. Spherical nanoparticles are frequently obtained in the synthesis of AgNPs using plant extracts; here, multishaped nanoparticles were observed in HR-TEM micrographs. The antimicrobial potential of multishaped AgNPs was tested against three microbes including two gram positive and one negative in a study, which

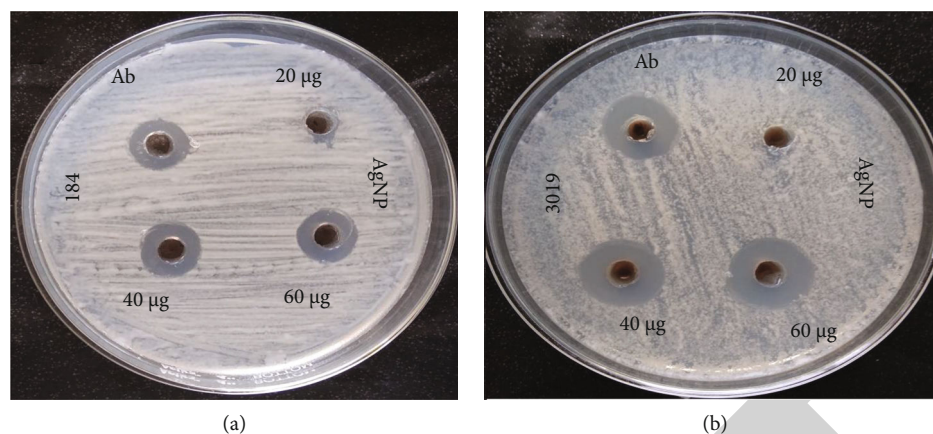


FIGURE 7: Anticandida activity of AgNPs. (a) *C. albicans* was highly susceptible to AgNP treatment, and (b) *C. glabrata* was the least susceptible species.

TABLE 1: Inhibition zone diameter of synthesized AgNPs.

S. no.	Pathogens	Inhibition zone (mm)		
		Distilled water	Amphotericin B	AgNPs
1	<i>C. albicans</i>	Nil	17 ± 0.3	20 ± 0.7
2	<i>C. krusei</i>	Nil	17 ± 0.2	18 ± 0.04
3	<i>C. parapsilosis</i>	Nil	15 ± 1.2	18 ± 0.1
4	<i>C. tropicalis</i>	Nil	13 ± 1.3	12 ± 0.3
5	<i>C. glabrata</i>	Nil	13 ± 2.1	9 ± 0.3

concluded that the antimicrobial properties of AgNPs were shape-dependent and Ag ion release was entirely based on the shape of the nanoparticles [27].

3.3. Free Radical Scavenging Activity of AgNPs. The free radical scavenging potential of the synthesized NPs was determined using three different *in-vitro* free radical scavenging assays. For all the assays, ascorbic acid (vitamin C) was taken as the antioxidant standard. Among the different tested concentrations, maximum inhibition of molecules containing unpaired electrons in their valence shell was evidenced at 25 µg/ml concentration. The ability of AgNPs to scavenge DPPH and H₂O₂ was excellent when compared to ABTS radicals. The IC₅₀ of DPPH radicals exposed to AgNPs was 8.3 ± 0.4 µg/ml, whereas 12.4 ± 1.2 µg/ml and 9.6 ± 0.2 µg/ml were recorded as the IC₅₀ for ABTS and H₂O₂ radicals, respectively. The inhibition ability augmented with increase in AgNPs concentration, indicating that the reaction was concentration/dilution-dependent. Free radical scavenging percentage recorded for ascorbic acid was 89%, 62.34%, and 81.12% for DPPH radicals, ABTS radicals, and H₂O₂ radicals, respectively. The scavenging percentage of AgNPs was 83.4%, 47.3%, and 79.1% for the above-mentioned radicals in the same order; this was almost similar to the ability of the standard. The results of the present study were similar to a study where AgNPs synthesized from *A. cepa* showed impressive antioxidant activity when compared to the activity of ascorbic acid. The free radical capacity of the AgNPs

can be related to the ability of the AgNPs to transfer electrons thus neutralizing the free radical production [28].

3.4. Antifungal Potency of AgNPs. The antifungal activity of the biosynthesized AgNPs examined by agar well-plate method is shown in Figure 7. *C. albicans* was observed as the least resistant species among the tested pathogens. AgNPs showed similar inhibitory effect when compared to the standard antibiotic amphotericin B (Table 1). Interestingly, all the tested pathogens were susceptible to the treatment of AgNPs. The inhibition area obtained for AgNPs against *C. albicans* was 20 ± 0.7 mm, and the lowest activity was observed for *C. glabrata* (9 ± 0.3 mm). Advancements in the development of antifungal drugs have been limited due to the eukaryotic nature of the fungi which is similar to higher organisms. Ergosterol synthesis pathway has always been a main target in the identification of antifungal drugs owing to its deviating nature from the mammalian pathways [29]. 30 different *Candida* species are estimated to affect humans; among these, 80% of the candidiasis cases are caused by *C. albicans*, *C. glabrata*, *C. parapsilosis*, and *C. tropicalis*. It has been identified that strains of *C. glabrata* and *C. krusei* are resistant to azole antifungal agents, whereas *C. parapsilosis* is less susceptible to the treatment of echinocandins [30]. Mutation in *Candida* strains has a major role to play in their resistance towards azole drugs. Point mutation in ERG11 gene can confer increased resistance of *C. albicans* towards azoles. This can also vary in

other *Candida* organisms; for example, *C. glabrata* does not show azole resistance based on ERG mutation, but the resistance is developed due to the mutation in CgPDR1 transcription factor [31].

Over a 10-year period, *C. glabrata* has showed the maximum resistance (more than 13%) towards antifungal agents. This was evidenced in the present study, also, *C. glabrata* was the least susceptible strain when exposed to standard antifungal agent, and similarly, the inhibitory effect of AgNPs was less on *C. glabrata* when compared to the other tested organisms. AgNPs synthesized using Hill garlic extract have been rarely tested against *Candida* strains. In a previous study, AgNPs synthesized using garlic extract were found to have mild effect on *C. albicans* but exhibited excellent activity against *S. aureus* and *E. coli* [32]. Similarly, in another study, the antibacterial activity against vaginal bacterial strains exerted by eco-friendly AgNPs synthesized using garlic extract was commendable [33]. Amphotericin B, the standard antifungal agent used in the study, also exhibited inhibitory effect on the tested *Candida* strains. Amphotericin B belongs to the class of polyene antifungal agents and acts by inducing pore formation in the outer membrane of the microorganism. Ergosterol acts as the main target for amphotericin B to which it binds strongly and leads to formation of pores. It has also been identified that this antifungal agent modulates the immune system and provides a protective effect against pathogens. However, the toxicity in the host on continuous use of amphotericin B must be taken into consideration [34]. AgNPs are presumed to aggravate membrane permeability and cellular damage that can plausibly lead to the discharge of cell content including nucleic acids and proteins resulting in the death of the organism [35]. Our results showed that AgNPs synthesized using Hill garlic extract can be a potential antifungal agent against five different *Candida* strains.

4. Conclusion

In this study, AgNPs were synthesized using Hill garlic ("Malai Poondu") extract by a feasible, robust, and environment-friendly approach in a single-reduction step without the use of chemical reducing agents. Multishaped AgNPs with an average size of 35.1 nm were obtained. The nanoparticles exhibited high free radical scavenging efficacy against DPPH, ABTS, and H₂O₂ free radicals. Strong inhibitory potential against five *Candida* strains was observed indicating the possibility of AgNPs to act as promising antifungal agents that have the possibility to reduce AMR and antibiotic pollution.

Data Availability

All data generated or analyzed during this study are included in the published article.

Conflicts of Interest

The authors declare that they have no competing interests.

Acknowledgments

The authors gratefully acknowledge the Department of Science and Technology, New Delhi, India, DST-SERB-Project (Ref. No. SB/EMEQ-431/2014). The authors would like to thank SAIF-Cochin for TEM analysis.

References

- [1] A. C. Singer, H. Shaw, V. Rhodes, and A. Hart, "Review of antimicrobial resistance in the environment and its relevance to environmental regulators," *Frontiers in Microbiology*, vol. 7, p. 1728, 2016.
- [2] A. F. Martins and P. Rabinowitz, "The impact of antimicrobial resistance in the environment on public health," *Future Microbiology*, vol. 15, no. 9, pp. 699–702, 2020.
- [3] N. Taneja and M. Sharma, "Antimicrobial resistance in the environment: the Indian scenario," *Indian Journal of Medical Research*, vol. 149, no. 2, pp. 119–128, 2019.
- [4] M. R. Gillings, "Lateral gene transfer, bacterial genome evolution, and the Anthropocene," *Transactions of the New York Academy of Sciences*, vol. 1389, no. 1, pp. 20–36, 2017.
- [5] L. Liu, W. Wu, J. Zhang, P. Lv, L. Xu, and Y. Yan, "Progress of research on the toxicology of antibiotic pollution in aquatic organisms," *Acta Ecologica Sinica*, vol. 38, no. 1, pp. 36–41, 2018.
- [6] S. Hooshmand, S. Kargozar, A. Ghorbani et al., "Biomedical waste management by using nanophotocatalysts: the need for new options," *Materials*, vol. 13, no. 16, p. 3511, 2020.
- [7] S. H. Ansari, F. Islam, and M. Sameem, "Influence of nanotechnology on herbal drugs: a Review," *Journal of Advanced Pharmaceutical Technology & Research*, vol. 3, no. 3, pp. 142–146, 2012.
- [8] Y. Park, "New paradigm shift for the green synthesis of antibacterial silver nanoparticles utilizing plant extracts," *Toxicological research*, vol. 30, no. 3, pp. 169–178, 2014.
- [9] D. Yadav, S. Suri, A. A. Choudhary, M. Sikender, B. N. Hemant, and N. M. Beg, "Novel approach: herbal remedies and natural products in pharmaceutical science as nano drug delivery systems," *Int J Pharm Tech*, vol. 3, pp. 3092–3116, 2011.
- [10] T. C. Dagal, A. Kumar, R. S. Majumdar, and V. Yadav, "Mechanistic basis of antimicrobial actions of silver nanoparticles," *Frontiers in Microbiology*, vol. 7, p. 1831, 2016.
- [11] H. A. Hemeg, "Nanomaterials for alternative antibacterial therapy," *International Journal of Nanomedicine*, vol. 12, pp. 8211–8225, 2017.
- [12] Y. N. Slavin, J. Asnis, U. O. Hafeli, and H. Bach, "Metal nanoparticles: understanding the mechanisms behind antibacterial activity," *J. Nanobiotechnology*, vol. 15, no. 1, p. 65, 2017.
- [13] B. V. Pedro, M. P. Matthew, C. Andreia et al., "Nano-strategies to fight multidrug resistant bacteria—"a battle of the titans"," *Frontiers in Microbiology*, vol. 9, p. 1441, 2018.
- [14] A. R. Im, L. Han, E. R. Kim, J. Kim, Y. S. Kim, and Y. Park, "Enhanced antibacterial activities of Leonuri herba extracts containing silver nanoparticles," *Phytotherapy Research*, vol. 26, no. 8, pp. 1249–1255, 2012.
- [15] S. H. Jun, S. H. Cha, J. Kim, S. Cho, and Y. Park, "Crystalline silver nanoparticles by using Polygala tenuifolia root extract as a green reducing agent," *Journal of Nanoscience and Nanotechnology*, vol. 15, no. 2, pp. 1567–1574, 2015.

Retraction

Retracted: Structural and Optical Properties of CdSe/CdTe Core-Shell Quantum Dots

Journal of Nanomaterials

Received 10 October 2023; Accepted 10 October 2023; Published 11 October 2023

Copyright © 2023 Journal of Nanomaterials. This is an open access article distributed under the Creative Commons Attribution License, which permits unrestricted use, distribution, and reproduction in any medium, provided the original work is properly cited.

This article has been retracted by Hindawi following an investigation undertaken by the publisher [1]. This investigation has uncovered evidence of one or more of the following indicators of systematic manipulation of the publication process:

- (1) Discrepancies in scope
- (2) Discrepancies in the description of the research reported
- (3) Discrepancies between the availability of data and the research described
- (4) Inappropriate citations
- (5) Incoherent, meaningless and/or irrelevant content included in the article
- (6) Peer-review manipulation

The presence of these indicators undermines our confidence in the integrity of the article's content and we cannot, therefore, vouch for its reliability. Please note that this notice is intended solely to alert readers that the content of this article is unreliable. We have not investigated whether authors were aware of or involved in the systematic manipulation of the publication process.

Wiley and Hindawi regrets that the usual quality checks did not identify these issues before publication and have since put additional measures in place to safeguard research integrity.

We wish to credit our own Research Integrity and Research Publishing teams and anonymous and named external researchers and research integrity experts for contributing to this investigation.

The corresponding author, as the representative of all authors, has been given the opportunity to register their agreement or disagreement to this retraction. We have kept a record of any response received.

References

- [1] G. Ramalingam, C. Ragupathi, B. Rangasamy et al., "Structural and Optical Properties of CdSe/CdTe Core-Shell Quantum Dots," *Journal of Nanomaterials*, vol. 2022, Article ID 6316716, 7 pages, 2022.

Research Article

Structural and Optical Properties of CdSe/CdTe Core-Shell Quantum Dots

G. Ramalingam ¹, **C. Ragupathi**,² **Baskaran Rangasamy** ³, **I. Colak** ⁴, **V. Vetrivelan** ⁵,
Neda Poudineh ⁶, **Balasubramani Ravindran** ⁷, **Soon Woong Chang**,⁷
and Robert M. Gengan ⁸

¹Department of Nanoscience and Technology, Science Campus, Alagappa University, Karaikudi, 630003 Tamil Nadu, India

²Department of Chemistry, Sriram College of Arts and Science, Perumalpattu, Tiruvallur, 602024, Tamilnadu, India

³Energy Storage Materials and Devices Lab, Department of Physics, School of Mathematics and Natural Sciences, The Copperbelt University, PO Box 21692, Riverside, Kitwe, Zambia

⁴Department of Electrical and Electronics Engineering, Nisantasi University, Istanbul, Turkey

⁵Department of Physics, Thanthai Periyar Government Institute of Technology, Vellore, 632002, Tamilnadu, India

⁶Department of Energy Systems Research, Ajou University, Suwon 16499, Republic of Korea

⁷Department of Environmental Energy and Engineering, Kyonggi University, Yeongtong-Gu, Suwon, Gyeonggi-Do 16227, Republic of Korea

⁸Department of Chemistry, Faculty of Applied Sciences, Durban University of Technology, Durban 4001, South Africa

Correspondence should be addressed to G. Ramalingam; ramanloyola@gmail.com
and Baskaran Rangasamy; baskaran.rangasamy@cbu.ac.zm

Received 7 November 2021; Revised 25 December 2021; Accepted 30 December 2021; Published 22 January 2022

Academic Editor: Karthikeyan Sathasivam

Copyright © 2022 G. Ramalingam et al. This is an open access article distributed under the Creative Commons Attribution License, which permits unrestricted use, distribution, and reproduction in any medium, provided the original work is properly cited.

A simple hydrothermal method is developed for the synthesis of high-quality type II core-shell CdSe/CdTe quantum dots (QDs). The XRD results reveal the formation of mixed phases of CdSe and CdTe with a grain size of 12.6 nm. SEM morphology confirms the uniformly distributed nanoscale CdSe/CdTe with no agglomeration. EDX confirms the elemental presence of Cd, Se, and Te in the compound. TEM results suggest that the size of spherical CdSe/CdTe core-shell QDs is in the range of 8~10 nm. Significant results of the SAED pattern confirm the core and shell components as CdSe and CdTe, respectively. The correlation between the synthesis procedures and the corresponding structures of the core-shell CdSe/CdTe QDs is discussed. The demonstrated monodispersed lattice structure of core-shell CdSe/CdTe QDs has excellent PL emission properties at $\lambda_{\text{emi}} \sim 585$ nm which is suitable for photovoltaic applications. The UV-Vis absorption bands at 455 nm and 560 nm confirm exciton emission due to the type II matrix of CdSe/CdTe QDs.

1. Introduction

Nanoscience and nanotechnology breakthroughs have unlocked several possibilities in various fields, including solar cell systems, photodetectors, electrical injection lasers, and optical waveguides [1]. With the rapid advancement of synthesis, characterization, and methods, scientists have discovered that combining multicomponent nanomaterials and

tuning their composition profile can result in more desirable properties such as textural morphology and electrical and optical behaviour which leads to enhancement of their applications in a wide variety of fields [2, 3]. Due to the tunable architecture, nanomaterials especially the core-shell nanostructures have an impact in most of the thrust research areas in recent years. Following solar energy conversion and in conjunction with the use of heterostructures, nanostructures

give various compensations, one of which is the quick exciton dissociation. In recent years, CdSe-CdTe heterostructures have been developed to improve the integration of CdTe and selenide components in solar cell structures for the compelling benefits of a number of these desirable features [4]. However, a critical factor limiting conversion capability is going to be the rapid relaxing of high-energy excitons (photostimulated) into low-energy excitons, resulting in excess energy from their conversion to heat energy via photon emission. Another factor affecting performance is photo-induced excitons dissociating into holes and free electrons, rather than recombination [5].

In general, the efficiency of unique photovoltaic device conversion is constrained by the solar energy distribution system which is associated with the host materials' bandgap. As a result, it is critical to synthesize materials with exceptional stability, a limited size range, and significant luminous performance [6]. At the moment, core-shell nanostructures of CdTe are being developed, in which conduction of core and valence bands are generally larger (or smaller) in comparison to that of the shell. Because of the exciton dispersion of heterostructure spatial separation, nanostructures can allow access to longer wavelengths than shell materials or single-core atoms [7].

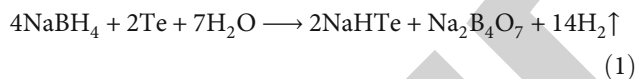
This present work deals with CdSe/CdTe core-shell-based structures of type II QDs that critically rely on their synthesis processes and are examined with traditional powder X-ray diffraction (PXRD), SEM-EDX, TEM, and SAED pattern and optical characterization (UV-Vis, PL spectrum). The correlation between the synthesis procedures and the corresponding structures of the QD for the photovoltaic and energy storage applications is discussed.

2. Experimental Section

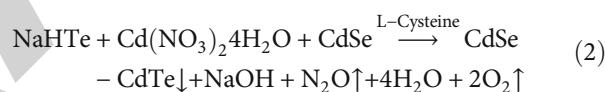
2.1. Materials. All the chemical reagents are of analytical grade (AR) and used without any further purification. The precursors, cadmium nitrate tetrahydrate ($\text{Cd}(\text{NO}_3)_2 \cdot 4\text{H}_2\text{O}$) (Merck 99%), sodium selenite (Na_2SeO_3) (Merck 98%), sodium borohydride (NaBH_4) (Sigma-Aldrich, >98%), Te (Merck), hydrazine hydrate ($\text{N}_2\text{H}_4 \cdot \text{H}_2\text{O}$) (Merck), ammonia ($\text{NH}_3 \cdot \text{H}_2\text{O}$), sodium tetra borate ($\text{Na}_2\text{B}_4\text{O}_7$) (Sigma-Aldrich, 99%), and L-cysteine ($\text{C}_3\text{H}_7 \cdot \text{NO}_2\text{S}$) (Sigma-Aldrich, 97%), are acquired and used for the synthesis of CdSe/CdTe quantum dots. Milli-Q water used for hydrothermal reactions is collected from Millipore Milli-Q lab water system.

2.2. Synthesis of CdSe/CdTe QDs. CdSe/CdTe QDs have been synthesized in a two-step process such that the CdSe nanoparticles are prepared separately and mixed with the precursors of CdTe in a hydrothermal process. The precursor materials used for CdSe synthesis are cadmium nitrate tetrahydrate ($\text{Cd}(\text{NO}_3)_2 \cdot 4\text{H}_2\text{O}$), sodium selenite (Na_2SeO_3), hydrazine hydrate ($\text{N}_2\text{H}_4 \cdot \text{H}_2\text{O}$), and ammonia ($\text{NH}_3 \cdot \text{H}_2\text{O}$). The raw materials $\text{Cd}(\text{NO}_3)_2 \cdot 4\text{H}_2\text{O}$ and Na_2SeO_3 are taken in a molar ratio of 2:1. The detailed synthesis procedure of CdSe nanoparticles has been carried out in a similar method as discussed in the earlier reports of the authors, Ramalingam et al. and Lin et al. [8, 9]. In order to prepare

CdTe, one of the precursor materials NaHTe is freshly prepared by mixing NaBH_4 with Te by a 2:1 molar ratio dissolved in aqueous solution as mentioned in the following reaction:



Stoichiometry amounts of NaBH_4 (0.75 g) is transferred to a conical flask which has already been chilled with ice, followed by 10 ml of H_2O and Te (2.55 g) powder. The reaction of NaBH_4 with Te is shown in equation (1). After 2 hours of stirring, the black Te powder is dissolved in sodium borohydride solution. The reaction of NaBH_4 with Te produces sodium tetra borate ($\text{Na}_2\text{B}_4\text{O}_7$) white precipitates at the bottom of the flask along with the supernatant sodium hydrogen telluride (NaHTe). A tiny exit is linked to the flask which allows the escape of hydrogen pressure developed. The supernatant NaHTe is separated by filtration for the CdTe preparation. In order to synthesize CdSe/CdTe core-shell structured quantum dots, a repeated precursor solution addition along with an L-cysteine capping agent has been carried out. Cadmium nitrate tetrahydrate ($\text{Cd}(\text{NO}_3)_2 \cdot 4\text{H}_2\text{O}$) is dissolved in a freshly prepared NaHTe solution along with 1.2 g of L-cysteine ($\text{C}_3\text{H}_7 \cdot \text{NO}_2\text{S}$) in 25 ml of Milli-Q water, and progressively CdSe is included. The overall reaction is shown in



The NaOH formed during the reaction could maintain the required solution pH as high as possible. The solution is shifted to a Teflon-lined autoclave and kept in an oven at 180°C for 6 hours. Figure 1 illustrates a step-by-step process of the CdSe/CdTe quantum dot synthesis process. As illustrated in Figure 1, as the first step, the cadmium nitrate tetrahydrate and sodium selenite are dissolved in double-distilled water separately. The dissociated Cd^{2+} ion in cadmium nitrate solution is turned into $\text{Cd}(\text{NH}_3)_4^{2+}$ complex ion when treated with ammonia. On the other hand, the Se source Na_2SeO_3 is dissociated when mixed with hydrazine hydrate, and subsequently hydrogen selenide (H_2Se) is formed in which the oxidation state of selenium changes to Se^{2-} . A CdSe cluster is formed when both of these Cd and Se solutions are mixed together which is then added to the precursor solution of CdTe as mentioned above. The ligand molecules of CdTe are bound with the CdSe surface to produce CdSe-wrapped CdTe quantum dots under hydrothermal treatment at 180°C as depicted in Figure 1.

After cooling down the hydrothermal reactor, the resulting solution is then transferred to a refluxing conical flask and heated to 110°C under refluxing in different duration to control the size of CdSe/CdTe QDs. The resultant solution is then centrifuged, and the precipitates are extracted through filtration. The precipitates are repeatedly washed with Milli-Q water and ethanol in order to remove traces of NaOH and impurities if any. The precipitates are

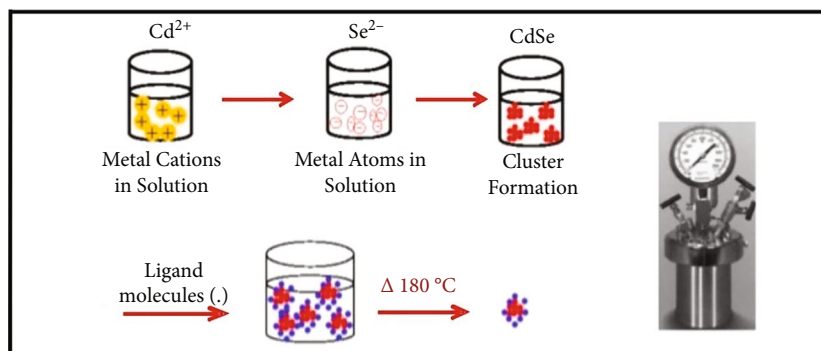


FIGURE 1: Schematic diagram of synthesis of CdSe/CdTe quantum dots.

extracted through vacuum suction filtration followed by heat treatment at 110°C for three hours. After heat treatment, a deep crimson CdSe/CdTe powder sample is obtained. The final powder is investigated by XRD, SEM-EDX, TEM, and SAED to confirm the formation of nanoscale CdSe/CdTe core-shell structure.

2.3. Characterization Techniques. The powder XRD patterns of the as-prepared nanocomposites are documented on a rich SEIFER alongside nickel-filtered (monochromatic) CuK α radiation of 1.5406 Å with a 0.02°/sec scanning rate. A JEOL Scanning Electron Microscope (SEM) at 10 kV along with EDX (energy-dispersive X-ray analyzer) (JSM 6310) is used for investigating the morphology of the nanostructured materials. A Transmission Electron Microscope (TEM) (JEOL-JEM 2010) with a 200 kV acceleration voltage is used to capture microscopic images of nanostructures. All samples are cleaned using hexanes, methanol extraction, and acetone precipitation. Copper grids covered with an ultrathin carbon film or formvar film are dipped into a toluene or hexane solution. A 120 cm camera is used to record “SAED (selected area electron diffraction patterns).” The absorption spectrum is acquired using a UV-Vis-NIR spectrometer in the 200 nm to 900 nm range (CARY 5E double beam). The emission spectrum is recorded using a spectrophotometer (FLOUROLET-3) in a spectral range of 300 nm to 600 nm with a xenon lamp with 380 nm excitation wavelength as a source.

3. Results and Discussion

3.1. Powder X-Ray Diffraction (XRD). The as-prepared CdSe/CdTe compound is characterized by powder XRD, and the corresponding XRD pattern is shown in Figure 2. The diffraction peaks observed at 24.19°, 27.62°, 42.28°, and 56.95° are ascribed to the planes (002), (101), (112), and (002), respectively, which reveals CdSe hexagonal phase formation. The diffraction peaks observed at 13.70°, 24.19°, 35.38°, and 39.87° are assigned to the planes (100), (111), (211), and (220) of the CdTe cubic phase, respectively. The characteristic peaks indicate the formation of the hexagonal CdSe and cubic CdTe polycrystalline compound. The diffraction peaks are of best match with JCPDS card no. 77-2304 and JCPDS card no. 89-3011 corresponding to CdTe

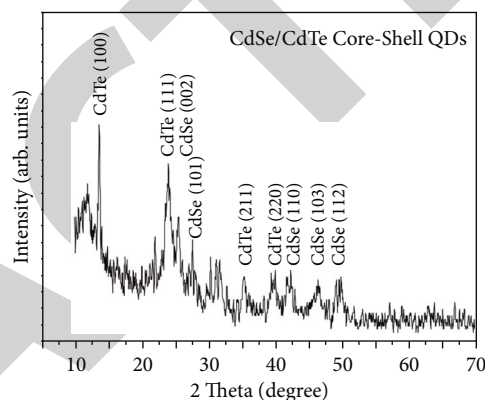


FIGURE 2: The X-ray powder diffraction patterns of CdSe/CdTe core-shell quantum dots.

and CdSe, respectively. The signatures of diffraction peaks are wider because of the constrained particle size. Though the CdSe is wrapped by CdTe, the diffraction peaks corresponding to the cubic structure of CdSe are revealed [8].

The crystallite size as well as the induced strain is calculated by the Williamson-Hall method [10] as per

$$\beta \cos \theta = \frac{K\lambda}{D} + 4\epsilon \sin \theta, \quad (3)$$

where β is the full width at half maximum of the intensity (FWHM), θ is Bragg's angle, K is the shape factor which could be used as 0.9, λ is the wavelength of the X-ray used, D is the crystallite size, and ϵ represents the strain. The grain size of CdSe/CdTe is found to be 12.6 nm by using the Williamson-Hall formula which indicates quantum dot (QD) formation. The unique nature of QD nanocrystals lies in the size of the particle and coordinated shape. In order to understand the shape and presence of elements, SEM-EDX and TEM measurements are carried out.

3.2. SEM-EDX Analysis. Figure 3(a) shows the SEM image of CdSe/CdTe nanoparticles. The surface morphology indicates uniform particle size distribution of CdSe/CdTe nanoparticles throughout the surface. The spherical nanoparticles are monodispersed without agglomeration. The surface view reveals circular shapes of the nanoparticles with particle

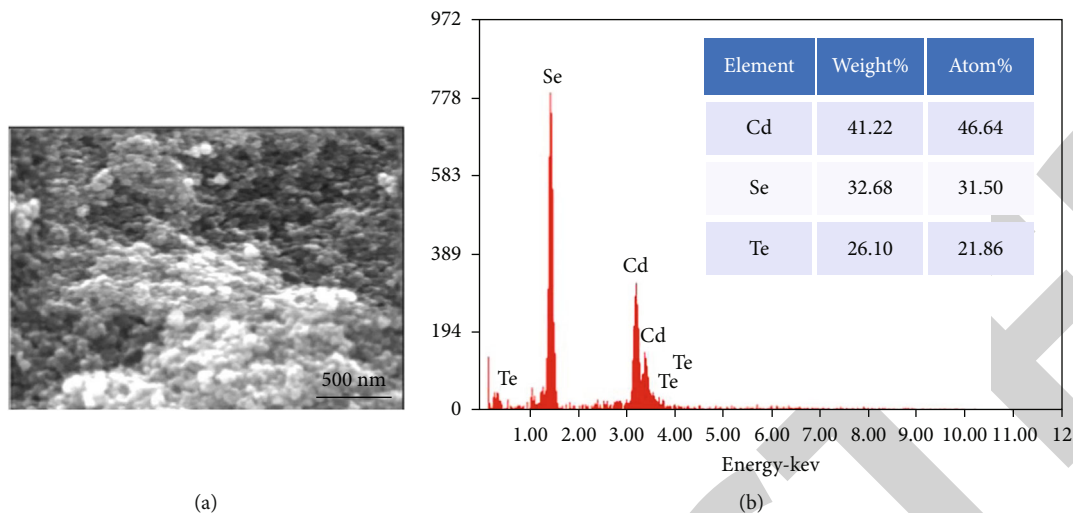


FIGURE 3: (a) SEM morphology and (b) EDX spectrum of CdSe/CdTe.

sizes in the range of 10~20 nm. However, the size of QDs is not precisely determined from SEM morphology for which TEM analysis is performed. The EDS spectrum of CdSe/CdTe indicates the presence of Cd, Se, and Te elements as shown in Figure 3(b). The atomic and weight percentage of Cd is high which reveals the presence of Cd bonding with both Se and Te as in CdSe and CdTe compounds.

3.3. TEM Analysis. The size and shape of QDs are investigated by using TEM imaging. Nonetheless, due to the presence of a fuzzy projection of the thin shell and to justify the lower contrast of electron density between the shell and core atmosphere, a vivid core-shell nanostructure illustrated by TEM images is reported by Sheu et al. [11]. In order to realize the particle size and shape of QDs, an effort is made to observe TEM morphology. The TEM images observed for CdSe/CdTe nanostructures are shown in Figures 4(a)–4(e). The TEM images observed at the 50–100 nm scale indicate extraordinarily highly monodisperse and spherical-shaped nanoparticles as shown in Figures 4(a) and 4(b). Further magnifications to the 20 nm scale as shown in Figure 4(c) reveal the most precise particle size in the order of 8~10 nm sized quantum dots which is in concurrence with XRD and SEM results.

The TEM morphology at higher magnifications also exemplifies freestanding particle dispersion without any agglomerates which is in good agreement with SEM morphology results. It is interesting to note that the as-prepared CdSe/CdTe nanostructures are found without any agglomeration which is naturally detected while using most of the alternative solvents. During the synthesis of CdSe/CdTe, L-cysteine is used as a capping agent which plays a major role in tuning the size of QDs and alleviating the agglomeration by producing freestanding nanoarchitectures [8, 9]. In order to reveal the core-shell structure of the CdSe/CdTe compound, further magnifications are performed at the particle level scale. On very high magnifications at 5 nm scales, the particle surface shows a merging of two different crystal structures which might be corre-

sponding to CdSe QDs surrounded with CdTe QD patches as shown in Figures 4(d) and 4(e).

The surface of CdSe and wrapping compound CdTe are indicated in circles in Figure 4(d). A mixed crystal phased regions are apparently evidenced in Figure 4(e) which reveals the presence of two different crystal structures in the compound. The TEM results at higher magnifications significantly at the 5 nm scale clearly evidence the core-shell structure of CdSe/CdTe quantum dots. The CdSe QDs are bound with the top layer CdTe in a heterojunction that forms an excellent core-shell structure as confirmed by TEM morphology.

The heterojunction core-shell structured QDs offer significantly more impacts on photovoltaic applications. When combined with effective exciton production and dissociation, they result in discrete channels for the transport of separated charge carriers [9]. It is now practically possible to construct heterojunction core-shell QDs with control at the atomic level over the core and shell positions as well as the composites throughout the interface using current colloidal chemistry techniques combined with a hydrothermal method. As a result, new routes to identify high or effective luminescence materials for photovoltaic device application have been unlocked [12]. In order to clarify the core and shell components, the SAED pattern is observed at a selected region as shown in Figure 4(f). The SAED pattern depicts two regions with different crystal structures. The inner circle region is attributed to the (002) plane of CdSe, and the outer circle region is attributed to the (100) plane of CdTe. The remarkable SAED pattern results evidently reveal the mixture of crystal phases corresponding to CdSe as a core and CdTe as a shell in the core-shell structured QDs. A schematic representation of core-shell structured CdSe/CdTe growth orientation and electron-hole trapping at the interface in the core-shell structure is demonstrated in Figures 5(a) and 5(b).

The nonpolar interfaces (10 $\bar{1}$ 0) of the surface facet are guided towards the wurtzite (0001) direction as shown in Figure 5(a). At the interface of the core-shell structure, a

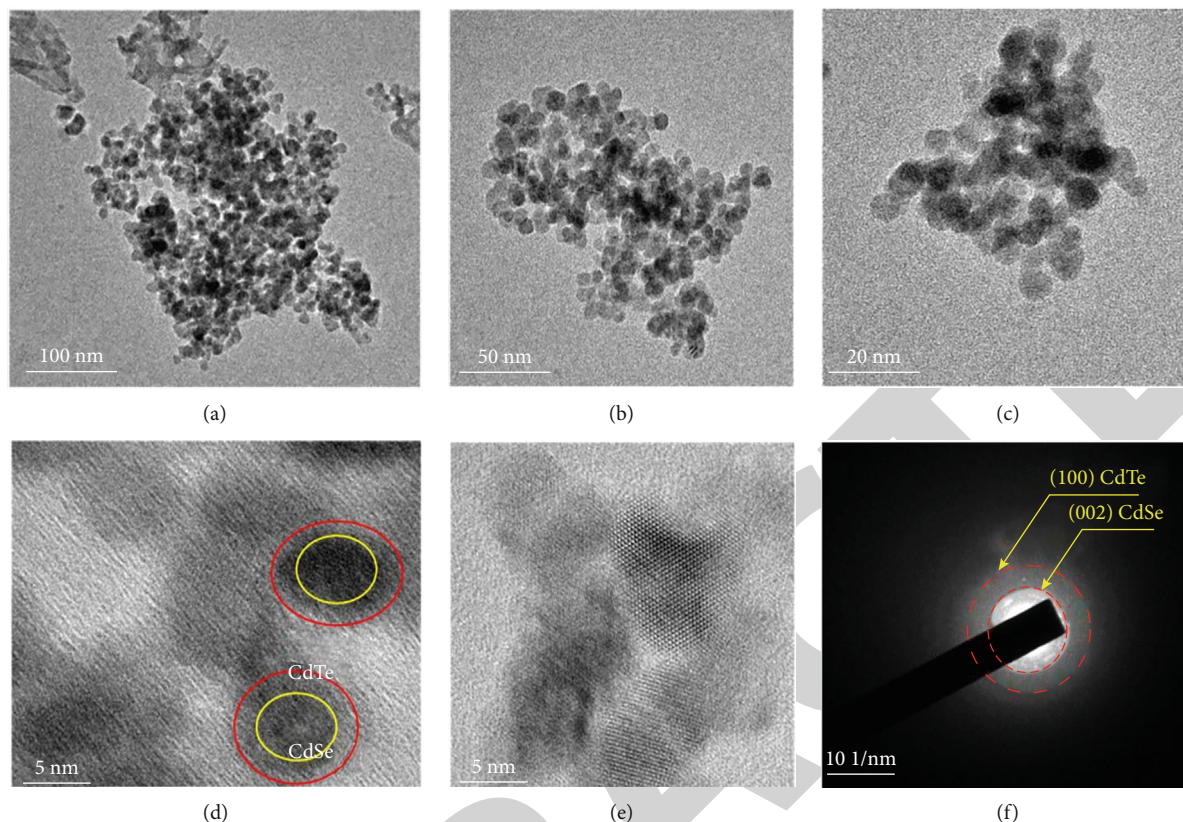


FIGURE 4: (a–e) TEM images and (f) SAED pattern of CdSe/CdTe core-shell quantum dots.

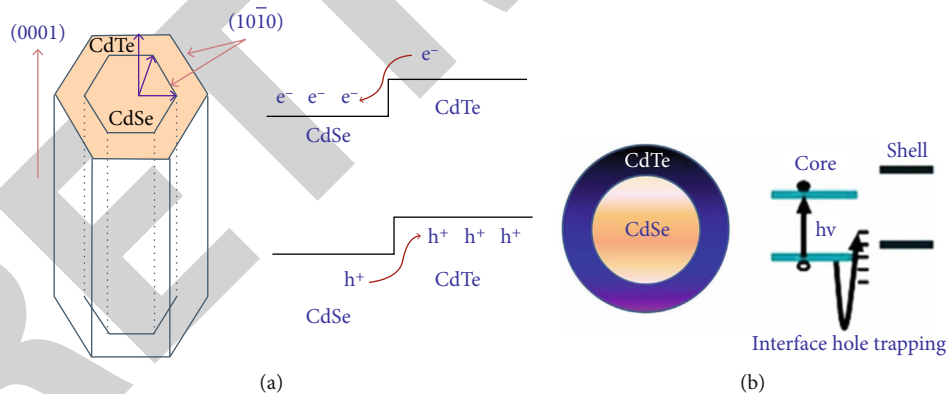


FIGURE 5: Schematic representation of CdSe/CdTe (a) growth orientation and (b) electron-hole trapping in the core-shell structure.

fraction of holes are trapped. The trapped holes at the interface might be acting as a cracking site or electron-hole recombination. It is predicted to be a dangling bond defect which is related to the defect centre due to the cracking site process and as a least possibility of which may be a recombination centre as illustrated in Figure 5(b). As discussed in TEM analysis, due to a significant lattice mismatch among many core-shell nanoparticle locations, a substantially less uniaxial pressure is required which could be due to the influence of band offsets or bandgap throughout the surface [13].

3.4. Nucleation Growth Mechanism. High-quality monodisperse quantum dots have been reported extensively; however, the following KHSe or NaHSe reagents have produced broadly with the source of “Se” as the Na_2SeO_3 compound that has been condensed by sodium borohydride (NaBH_4) at normal reaction conditions to create Se^{2-} [14]. In the present work, hydrogen selenide (H_2Se) and sodium hydrogen telluride (NaTeH) are used as reagents along with cadmium nitrate for CdSe and CdTe, respectively. The reaction has been performed in an open-air condition which makes the process easier and less time-consuming. The nucleation growth followed

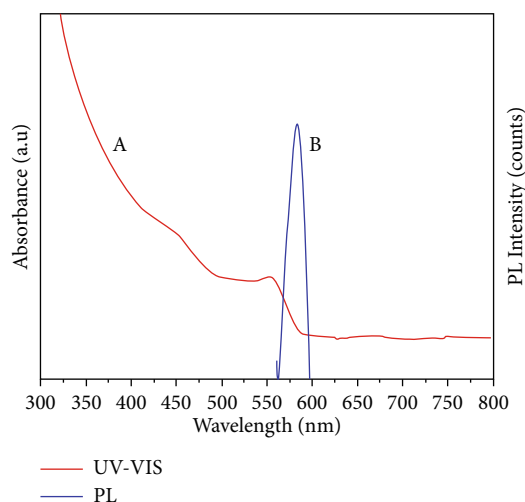


FIGURE 6: (a) Optical absorption and (b) photoluminescence spectrum of CdSe/CdTe core-shell quantum dots.

by a larger enhancement at higher temperature may increase the quantum efficiency and possible growth mechanism. The surface and interface nature of the CdSe/CdTe core-shell quantum dots may have the available source of interactions between the interfacial charge-carrier boundaries which are caused by trapping due to the variance of lattice direction [15]. The defects of the interface of the CdSe/CdTe core-shell quantum dots are due to the greater variance between lattices and impact of graded interfaces. In our knowledge, the graded core-shell creation could perhaps have multifolded benefits such as (i) possible production of defects at the interface and (ii) generation of variance in energy bands that could enhance charge transfer flowing across the interface that leads the internal electric field. The band alignment creates tunneling of charge carriers across the interface of the core-shell structure. The schematic diagram displays a charge transfer mechanism using core-shell activities along with the reverse path of electron-hole recombination in the CdSe/CdTe QDs [16].

3.5. Optical Absorption and Photoluminescence Properties. Figure 6 shows both emission and absorption spectra of CdSe/CdTe QDs. The UV-visible absorption spectrum of CdSe/CdTe QDs has been recorded in the 200 nm to 800 nm spectral range. The CdSe/CdTe QDs shows an excitonic peak at 560 nm as shown in Figure 6(a). On the other hand, Figure 6(b) suggests the monodispersed CdSe/CdTe QDs and narrow size distribution of PL emission spectra at $\lambda_{\text{emi}} \sim 585$ nm which indicates emission near the band edge. Moreover, it is indicated that there is an increase in emission due to HOMO and LUMO charge carriers implying direct recombination when PL emission spectral maximum lies closer to its absorption onset [17]. The absorption spectrum of CdSe/CdTe QDs indicates a formation of type II core-shell nanostructure characteristics. Therefore, the charge spatial separation transport of quantum yield reduction is because of wave function (focused) coverage among holes trapped at the shell surface and localized electrons at the het-

erostructure matrix. The UV-Vis absorption band at 455 nm and a broad band at 560 nm along with a PL emission peak at 585 nm indicate exciton emission of the type II matrix which has a wider band due to the trapping mode as observed in emission spectra [18].

The emission observed in the $\lambda_{\text{emi}} \sim 560$ -590 nm wide regions is resulted by the existence of several structural defects in the synthesized CdSe/CdTe material. The possible reason for visible emission may be due to the surface to volume (s/v) substantial ratio that resulted in creating interstitials as well as vacancies (high-density surface defects) which can cause a trap level. The nature of defects and dopants at grain boundary leads to decreasing free carrier movement and bulk counterpart surface [19].

Even though free carriers are scattered when in contact with charged dopants or closer defects, there is a possible decrease in mobility which restricts carrier separation [20]. In this context, the CdTe doping at low concentration results in the development of radiative recombination with extra centres at the CdSe which leads to the improvement in photoluminescence emission intensity. The graded core-shell formation offers a multifold benefit as evidenced from UV-Vis and PL emission spectral analyses. Based on the optical properties, three different arguments are categorized such as (i) band alignment experiences at the heterointerfaces with a lesser amount of strain at the graded core-shell in comparison with ungraded conditions, (ii) a decrease in defect locations at the interface, and (iii) the positioning ending up with cascading of charge transfer locally. These factors of CdSe/CdTe core-shell structured QDs contribute greatly to enhancing the yield of charge separation and charge carrier mechanism which might have an effect on the photovoltaic device efficiency enhancements. The uniform spherical core-shell structured CdSe/CdTe QDs with excellent size and shape properties could be utilized as an electrode in energy storage applications which may have excellent electrochemical properties.

4. Conclusions

In summary, the particular work emphasizes a controlled synthesis of core-shell structured CdSe/CdTe quantum dots by a colloidal chemistry approach equipped with the hydrothermal technique. The CdSe/CdTe compound has been investigated by powder XRD which reveals the mixture phase polycrystalline hexagonal CdSe and cubic CdTe formation. The grain size determined from XRD results by the Williamson-Hall method indicates 12.6 nm. The SEM morphology indicates uniform monodispersed spherical nanoscale particles of CdSe/CdTe. The EDX confirms the presence of Cd, Se, and Te in the CdSe/CdTe compound. TEM investigations confirm the spherical-shaped core-shell structured quantum dots and precise particle sizes ranging between 8 and 10 nm which is in good agreement with XRD and SEM results. The SAED analysis of CdSe/CdTe confirms the core and shell components as CdSe and CdTe, respectively, which significantly proves the core-shell structure elements. With the existence of an absorbance characteristic, the SAED pattern that approximated the core-shell

Retraction

Retracted: Experimental Investigation of Spirulina Microalgae Biodiesel with Metal Nanoadditive on Single-Cylinder Diesel Engine

Journal of Nanomaterials

Received 10 October 2023; Accepted 10 October 2023; Published 11 October 2023

Copyright © 2023 Journal of Nanomaterials. This is an open access article distributed under the Creative Commons Attribution License, which permits unrestricted use, distribution, and reproduction in any medium, provided the original work is properly cited.

This article has been retracted by Hindawi following an investigation undertaken by the publisher [1]. This investigation has uncovered evidence of one or more of the following indicators of systematic manipulation of the publication process:

- (1) Discrepancies in scope
- (2) Discrepancies in the description of the research reported
- (3) Discrepancies between the availability of data and the research described
- (4) Inappropriate citations
- (5) Incoherent, meaningless and/or irrelevant content included in the article
- (6) Peer-review manipulation

The presence of these indicators undermines our confidence in the integrity of the article's content and we cannot, therefore, vouch for its reliability. Please note that this notice is intended solely to alert readers that the content of this article is unreliable. We have not investigated whether authors were aware of or involved in the systematic manipulation of the publication process.

Wiley and Hindawi regrets that the usual quality checks did not identify these issues before publication and have since put additional measures in place to safeguard research integrity.

We wish to credit our own Research Integrity and Research Publishing teams and anonymous and named external researchers and research integrity experts for contributing to this investigation.

The corresponding author, as the representative of all authors, has been given the opportunity to register their agreement or disagreement to this retraction. We have kept a record of any response received.

References

- [1] J. Arunprasad, A. S. Sener, R. Thirugnanasambantham, T. Elango, and T. Bothichandar, "Experimental Investigation of Spirulina Microalgae Biodiesel with Metal Nanoadditive on Single-Cylinder Diesel Engine," *Journal of Nanomaterials*, vol. 2022, Article ID 4701610, 7 pages, 2022.

Research Article

Experimental Investigation of Spirulina Microalgae Biodiesel with Metal Nanoadditive on Single-Cylinder Diesel Engine

J. Arunprasad ¹, Arif Senol Sener ², R. Thirugnanasambantham ¹, T. Elango ³,
and T. Bothichandar ⁴

¹Department of Mechanical Engineering, Dhanalakshmi Srinivasan Engineering College, Perambalur, India

²Department of Mechanical Engineering, Engineering and Architecture Faculty, Nisantasi University, Istanbul, Turkey

³Department of Mechanical Engineering, Mahendra Institute of Technology, Mallasamudram, India

⁴Department of Industrial Engineering, Ambo University, Ambo, Ethiopia

Correspondence should be addressed to T. Bothichandar; bothi.chandar@ambou.edu.et

Received 28 October 2021; Revised 23 November 2021; Accepted 7 December 2021; Published 7 January 2022

Academic Editor: Karthikeyan Sathasivam

Copyright © 2022 J. Arunprasad et al. This is an open access article distributed under the Creative Commons Attribution License, which permits unrestricted use, distribution, and reproduction in any medium, provided the original work is properly cited.

Nanoparticles are an emerging concept for increasing fuel properties. The purpose of this research work is to determine the effect of magnesium oxide nanoparticles on the performance and emission characteristics of diesel engines that run on a spirulina microalgae biodiesel blend (B20) as a fuel. The ultrasonication was used to disperse MgO nanoparticles in B20 fuel at various concentrations (25, 50, 75, and 100 ppm). The significant findings indicated that B20+100 blends reduced specific fuel consumption by 20.1% and had a 5.09% higher brake thermal efficiency than B20. B20+100 blends reduced CO, hydrocarbon, and smoke emissions by a maximum of 32.02%, 30.03%, and 26.07%, respectively, compared to B20.

1. Introduction

Fossil fuels are considered conventional and nonrenewable sources. These fossil fuel resources gradually decrease, and their adverse effects on the atmosphere increase day by day. Diesel engines, in particular, are a significant contributor to major environmental issues such as global warming, ozone depletion, and unpredictable climate change. There are various effective methods for lowering diesel engine emissions, including engine modification, combustion enhancement, and exhaust gas treatment systems. Engine combustion appears to be the most preferred method, as it requires only minimal changes to existing engine systems rather than new designs. This is performed by modifying the fuel injection system, using fuel additives, and adjusting the fuel characteristics. The fast depletion of petroleum fuel stocks and severe environmental impacts have motivated us to seek environmentally friendly alternative energy sources. In comparison to other crops, algae are the most

promising source of oil due to their rapid development, capacity to grow in various situations, the potential for larger yields, and similar qualities to standard biodiesel. The amount of oxygen present in a microalgae-based bio-oil is more significant than that in fossil fuels. However, biodiesel has several disadvantages, such as lower fuel atomization and higher viscous nature, resulting in lower NO_x emissions and BTE reductions. Recent advancements in nanotechnology have allowed nanotechnology to develop nanosized molecules, which aid in improving thermal properties, thus assisting combustion with its significant volume-surface ratio to improve fuel characteristics and performance while lowering diesel engine emissions [1]. Metal oxide nanoparticles have been used as a viable additive with fuels to enhance their performance and combustion characteristics. The various metal oxide nanoadditives are aluminum, titanium, and zirconium. Manganese, copper, cerium, and zinc have been used as catalysts for complete combustion and reduced emissions from the exhaust. In a single-cylinder diesel

engine, they were tested using hinge methyl oil esters and carbon nanotubes. The carbon nanotube blended biodiesel with a concentration between 25 ppm and 50 ppm improved the engine performance with reduced emissions. They conclude that B20 using 40 ppm titanium oxide nanoparticles improved performance and combustion properties [2]. With the use of nanoadditions, engine exhaust emissions were reduced dramatically. The titanium oxide nanoparticle additive with *Calophyllum inophyllum* biodiesel has reduced the brake-specific fuel consumption increasing the brake thermal efficiency [3]. In conjunction with various biodiesel fractions, the impact of titanium oxide on engine performance and emission characteristics was investigated. They discovered a significant enhancement in thermal efficiency and reduced pollutants such as hydrocarbons, carbon monoxide, and nitrogen oxides [4]. The effects of alumina nanoparticles in biodiesel generated from spent cooking oil have been studied. The carbon monoxide and hydrocarbon emissions are decreased by 2.94 and 20.56%, respectively, whereas $N O_x$ emissions increased by 43.61% [5]. According to the literature review, incorporating nanoparticles into blends is the most inventive strategy for improving performance and emission characteristics. The current study investigates the extraction of oil from spirulina microalgae and its transesterification to methyl ester. The magnesium oxide nanoparticles were mixed with a spirulina methyl ester at various doses, including 25, 50, 75, and 100 ppm. The compression ignition engine's performance and emission characteristics were assessed.

2. Materials and Methods

2.1. Spirulina Algae Oil. Spirulina represents biomass called cyanobacteria. Spirulina thrives in an alkaline environment at a pH of around 8.5 and above and a temperature around 30°C. They are autotrophic in nature. Biodiesel made from dried spirulina algae would be made available as an excellent replacement fuel for diesel engines. It may thrive in both freshwater and saltwater. Spirulina has a lipid content ranging from 10% to 25% by weight. The primary benefit would be the cost and abundance of this fuel since spirulina algae can be quickly harvested regularly. Because of the consistent availability of this fuel, the demand for it can be easily supplied [6]. The spirulina biomass is shown in Figure 1. Its production can be doubled in less time if grown in controlled climatic conditions. The high lipid content in the algae makes it suitable for the extraction of methyl ester and its use as an alternate fuel. Table 1 shows the biomass and lipid productivity of the selected microalgal species.

2.2. Transesterification. In most cases, biodiesel is made by reacting vegetable oil with methanol in the presence of a catalyst to form monomethyl esters and glycerine as a by-product. The reaction temperature, the molar ratio of alcohol and oil, the catalyst, the reaction time, and the presence of FFA concentration all influence the conversion of methyl esters from vegetable oil. The temperature of reaction at atmospheric pressure between 45 and 70°C gives maximum yields of methyl ester. The percentage of biodiesel yield



FIGURE 1: Spirulina biomass.

mainly depends on the type of transesterification it undergoes. During the transesterification process, the molar ratio of alcohol used plays a vital role in forming methyl esters. Most studies reported that a molar ratio of 5 : 1 yields the maximum biodiesel yield during the transesterification process. The type of catalyst used in the process enhances the reaction during the production of biodiesel. Acid or alkaline catalyst is used depending on the type of transesterification process during the reaction. The reaction time normally is 8-12 hours for acid transesterification to reduce the FFA content below 2%. Then, the process undergoes alkaline transesterification due to alcohol and a catalyst for 6-8 hours for yielding maximum biodiesel. The reaction time of biodiesel yields varies from oil to oil and the type of FFA content in it. The glycerine was the denser liquid, which collects at the bottom after a few hours of settling. This phase was completed within 3-4 hours of settling. After transesterification of spirulina microalgae biodiesel, the viscosity was reduced, which is closer to the diesel.

2.3. Magnesium Oxide Nanoparticle. Magnesium oxide has been the subject of intense study due to its unusual characteristics, including a heavy ionic character, simple stoichiometry, crystal structure, and surface structural defects. Due to the peculiar composition of nanoscale, magnesium oxide possesses unique optical, electrical, electromagnetic, thermal, mechanical, and chemical properties. Table 2 indicates the physical and chemical properties of magnesium oxide nanoparticle.

2.4. Preparation of Samples with Nanoparticle. The nanomixes were made one at a time with B20 made from spirulina methyl ester and the nanoparticle MgO , with B20 concentrations of 25, 50, 75, and 100 ppm added to each blend using an ultrasonicator. Ultrasonication is the most appropriate technique for dispersing nanoparticles in a base solution since it enables the reaggregation of nanoparticles to the nanometre scale. The nanoparticles were scattered in both biodiesel blends, weighted to 25 ppm of volume concentrations, and stretched for 30 minutes in both blended fuels using a 120-watt and 40 kHz ultrasonicator, respectively, to produce nanoparticle-based biodiesel fuel B20

TABLE 1: Biomass and lipid productivity of the selected microalgal species.

S. no	Microalgae	Biomass concentration (mg/L)	Lipid content (%)	Lipid productivity (mg/L-d)	Biomass productivity (mg/L-d)
1.	Spirulina	610 ± 0.001	68 ± 0.002	29 ± 0.001	43 ± 0.002
2.	Chlorella vulgaris	367 ± 0.002	38 ± 0.001	10 ± 0.001	26 ± 0.001
3.	Volvox carteri	226 ± 0.001	33 ± 0.003	5 ± 0.003	16 ± 0.001

TABLE 2: Properties of magnesium oxide.

Specification of nanoparticles	
Supplier	M/s Sigma-Aldrich
Chemical formula	MgO
Appearance	White powder
Density (g/cm ³)	3.6
Melting point (K)	3125
Boiling point (K)	3870
Molar mass (g/mol)	40.304

+25 ppm of MgO. Biodiesel fuels with mass fractions of 50, 75, and 100 ppm were mixed using the same method. The test fuel qualities were analyzed in the American Society for Testing and Materials standards after the blend was prepared, as shown in Table 3.

2.5. Experimental Setup. A single-cylinder, water-cooled diesel engine was used to test the fuel samples. The cylinders are 87.5 mm in diameter and 110 mm in length. With a steady speed of 1500 rpm and a compression ratio of 16.5:1, the engine's maximum performance is 5.2 kW. The injection pressure was 210 bar, with a 23° bTDC injection timing. The diesel engine was inherently related to the dynamometer used to change the load. The load for the engine is between 0% and 100%, with every phase increasing by 25%. The AVL 437 C smoke meter was used in this study. A smoke meter was used to determine the test engine's smoke opacity. The pollutants produced by the engine are composed of numerous gases and smoke evaluated using a five-gas pollution analyzer. The exhausts of CO, HC, and NO_x were examined using a five-gas contaminant analyzer. Table 4 shows that the emissions were measuring instruments with accuracy. A schematic arrangement of the experimental setup is shown in Figure 2.

3. Results and Discussion

3.1. Brake-Specific Fuel Consumption. The BSFC is a ratio computed by dividing the amount of fuel spent by the amount of energy produced over a given period. For all test fuels, the variation in brake-specific fuel consumption as a function of load is illustrated in Figure 3. The average drop in BSFC was 4.2%, 13.5%, 18.3%, and 20.1% for MgO concentrations of 25, 50, 75, and 100 ppm, respectively. When B20+100 ppm is substituted for B20 at full load, the BSFC decreases by 20.1%. The BSFC value of B20+100 ppm com-

binations was found to be lower than that of the other blends. Complete combustion occurs due to the magnesium oxide nanoparticles acting as oxygen boosters, resulting in lower fuel use than pure biodiesel [7].

3.2. Brake Thermal Efficiency. Brake thermal efficiency is related to the engine's actual braking power and power transmitted to the engine. Figure 4 depicts the percentage load vs. the tested fuel blends' brake thermal efficiency values. When B20 is compared to B20+25, B20+50, B20+75, and B20+100, the percentage increase in BTE is 1.8, 2.5, 3.1, and 5.09, respectively. At full load, the maximum BTE increased by 5.09% when B20+100 ppm fuel was used. Nanoparticles accelerate the mixing of A/F, resulting in more efficient fuel burning. Increased oxygen, increased evaporation, microexplosions, and a larger surface-to-volume ratio of nanoparticles also contribute to a higher BTE. It was also discovered that increasing the concentration of MgO nanoparticles boosts BTE because heat is released more quickly during the combustion process [8].

3.3. Carbon Monoxide. Carbon monoxide emissions are usually a consequence of insufficient oxygen in the combustion chamber, which prevents the fuel from being completely burnt. Engine speed, fuel type, injection time, injection pressure, and air/fuel ratio are all elements that affect carbon monoxide emissions [9]. Figure 5 shows the variance in CO emissions with load for all of the fuels that were evaluated. B20 emits more carbon monoxide than B20 with MgO nanoparticle combinations because of the lower oxygen concentration of the spirulina methyl ester. The experiment results indicate that the B20+100 ppm fuel produces less carbon monoxide than the other tested fuels. The CO emissions of the B20+100 ppm blend are 32.02% lower than those of B20. The greater concentration of oxides in nanoadditive blend fuels ensures enough oxygen for complete combustion. The complete burning of MgO nanoparticle-mixed SME biodiesel reduces CO emissions.

3.4. Hydrocarbon Emission. When fuel is burned inefficiently and the flame is quenched near the combustion chamber walls, hydrocarbons are formed [10]. Figure 6 depicts the variation in HC emissions as a function of applied load for all test fuels. B20, B20+25, B20+50, B20+75, and B20+100 ppm are used in this proportion. HC emissions were 33, 31, 29, 26, and 23. Compared to B20, the percentage drop in hydrocarbon for B20+100 ppm MgO at maximum load was 30.03%. The experimental results indicate that B20+100 ppm blends had a lower hydrocarbon content than other blends examined. By aiding complete combustion

TABLE 3: Properties of biodiesel and biodiesel with different concentrations of nanoadditives.

Fuel properties	Test method	Biodiesel with nanoparticle				
		B20	B20+25	B20+50	B20+75	B20+100
Specific gravity	ASTM D891	0.843	0.852	0.858	0.863	0.868
Kinematic viscosity (mm ² /s)	ASTM D445	2.41	2.46	2.53	3.01	3.03
Flash point (°C)	ASTM D93	87	85	76	74	71
Calorific value (kJ/kg)	EN 14214	41154	41234	41523	41656	41754
Pour point (°C)	ASTM D97-12	4	3	2	1	1

TABLE 4: Emissions were measuring instruments with accuracy.

S. no	Instruments	Range	Accuracy
1	Exhaust emission analyzer	CO: 0-10%	Vol ± 0.01%
		HC: 0-10000 ppm	±10 ppm
		CO ₂ : 0-20%	Vol ± 0.02%
		NO _x : 0-5000 ppm	±10 ppm
		0-100%	±1%
2	AVL smoke meter	0-100%	±1%

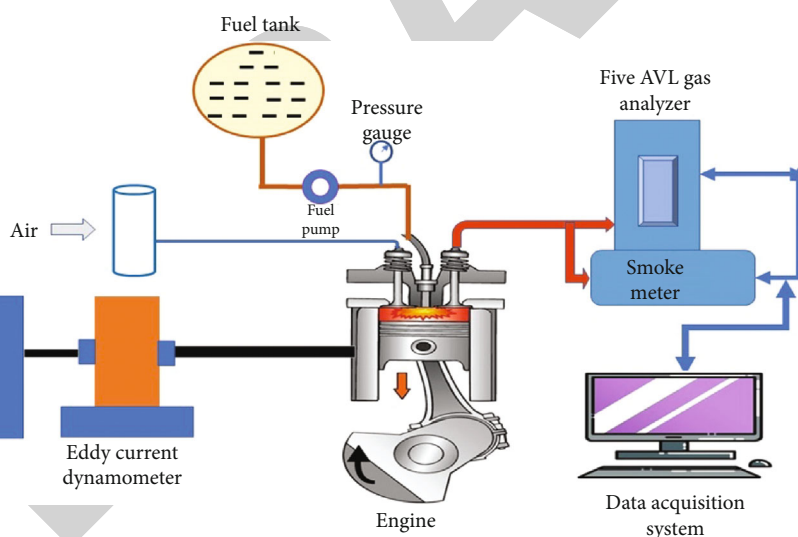


FIGURE 2: Block diagram of the experimental work.

and acting as an oxygen shield, MgO nanoparticles contribute to additional reductions in hydrocarbon emissions by delivering enough oxygen at greater loads to achieve consistent fuel combustion [10].

3.5. Smoke Opacity. Smoke emissions are attributed to an overabundance of oxygen in the fuel mixture, low combustion rate, atomization factors, fuel injection phenomena, and the formation of rich mixer zones [11]. Figure 7 depicts the influence of load on smoke density for different blends.

Due to several affluent mixing zones within the combustion chamber, smoke emission increases significantly as load increases, resulting in inadequate combustion and increased smoke opacity. According to the graph, the smoke density for B20+100 ppm blends is less than that for B20 fuel. Compared to B20 at full load, the B20+100 ppm sample reduced smoke opacity by nearly 26.7%. The reduction in smoke pollution resulted from the MgO nanoparticle-blended fuels' shortened ignition latency, rapid evaporation rate, and enhanced ignition characteristics [12].

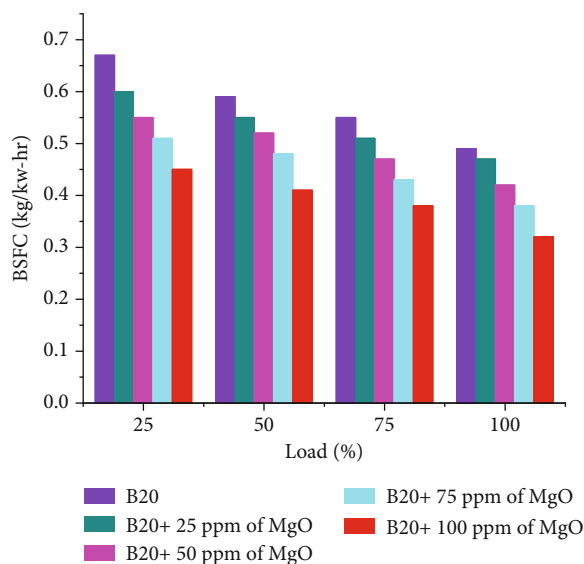


FIGURE 3: Brake-specific fuel consumption vs. load.

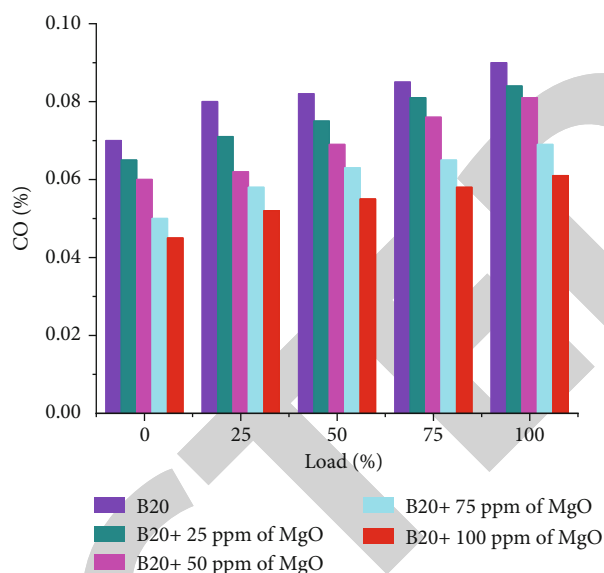


FIGURE 5: Carbon monoxide emission vs. load.

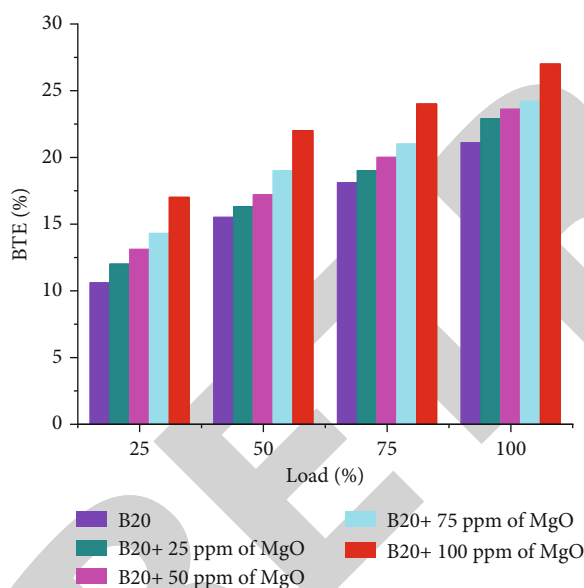


FIGURE 4: Brake thermal efficiency vs. load.

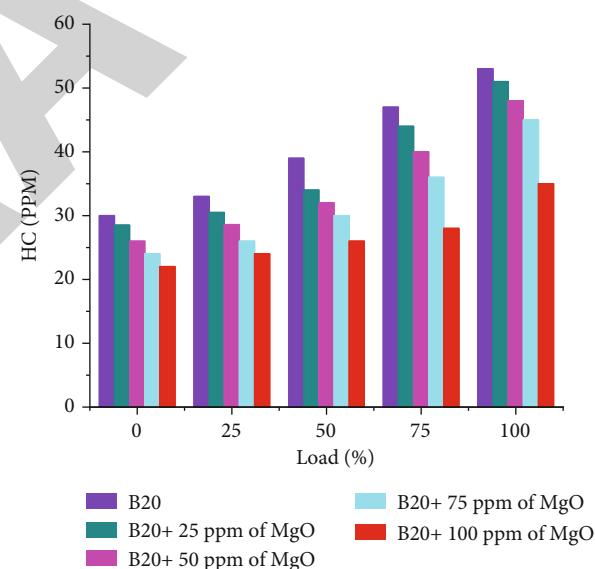


FIGURE 6: Hydrocarbon emission vs. load.

3.6. Nitrogen Oxide Emission. NO_x is a chemical molecule generated during the combustion process of an internal combustion engine when nitrogen and oxygen react at elevated temperatures. Figure 8 depicts the variance in NO_x emissions as a function of applied load for all test fuels. The graph demonstrates that spirulina methyl ester with magnesium oxide blends emits more NO_x than B20. NO_x emissions in ppm for B20, B20+25, B20+50, B20+75, and B20+100 were determined to be 785, 815.2, 820, 835, and 851.3, respectively, at maximum load circumstances. The addition of MgO nanoparticles to the B20 blend increased

NO_x emissions. This is because biodiesel contains more oxygen, and the combustion chamber is heated to a high degree. The thermal process describes the reaction between oxygen and nitrogen in the combustion chamber at high temperatures through chemical phases. Improved combustion of biodiesel blends with MgO additives results in higher NO_x emissions, which leads to higher combustion temperatures [13].

4. Conclusions

These experiments assessed the impact of a 20% spirulina microalgae biodiesel blend with diesel on magnesium oxide

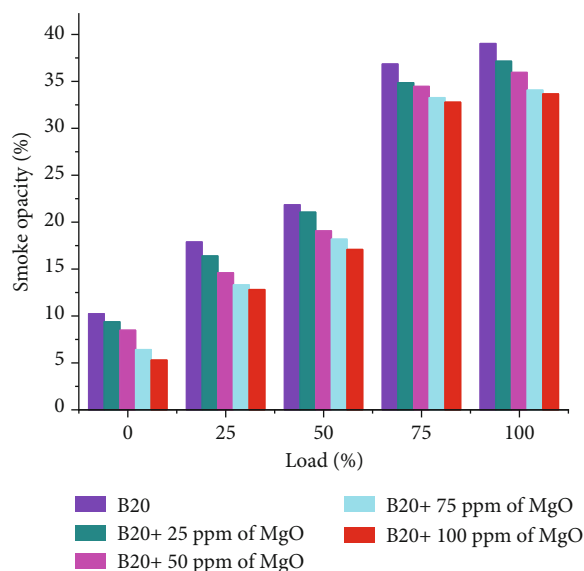


FIGURE 7: Smoke emission vs. load.

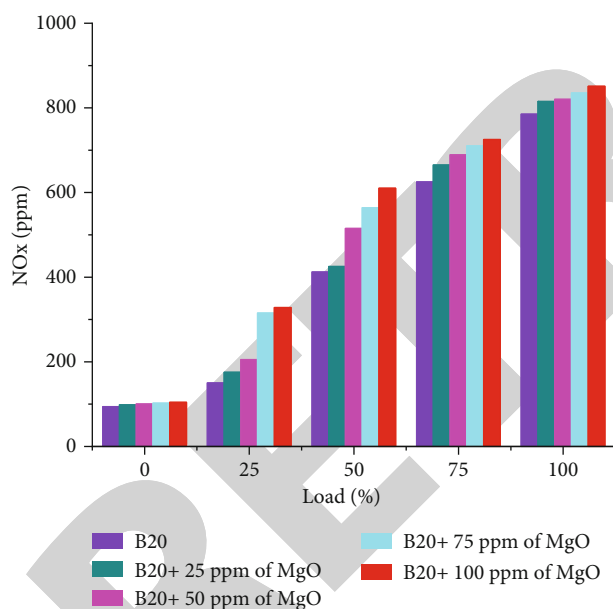


FIGURE 8: Nitrogen oxide emission vs. load.

nanoparticles. Tests were done to measure the impact of a spirulina microalgae biodiesel blend of 20% with diesel in magnesium oxide nanoparticles. A B20 mixture was added to MgO nanoparticles at 25, 50, 75, and 100 ppm. By varying the amount of magnesium oxide nanoparticles added to the test for fuel B20, the performance and emissions of a single-cylinder diesel engine were experimentally tested. Spirulina microalgae biodiesel has poor BTE and BSFC fuel properties due to its low calorific value.

When MgO was combined with spirulina methyl ester, its catalytic behavior dramatically increased BTE and reduced BSFC.

As a consequence of the experiment, substantial reductions in greenhouse gases such as CO, HC, and smoke were detected. The BSFC percentage was reduced to 20.1% in the B20+100 ppm combination, whereas BTE was raised by roughly 5.09%. In CO, HC, and smoke greenhouse gases, emissions from CO, HC, and smoke dropped by about 32.02%, correspondingly 30.03% and 26.7%, compared to the maximum loaded blend from B20. Because of the rise in the combustion temperature, B20+100 ppm blends of nitrogen oxide are at the maximum load marginally higher than B20. Without incurring additional expenditures, spirulina biodiesel enhanced with magnesium oxide nanoparticles may be utilized in diesel engines to replace diesel.

Abbreviations

BTE:	Brake thermal efficiency
BSFC:	Brake-specific fuel consumption
B20:	20% spirulina methyl ester+80% pure diesel
B20+25 ppm:	20% spirulina methyl ester+80% pure diesel +25 ppm of MgO
B20+50 ppm:	20% spirulina methyl ester+80% pure diesel +50 ppm of MgO
B20+75 ppm:	20% spirulina methyl ester+80% pure diesel +75 ppm of MgO
B20+100 ppm:	20% spirulina methyl ester+80% pure diesel +100 ppm of MgO
bTDC:	Before top dead centre
CO:	Carbon monoxide
EDX:	Energy-dispersive electron microscope
HC:	Hydrocarbon
kHz:	Kilohertz
Kw:	Kilowatts
MgO:	Magnesium oxide
Nm:	Nanometer
NO _x :	Nitrogen oxide
O:	Oxygen
ppm:	Parts per million
rpm:	Revolution per minute
SMB:	Spirulina microalgae biodiesel
SME:	Spirulina methyl ester
TiO ₂ :	Titanium oxide
ZrO ₂ :	Zirconium oxide.

Data Availability

The data used to support the findings of this study are included within the article.

Conflicts of Interest

The authors declare that they have no conflicts of interest.

Retraction

Retracted: Newly Synthesized Micro-Nano Transition Metal Complexes of Hexadecanoic Acid as Anti-Microbial Agents: Synthesis, Characterization, and Biological Investigations

Journal of Nanomaterials

Received 11 July 2023; Accepted 11 July 2023; Published 12 July 2023

Copyright © 2023 Journal of Nanomaterials. This is an open access article distributed under the Creative Commons Attribution License, which permits unrestricted use, distribution, and reproduction in any medium, provided the original work is properly cited.

This article has been retracted by Hindawi following an investigation undertaken by the publisher [1]. This investigation has uncovered evidence of one or more of the following indicators of systematic manipulation of the publication process:

- (1) Discrepancies in scope
- (2) Discrepancies in the description of the research reported
- (3) Discrepancies between the availability of data and the research described
- (4) Inappropriate citations
- (5) Incoherent, meaningless and/or irrelevant content included in the article
- (6) Peer-review manipulation

The presence of these indicators undermines our confidence in the integrity of the article's content and we cannot, therefore, vouch for its reliability. Please note that this notice is intended solely to alert readers that the content of this article is unreliable. We have not investigated whether authors were aware of or involved in the systematic manipulation of the publication process.

Wiley and Hindawi regrets that the usual quality checks did not identify these issues before publication and have since put additional measures in place to safeguard research integrity.

We wish to credit our own Research Integrity and Research Publishing teams and anonymous and named external researchers and research integrity experts for contributing to this investigation.

The corresponding author, as the representative of all authors, has been given the opportunity to register their

agreement or disagreement to this retraction. We have kept a record of any response received.

References

- [1] K. Govindarajan, V. Parasuraman, P. Perumalswamy Sekar, I. Colak, and B. Z. Hailemeskel, "Newly Synthesized Micro-Nano Transition Metal Complexes of Hexadecanoic Acid as Anti-Microbial Agents: Synthesis, Characterization, and Biological Investigations," *Journal of Nanomaterials*, vol. 2022, Article ID 1678894, 10 pages, 2022.

Research Article

Newly Synthesized Micro-Nano Transition Metal Complexes of Hexadecanoic Acid as Anti-Microbial Agents: Synthesis, Characterization, and Biological Investigations

Kavitha Govindarajan,^{1,2} Vijayarohini Parasuraman,³ Parasuraman Perumalswamy Sekar,³ Ilhami Colak,⁴ and Balkew Zewge Hailemeskel⁵ 

¹Department of Chemistry, Loyola-ICAM College of Engineering and Technology, Chennai, India

²Department of Chemistry, D.G. Vaishnav College, University of Madras, Chennai, India

³Department of Environmental Sciences & Biotechnology, Hallym University, Republic of Korea

⁴Department of Electrical & Electronics Engineering, Nisantasi University, Istanbul, Turkey

⁵Department of Chemistry, College of Natural and Computational Science, Debre Berhan University, Ethiopia

Correspondence should be addressed to Balkew Zewge Hailemeskel; balkewzewge@dbu.edu.et

Kavitha Govindarajan and Vijayarohini Parasuraman contributed equally to this work.

Received 1 November 2021; Revised 27 November 2021; Accepted 11 December 2021; Published 3 January 2022

Academic Editor: Karthikeyan Sathasivam

Copyright © 2022 Kavitha Govindarajan et al. This is an open access article distributed under the Creative Commons Attribution License, which permits unrestricted use, distribution, and reproduction in any medium, provided the original work is properly cited.

The synthesis of several metal complexes of d-block elements of hexadecanoic acid (palmitic acid) and its antimicrobial activity was reported in this study. UV-Vis and FT-IR spectroscopy studies were used to characterize and confirm the produced metal complexes by the shift in the absorbance and the formation of M-O linkage. The X-ray diffraction method was mainly used to examine the crystallographic faces of the complexes based on the transition metals. Thermal gravimetric investigation revealed that all metal palmitate complexes had high thermal stability in the range of 250-300°C. The metal complexes of hexadecanoic acid were examined for microbicidal activity against diverse bacterial strains and fungal pathogens using the agar well diffusion method. The copper palmitate complex presented excellent antibacterial activity among the other metal complexes. These outcomes suggest of using fatty acid metal complexes as a suitable candidate in several biomedical applications.

1. Introduction

Metal-ligand complexes have gained much importance in biomedical research, owing to their physicochemical features, as well as their numerous oxidation states and stereochemistry, which make them ideal candidates for the establishment of innovative metal-based therapeutic agents. Furthermore, depending on the structure of the ligand, the biological effects and reactivity of metal-based medications can be easily modified. As a result of the interaction of metal ions with physiologically active ligands, a single metal coordination complex integrates multifunctional applications.

Palmitic acid (Hexadecanoic acid) has formula $\text{CH}_3(\text{CH}_2)_{14}\text{COOH}$ that is the long-chain fatty acid present in

many plants resources and animals. It is extensively present in palm oil and coconut oil. It is also naturally found in milk products, cocoa butter, sunflower oil, and soybean oil. Hexadecanoic acid is formed during fatty acid synthesis (lipogenesis). As a result, it is found in adipose tissue [1] and breast milk of humans [2]. Palmitic acid is used in cosmetic industries as well as in the manufacture of soaps. The aluminum salt of palmitic acid is used as a solidifying component of napalm for military uses [3]. Palmitate ester is administered intramuscularly for curing schizophrenia. Retinyl palmitate or vitamin A palmitate is further added to low-fat milk to compensate the vitamin loss during the removal of fats in milk. Palmitic acid is noted to increase metastasis in mice which are similar to that of human oral cancer cells

TABLE 1: Physical characteristics of metal coordinated complexes of palmitic acid.

Empirical formula of the complex	Molecular weight	m.p (°C)	Color	Yield (%)
$C_{32}H_{66}O_6Mn$	600.9	117.2	White	66
$C_{32}H_{70}O_8Co$	640.9	109.1	Purple	75
$C_{32}H_{66}O_6Ni$	604.7	128.2	Light green	64
$C_{32}H_{66}O_6Cu$	609.5	120	Blue	60
$C_{32}H_{70}O_8Zn$	647.4	123	White	71

TABLE 2: UV-Vis spectral data for ligand palmitic acid and metal palmitates.

Compound	Wavelength (nm)	Assignment
Ligand palmitic acid	273	$n \rightarrow \pi^*$
Manganese palmitate	210	$\pi \rightarrow \pi^*$
	290	$n \rightarrow \pi^*$, CT
Cobalt palmitate	208	$\pi \rightarrow \pi^*$
	284	$n \rightarrow \pi^*$
Nickel palmitate	532	d-d transition, CT
	217	$\pi \rightarrow \pi^*$
	264	$n \rightarrow \pi^*$
Copper palmitate	553	d-d transition, CT
	233	$\pi \rightarrow \pi^*$
Zinc palmitate	705	d-d transition, CT
	211	$\pi \rightarrow \pi^*$, CT

[4]. Palmitic acid displays antioxidant properties and helps in the prevention of atherosclerosis in rats.

Saturated fatty acids with longer chain length like palmitic acid have been reported as potential antibacterial agents (gram positive and negative bacterial strains) for more than two decades [5–9]. The lipophilicity of fatty acids promotes its adsorption to penetrate easily into the cell membrane which enhances the antimicrobial activity. Also, the unsaturated fatty acids have more bactericidal action than the saturated fatty acids because of the double bonds which disrupt easily and penetrate into the cell membrane. Kim et al. also reported the antimicrobial property of various fatty acids (oleic acid, linoleic acid, and palmitoleic acid) [10]. Meanwhile, when employing these unsaturated fatty acids in biomedical products, oxidation instability of the formula must be noted. Abraham et al. reported the effectiveness of linoleic acid in inhibition of *Staphylococcus aureus* biofilms due to the release of protease that increases the cell disruption [11], because, for instance, linoleic acid degrades into ketonic compounds via peroxide production which is not biocompatible [12].

However, no comprehensive reports or research on the metal complexes of saturated fatty acid for antimicrobial infections are not done. In this present research work, we therefore study the synthesis of various transition metals ($M = Mn, Co, Ni, Cu, \text{ and } Zn$) complex with hexadecanoic acid. The investigation of antimicrobial applications of vari-

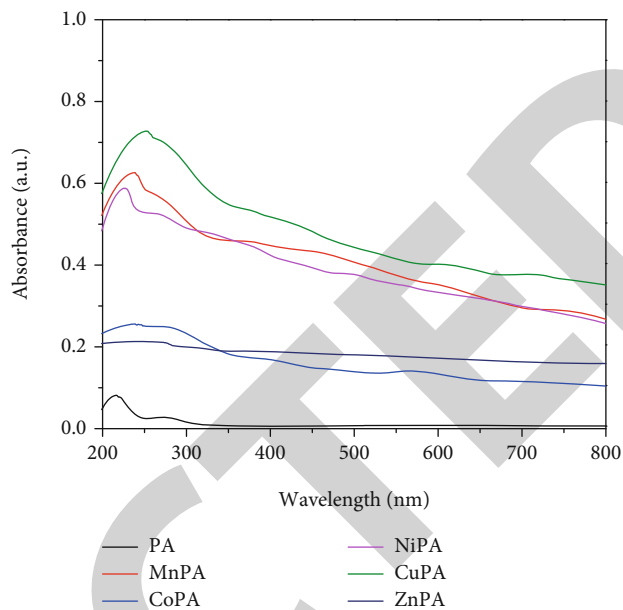


FIGURE 1: Absorption spectra of palmitic acid and its metal complexes.

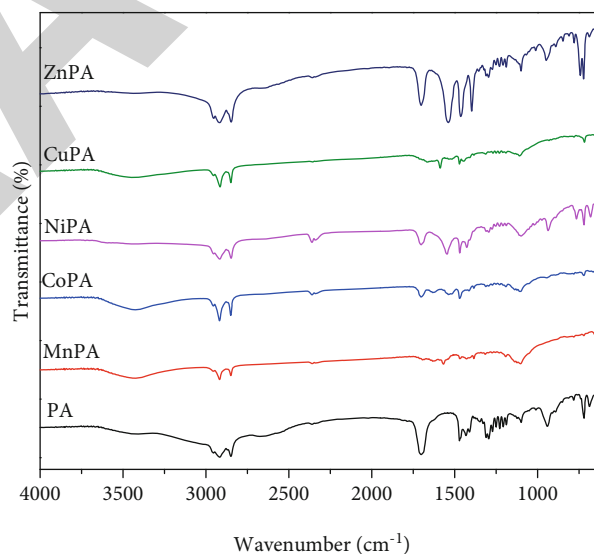


FIGURE 2: FT-IR spectra of palmitic acid and its metal complexes.

ous metal coordinated complexes of hexadecanoic acid has been well discussed.

2. Experimental Procedure

2.1. Materials. Palmitic acid (formula weight = 256.42) was purchased from Sigma-Aldrich. The transition metal salts (manganese (II), copper (II), cobalt (II), nickel (II), and zinc (II)) were purchased from Merck. Ethanol was purchased from Merck, and its purification process was carried out according to the Vogel standard procedures. Demineralized water was used for all experiments.

TABLE 3: Vibrational spectrum data of ligand palmitic acid and metal palmitate complexes.

Palmitic acid	Manganese palmitate	Cobalt palmitate	Nickel palmitate	Copper palmitate	Zinc palmitate	Assignment
—	3437	3406	3436	3233	3429	O-H
2917	2918	2851	2954	2915	2951	C-H stretching of CH ₂ and CH ₃
2849	2849	2918	2918	2849	2918	
1700	1691 1567	1529	1547	1667 1586	1538	Carbonyl and ester group
1466	1466	1467	1468	1447	1461	C-O stretching of COOH
1431	1426		1427	1470	1397	
1295	1274	1109	1295	1111	1019	C-C (stretching)
1099	974	946	1095	915	1298	
782	720	722	763	717	723	C-H (bending)
722			721			
—	552	462	516	472	462	M-O

2.2. Synthesis of Metal Coordinated Complexes of Hexadecanoic Acid. Ligand hexadecanoic acid was added and stirred continuously to dissolve in the ethanol. 0.01 M metal salt solution ($Mn^{2+}/Co^{2+}/Ni^{2+}/Cu^{2+}/Zn^{2+}$) was added in dropwise and refluxed for 3 hours at 50-55°C. Sodium hydroxide solution (0.1 M) was further added in drops to maintain pH 9-10. White colored-manganese and zinc, pink-cobalt, pale green-nickel, and blue-copper complexes were formed, filtered, rinsed with water and alcohol, and dried at 50°C.

2.3. Characterization of Metal Complexes of Hexadecanoic Acid. The absorption spectrum for the formation of metal complexes of palmitic acid was characterized using UV-Vis spectrophotometer in the wavelength range of 200-800 nm (Perkin Elmer Lambda 950). The vibrational frequencies of metal coordinated complexes were recorded using Nicolet 6700 spectrometer (Thermo, USA). The crystallographic nature of the complexes was analyzed in the range of 5-90° using copper source. The XRD peaks of the metal-hexanoic acid complexes were investigated using Phillips Xpert Pro (PCPDFWIN.V.2.1). TA (Q-500) instrument was used to study thermal degradation pattern with consistent weight loss of the complexes which was studied at a fixed heating rate (10°C/min) under N₂ atmosphere. The morphology of solid transition metal hexanoates was photographed through field emission scanning electron microscopy instrument, JSM 6500F, JEOL. The composition of corresponding transition metal, carbon, and oxygen in the complexes was analyzed from EDS spectrum.

2.4. Cytotoxicity. For cell growth, the cells were placed in 96-well plates containing 1% glutamine, 1% antibiotic, 10% FBS, 5% carbon dioxide, and 1% sodium pyruvate incubated

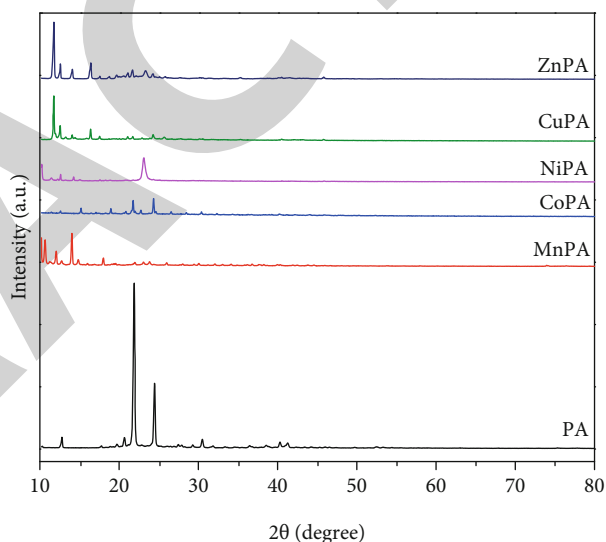


FIGURE 3: XRD spectrum of metal palmitates.

overnight at 37°C with a density of 3.0×10^5 cells per well. After the cells were grown well, various concentrations of metal complexes and ligand were added to it. To attain the final concentration, 5 mg/ml MTT (3-(4,5-dimethylthiazol-2-yl)-2,5-diphenyltetrazolium bromide) was added. The cells were incubated for the formation of formazan dye for 4 hours, and then absorbance was measured [13]. After comparing the untreated cells with the treated cells as a control, the analytical results were ensuing as the percentage of cell viability. Each analysis was performed in triplicate to ensure accuracy. The survival rate of the cells was calculated by the following expression.

$$\text{Percentage of Cell viability} = \left(\frac{\text{Measured absorbance of the sample treated cells}}{\text{Absorbance of untreated cells}} \right) \times 100 \quad (1)$$

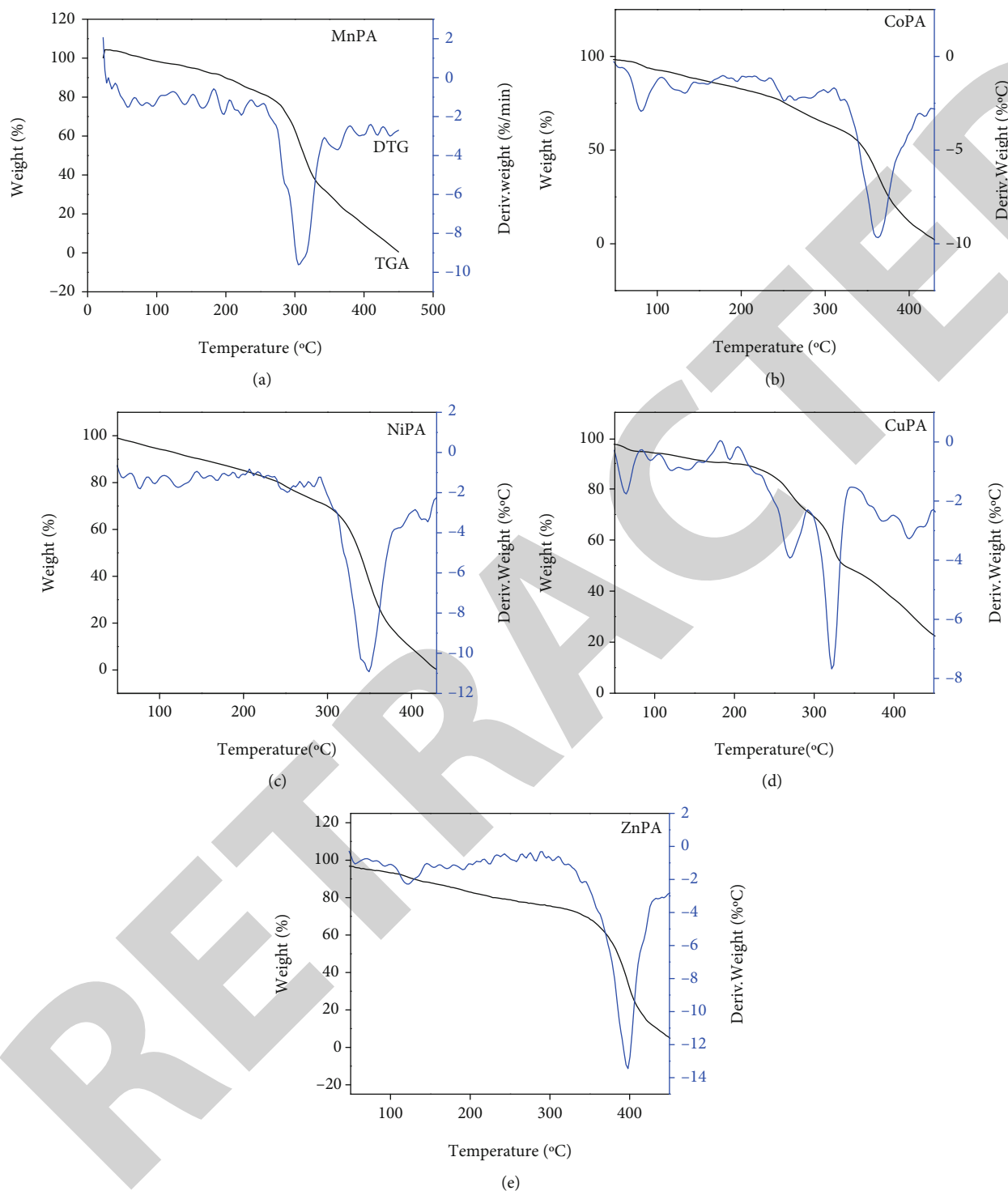


FIGURE 4: TGA/DTG curves of metal complexes of palmitic acid.

2.5. Antimicrobial Potency of Synthesized Metal Complexes

2.5.1. The Antibacterial Activity of Metal Palmitates. Both gram positive and gram negative bacteria strains (comprising *Enterococcus faecalis* and *Staphylococcus aureus*) were tested for bactericidal activity against metal palmitate complexes. Using ethanol as a solvent, metal palmitates (10 mg/

ml) were prepared for the analysis. Nutrient Agar is used to incubate species on plates. In order to test bactericidal activity, specific strengths (400, 600, 800, 1000 g/ml) of complexes were added to wells, while tetracycline was used as standard control. The antibacterial activity was examined after 24 hours incubated at 37°C, and the growth of an inhibition zone was measured.

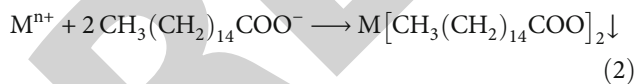
TABLE 4: TGA/DTG study of metal palmitates.

Complex	Temperature range (°C)	DTG (°C)	Weight loss (%)		Assignment
			Calc.	Obs.	
Mn(CH ₃ (CH ₂) ₁₄ COO) ₂ ·2H ₂ O	100-250	160	2.16	2.42	2H ₂ O + (C ₁₅ H ₃₁ COO) ₂ MnMnO ₂
	300-400	304	72.8	71.1	
Co(CH ₃ (CH ₂) ₁₄ COO) ₂ ·4H ₂ O	50-100	83	5.76	5.64	4 H ₂ O + C ₃₀ H ₆₂ O ₂ Co ₃ O ₄
	300-400	365	84.42	85.11	
Ni(CH ₃ (CH ₂) ₁₄ COO) ₂ ·2H ₂ O	50-100	168	2.44	2.58	2H ₂ O + C ₁₂ H ₂₆ C ₁₁ H ₂₀ + CO + CO ₂ + NiO
	300-400	349	74.42	72.73	
Cu(CH ₃ (CH ₂) ₁₄ COO) ₂ ·2H ₂ O	50-100	65	3.48	3.76	2H ₂ O + C ₃₀ H ₆₂ O ₂ Cu ₂ O
	250-510	270,323, 500	88.86	89.57	
Zn(CH ₃ (CH ₂) ₁₄ COO) ₂ ·4H ₂ O	100-150	134	7.38	7.68	4H ₂ O + C ₂₀ H ₄₂ C ₃ H ₄ +2 CO + ZnO
	350-450	399	81.12	80.14	

2.5.2. *The Antifungal Activity of Metal Palmitates.* *Aspergillus Niger* fungi species was inoculated on Potato Dextrose Agar plates at 28°C for consecutive five days. Various concentrations of complexes were added to each well in amounts of 400, 600, 800, and 1000 g/ml, respectively, and incubated for 48 hours at temperature 37°C. Standard control used was ketoconazole, and zone of inhibition (in diameter) was measured.

3. Results and Discussion

3.1. *Physical and Chemical Characterization of Metal Palmitates.* In the binary solvent medium (aqueous-ethanol), metal palmitate complexes were synthesized by simple method through the interaction of respective metal ions with hexadecanoic acid. All complexes were having high stability. The physical characteristic properties of the produced metal palmitates were given in Table 1. The versatile color of the metal palmitates depends on the metal ions and the oxidation state of the metals. This general reaction given below could be used to describe the reaction of palmitic acid with various metal ions.



3.2. *The Absorption Spectra of Metal Palmitate Complexes.* Electronic absorption spectrum of palmitic acid and metal complexes was shown in Table 2 and spectrum represented in Figure 1. The absorption spectra signify the formation of metal complexes with their shift in wavelength. Absorption of palmitic acid was attributed to the $n \rightarrow \pi^*$ transition at around 270-280 nm which were forbidden transitions [14]. The complexation of ligand with respective metal ions could be confirmed by the shift of absorption to longer wavelengths. Cobalt and nickel complexes showed absorption bands owing to d-d transition, but zinc complex did not show significant changes as it has completely filled d-orbitals. The broad band observed at longer wave length for the copper complex indicates d-d

transition characterized by octahedral geometry of the metal atoms [15].

3.3. *The Infrared Spectral Studies of Metal Palmitate Complexes.* The vibrational spectra of ligand palmitic acid and its corresponding metal complexes were depicted in Figure 2, and stretching vibrational frequencies labeled in Table 3. The vibration of C=O of the carboxylic acid appeared at 1700 cm⁻¹ for the pristine ligand. The disappearance of this band at 1700 cm⁻¹ and appearance of new band at 1567, 1529, 1547, 1586, and 1538 cm⁻¹ for all the metal carboxylates confirmed the complexation. These bands were due to carbonyl group present in coordinated COO⁻ moieties with metal ions.

The metal complexes exhibited a broad band in 3406-3437 cm⁻¹ region which was assigned to the OH stretching of coordinated water molecules [16]. The stretching (both asymmetric & symmetric) frequencies $\nu(\text{COO}^-)$ of the metal bound carboxylates were shown absorption in the range of 1700 cm⁻¹ and 1400 cm⁻¹. The appearance of new band in the range of 462-552 cm⁻¹ was due to M-O bond stretching. The observation could be correlated to the coordination of ligand to the metal through oxygen donor atom. IR stretching frequencies between $\nu_{\text{ass}}(\text{COO}^-)$ and $\nu_{\text{s}}(\text{COO}^-)$ was less than 200 cm⁻¹ could be associated to bidentate bonding of metal palmitate complexes in powdered state. The lowering of $\nu_{\text{ass}}(\text{COO}^-)$ and rise of $\nu_{\text{s}}(\text{COO}^-)$ illustrates the bidentate nature of the ligand. $\nu(\text{C-H})$ of the CH₃ group occurs in the range of 2915-2954 cm⁻¹, and $\nu(\text{C-H})$ of methylene also occurs in the short range of 2848-2851 cm⁻¹.

3.4. *Crystallographic Study of the Metal Palmitates.* The powdered samples of metal complexes peaks were recorded by XRD shown in the Figure 3. Sharp and well-defined diffraction peaks were obtained attributed to the crystalline phase of the complexes. The manganese (II) palmitate, cobalt (II) palmitate, nickel (II) palmitate, copper (II) palmitate, and zinc (II) palmitate complexes have an average crystallite size of 23, 21, 10, 35, and 12 nm, respectively. The experiential values of Mn (II) and Cu (II) complexes were good fit for the tetragonal crystal system, whereas Co(II) and Ni(II)

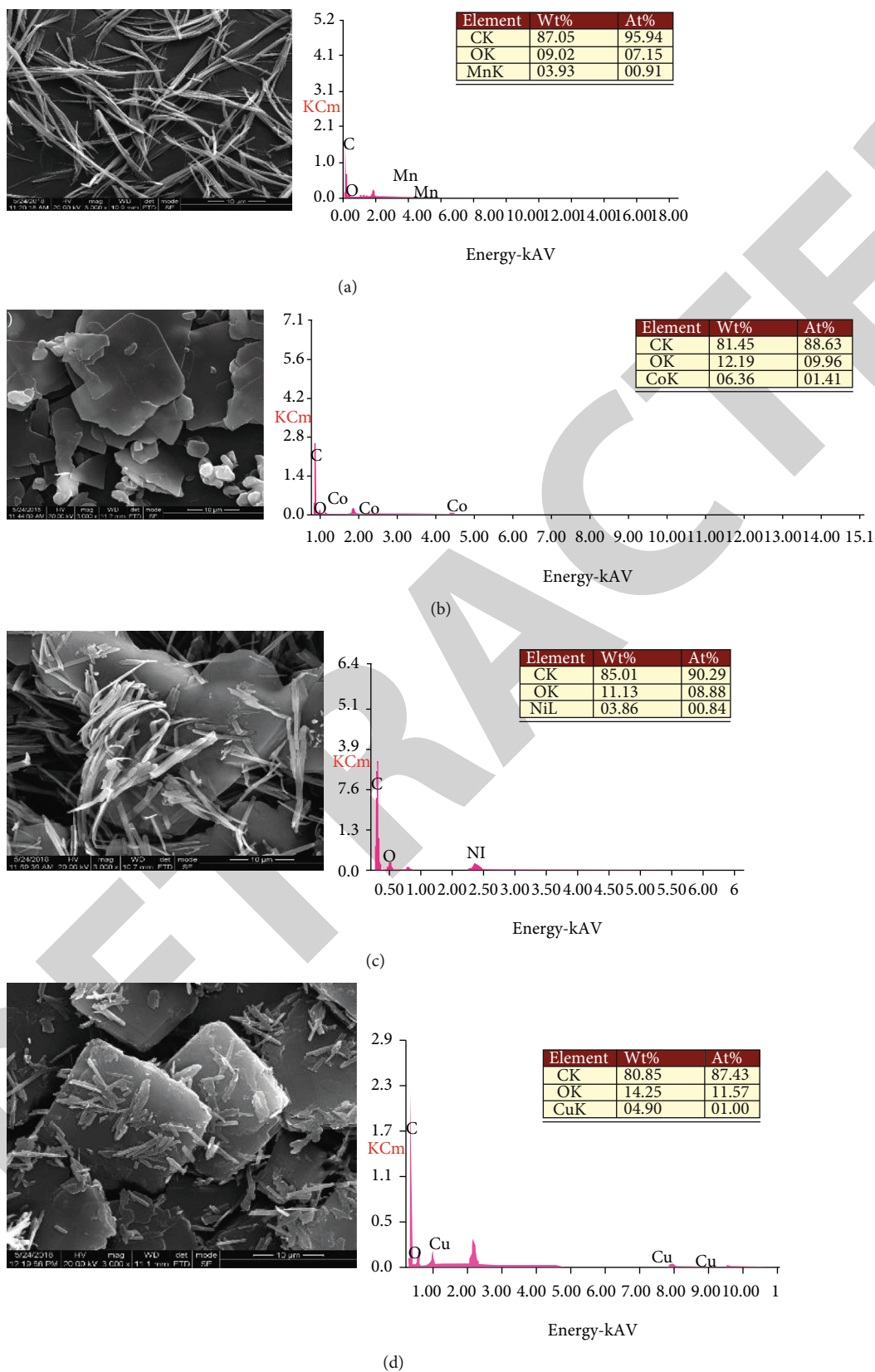


FIGURE 5: Continued.

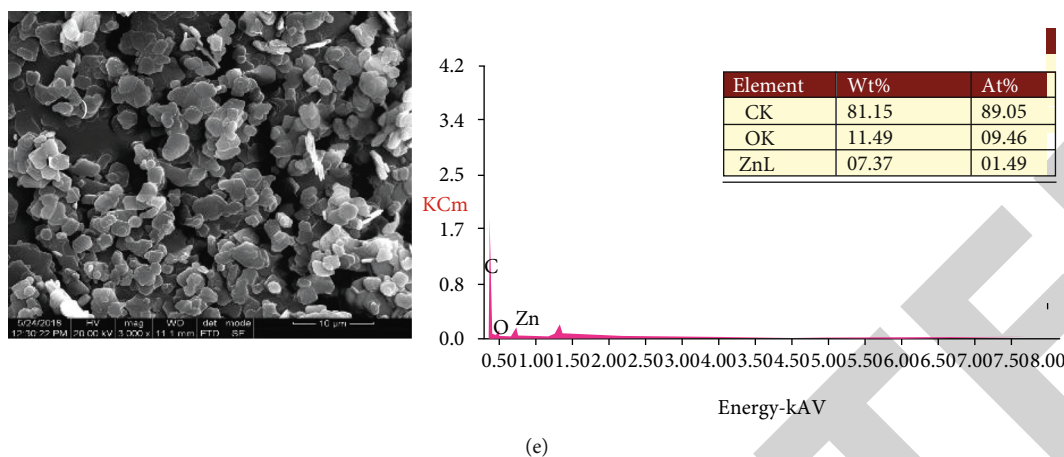


FIGURE 5: SEM images and EDS spectra of (a) manganese(II) palmitate and (b) cobalt (II) palmitate, (c) nickel (II) palmitate, (d) copper (II) palmitate, and (e) zinc (II) palmitate.

complexes were good fit for the monoclinic system, and Zn (II) complex was good fit for the triclinic system [17, 18].

3.5. The Study of Thermogravimetric Analysis. The study of thermal analysis of the synthesized metal palmitate complexes was done to analyze the decomposition behavior and thermal stability. TGA and DTG thermograms were presented in Figure 4. The complexes undergo dehydration initially to give anhydrous complex in the temperature range of 60–200°C. The dehydration of uncoordinated and lattice water molecules occurs at less than 100°C. Decomposition occurs between 100 and 200°C that is due to the loss of coordinated water molecules. The stability of the complexes in terms of intermediate and volatiles established on the concurrence between the calculated and observed values were given in Table 4. It was found that all the theoretical and experimental values were good in agreement, endorsing the molecular formula similar to that proposed by other spectroscopic techniques.

3.5.1. Manganese Palmitate Complex. The decomposition of solid complex appeared as endothermic peaks over the range 0–600°C. The first step occurs from 100 to 250°C corresponding to the removal of two water molecules representing 2.4% weight loss. The second step from 300 to 400°C corresponding to the disintegration of organic moiety representing 71.1% weight loss.

3.5.2. Cobalt Palmitate Complex. The thermal destruction of cobalt palmitate occurred in two stages. The first stage of decomposition occurred in the range of 50–100°C could be assigned to the elimination of four water molecules representing 5.63% weight loss. The second step occurred between 300–400°C with the weight loss of 85.11% due to the breakdown of organic moiety. Cobalt oxide could be the final residue [19].

3.5.3. Nickel Palmitate Complex. The first stage of decomposition was in 50–100°C recording a weight loss (2.58%) due to the dehydration of the complex. The next stage decomposition occurred in the range of 300–400°C due to decomposi-

tion of organic moiety into volatile compounds (72.73%). The final residue could be nickel oxide [20].

3.5.4. Copper Palmitate Complex. Degradation of the complex in terms of dehydration occurred at 50–100°C. The significant decomposition between the range of 250–510°C was observed for the decomposition and formation of organic moiety and metallic residue, respectively [21].

3.5.5. Zinc Palmitate Complex. The first step was in the range of 100–150°C corresponding to loss of four uncoordinated water molecules representing the weight loss of 7.6%. The second stage of decomposition occurred at 300–450°C conforming to the degradation of organic compound to CO and ZnO [22].

3.6. Morphology of Synthesized Complexes and EDX Analysis. The morphology of metal palmitates was displayed in Figure 5. The formation of micro- and nanostructures could be attributed to their significant results. Typically, manganese palmitate complex formed thread like structures with a size of approximately 1.20 μm and thickness of approximately 204 nm. The cobalt palmitate complex displayed petal like structures with a thickness of approximately 285 nm. The nickel palmitate complex showed both petal and thread like structures. The copper palmitate complex formed both plate and rod shaped structures with a size of approximately 4.17 μm and thickness of approximately 409 nm. The zinc palmitate complex formed plate like structures with a size of approximately 1.2 μm and thickness of approximately 132 nm [23]. The synthesized complexes were analyzed on material surfaces by energy dispersive spectral analysis (EDX). The presence of carbon, oxygen, and respective metals has been observed. The EDX analysis also confirmed there were no other impurities detected in the metal complexes.

3.7. Cell Viability Study of Ligand and Metal Complexes. Nemezc et al. studied the cell viability of palmitic acid in combination with oleic acid on beta cells, and they reported that the cotreatment enhances the effect of proliferation and

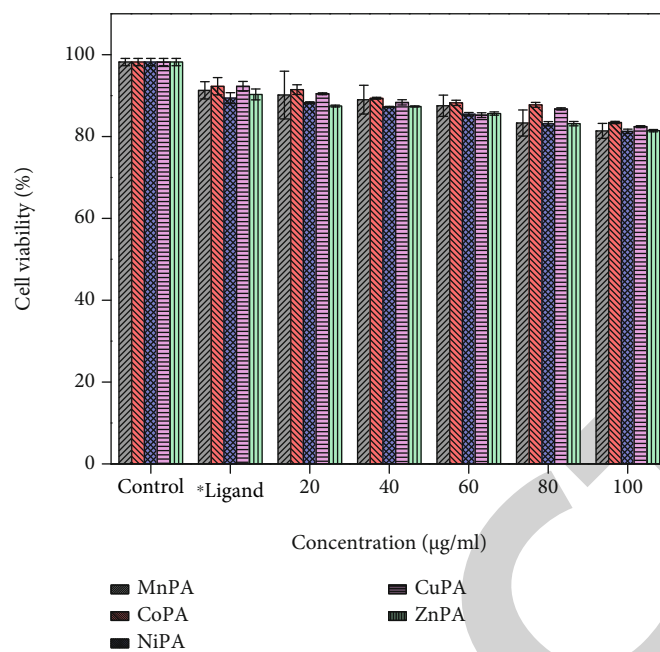


FIGURE 6: Cell viability of ligand palmitic acid and metal palmitates.

TABLE 5: Antibacterial and antifungal activity data for metal palmitates.

Complex	Inhibition zone in diameter (mm)				
	<i>Enterococcus faecalis</i>	<i>Escherichia coli</i>	Bactericidal*		Fungicidal**
			<i>Pseudomonas aeruginosa</i>	<i>Staphylococcus aureus</i>	<i>Aspergillus Niger</i>
MnPA	Nil	Nil	Nil	14	16
CoPA	Nil	Nil	15	Nil	12
NiPA	Nil	Nil	Nil	12	Nil
CuPA	Nil	Nil	14	13	16
ZnPA	Nil	Nil	Nil	Nil	16
Tetracycline*					
Ketaconazole**	30	30	30	30	28

*Denotes standard bactericidal drug and **denotes standard fungicidal drug.

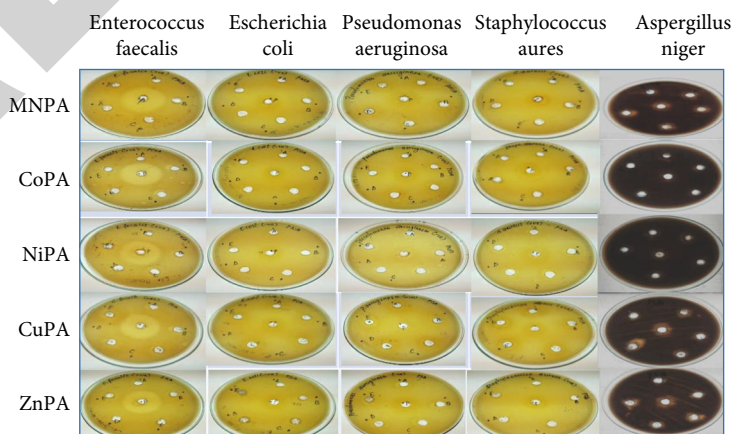


FIGURE 7: Antimicrobial activities of metal palmitate complexes.

cell viability [24]. Toxic nature of metal palmitates and ligand palmitic acid was evaluated by MTT assay. The cell viability of the ligand (concentration -100 $\mu\text{g/ml}$) was found to be more than 80% which was represented in Figure 6. The toxic effect of the metal complexes was very less and coincides with the biocompatibility of the ligand. Cobalt palmitate and copper palmitate complexes seem to have more viability than other complexes. The biocompatibility of metal palmitates could be inferred to decide on their biological applications from their cell viability.

3.8. Microbicidal Activity of Metal Palmitates. Bactericidal activities of ligand Palmitic acid were already reported. Palmitic acid coatings exhibited higher bactericidal performance against the *S. Aureus* cells. Few studies showed that palmitic acid crystallites were shown marked activity against bacteria. The copper complex of palmitic acid displayed the strongest activity against different bacterial strains. The antibacterial activity of the metal complexes is due to the metal chelation effect. The reactive oxygen species induced by the copper ions causes the toxicity disrupts the cell membrane which leads to apoptosis. The antibacterial activity of synthesized metal palmitates was studied shown in Table 5 and represented in Figure 7. The bactericidal activity of manganese complex, cobalt complex, and nickel complex was found to be moderate. Zinc complex of palmitic acid was resistant to bacteria and did not show any significant bactericidal activity due to its poor solubility. This weak bactericidal activity may be due to its low solubility [25]. These reports can throw more light on the design of bactericidal drugs. Antifungal effects of metal salts of palmitic acid against *S. Apiospermum* were investigated under different water conditions, indicating that the combination of palmitic acid soap and ultrapure soft water had the strongest antifungal activity [26].

4. Conclusion

In the current research work, metal complexes of hexadecanoic acid have been synthesized in binary solvent media and characterized. FT-IR spectra indicated the formation of M-O linkage for all the complexes. The various morphologies of complexes of different metal ions were also studied. The complexes were formulated after interpreting the analytical data. All the synthesized complexes were proven to have very less cytotoxicity and to have more than 80% cell viability, which will be used for many biomedical applications as they were biocompatible. Most of the complexes were found to have promising bactericidal activity. And all the complexes have strong fungicidal activity except the nickel palmitate complex.

Data Availability

No data were used in this study.

Conflicts of Interest

The authors declare that they have no conflicts of interest regarding the publication of this paper.

Authors' Contributions

Kavitha Govindarajan and Vijayarohini Parasuraman contributed equally to this work and shared first author.

References

- [1] C. A. Francois, S. L. Connor, L. C. Bolewicz, and W. E. Connor, "Supplementing lactating women with flaxseed oil does not increase docosahexaenoic acid in their milk," *The American Journal of Clinical Nutrition*, vol. 77, no. 1, pp. 226–233, 2003.
- [2] T. Chantadee, W. Santimaleworagun, Y. Phorom, and T. Phaechamud, "Saturated fatty acid-based in situ forming matrices for localized antimicrobial delivery," *Pharmaceutics*, vol. 12, no. 9, p. 808, 2020.
- [3] T. Johnson, "Napalm: An American Biography. By Robert M. Neer. (Cambridge, MA: Belknap Press of Harvard University Press, 2013. Pp. 352. \$29.95)," *The Historian*, vol. 77, no. 1, pp. 134–135, 2015.
- [4] A. Britschgi, S. Duss, S. Kim et al., "The hippo kinases LATS1 and 2 control human breast cell fate via crosstalk with ER α ," *Nature*, vol. 541, no. 7638, pp. 541–545, 2017.
- [5] C. B. Huang, B. George, and J. L. Ebersole, "Antimicrobial activity of n-6, n-7 and n-9 fatty acids and their esters for oral microorganisms," *Archives of Oral Biology*, vol. 55, no. 8, pp. 555–560, 2010.
- [6] A. P. Desbois and V. J. Smith, "Antibacterial free fatty acids: activities, mechanisms of action and biotechnological potential," *Applied Microbiology and Biotechnology*, vol. 85, no. 6, pp. 1629–1642, 2010.
- [7] G. Agoramorthy, M. Chandrasekaran, V. Venkatesalu, and M. J. Hsu, "Antibacterial and antifungal activities of fatty acid methyl esters of the blind-your-eye mangrove from India," *Brazilian Journal of Microbiology*, vol. 38, no. 4, pp. 739–742, 2007.
- [8] Y. García-Cazorla, M. Getino, D. J. Sanabria-Ríos et al., "Conjugation inhibitors compete with palmitic acid for binding to the conjugative traffic ATPase TrwD, providing a mechanism to inhibit bacterial conjugation," *Journal of Biological Chemistry*, vol. 293, no. 43, pp. 16923–16930, 2018.
- [9] B. K. Yoon, J. Jackman, E. Valle-González, and N. J. Cho, "Antibacterial free fatty acids and Monoglycerides: biological activities, experimental testing, and therapeutic applications," *International Journal of Molecular Sciences*, vol. 19, no. 4, p. 1114, 2018.
- [10] C. J. Zheng, J. S. Yoo, T. G. Lee, H. Y. Cho, Y. H. Kim, and W. G. Kim, "Fatty acid synthesis is a target for antibacterial activity of unsaturated fatty acids," *FEBS Letters*, vol. 579, no. 23, pp. 5157–5162, 2005.
- [11] K. T. Yuyama, M. Rohde, G. Molinari, M. Stadler, and W. R. Abraham, "Unsaturated fatty acids control biofilm formation of *Staphylococcus aureus* and other gram-positive bacteria," *Antibiotics*, vol. 9, no. 11, p. 788, 2020.
- [12] J. J. Villaverde, S. A. O. Santos, M. M. Q. Simões, C. P. Neto, M. R. M. Domingues, and A. J. D. Silvestre, "Analysis of linoleic acid hydroperoxides generated by biomimetic and enzymatic systems through an integrated methodology," *Industrial Crops and Products*, vol. 34, no. 3, pp. 1474–1481, 2011.
- [13] G. M. L. Sys, L. Lapeire, N. Stevens et al., "The *In ovo* CAM-assay as a xenograft model for sarcoma," *Journal of Visualized Experiments*, vol. 77, no. 77, article e50522, 2013.

Retraction

Retracted: Evaluation of Physicothermal Properties of Solar Thermic Fluids Dispersed with Multiwalled Carbon Nanotubes and Prediction of Data Using Artificial Neural Networks

Journal of Nanomaterials

Received 11 July 2023; Accepted 11 July 2023; Published 12 July 2023

Copyright © 2023 Journal of Nanomaterials. This is an open access article distributed under the Creative Commons Attribution License, which permits unrestricted use, distribution, and reproduction in any medium, provided the original work is properly cited.

This article has been retracted by Hindawi following an investigation undertaken by the publisher [1]. This investigation has uncovered evidence of one or more of the following indicators of systematic manipulation of the publication process:

- (1) Discrepancies in scope
- (2) Discrepancies in the description of the research reported
- (3) Discrepancies between the availability of data and the research described
- (4) Inappropriate citations
- (5) Incoherent, meaningless and/or irrelevant content included in the article
- (6) Peer-review manipulation

The presence of these indicators undermines our confidence in the integrity of the article's content and we cannot, therefore, vouch for its reliability. Please note that this notice is intended solely to alert readers that the content of this article is unreliable. We have not investigated whether authors were aware of or involved in the systematic manipulation of the publication process.

Wiley and Hindawi regrets that the usual quality checks did not identify these issues before publication and have since put additional measures in place to safeguard research integrity.

We wish to credit our own Research Integrity and Research Publishing teams and anonymous and named external researchers and research integrity experts for contributing to this investigation.

The corresponding author, as the representative of all authors, has been given the opportunity to register their

agreement or disagreement to this retraction. We have kept a record of any response received.

References

- [1] K. C. Sekhar, R. Surakasi, I. Garip, S. Srujana, V. V. P. Kumar, and N. Begum, "Evaluation of Physicothermal Properties of Solar Thermic Fluids Dispersed with Multiwalled Carbon Nanotubes and Prediction of Data Using Artificial Neural Networks," *Journal of Nanomaterials*, vol. 2021, Article ID 7306189, 13 pages, 2021.

Research Article

Evaluation of Physicothermal Properties of Solar Thermic Fluids Dispersed with Multiwalled Carbon Nanotubes and Prediction of Data Using Artificial Neural Networks

K. Ch. Sekhar ¹, Raviteja Surakasi ¹, ilhan Garip ², S. Srujana ³,
V. V. Prasanna Kumar ¹ and Naziya Begum ⁴

¹Department of Mechanical, Lendi Institute of Engineering and Technology, Jonnada, Vizianagaram, India

²Department of Electrical and Electronics Engineering, Engineering and Architecture Faculty, Nisantasi University, Istanbul, Turkey

³Department of Biotechnology, Center for Post Graduate Studies, Jain University, Bengaluru, India

⁴Department of Chemistry, College of Natural and Computational Science, Debre Berhan University, Debre Berhan, Ethiopia

Correspondence should be addressed to Naziya Begum; drnaziyaBegum15@dbu.edu.et

Received 6 November 2021; Revised 19 November 2021; Accepted 20 November 2021; Published 29 December 2021

Academic Editor: Karthikeyan Sathasivam

Copyright © 2021 K. Ch. Sekhar et al. This is an open access article distributed under the Creative Commons Attribution License, which permits unrestricted use, distribution, and reproduction in any medium, provided the original work is properly cited.

A review of multiwalled carbon nanotubes as solar thermic fluids and their thermophysical properties is done in this article. The basic fluids were ethylene glycol and water in ratios of 100 : 0, 90 : 10, and 80 : 20. To investigate how surface modification impacts thermophysical properties, three base fluids were combined with surfactant-assisted MWCNTs and oxidized MWCNTs in weight fractions of 0.125, 0.25, and 0.5 percent, respectively. It takes two months to check whether the dispersion stays constant. Thermal conductivity and viscosity measurement were done using heated discs and Anton Paar viscometers. Using oxidized MWCNTs to disperse, the base fluids increased thermal conductivity by 15% to 24%. Surfactant-assisted MWCNTs in nanofluids perform worse than oxidized MWCNTs. The dynamic viscosity of nanofluids is higher than that of basic fluids between 50 and 70°C. During a mathematical computation, all of the MWCNT weight fractions and ethylene glycol volume percentages are included. The correlation may be a good fit for the experimental data within limits. The characteristics are forecasted using feed-forward backpropagation. In this research, buried layer neurons and factors are examined.

1. Introduction

Studies show suggested nanofluids could be used in a variety of applications, such as heat exchangers, cooling systems for engines but also solar thermal systems, and electronic cooling and tribology. Their use may help industrial equipment transmit heat more efficiently. A nanofluid is a mixture of one or many nanoparticles in a basic fluid. Nanofluid. The dispersing in base fluids of a number of nanomaterials [1–19] is currently being studied. Thermic fluids made of ethylene glycol and water may be used to heat water. These fluids may also be utilised in heat exchangers and industrial

applications. The thermophysical characteristics of ethylene glycol may be adjusted by diluting it with water. An ethylene glycol-water combination with thermophysical characteristics is given in Table 1. Several researches assessed the impact of carbon nanotubes on nanofluid thermophysical characteristics. To improve the nanofluids thermal conductivity, viscosity and density researchers discovered that volume percentage increment leads to decreased specific heat while increasing thermal conductivity. Temperature enhanced thermal conductivity and specific heat. The researchers found that raising volume percent reduced specific heat while boosting thermal conductivity in order to

enhance nanofluid's thermal conductivity, density, and viscosity. Thermal conductivity and specific heat increased in direct proportion to temperature. As the temperature rises, so do the viscosity and density. Almost all research experiments generate large amounts of foam as a result of a lack of surface modification techniques and surfactant usage.

1.1. Present Studies. One of the most significant problems concerning nanofluids is their inappropriate behavior. Excessive foaming was shown to be a problem in almost all of the investigations. MWNTs with acid surface functionalization are used to dissolve ethylene glycol. Two months is an unusually long time for one nanofluid stability research. Comparison of nanofluids with and without surfactants was done for thermal conductivity. Thermic fluids including EG-water mixes are used in this study, as opposed to earlier studies that used other fluids. It is possible to heat ethylene glycol-water mixtures to temperatures up from 100 degrees Celsius to 194 degrees Celsius. In terms of thermophysical properties, they are tested from 50°C up to just below boiling. Prediction of both thermal conductivity and also viscosity to be affected by temperature and MWCNT mass fraction.

2. Materials and Methodology

2.1. Materials. CheapTubes Inc., USA, supplied MWCNTs produced via CVD. The MWCNTs are highly entangled, 95% pure, 30–50 nm in diameter, and 3–15 m long. All additional chemicals and surfactants used are analytical grade and obtained from M/s Sigma-Aldrich.

2.2. Multiwalled Carbon Nanotube Surface Modification. Many researches have shown that for nanofluid, there is a significant function for stability and dispersion in enhancing the fluid's thermophysical characteristics, especially its thermal conductivity. Nanofluids were evaluated for their final properties based on their dispersion stability. Multiwalled carbon nanotubes, as previously discovered, are very resistant to a variety of chemicals but do not dissolve in polar solvents. Nanotube clusters form and settle in liquid environments due to their hydrophobicity, losing their properties. To disperse CNTs in base fluids, scientists often use a surfactant. Surfactants reduce heat transfer rates by increasing fluid foaming. Open-ended pure carbon nanotubes have been demonstrated by Hou et al. [2] as well as Chen et al. [3]. Through acid treatment, Rosca et al. [4] and Vaisman et al. [5] as well as Chiang et al. [6] have shown MWCNTs are hydrophilic in nature. Two distinct surface modification methods were used on MWCNTs. There are two methods used: surface modification using surfactants and oxidation to generate carboxyl and carbonyl groups. Ultrasonically dispersing CTAB and MWCNTs for 10 minutes in methanol is the first technique. Following full evaporation of the solvent, the MWCNTs may be reclaimed. It takes three hours for MWCNTs to decompose in a solution of $H_2SO_4:HNO_3$. In the morning, the burnt leftovers were washed thoroughly to a pH of 7 before being baked again at 60°C overnight. FESEM was used to characterise the structure of MWCNTs.

TABLE 1: Base fluid coolant configuration.

S.No	Composition
1.	Monoethylene glycol (100:0)
2.	Monoethylene glycol and distilled water (90:10)
3.	Monoethylene glycol and distilled water (80:20)

HRSEM images of unoxidized CNTs are shown in transform infrared spectroscopy for functional group detection (A and B). Pristine multiwalled carbon nanotubes are shown in Figure 1(a). Purification of MWCNTs, as shown in Figure 1(b), allows the tips to be opened.

Figure 2 shows the FTIR spectra both for pure and oxidized MWCNTs. In contrary to Figure 2(a)'s pristine MWCNTs, Figure 2(b) displays increases within spectral at 1125 and 1740 cm^{-1} , indicating the production of hydroxyl and carboxyl groups. These hydrophilic groups make MWCNTs highly water dispersible. A high dispersibility nanofluid has better characteristics than unsteady nanofluids.

3. Base Fluid Preparation

In the present research, three different kinds of thermic fluids are being used. In the coolant configuration shown in Table 1, oxidized multiwalled CNTs distributed in three different weight-percentage ranges utilise an ultrasonic probe; the base fluids were mixed with the coolants.

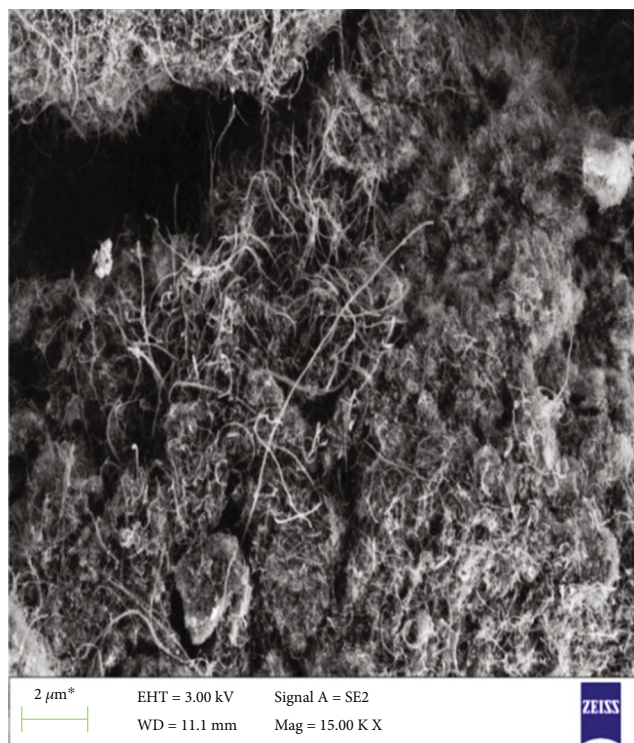
4. Physicothermal Property Evaluation

Thermal conductivity of liquids is difficult to determine during a test because of the significant convective heat transfer in fluids. Thermal conductivity is now measured using the Hot Disk method, which reduces the possibility of making errors while evaluating liquid thermal conductivity. In order to minimise convection, the Kapton sensor 7577 is selected for the testing. We ran three separate sets of tests with varying measurement durations on the samples, and the averages are shown in the following.

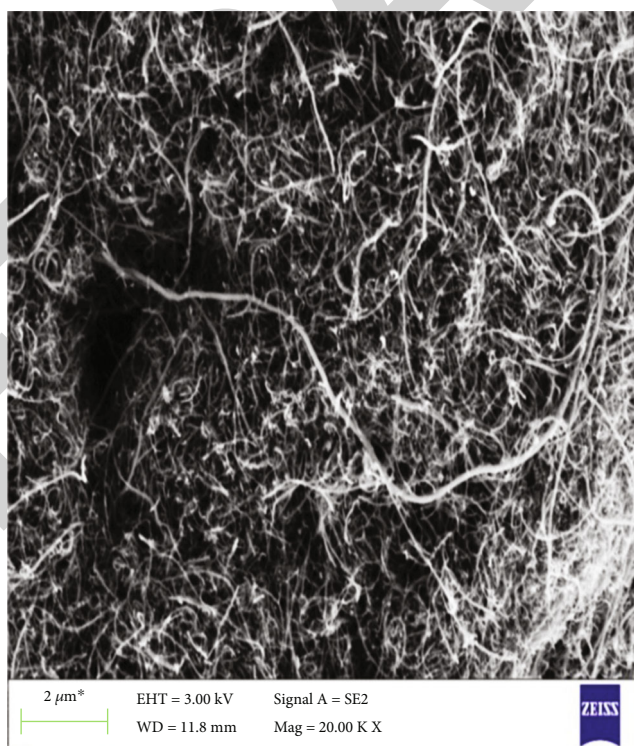
The Anton Paar MCR 302 Rheometer is fluid strain that can be adjusted rapidly and accurately, resulting in extremely accurate findings for evaluating dynamic viscosity. The samples are put through three rounds of testing, each with a different temperature, and the average result is calculated. It is important to make sure the sample is air-free before placing it in a rheometer, where the results were recorded at steady-state temperatures. Dynamic viscosity and thermal conductivity are determined for all samples at temperatures ranging from 50 to just below boiling.

5. Prediction of Data Using ANN

Physicothermal properties of thermic fluids are predicted using an artificial neural network. Also studied is the impact of variables and hidden layer neurons on prediction accuracy. For example, in medical diagnosis, financial



(a)

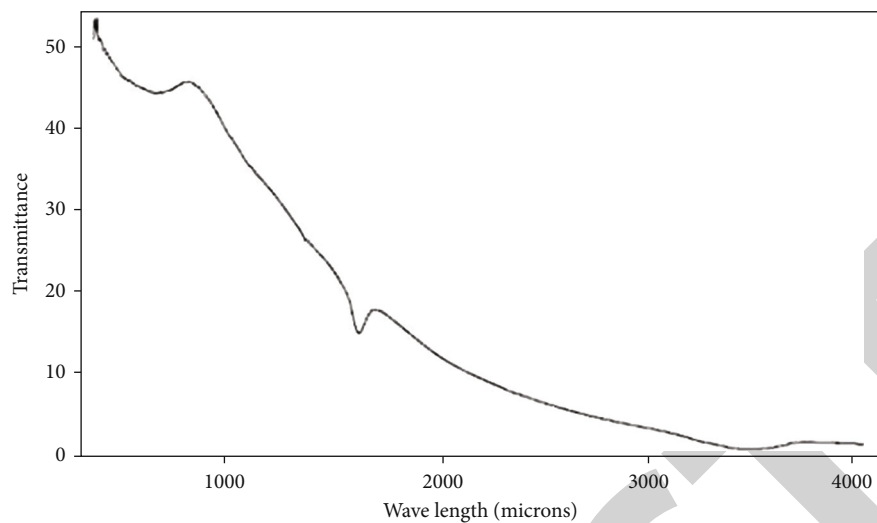


(b)

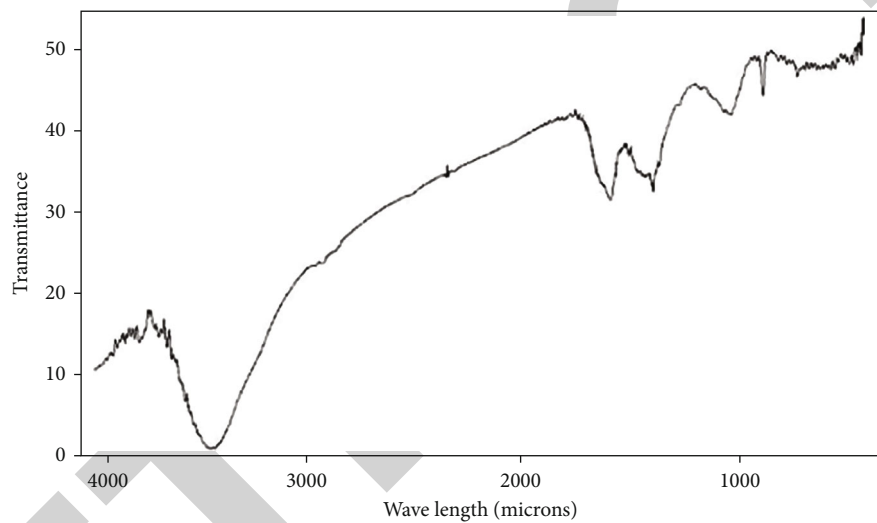
FIGURE 1: (a) Pristine multiwalled carbon nanotube and (b) oxidized multiwalled carbon nanotube FESEM image.

forecasting, and many engineering applications, artificial neural networks are a powerful and effective tool. Input data signals are analysed by ANNs to predict output signals. This technique can predict, categorise, and estimate

scientific data very accurately. ANNs are a kind of AI technique. It may be used for nonlinear prediction, optimization, pattern recognition, and other purposes. It may also be used to model and simulate data from many



(a)



(b)

FIGURE 2: (a) Pristine MWCNT and (b) oxidized MWCNT FTIR analysis.

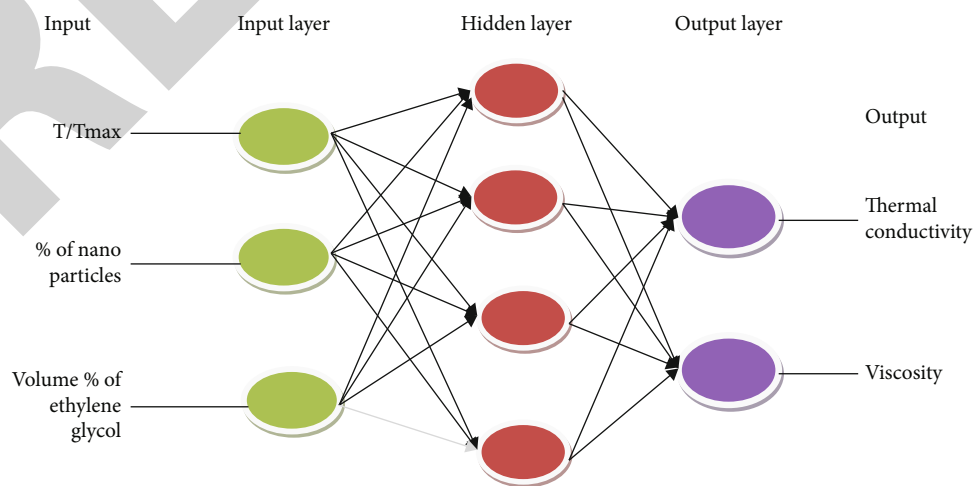


FIGURE 3: ANN architecture of the proposed model.

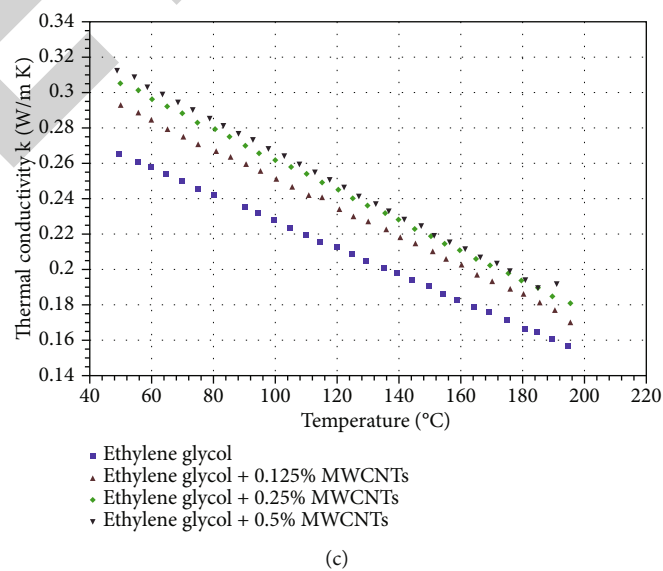
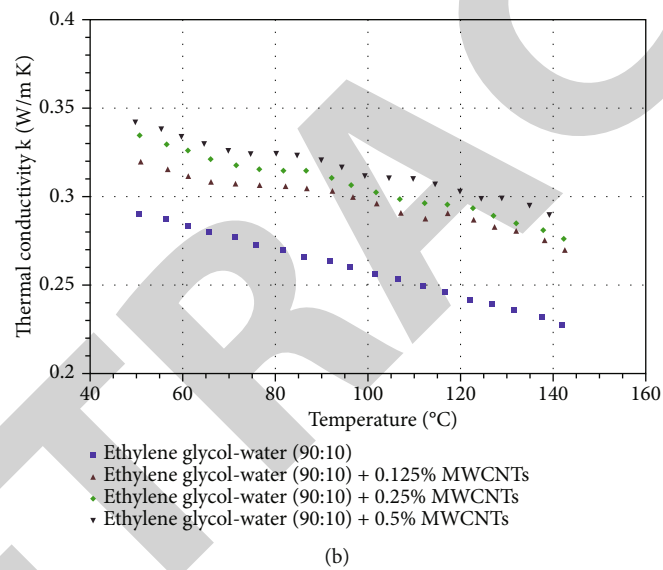
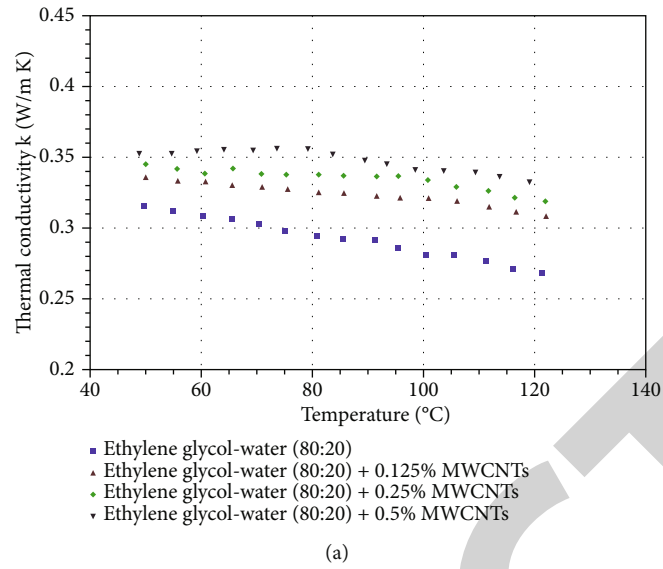
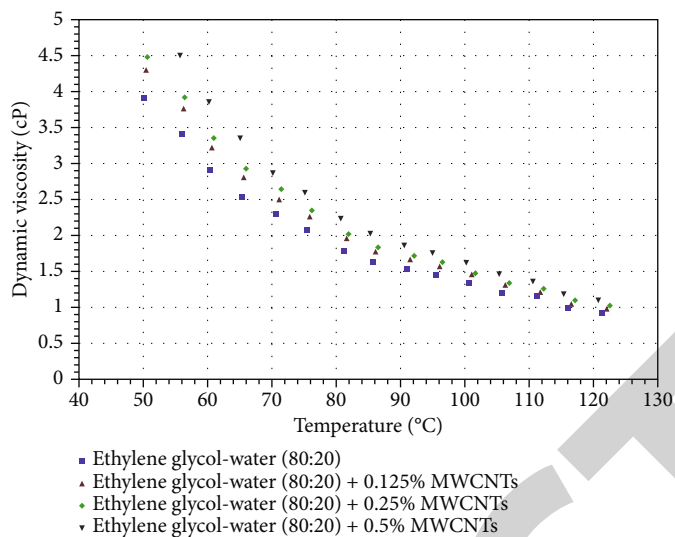
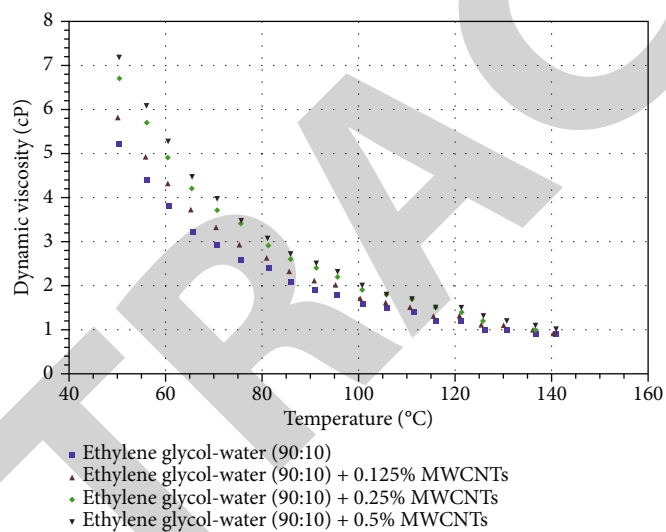


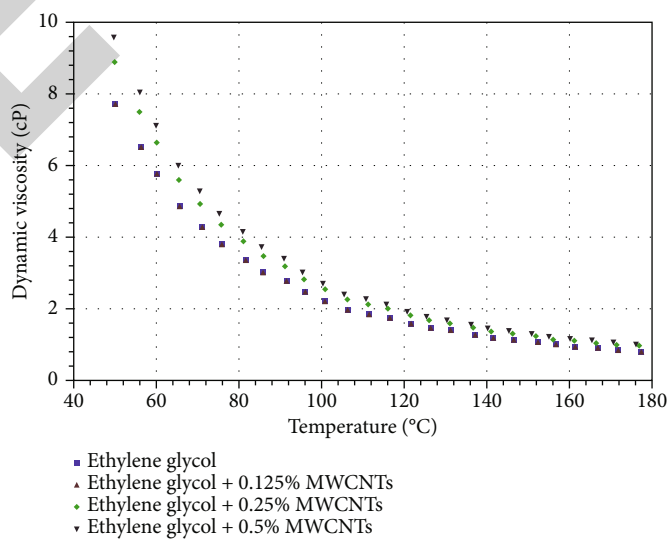
FIGURE 4: Effect of ethylene glycol and water combination concentration on thermal conductivity.



(a)



(b)



(c)

FIGURE 5: Ethylene glycol-water combination concentrations vary with respect to dynamic viscosity with respect to temperature.

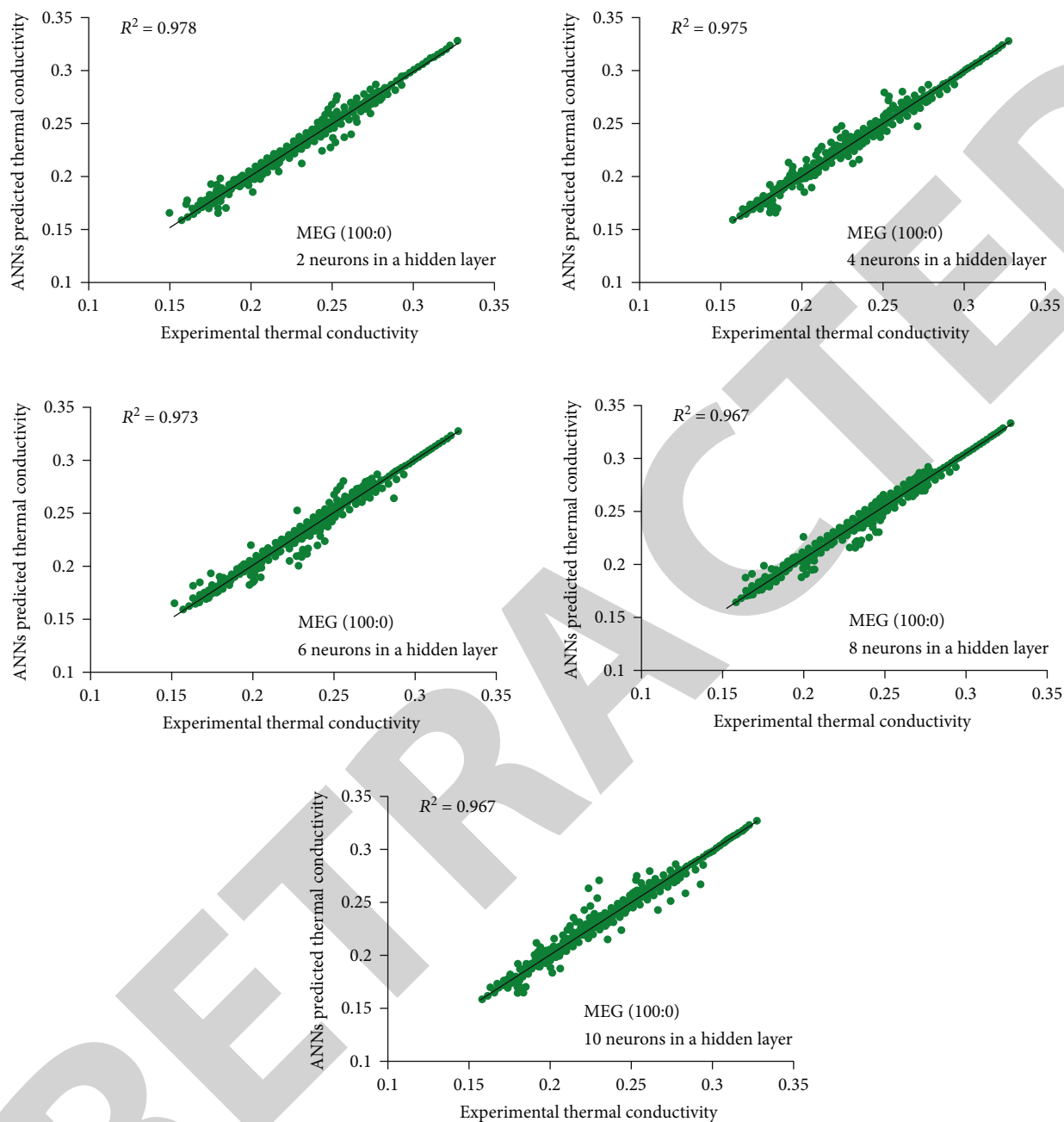


FIGURE 6: Thermal conductivity for monoethylene glycol (100:0)-based fluid validation using a variety of different hidden layer neurons.

sources. Unknown data relationships may be discovered by ANNs via training. It can also deal with nonlinear, complicated, and noisy data sources. It is known for its accuracy and speed. Notably, even with little knowledge, the ANN technique is able to accurately anticipate a dataset's outcome.

A neural network comprises of three layers: an "input layer" of neurons, an "input hidden layer" that handles inputs, and an "output layer" that predicts the model's output. Experts advise increasing the number of hidden layers in neural networks to increase their accuracy. The input layer has input neurons for the ANNs' hidden layer. The

"hidden layer" transmits data generated as from the input layer to the output layer. Synapses are "weighted inputs" that define the output of a neuron when given an input. In an adaptive system, synapses convert a neural network.

The TC of alumina–water nanofluid was predicted using an ANN model and experimental data correlation. Nanofluid TC (25–60°C) is utilised to train ANNs. The experimental findings suggest a relationship between the nanofluid thermal conductivity, volume percentage, and temperature. The correlation predicts the TC of nanofluids. The ANN model also agreed well with the experimental

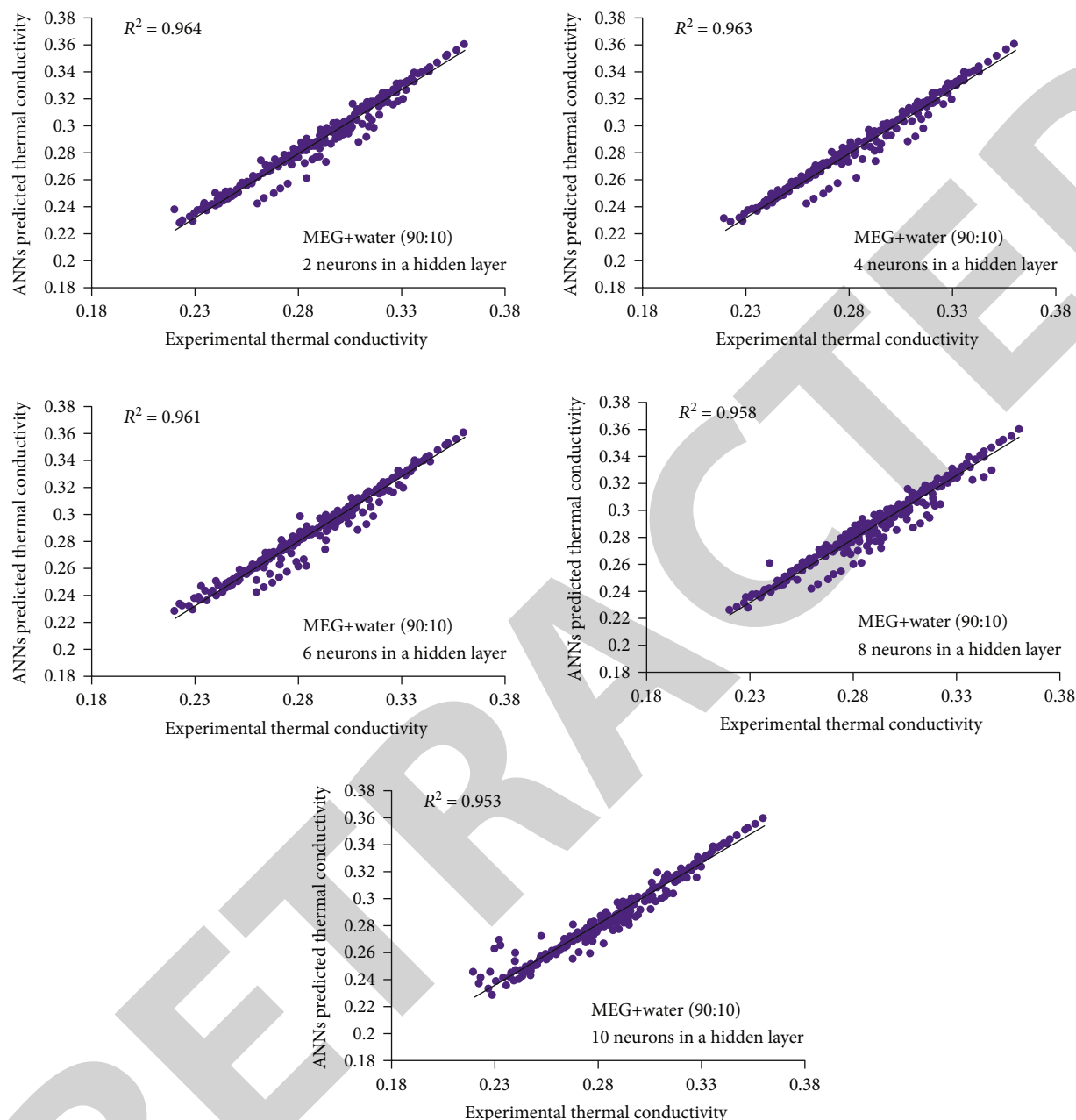


FIGURE 7: Thermal conductivity for monoethylene glycol (90 :10)-based fluid validation using a variety of hidden layer neurons.

findings which were studied by Esfe et al. [20]. To compare empirical and ANN-based models for prediction of experimental TC of MgO-water nanofluid, as used by Afrand and Esfe [21], the seven-neuron network predicted the results best. Last but not the least, ANN predicted the nanofluid TC improvement better than the curve-fit model. Yousefi et al. [22] developed a DNN to mimic nanofluid TC. Adding alumina, titania, and silica nanoparticles to nanofluids predicted relative viscosity. A base liquid comprising propylene glycol, ethylene glycol, and water was utilised. Other models and results were compared [23–25]. The DNN estimated relative viscosities of dispersions match the

published data. In the current study, backpropagation ANNs are used to compute the contribution of error by each neuron after a batch of data is processed. The experiments are performed with pure ethylene glycol-water and ethylene glycol-water (90 :10 and 80 :20) suspended with MWCNTs in 0.125%, 0.25%, and 0.5% weight fractions of MWCNTs. The data from the experimentation is taken and modeled using ANNs. Figure 3 shows the ANN architecture of the proposed model.

An ANN model with three inputs, two outputs, and 10 hidden neurons was constructed. Heat transfer and viscosity are calculated using temperature, MWCNT percentage, and

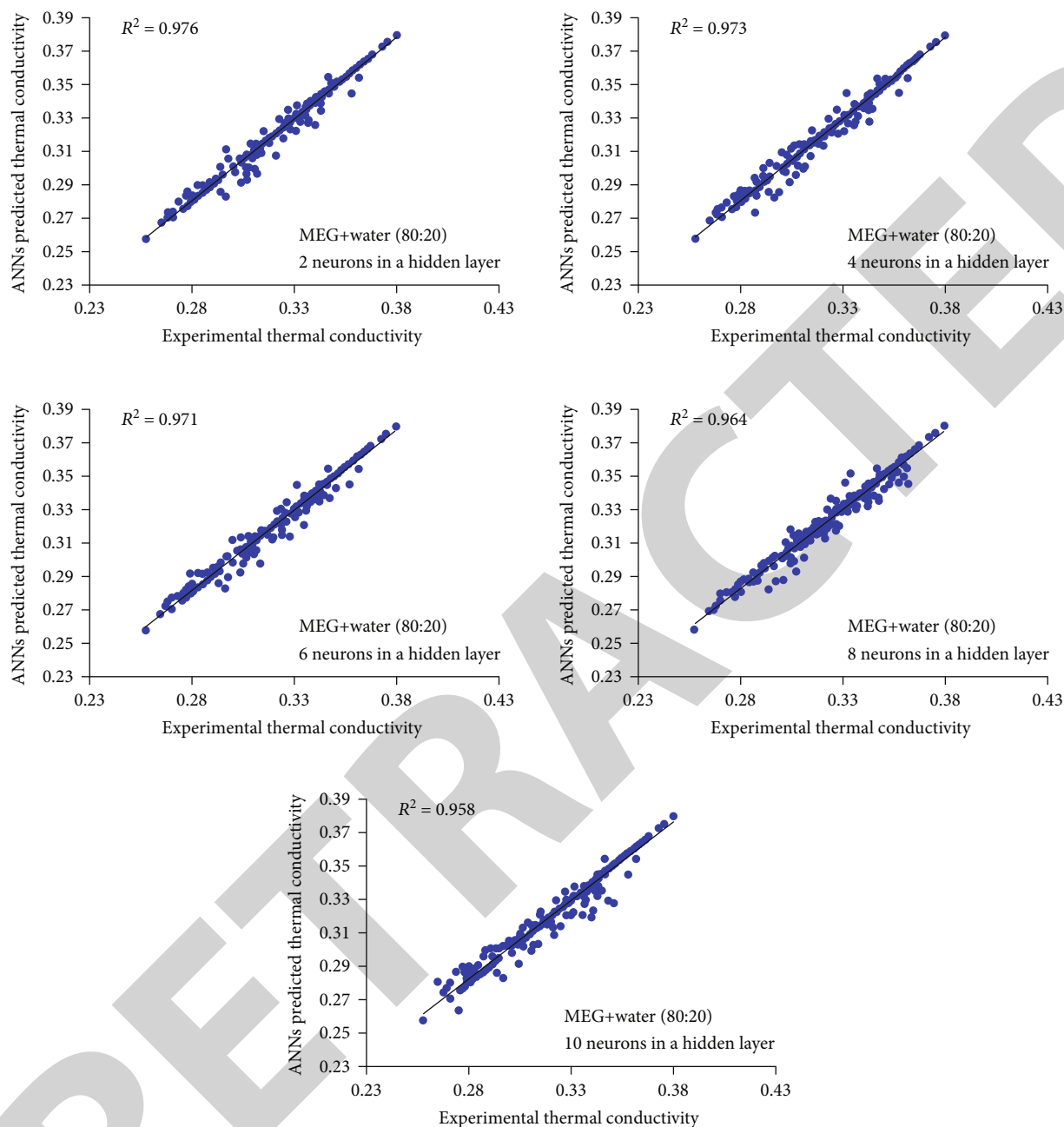


FIGURE 8: Thermal conductivity for monoethylene glycol (80 : 20)-based fluid validation using a variety of different hidden layer neurons.

ethylene glycol volume percent. To train the ANN, all neuron weights were modified for expected and measured outputs. Performance-wise, we selected pure linear and tangent sigmoid activation functions. The parameter R^2 predicts the performance of ANNs. R^2 compares the experimental and anticipated values. It improves evaluation precision. The following equation computes the observed and expected results.

$$R^2 = 1 - \frac{\sum_j (t_j - o_j)^2}{\sum_j (o_j)^2} \quad (1)$$

To determine the best fit model, the hidden layer's number of neurons is changed from 2 to 10. The experimental values are learned using MATLAB using input and output values to forecast the error. The constructed network has input values of ethylene glycol volume %, MWCNT mass fraction, temperature, and output values of TC and viscosity.

6. Results and Discussions

Figure 4 demonstrates that the thermal conductivity of ethylene glycol-water which is solar thermic fluid mixes increases with rising water content and multiwalled carbon

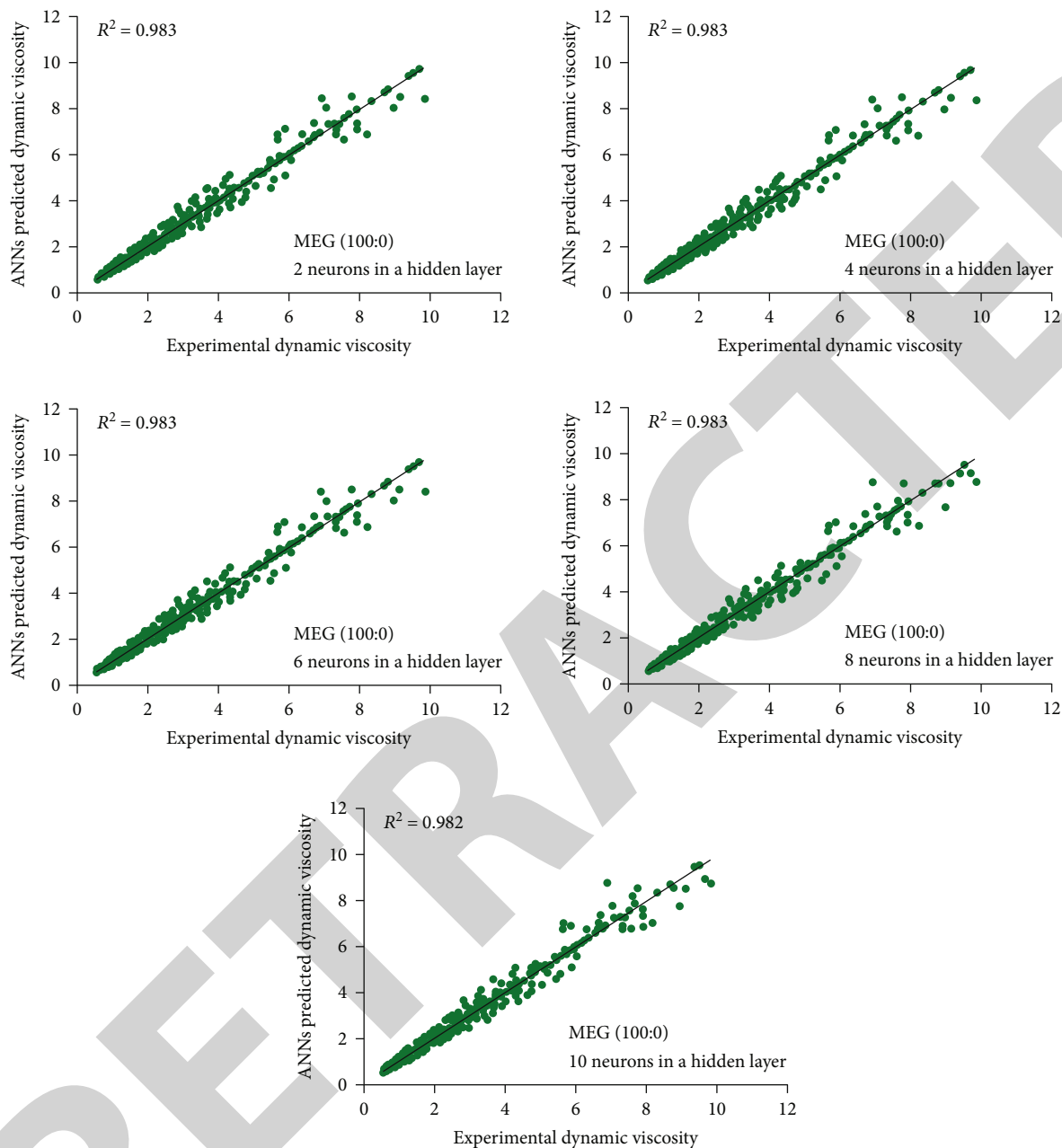


FIGURE 9: Validation of dynamic viscosity data for monoethylene glycol (100:0)-based fluids with varying hidden layer neurons.

nanotube weight fraction as the water content and weight fraction increase. The thermal conductivity of a material decreases as the temperature rises. If you heat ethylene glycol at 10% or 20% concentration, the thermal conductivity increases initially but subsequently decreases as the temperature increases. Using MWCNTs to disperse fluids, we found that they performed effectively for all weight and water percentages that we tested, including 100 percent water.

Figure 5 shows temperature-dependent dynamic viscosity variation of nanofluids. The temperature connection of dynamic viscosity for EG/water is projected. Ethylene glycol with 10% water changes dynamic viscosity from 50 to 150°C, while ethylene glycol alone changes from 50 to 175°C. The

variation in temperature increase is attributed to the reason that water influences the substance's boiling point. Warm fluids decrease viscosity. It is difficult to tell MWCNT dispersion from base fluid. The difference in dynamic viscosity between nanofluids and base fluids at lower temperatures is significant.

Thermal conductivity results of predicted values using ANNs are plotted against experimental values as shown in the graphs from Figures 6–8.

The influence of number of “hidden layer neurons” on the error or the network is shown in the following figures. The optimum number of neurons is found to be 4. Because as number of hidden layer neurons increases beyond 6, the

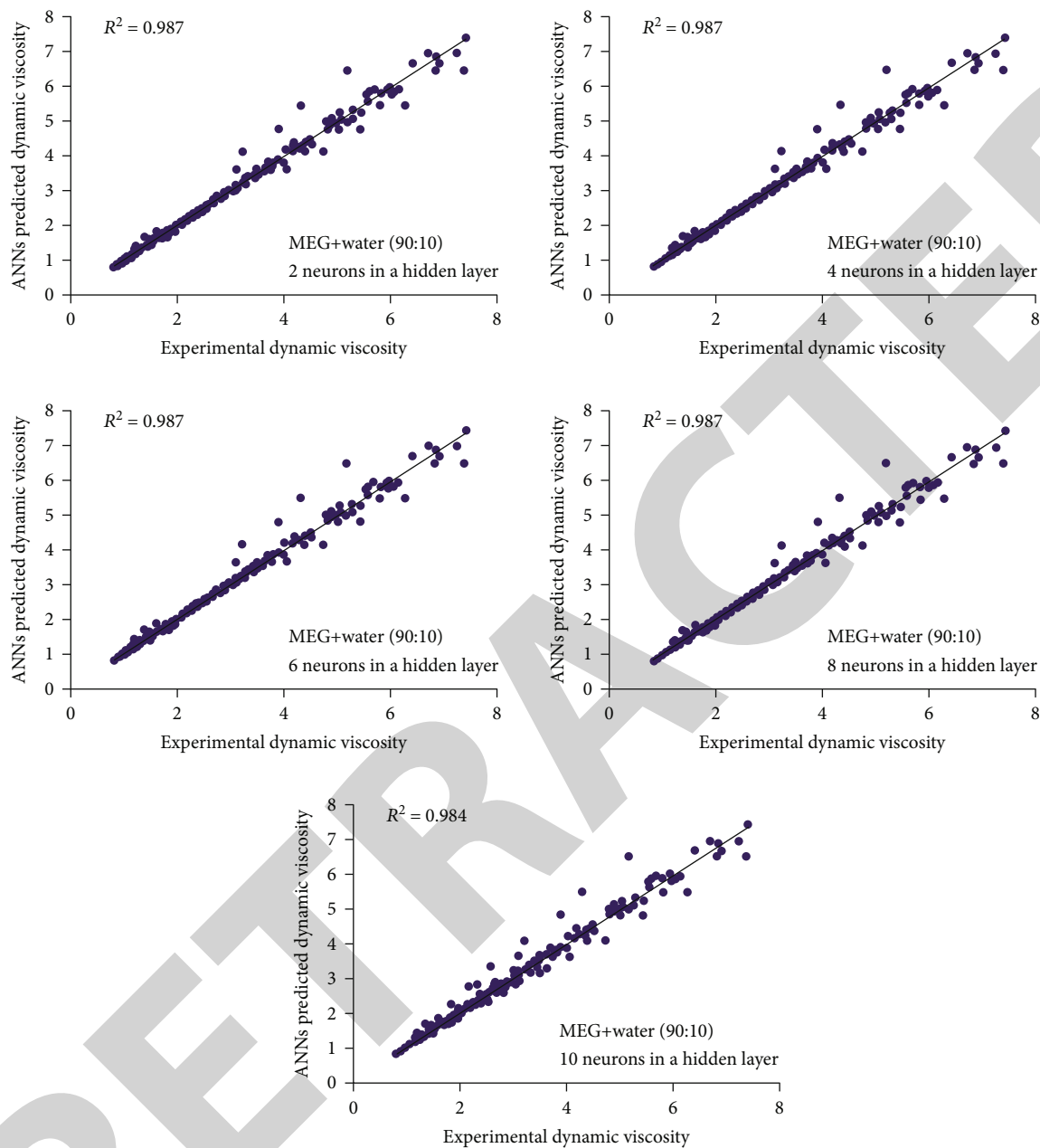


FIGURE 10: Validation of dynamic viscosity data of monoethylene glycol (90 : 10)-based fluid with varying hidden layer neurons.

correlation coefficient decreases somewhat, indicating that prediction noise is strong. Figure 6 shows the thermal conductivity for monoethylene glycol (100:0)-based fluid validation using a variety of different hidden layer neurons. Figure 7 shows the thermal conductivity for monoethylene glycol (90:10)-based fluid validation using a variety of different hidden layer neurons. Figure 8 shows the thermal conductivity for monoethylene glycol (80:20)-based fluid validation using a variety of different hidden layer neurons.

The results of values of dynamic viscosity forecasted using ANNs are plotted against experimental values as shown in the graphs from 9 to 11. The influence of “number of hidden layer neurons” on the error or the network is

shown in the following figures. The effect of number of hidden layers on the error I found to be negligible with the network predicting the values even with minimum number of 2 hidden layer neurons. This suggests the accuracy of experimentation. Figure 9 shows the dynamic viscosity for monoethylene glycol (100:0)-based fluid validation using a variety of different hidden layer neurons.

Figure 10 shows the dynamic viscosity for monoethylene glycol (90:10)-based fluid validation using a variety of different hidden layer neurons.

Figure 11 indicates the dynamic viscosity for monoethylene glycol (80:20)-based fluid validation using a variety of different hidden layer neurons.

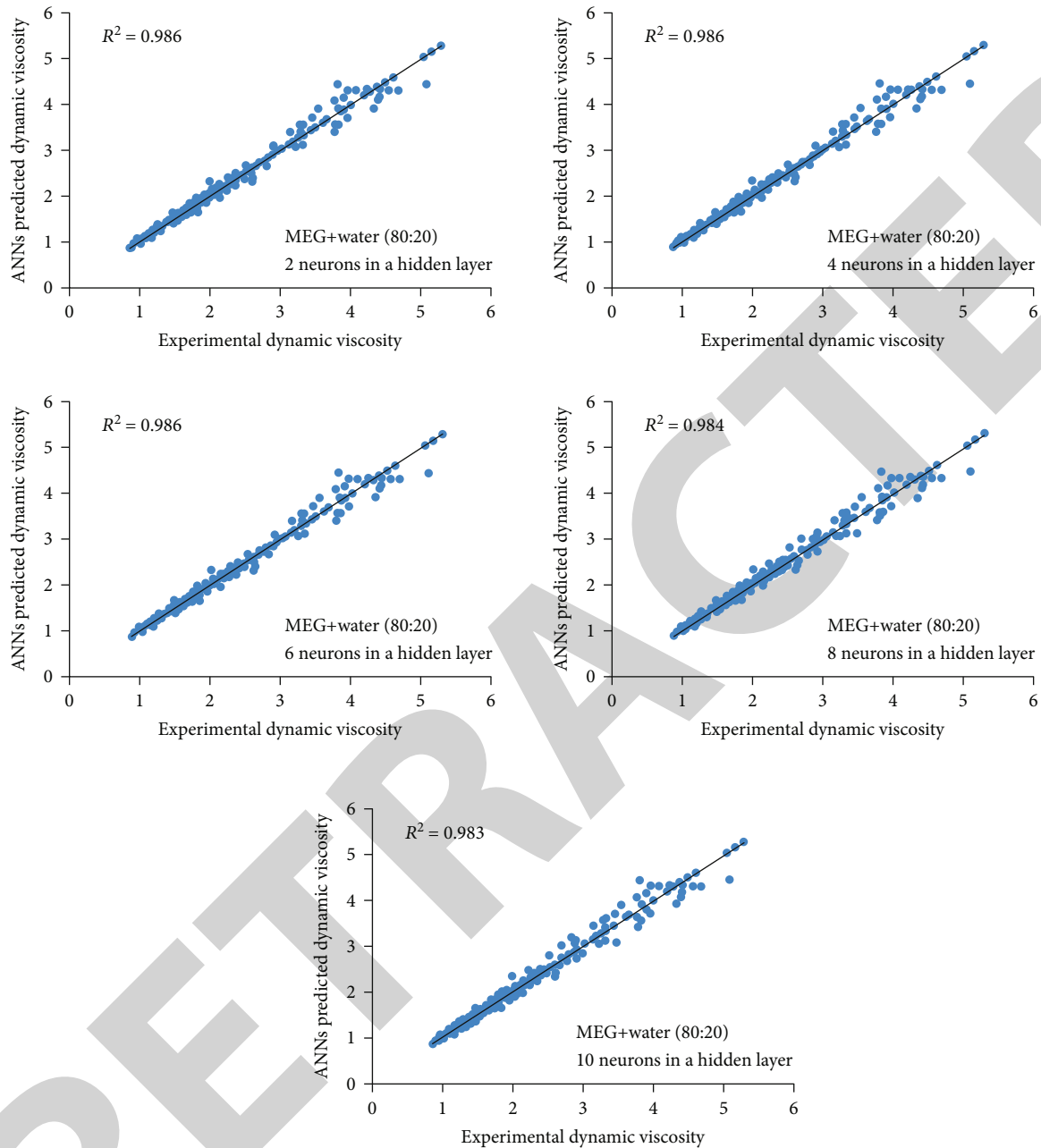


FIGURE 11: Validation of dynamic viscosity data of monoethylene glycol (80:20)-based fluids with varying hidden layer neurons.

7. Conclusions

According to the findings of the research, the following conclusions may be drawn:

- (1) By adding functional groups to a surface of MWCNTs, after a period of time, they become more stable in ethylene glycol-water combinations than pure MWCNTs
- (2) Nanofluid zeta potential study showed that oxidized MWCNTs were more stable in ethylene glycol-water combinations than pure MWCNTs
- (3) Oxidized MWCNT dispersion for all ethylene glycol-to-water ratios, the heat conductivity rose by 10 percent to 20 percent on average
- (4) A greater dynamic viscosity is seen in nanofluids than in base fluids when the temperature range is between 50 and 70 degrees Celsius. At higher temperatures, the viscosity of the base and nanofluids, on the other hand, does not change much. Thermal conductivity and dynamic viscosity may be accurately predicted using artificial neural networks. Best results are observed when predicted using the backpropagation method with 2 or 4 number of hidden layer neurons

Retraction

Retracted: Evaluation of Physicothermal Properties of Silicone Oil Dispersed with Multiwalled Carbon Nanotubes and Data Prediction Using ANN

Journal of Nanomaterials

Received 10 October 2023; Accepted 10 October 2023; Published 11 October 2023

Copyright © 2023 Journal of Nanomaterials. This is an open access article distributed under the Creative Commons Attribution License, which permits unrestricted use, distribution, and reproduction in any medium, provided the original work is properly cited.

This article has been retracted by Hindawi following an investigation undertaken by the publisher [1]. This investigation has uncovered evidence of one or more of the following indicators of systematic manipulation of the publication process:

- (1) Discrepancies in scope
- (2) Discrepancies in the description of the research reported
- (3) Discrepancies between the availability of data and the research described
- (4) Inappropriate citations
- (5) Incoherent, meaningless and/or irrelevant content included in the article
- (6) Peer-review manipulation

The presence of these indicators undermines our confidence in the integrity of the article's content and we cannot, therefore, vouch for its reliability. Please note that this notice is intended solely to alert readers that the content of this article is unreliable. We have not investigated whether authors were aware of or involved in the systematic manipulation of the publication process.

Wiley and Hindawi regrets that the usual quality checks did not identify these issues before publication and have since put additional measures in place to safeguard research integrity.

We wish to credit our own Research Integrity and Research Publishing teams and anonymous and named external researchers and research integrity experts for contributing to this investigation.

The corresponding author, as the representative of all authors, has been given the opportunity to register their agreement or disagreement to this retraction. We have kept a record of any response received.

References

- [1] R. Surakasi, K. C. Sekhar, E. Yanmaz et al., "Evaluation of Physicothermal Properties of Silicone Oil Dispersed with Multiwalled Carbon Nanotubes and Data Prediction Using ANN," *Journal of Nanomaterials*, vol. 2021, Article ID 3444512, 11 pages, 2021.

Research Article

Evaluation of Physicothermal Properties of Silicone Oil Dispersed with Multiwalled Carbon Nanotubes and Data Prediction Using ANN

Raviteja Surakasi ¹, K. Ch. Sekhar ¹, Ekrem Yanmaz ², G. Yuvaraj ³,
Jayaprakash Venugopal ⁴, S. Srujana ⁵ and Naziya Begum ⁶

¹Department of Mechanical, Lendi Institute of Engineering and Technology, Vizianagaram, India

²Department of Electrical and Electronics Engineering, Engineering and Architecture Faculty, Nisantasi University, Istanbul, Turkey

³Department of Mechanical Engineering, Easwari Engineering College, Chennai, India

⁴School of Mechanical, Sathyabama Institute of Science and Technology, Chennai, India

⁵Department of Biotechnology, Center for Post Graduate Studies, Jain University, Bengaluru, India

⁶Department of Chemistry, College of Natural and Computational Sciences, Debre Berhan University, Debre Berhan, Ethiopia

Correspondence should be addressed to Naziya Begum; drnaziyaBegum15@dbu.edu.et

Received 21 November 2021; Revised 5 December 2021; Accepted 6 December 2021; Published 27 December 2021

Academic Editor: Karthikeyan Sathasivam

Copyright © 2021 Raviteja Surakasi et al. This is an open access article distributed under the Creative Commons Attribution License, which permits unrestricted use, distribution, and reproduction in any medium, provided the original work is properly cited.

The researchers wanted to see whether MWCNTs changed the physicothermal properties of solar thermal working fluids. Assessing thermal properties is vital for solar thermal efficiency. Lubricant contains silicone oil resurfaced. It contains 0.25, 0.5, 0.75, and 1.0% multiwalled carbon nanotubes. Before dispersion in thermic fluids, nanomaterials must be properly surface modified. Between 100°C and 300°C, a fluid's thermal conductivity and specific heat physical characteristics like viscosity and density may be inferred from data collected between 50°C and 150°C. Thermal conductivity increases by 15% to 20% when carbon nanotubes are dispersed. The pressure drop is minimal at 0.5 percent weight fraction, demonstrating the suitability of nanofluids in closed loop systems. The characteristics are forecasted using feed-forward backpropagation method and GRNN, and the best of them is selected for prediction. In this research, hidden layer neurons and factors are examined.

1. Introduction

Nanofluid research relies heavily on the study of thermophysical characteristics, which are the primary determinant of heat transmission and flow behaviour. As is the case with typical solid-liquid suspensions that may support particles as small as millimeters or micrometers in size, several studies show that the average density and specific heat of nanofluids can be estimated using energy conservation as well as mass conservation concepts. Due to variances in preparation technique, measurement methodologies, and data analysis methods, there are few agreements on other critical thermophysical parameters of nanofluids (particularly for thermal conductivity and viscosity). Numerous researchers [1–6] examined the progress on nanofluid thermophysical characteristics from various experimental and theoretical studies.

According to their study, adding nanoparticles to base fluid increased thermal conductivity and viscosity to variable degrees, depending on nanoparticle attributes, temperature, and base fluid. Determining the impact of nanoparticle attributes, base liquid types as well as temperature on overall thermophysical properties of nanoparticles was also based on experimental data. However, as the improved transport characteristics of nanofluids may be impacted by various variables, the present studies have difficulties mostly in prediction for nanofluid thermophysical properties by applying the model-based method. As ANNs have significant nonlinear mapping capabilities, they may describe complex mapping connections amongst input components as well as output targets without the need for accurate mathematical modelling. The usage of ANN in thermal research, including such modelling thermophysical properties and

forecasting heat transfer behaviour, has increased in recent years. Unfortunately, despite the fact that some studies revealed that ANNs were an effective technique for predicting the thermal physical properties of nanoparticles, there were considerable differences in the types of ANNs used and the ANN structures determined. The modelling approach and effectiveness of ANN for predicting nanofluid thermophysical parameters will need to be further investigated to better comprehend this issue. Thermophysical characteristics of carbon nanotubes and silicone oil are being studied in the current study.

CNTs are nanometer-sized carbon tubes. CNTs' atomic bonding and aspect ratios are unique. Carbon nanotubes are 100 times stronger than steel. It has two origins. Covalent bonds provide the initial strength. Many uses are possible because of its unique aspect ratio, strength, and heat conductivity. Carbon-based materials absorb the most sunlight. SWCNTs are produced by wrapping graphene around graphite. CNT nanofluid are also used in solar thermal collectors. This is due to a lack of dispersion in basic fluids. It is difficult to separate because of hydrophobicity and strong interparticle interactions. CNTs produce unstable CNT dispersions. Sadly, previous research was narrowed. There is stability of dispersion in solar thermal collectors. Dispersion of CNTs by ultrasonication or surfactants is possible, but unstable. Use it to create solutions that are stable even when left open. Choosing the appropriate base fluid, CNTs, and dispersants is the initial step. So far, several CNT solutions have not been tested at high temperatures. STCs' UV-VIS-NIR stability was tested. The CNTs are characterized using EDX, HRSEM, and TEM techniques at each stage of the preparation process. Figure 1 shows the simple structure of a carbon nanotube.

The structure of silicone oil is shown in Figure 2. Polymerized siloxane with organic side chains is silicon oil. For their stability and lubricating qualities, they are very commercial. Thermic fluid is the primary benefit of silicone oil. Alternating silicon and oxygen atoms (Si-O). Linear polymers and cyclosiloxanes are common.

Silicone oil is a great lubricant since it is nonreactive and very slippery. Silicone oil is often used because of its distinct chemical structure, unique combination of properties, low viscosity temperature change, and lack of corrosiveness. When it comes to lubricants and hydraulic fluids, silicone oils are a go-to choice because of their versatility. To heat baths in labs, they are often employed because of their excellent heat transmission and stability at a range of temperatures. This source also powers oil-filled heaters and diffusion pumps.

DPDM400 High Temperature Silicone Heat Transfer Fluid has a viscosity of 400 cSt at 25°C. High oxidation resistance, dielectric strength, and hydrophobicity characterize DPDM400 High Temperature Silicone Heat Transfer Fluid (insoluble in water). Its high viscosity-to-temperature coefficient allows it to flow easily.

2. Literature Review

According to Agarwal et al. [7], TC of alumina nanofluids produced from various base liquids were synthesised, char-

acterized, and sensitivity tested. The synthesis combustion solution technique was used to produce the specimens at three different temperatures. They discovered that increasing the combustion temperature increases particle size. It took two steps to scatter alumina nanoparticles of 52 nm size, combusted at 10000°C, in water and ethylene glycol. For water- and EG-based nanofluids, the TC increased by 30% and 31%, respectively, from 10 to 700°C and 0 to 2 volume %. The sensitivity analysis shows that TC variation increases with volume %.

Reddy and Rao [8] investigated ethylene glycol-water mixtures at three different concentrations of nanoparticles. It is possible to create nanofluids by dissolving small amounts of nanoparticles using basic liquids such as water, 40:60 ethylene glycol/water, or 50:50 ethylene glycol/water. They discovered that when nanoparticle volume % and temperature rose, the TC climbed from 30°C to 70°C.

Surakasi et al. [9] have done studies using the basic fluids being monoethylene glycol and water. Nanofluids are administered at concentrations ranging from 100:0 to 90:10 to 80:20. They were mixed with purified and oxidized multiwalled carbon nanotubes in 0.125, 0.25, and 0.5 weight percent weight fractions, respectively.

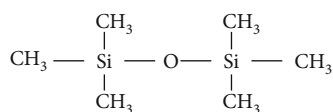
According to Esfe et al. [10], the TC of an alumina-water nanofluid was predicted using an ANN model as well as correlation of experimental data at multiple temperatures and volume percentages. The training data employed in the ANNs is the TC of the nanofluids at several fluid temperatures, extending from 25 to 60°C. Additionally, centred on the experimental data, a correlation for predicting the thermal conductivity of the nanofluid vis-a-vis temperature and volume percentage is suggested. The findings indicate that the suggested correlation could forecast the TC of the nanofluids. Further, the ANN model also showed excellent matching with the findings of the experimentation.

Afrand and Esfe [11] compared empirical-based and ANN-based models for the prediction of experimental of TC of MgO-water nanofluid by using a curve fit model to develop a correlation, and then, the data was forecasted using artificial neural networks (ANNs) with the input variables as volume fraction of MgO and temperature and the output variable as TC. The findings revealed that the network consisting of seven neurons correctly anticipated the outcomes with the least amount of error. Ultimately, a comparison of both models has shown that ANN modelling was more precise than the curve-fit model in forecasting the TC improvement of the nanofluid.

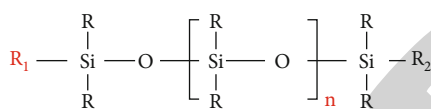
Yousefi et al. [12] established a diffusional neural network structure to model the TC of several nanofluids. They extended the neural network's technique to forecast the relative viscosity of nanofluids suspended with nanosized copper oxide, alumina, titania, and silica. The base liquids selected were propylene glycol-water, ethylene glycol-water, distilled water, and ethanol. The results were compared with other theoretic models as well as experimental values. The projected relative viscosities of dispersions through diffusional neural networks (DNN) are in line with the data found in the literature.



FIGURE 1: Carbon nanotube.



[1] Polydimethylsiloxan



[2] General formula of the silicone oil

FIGURE 2: Structure of silicone oil.

3. Methodology and Experimentation

3.1. Resources. Cheap Tubes Inc. in the United States provided the CVD-produced multiwalled carbon nanotubes used in this research. In the CVD process, manufacturers can combine a metal catalyst (such as iron) with carbon-containing reaction gases (such as hydrogen or carbon monoxide) to form carbon nanotubes on the catalyst inside a high-temperature furnace. The CVD process can be purely catalytic or plasma-supported. MWCNTs have a 20-40 nm diameter, 25-micron length, and 95% purity. Other than that, all of the chemicals I have bought have been of the GR kind. AR grade surfactant was obtained from Sigma-Aldrich India Pvt Ltd. as part of the project. As a hydrocarbon-based thermic, silicone oil is used. Pristine multiwalled carbon nanotubes indicate the presence of impurities like metal particulates and soot entangling CNTs which form agglomerates. The HRSEM image of oxidized CNTs indicates the disentanglement of CNTs due to oxidative treatment with clearly visible open tips. The HRSEM picture of long-length entangled MWCNTs is shown in Figure 3.

3.2. Surface Modification of MWCNTs. A three-step process is implemented (calcination, reflection, and cleaning) for the purification of carbon nanotubes. Pure MWCNTs prefer to

group together when submerged in a liquid. It also causes the MWCNTs to become more entangled, as well as compressing the MWCNTs. To detangle and stabilise MWCNTs in liquid, steric repulsions are created using a surfactant. MWCNTs have a surfactant added to their surface to assist keep them stable in liquid environments. Nonionic surfactant span 80 has a hydrophilic-lipophilic balance of 4.6%. Particle aggregation is inhibited, and surface energy is reduced, modifying ethylene glycol water mixtures with cetrimonium bromide.

To make MWCNTs with changed surfaces, scientists utilise an ultrasonic bath with a surfactant and MWCNTs in it. The MWCNTs get coated as a result of this reaction.

3.3. Preparation of Nanofluids. The 0.125, 0.25, 0.5, and 1 weight percent surface-modified MWCNTs are disseminated in silicone oil mixtures by processing them for approximately 30 minutes in a probe ultrasonicator. The nanoparticle dispersion in liquid coolant up to some proportions is acceptable, since the thermophysical properties could alter with higher proportions. Besides, the issue with nanoparticle stability can be encountered at higher proportions of nanoparticles or nanomaterials that would lead to increased pumping power due to increased viscosity. Hence, the nanoparticle percentage was limited up to 0.5%. Light scattering methods and a zeta sizer are used to assess the stability of thermic fluids distributed with MWCNTs (Horiba SZ 100). A measure of MWCNT dispersion stability in liquid media was measured using the zeta potential.

4. Physicochemical Property Evaluation

4.1. Thermal Conductivity. The major reason for developing nanofluids was to boost a fluid's thermal conductivity by adding nanoparticles to the mixture. Recent decades have seen a great deal of research into the nanofluids thermal conductivity utilising a number of methodologies including the transient hot-wire method as well as the temperature oscillation approach [13]. Nanofluids were shown to

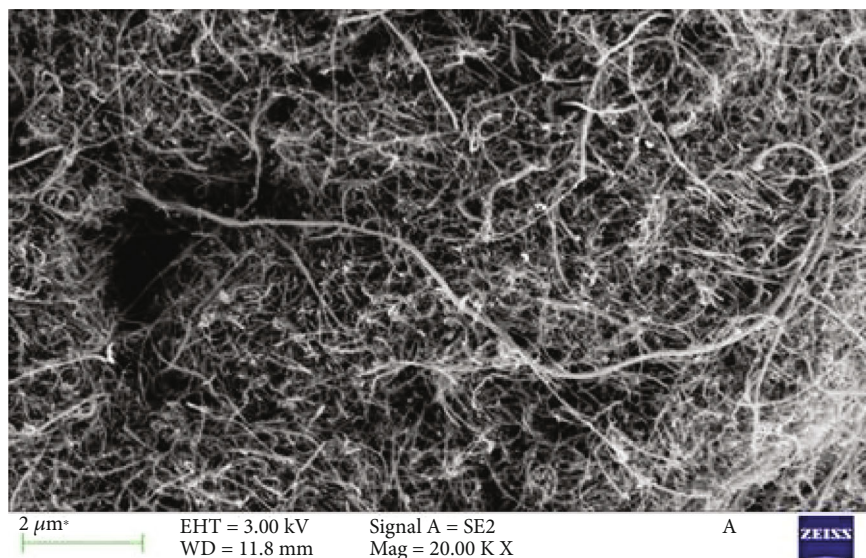


FIGURE 3: HRSEM images of pristine MWCNTs.

improve heat conductivity to variable degrees in most of the studies that were conducted. Nanofluid thermal conductivity may increase due to a variety of macroscopic variables, including decentralised processing techniques, the fundamental characteristics of nanoparticles and base fluids, and temperature. A Hot Disk™ Heat analyzer TPS 500 measures the discs' thermal conductivity. A study is being conducted on the thermal conductivity of fluids containing MWCNTs.

4.2. Dynamic Viscosity. The viscosity of a fluid is a property that indicates its resistance to flow. It is a word that refers to a fluid's internal friction. Viscosity, another critical thermophysical parameter, describes the internal flow resistance of nanofluids. Viscosity affects cranking power as well as heat transfer rate in industrial settings. To better understand the rheological properties of nanofluids, further research on the effect of nanoparticles on base fluid viscosity is needed. Carbon nanotube-containing nanofluid viscosity is being investigated experimentally at various CNT mass percentages and temperatures, as previously reported. The viscosity of liquids and nanofluids is determined using an absolute viscosity viscometer, such as the Wells-Brookfield C&P. A cone and plate viscometer are used to precisely measure torque over a range of rotating speeds. When determining the rotational resistance of a sample fluid, the torque measurement instrument employs a beryllium-copper spring calibrated to the fluid's specific gravity.

4.3. Artificial Neural Networks. Humans have used artificial neural networks (ANN) to solve problems in fields including health, economics, and engineering. Like the human brain, ANNs may learn patterns from input data before predicting output. That is not all it can do. It is an all-round tool to model and simulate scientific data. It may be used for pattern recognition and nonlinear prediction. It is possible to model and forecast nanofluid thermophysical characteristics using a variety of approaches, the most common of which are theoretical model-based, empirical correlation-

based, or data-driven. The ANN's superior modelling, non-linear mapping, and recognition capabilities have drawn substantial attention in the recent years when compared to the other two techniques [14]. ANN was constructed based mainly on feed-forward back propagation algorithm and TRAINLM training function in which the weights of all neurons are tuned for predicted and measured outputs.

ANN models are comprised of feed-forward, recurrent neural networks, "hybrid neural networks," "radial basis function," "multilayer perceptron," "probabilistic neural networks," "generalized regression neural network," and "reformulated neural networks."

As a rule, a neural network consists of three layers: input, hidden, and output. They recommend adding hidden layers to improve accuracy of neural networks. The input neurons feed the buried layer of ANNs. The "hidden layer" moves data from one layer to another. When an input is given, synapses outline the result. Synapses are flexible components that make up a system. The hidden layer's number of neurons is adjusted from 2 to 6. MATLAB learns the experimental values by comparing input and output values. With silicone oil's volume percent, MWCNT mass fraction, temperature taken as input values and TC and viscosity are taken as output values.

4.4. Back Propagation Method. It is also known as backward propagation in supervised learning using gradient descent. This is called "backward error propagation." It is a common way of calculating a network's loss function's slope. Reweighting neural networks based on errors are called backpropagation. Correct weight adjustment reduces errors and increases model consistency. This method produces the error gradient function given the ANN values and the weights of neural networks.

To train a neural network, backpropagation is used to fine tune the weights (iteration). Weight modification minimises error and improves model reliability.

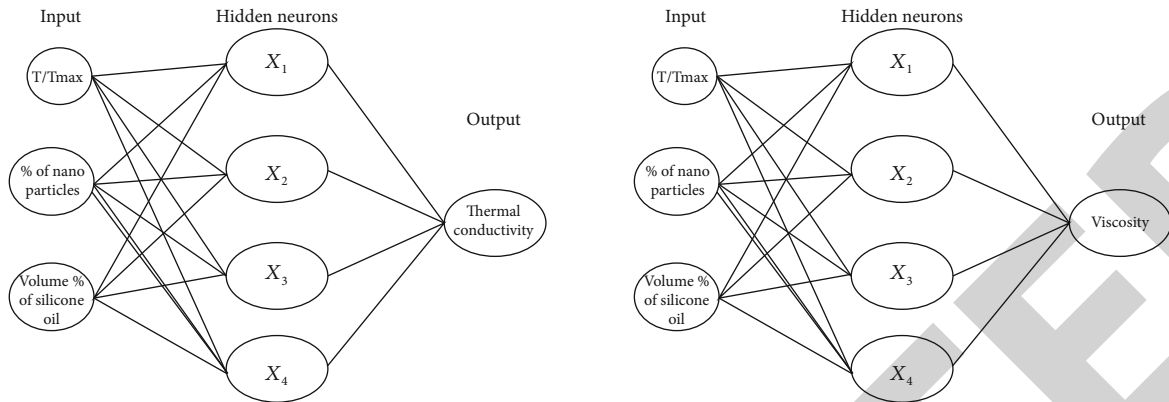


FIGURE 4: Backpropagation method for prediction of thermal conductivity and viscosity.

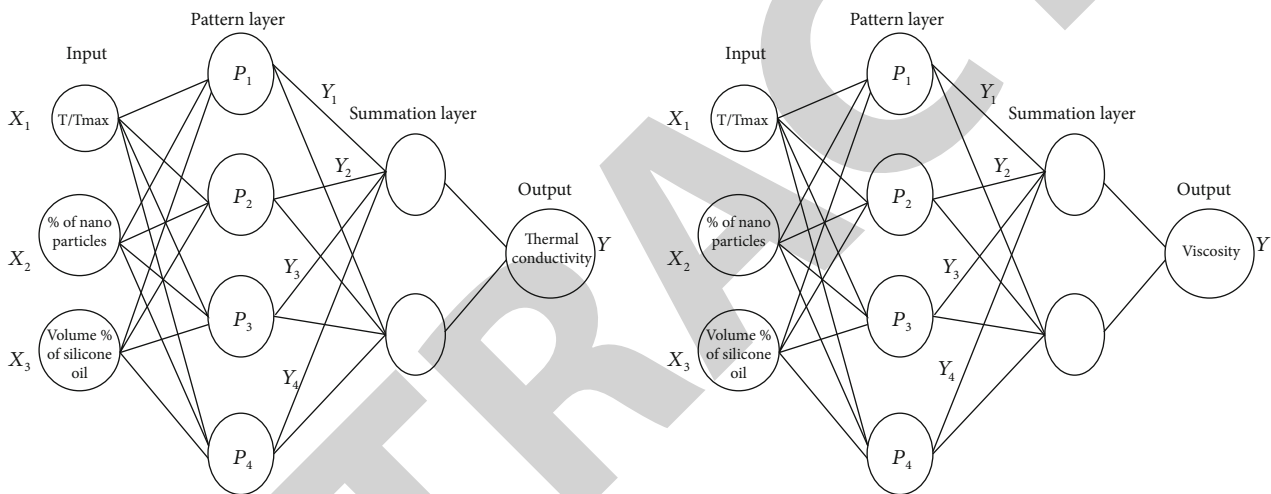


FIGURE 5: Generalized regression neural network function method for prediction of thermal conductivity and viscosity.

4.5. Working of Backpropagation Method. Inputs are sent to the hidden layer. Actual weights W are chosen to model input. Each hidden layer neuron computes output from the input layer to the output layer. Calculate the output prediction error. In case of high error detection, the model uses the hidden layer to return signals from the output to the input layer, reducing the error. Iterate until the required output is achieved with little error.

$$\text{Error } B = \text{actual output} - \text{desired output}. \quad (1)$$

The typically employed activation functions are “Linear,” “Step,” “Sigmoid,” “TanH,” and “rectified linear unit” (ReLU). Figure 4 shows the structure of backpropagation method for prediction of thermal conductivity and viscosity. An ANN model with three inputs, two outputs, and 10 hidden neurons was constructed. Thermal conductivity and viscosity are calculated using temperature, MWCNT percentage, and silicone oil volume percent. To train the ANN, all neuron weights were modified for expected and measured outputs. Performance-wise, we selected pure lin-

ear and tangent sigmoid activation functions. The parameter R^2 predicts the performance of ANNs. R^2 compares the experimental and anticipated values. It improves evaluation precision. It computes the observed and expected results.

4.6. Generalized Regression Neural Network Function. It has 4 layers: input, pattern, summation, and output. GRNN is a variant on radial basis neural networks. The first layer is made up of input vectors. This layer’s outputs are sent to the summation units of the third layer, which have pattern units. The output units are covered by the final layer. Figure 5 depicts the system’s architecture. GRNN uses Parzen’s nonparametric estimator to estimate the probability density function instead of the nonlinear activation function often employed in ANN. Basically, the projected value is a weighted sum of the expected values of training sets that are similar to the input pattern. The only parameter that may be changed is the smoothing factor, which represents the RBF’s width. The function `newgrnn` in Matlab generates GRNN, a parallel distributed radial basis network model. GRNN model performance was impacted by the number

of input vectors and the smooth factor (σ) of the RBF. The GRNN model's input vectors were derived from the main component scores. There were anything from one to ten primary components. RBF's regularisation parameter, the smooth factor, acts as a regularizer. Smoothing the predicted density with a high smoothing parameter causes it to become multivariate Gaussian, with covariance 2, in the limit. The estimated density may take on non-Gaussian forms with a lower value, but there is a risk that wild points will have an excessive impact on the estimate.

5. Discussion and Findings

5.1. Nanofluid Stability. When the zeta potential value is less than 40, it means the system is stable. Higher zeta potential values are found when surface-modified MWCNTs are dispersed in liquid samples. Table 1 displays the outcomes of the experiment.

Thus, poor stability may be inferred from the low zeta potential with pure MWCNTs. Because of this, surface modified MWCNTs have the greatest stability. This is because surfactant exhibits steric repellent forces, which reduce agglomeration rates.

5.2. Thermal Conductivity of Silica Nanofluids. Figure 6 shows that dispersion of nanomaterials improves thermal conductivity. The base fluids, mass fraction, and temperature all play a function in improving thermal conductivity. The thermal conductivity of silicone oil-MWCNT mixes improved more than that of ethylene glycol-water combinations.

5.3. Dynamic Viscosity of Silica Nanofluids. Figure 7 shows the changes in viscosity of several test fluids over time. Viscosity increases considerably as temperature decreases, as shown in the graph below. Higher temperatures, on the other hand, only cause a little rise in viscosity. Since a smaller mass percentage of CNTs is employed in the production of nanofluids, the rise in viscosity is reduced.

6. Prediction of Data Using ANN

6.1. Backpropagation Method. Counting hidden neurons is presently a guessing game. Many studies proposed different ways to distribute ANN hidden neurons. These are pruning techniques. Begin with a modest network (a few neurons); then add hidden neurons. The oversized network is initially pruned to find the smallest size. This study increases the number of hidden layer neurons from 2 to 6. Figure 8 compares ANN-projected dynamic viscosity to experimental values. Here are some graphs showing how many hidden layer neurons affect the error or network. The optimum neuron count is 4. The correlation coefficient falls as the number of hidden layer neurons rises.

The results of values of thermal conductivity forecasted using ANNs are plotted against experimental values as shown in Figure 9. The influence of "number of hidden layer neurons" on the error or the network is shown in the following figures. According to the findings, the hidden layers have no influence on the network's ability to predict values even

TABLE 1: Zeta potential of silicone oil dispersed with MWCNTs.

Sample	Zeta potential (mV)
Silicone oil + 1%pristine MWCNTs	13.8
Silicone oil + 1%surface modified MWCNTs	54.2

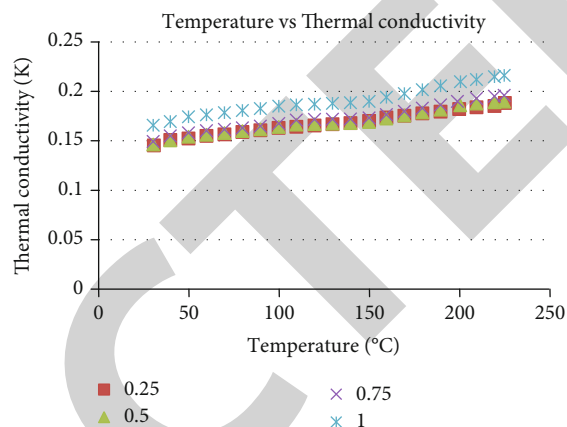


FIGURE 6: Graph indicates the relation between temperature and thermal conductivity at different % of volume fraction.

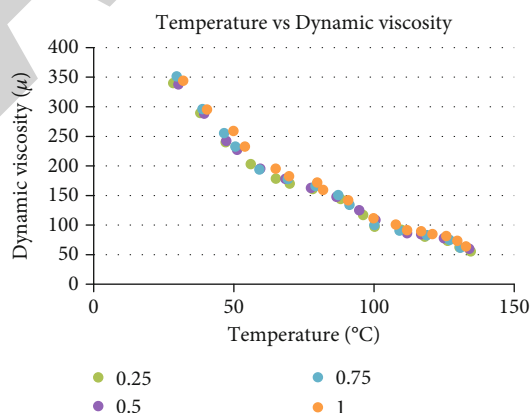


FIGURE 7: Graph indicates the relation between temperature and dynamic viscosity at different % of volume fraction.

when the network has just two hidden layer neurons at the most. This suggests the accuracy of experimentation.

6.2. GRNN Method. Figure 10 compares ANN-projected dynamic viscosity to experimental values. Here are some graphs showing how many hidden layer neurons affect the error or network. The optimum neuron count is 4. The correlation coefficient falls as the number of hidden layer neurons rises.

Figure 11 compares ANN-projected thermal conductivity to experimental values. Here are some graphs showing how many hidden layer neurons affect the error or network. The optimum neuron count is 4. The correlation coefficient falls as the number of hidden layer neurons rises.

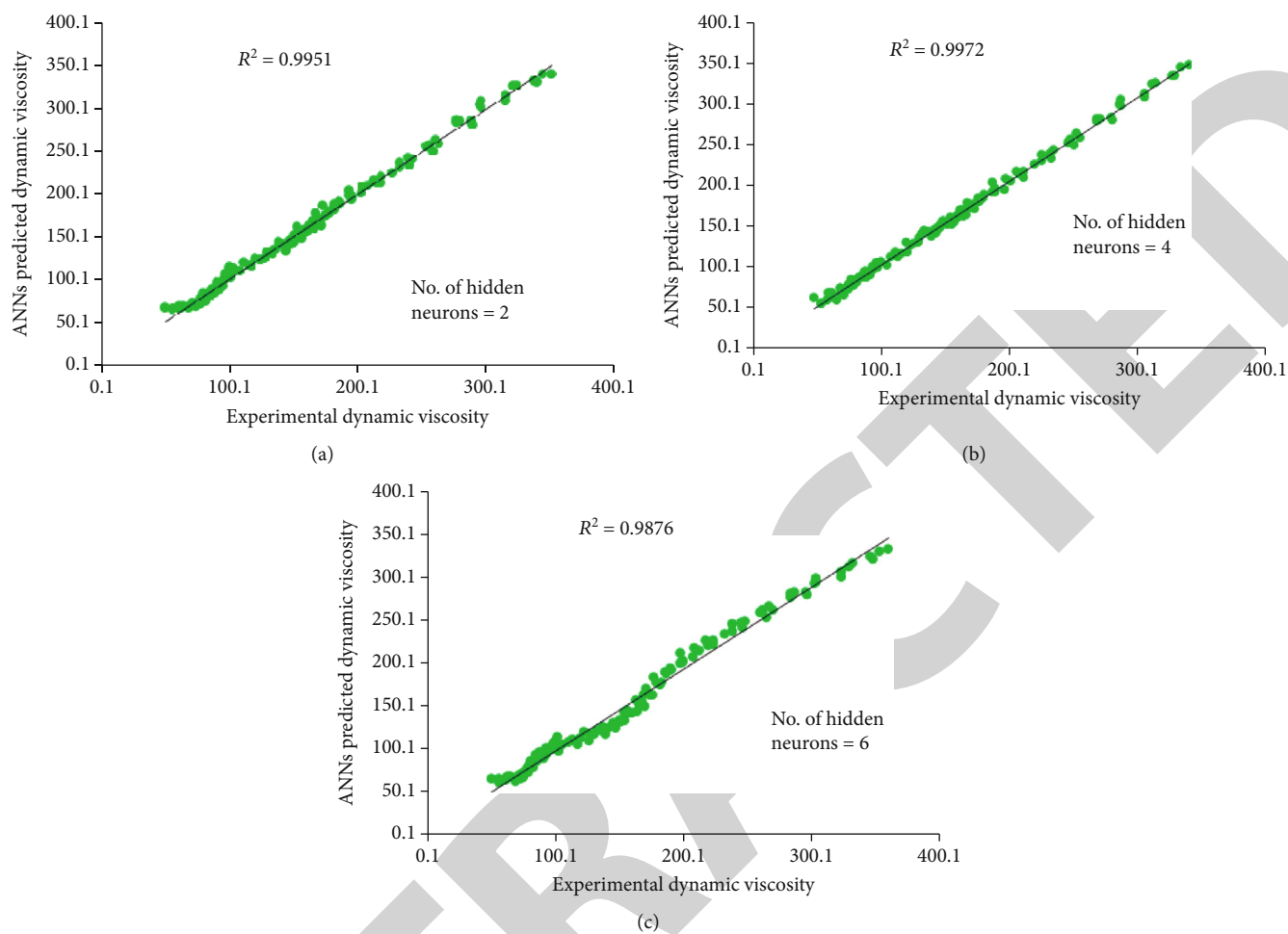


FIGURE 8: Validation of dynamic viscosity data for silicone oil based fluids with varying hidden layer neurons (a) 2 neurons, (b) 4 neurons, and (c) 6 neurons.

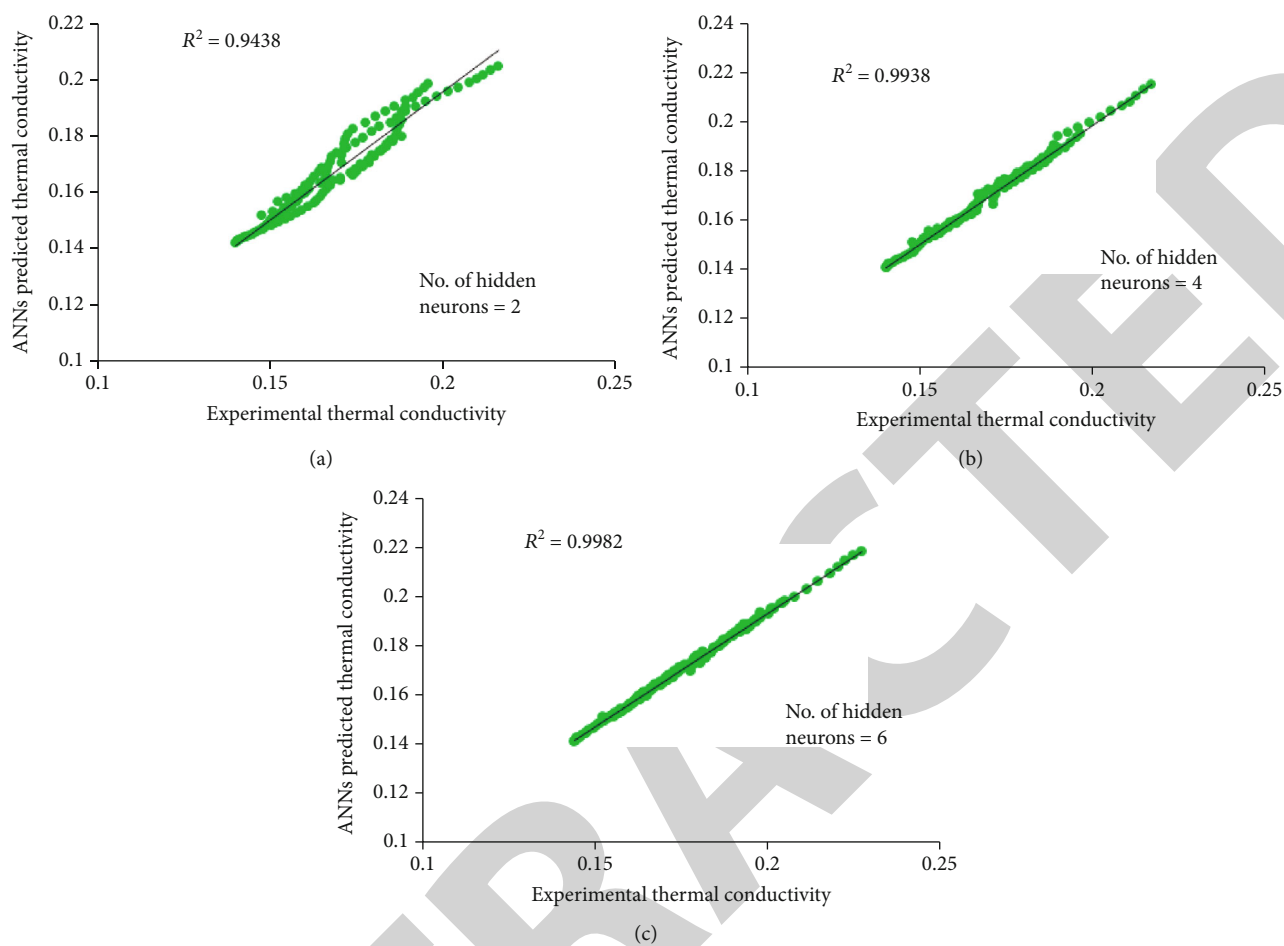


FIGURE 9: Validation of thermal conductivity data for silicone oil based fluids with varying hidden layer neurons (a), 2 neurons, (b) 4 neurons, and (c) 6 neurons.

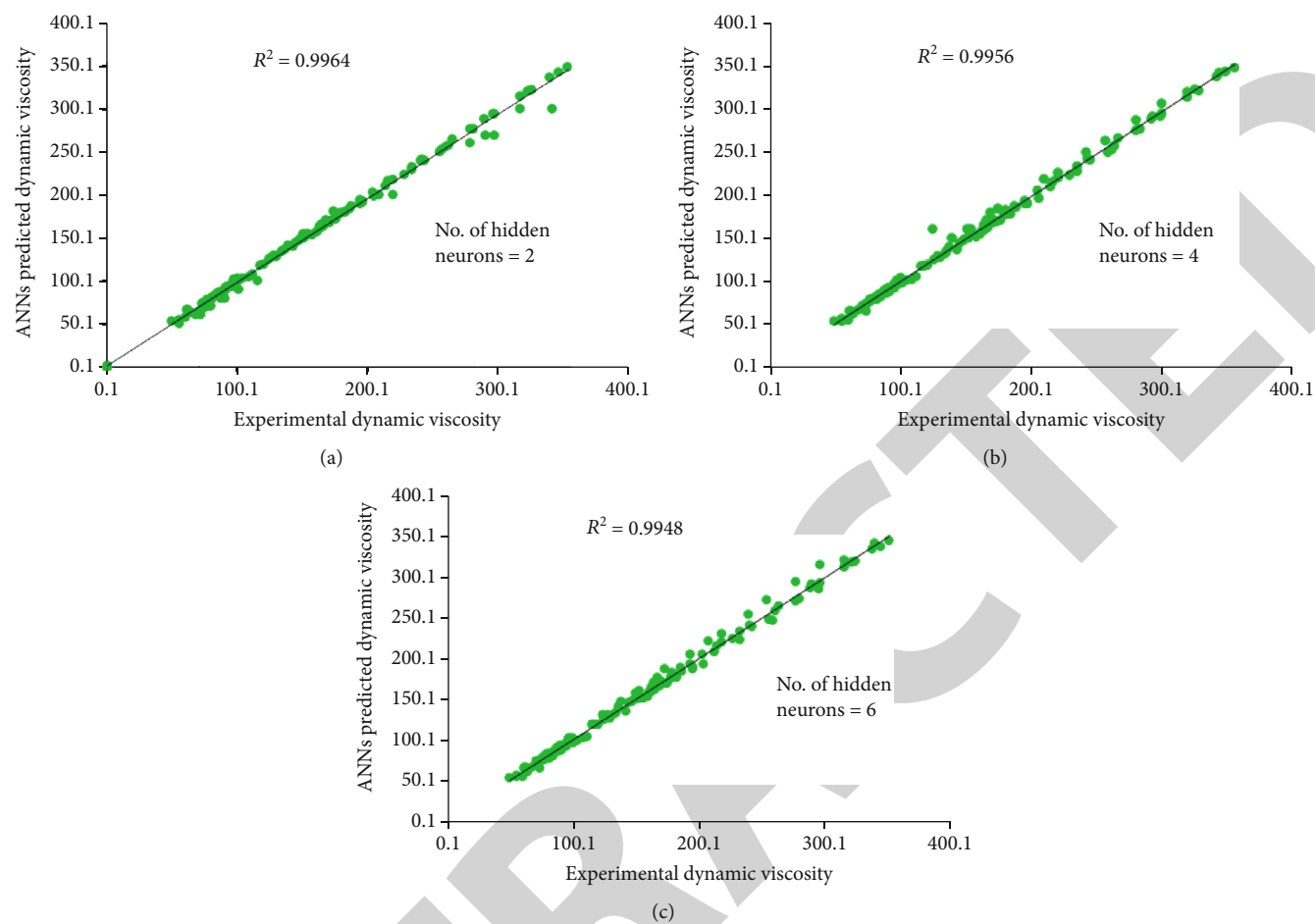


FIGURE 10: Validation of dynamic viscosity data for silicone oil based fluids with varying hidden layer neurons (a), 2 neurons, (b) 4 neurons, and (c) 6 neurons.

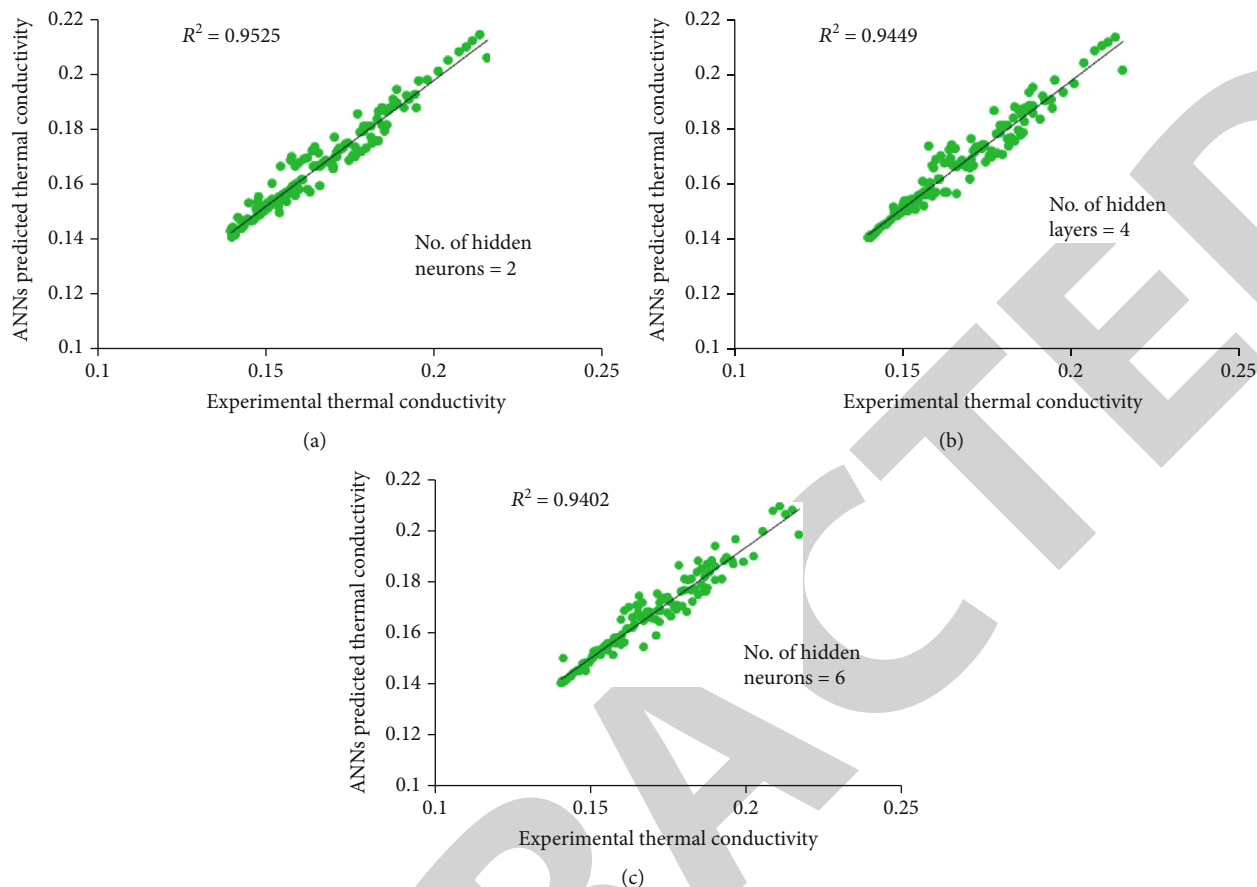


FIGURE 11: Validation of thermal conductivity data for silicone oil based fluids with varying hidden layer neurons (a), 2 neurons, (b) 4 neurons, and (c) 6 neurons.

7. Conclusions

From the results, it can be concluded that the dispersion of MWCNTs in thermic fluids improves the thermal properties. The thermal conductivity increased as the mass fraction increased, and the rise was in the range of 5 percent to 20 percent. There is no variation for viscosity values. The data of thermal conductivity as well as dynamic viscosity can be predicted accurately using artificial neural networks. Prediction of data is done using two methods of ANN that is the backpropagation method and GRNN out of which the value of R^2 for dynamic viscosity is maximum for backpropagation method at number of hidden layers at 4. The value of R^2 for thermal conductivity is maximum for backpropagation method at number of hidden layers is equal to 6. Out of both, the methods for the prediction of the data backpropagation method are found to be the most suitable method compared to other methods, and the back propagation method was given good correlation between experimental and ANN predicted values. The correlation coefficient (R^2) was attained better and improved the accuracy of predictions using back propagation technique. Thus, the back propagation technique was chosen (fixed) for prediction even though other methods were also used. The value of correlation coefficient is found to be declining if the number of hidden layers is increased above 6.

Data Availability

The data used to support the findings of this study are included in the article.

Conflicts of Interest

The authors declare that they have no conflicts of interest regarding the publication of this paper.

References

- [1] Y. Li, J. Zhou, S. Tung, E. Schneider, and S. Xi, "A review on development of nanofluid preparation and characterization," *Powder Technology*, vol. 196, no. 2, pp. 89–101, 2009.
- [2] M. Corcione, "Empirical correlating equations for predicting the effective thermal conductivity and dynamic viscosity of nanofluids," *Energy Conversion and Management*, vol. 52, no. 1, pp. 789–793, 2011.
- [3] I. M. Mahbubul, R. Saidur, and M. A. Amalina, "Latest developments on the viscosity of nanofluids," *International Journal of Heat and Mass Transfer*, vol. 55, no. 4, pp. 874–885, 2012.
- [4] J. Sarkar, P. Ghosh, and A. Adil, "A review on hybrid nanofluids: recent research, development and applications," *Renewable and Sustainable Energy Reviews*, vol. 43, pp. 164–177, 2015.

Retraction

Retracted: Wire Electrical Discharge Machining (WEDM) of Hybrid Composites (Al-Si12/B₄C/Fly Ash)

Journal of Nanomaterials

Received 11 July 2023; Accepted 11 July 2023; Published 12 July 2023

Copyright © 2023 Journal of Nanomaterials. This is an open access article distributed under the Creative Commons Attribution License, which permits unrestricted use, distribution, and reproduction in any medium, provided the original work is properly cited.

This article has been retracted by Hindawi following an investigation undertaken by the publisher [1]. This investigation has uncovered evidence of one or more of the following indicators of systematic manipulation of the publication process:

- (1) Discrepancies in scope
- (2) Discrepancies in the description of the research reported
- (3) Discrepancies between the availability of data and the research described
- (4) Inappropriate citations
- (5) Incoherent, meaningless and/or irrelevant content included in the article
- (6) Peer-review manipulation

The presence of these indicators undermines our confidence in the integrity of the article's content and we cannot, therefore, vouch for its reliability. Please note that this notice is intended solely to alert readers that the content of this article is unreliable. We have not investigated whether authors were aware of or involved in the systematic manipulation of the publication process.

Wiley and Hindawi regrets that the usual quality checks did not identify these issues before publication and have since put additional measures in place to safeguard research integrity.

We wish to credit our own Research Integrity and Research Publishing teams and anonymous and named external researchers and research integrity experts for contributing to this investigation.

The corresponding author, as the representative of all authors, has been given the opportunity to register their agreement or disagreement to this retraction. We have kept a record of any response received.

References

- [1] J. Udaya Prakash, P. Sivaprakasam, I. Garip et al., "Wire Electrical Discharge Machining (WEDM) of Hybrid Composites (Al-Si12/B₄C/Fly Ash)," *Journal of Nanomaterials*, vol. 2021, Article ID 2503673, 10 pages, 2021.

Research Article

Wire Electrical Discharge Machining (WEDM) of Hybrid Composites (Al-Si12/B₄C/Fly Ash)

J. Udaya Prakash ¹, P. Sivaprakasam ², Ilhan Garip,³ S. Jebarose Juliyana,¹ G. Elias ²,
G. Kalusuraman ⁴ and Ilhami Colak³

¹Department of Mechanical Engineering, Vel Tech Rangarajan Dr. Sagunthala R&D Institute of Science and Technology, Chennai, India

²Department of Mechanical Engineering, College of Electrical and Mechanical Engineering, Addis Ababa Science and Technology University, Addis Ababa, Ethiopia

³Department of Electrical and Electronics Engineering, Nisantasi University, Istanbul, Turkey

⁴Department of Agricultural Engineering, Kalasalingam Academy of Research and Education, Krishnankoil, Tamil Nadu, India

Correspondence should be addressed to P. Sivaprakasam; shiva@aastu.edu.et and G. Elias; elias.gmichael@aastu.edu.et

Received 24 October 2021; Revised 21 November 2021; Accepted 24 November 2021; Published 13 December 2021

Academic Editor: Karthikeyan Sathasivam

Copyright © 2021 J. Udaya Prakash et al. This is an open access article distributed under the Creative Commons Attribution License, which permits unrestricted use, distribution, and reproduction in any medium, provided the original work is properly cited.

The present study looks into the effect of WEDM process parameters on the material removal rate (MRR) and surface roughness (SR) responses when machining hybrid composites (Al-Si12/boron carbide/fly ash) using the Taguchi technique. Fly ash and boron carbide (B₄C) particles were used for reinforcement (3%, 6%, and 9% by weight), and aluminium alloy (Al-Si12) was used as a matrix material. ANOVA was used to find out the importance of machining factors that affect the quality features of the WEDM process, as well as the relative role of input parameters in determining the WEDM process' responses. The greatest impact on the response is finalised by the signal-to-noise (S/N) ratio response analysis. However, as a last step, a confirmation experiment with the best combination was carried out to predict and validate the accuracy of the observed values. As the pulse on time and reinforcement increases, MRR also increases. As the gap voltage, wire feed, and pulse off time decrease, it increases. SR is increased by increasing the gap voltage, pulse on time, and pulse off time, wire feed, and reinforcement. The maximum MRR of 38.01 mm³/min and the minimum SR of 3.24 μm were obtained using optimal machining conditions.

1. Introduction

Composite materials are produced by combining two or additional materials in order that they mechanically function as one single entity. A hard phase may be incorporated into a soft phase or vice versa. The hard phase functions as a reinforcing agent in most composite materials, increasing elastic modulus, while the soft phase serves as a matrix. The advantage of using composites is that they can achieve proved to be beneficial and may end up in a variety of service advantages such as enhanced strength, significantly reduced weight, enhanced wear resistance, and high elastic modulus [1]. The foremost benefit of composites is the potential of their mechanical and physical properties to be

aimed at meeting unique design standards. Particulate-reinforced metal matrix composites (MMCs) possess high stiffness but low strength, as well as outstanding fabricability, less cost, and homogeneity. The traditional reinforcement materials for AMCs are SiC and Al₂O₃. Because B₄C powder is more expensive than SiC and Al₂O₃, there have been few studies on boron carbide-reinforced MMCs. There is a growing demand for composites with low-density, low-cost reinforcement particles. Fly ash is a lightweight, lower cost material that is widely available [2]. As a result, fly ash-reinforced composites are liable to break through the price barrier for the widespread use in automobiles. The insertion of fly ash particles increases the hardness, rigidity, impact resistance, and damping qualities of

Al alloys while decreasing their density. Al-fly ash composites offer potential uses in the automobile, turbocharged engine, and electrical industries as cloaks, shells, shafts, coverings, plates, manifolds, valve encompasses, brake discs, and other engine parts.

Metal matrix composites have the potential to outperform traditional metals in terms of efficiency, dependability, and mechanical performance. When compared to continuously reinforced competitors, particle-reinforced MMCs are particularly appealing since they display isotropic characteristics [3]. Particulate-reinforced MMCs have the added benefit of being malleable and workable. The fundamental disadvantage of MMCs is that they have poor mechanical properties and fracture toughness in comparison to their matrix material. Stir casting is the most cost-effective of all MMC industrial uses. It entails mechanically mixing the reinforcing particles into a liquid metal bath and directly moving the mix to a mould [4]. The most important aspect of this technique is achieving adequate wetting between both the particle reinforcements and the molten metal. Because of the contact between flocculated ceramic particles and the solid-liquid interface, it is difficult to achieve homogeneous reinforcement distribution in these cast composite materials. This method may be used to create very big components. A considerable number of engineers and scientists are now researching the synthesis, characterisation, and performance assessment of DRMMCs in universities and research institutes. DRMMCs have found applications in aircraft, automotive, and a variety of other scientific and commercial fields.

Clearly, the liquid metallurgical process is the most economically feasible of all MMC manufacturing techniques. The stir casting process, often known as the vortex technique, is the most basic and widely used technique. In general, ceramic particles with sizes ranging from 5 to 100 μm may be included in a wide spectrum of molten aluminium alloys. Furthermore, this technique enables the fabrication of very massive components. The microstructure and hardness of composites are influenced by the stirring speed and duration. At 600 rpm and 10 minutes of stirring, uniform particle dispersion and higher hardness values were attained [5].

In the aluminium 2024 matrix, larger B_4C particles 71 μm were typically homogenous, but smaller particles (29 μm) caused clumping, segregation, and high porosity. The density of the composites dropped as the volume percentage of the particles increased and the particle size decreased; the porosity and hardness of the composites increased as the content increase and the particle size decreased [6]. The inclusion of B_4C particles significantly enhanced the abrasive wear characteristics of the 2024 aluminium alloy. According to microstructural analysis, the B_4C particles were uniformly dispersed. In the stir casting process, the particle dispersion of B_4C enhanced by the inclusion of 250°C warmed particles, which resulted in a homogeneous grain structure in the composite [7]. Si is crucial in the development of a barrier layer, which can restrict B_4C breakdown and increase B_4C stability in the aluminium melt.

Magnesium plays a critical role in composite fabrication by removing O_2 first from dispersed surfaces, reducing the gaseous layer, and enhancing wetting. The first 1 wt% Mg addition results in a very dramatic drop in surface tension. However, as Mg concentration increases, the reduction becomes extremely minor. Magnesium and aluminium mixtures appear to have a synergistic impact on wetting. The particle dispersion of fly ash is consistent and strong interfacial bonding exists between the matrix and the fly ash particles.

Fly ash is abundant as a waste by-product of coal-fired power plants' combustion processes. It is used in aluminium castings to reduce energy capacity, material content, price, and mass of components, as well as enhance wear resistance. The matrix and fly ash particles have strong interfacial bonding. The hardness rises as the fly ash concentration increases. The composite's mechanical characteristics are improved, but its ductility is decreased when the weight of the fly ash particles increases. The micrographs of the samples indicate that the fly ash particles are distributed uniformly [8].

ANOVA is used to assess the significance of machining factors on MRR and SR. S/N ratio analysis is used to find the optimal machining settings. The effects of machining parameters on SR in WEDM finish cuts and discovered that SR may be reduced by reducing both pulse on time and current. Different methods are used for improving the performance of wire electro-discharge machining by utilising pulse train features. The analysis indicates that the Taguchi technique is better suited to solving the stated problem with fewer experiments than a complete factorial design [9].

Nowadays, MMCs are widely used in industries; their higher hardness and reinforcement make conventional machining challenging, especially when complicated forms and precise components are required. Because it is easier to cut and complex forms, WEDM is the ideal choice for machining composites. The manufacturer's machining parameters database is useful, but it is inadequate. Furthermore, it is traditional machining and does not lead to optimal and cost-effective machine use. As a result, optimizing the WEDM process parameters is unavoidable [10].

Traditional technology used to process tough composite materials produces tool wear [11]. Although in other sophisticated nonconventional machining, the equipment is expensive and the work piece height is limited. The machining parameters sometimes fail to satisfy the criteria and provide suitable guidance to production engineers. As a result, a suitable selection of WEDM process parameters is required.

WEDM provides enormous potential for diversity of application and complicated physical processes in unconventional machining techniques. Intricate and complicated forms can be machined. WEDM removes material via spark erosion all across the wire electrode and work piece. Electromachining can shape and treat electrically conductive materials. Its machining, however, varies from that of typical metallic materials. It is common knowledge that increasing the hardness of the work material during typical machining processes results in a decrease in economic cutting speed [12].

TABLE 1: Aluminium alloy (Al-Si12) chemical composition.

Constituent	Fe	Cu	Si	Mg	Ni	Ti	Zn	Mn	Al
Weight %	0.52	0.013	11.48	0.02	0.01	0.02	0.01	0.01	Remainder

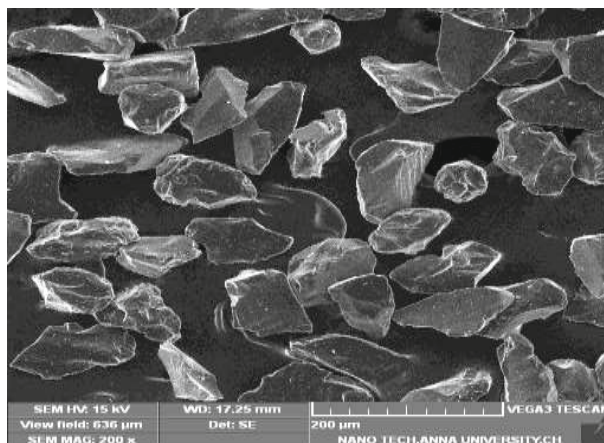


FIGURE 1: SEM image of boron carbide particles.

TABLE 2: Fly ash chemical composition.

Constituent	Si	O	Al	Fe	Ti	Ca	K	LOI
Weight %	26.43	38.88	16.73	3.82	1.42	0.5	0.99	Remainder

Tool materials that are extremely hard and strong to cut materials that is no longer available. Traditional techniques of producing complicated forms in such materials are still more challenging; additionally, it requires greater finish, low tolerance values, larger production rates, complex shapes, and so forth. To address all of these challenges, advanced machining techniques, also known as nontraditional machining processes, have been created. According to the research, using a magnetic field to enhance micro-EDM has a larger MRR than using one without a magnetic field [13, 14]. Adding graphite nanopowder to a dielectric fluid while utilising micro-WEDM can greatly improve the surface finish [15].

The ever-increasing need in the car industry for low weight, fuel efficiency, and comfort has resulted in the development of sophisticated lightweight composite materials with optimal design. The use of aluminium matrix composites in vehicles has the potential to improve fuel efficiency. Abrasion resistance is enhanced by the presence of hard boron carbide in the Al matrix. Similarly, the inclusion of fly ash in an Al matrix might result in a low-weight composite. Lightweight abrasion-resistant composites for wear resistance applications may be created by combining boron carbide with fly ash [16]. Hard boron carbide in the Al alloy matrix limits machinability, and standard tools are ineffective. The motivation for selecting the reinforcing mass fractions and sizes is based on the ease with which the particles may be incorporated into the matrix and castability. One of the potential technologies for efficient machining of hard particle-reinforced metal matrix composites is WEDM. The most popular Al-cast alloy used in the automobile industry is Al-Si12. As a result, an attempt was made to

investigate the possibility of producing Al-Si12-reinforced with fly ash and boron carbide. The scope also includes measuring density, hardness, and WEDM machinability investigations.

2. Materials and Methods

2.1. Aluminium Alloy. Aluminium alloy (Al-Si12) has good corrosion resistance. It has the ability to be cast into thinner and more complex pieces than other form of casting alloy. Table 1 shows the composition of Al-Si12.

2.2. Boron Carbide. Boron carbide (B_4C) particles with a diameter of $63\ \mu\text{m}$ were employed as one of the reinforcing materials in this investigation. B_4C has a number of attractive characteristics, including widespread application as cermets and armour materials. Figure 1: SEM image depicting the shape of boron carbide particles.

2.3. Fly Ash. Another reinforcement material employed in this investigation was fly ash ($12\ \mu\text{m}$) particles. The inclusion of fly ash particles into aluminium alloys lowers their density and enhances their mechanical properties. Fly ash particles are cheap and low-density waste by products of thermal power plants that are available in huge quantities. The low thermal conductance, high electrical resistance, and low density of the material may be advantageous in the creation of lightweight insulating composites. Chemical analysis was used to determine the composition of fly ash. Table 2 shows the chemical composition, and Figure 2 shows the SEM image of fly ash.

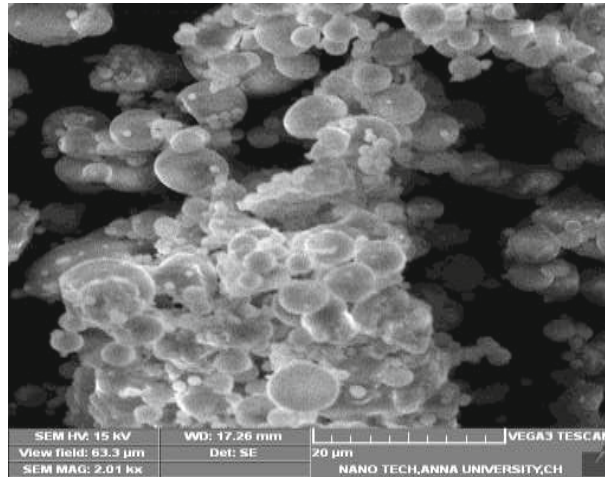


FIGURE 2: SEM image of fly ash particles.

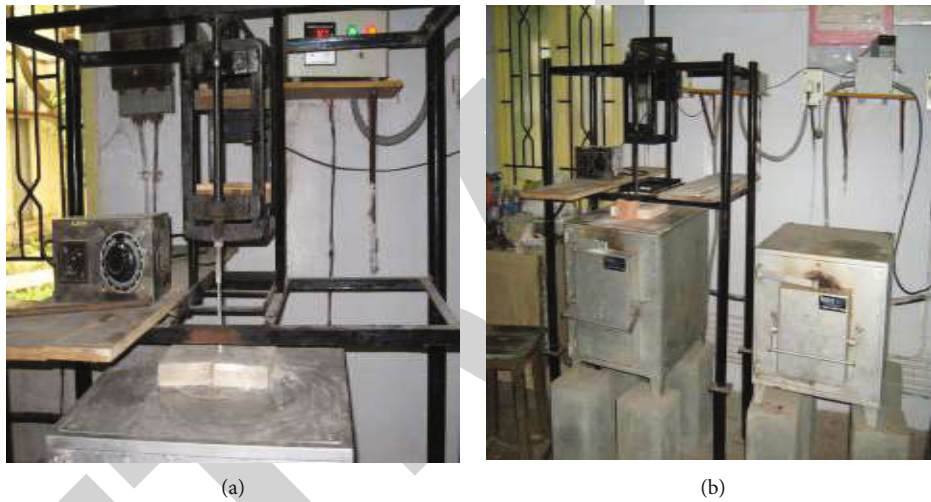


FIGURE 3: (a) Stir casting setup (b) with furnace.



FIGURE 4: Photograph of wire EDM machine.

TABLE 3: WEDM input parameters and their levels.

Level	Input parameters				
	Gap voltage (V)	Pulse on time (μ s)	Pulse off time (μ s)	Wire feed (m/min)	Reinforcement (%)
1	30	2	2	4	3
2	50	6	6	6	6
3	70	10	10	8	9

2.4. Stir Casting. The composites were made using a stir casting process. This is a liquid-state composite production method. Stir casting is the modest and most useful liquid state manufacturing process. Figure 3 shows the stir casting setup for composites.

2.4.1. Fabrication of Hybrid Composites. Al-Si12 (aluminium alloy) ingots were liquefied in an electric furnace using a graphite crucible. The temperature was progressively increased to 850°C. A degasser (hexachloroethane) was used to degass the melt at 800°C. The fluid metal was stirred, and

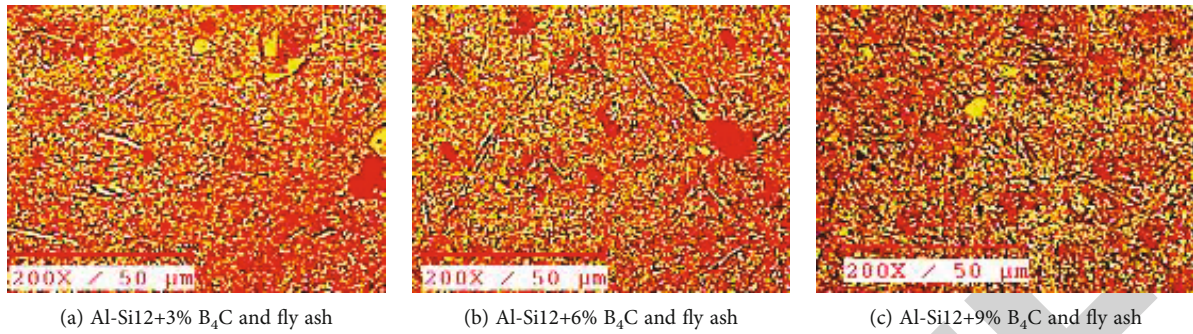


FIGURE 5: (a–c) Micrographs of fabricated composites.

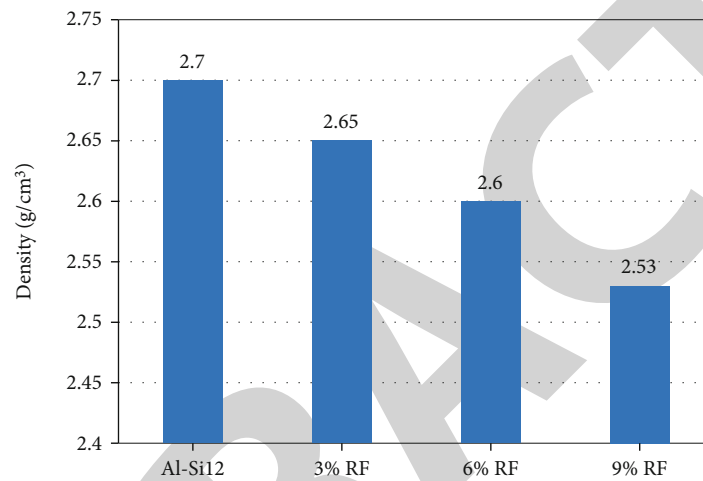


FIGURE 6: Effects of boron carbide and fly ash on composite density.

then, particles of B_4C and fly ash were added at $250^\circ C$. For 10 minutes, the slurry was mixed at 600 rpm [17]. In the molten metal, potassium hexafluorotitanate (1% wt) was introduced. The inclusion of titanium into the Al/ B_4C composite casting results in the formation of a reactive zone on the interfaces, which improves water solubility, interfacial interaction, and the elimination of the oxide deposition on the metal substrate. The tiny quantity of these additions had no discernible effect on the matrix alloys' properties (1 wt. percent). Boron carbide was added in quantities of 1.5, 3, and 4.5 percent by weight, respectively. The fly ash was delivered in weight fractions of 1.5, 3, and 4.5 percent. The liquid metal was poured into cast iron moulds that had been preheated to $650^\circ C$ and then allowed to solidify.

2.5. Working Principle. In wire EDM, a nozzle injects deionized water (dielectric) into the machining area. A pulsed DC supply is used to power the electrodes (wire and work piece). The heat generated by sparking causes the work piece and wire material to melt, and a portion of the material may even vaporise, as in traditional EDM. A positioning system maintains a constant separation between the tool (wire) and the work piece. This method cuts complex curves, especially in materials that are tough to process. This approach provides a high level of precision as well as a good surface finish

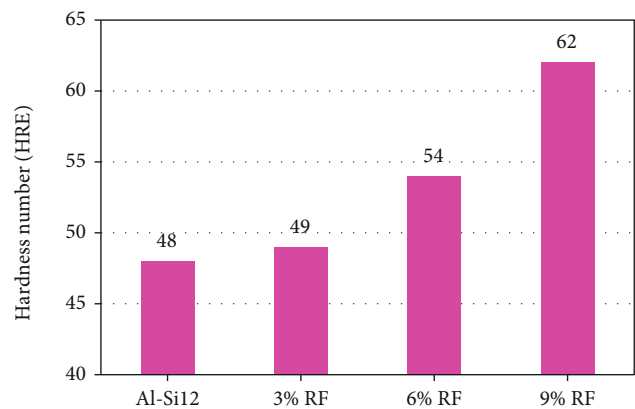


FIGURE 7: Effects of boron carbide and fly ash on composites (HRE).

[18]. The experimental set up used for WEDM of composites shown in Figure 4.

2.6. Design of Experiments. The design of experiments (DoE) method is used to identify factors that influence a product. DoE reduces the number of experimental runs required to collect the necessary data significantly. DoE utilizing the Taguchi method has turned out to be a far more useful tool for practicing engineers and scientists.

TABLE 4: Experimental results of MRR and SR (Al-Si12/B₄C/fly ash).

Ex. no	A Gap voltage (V)	B Pulse on time (μ s)	C Pulse off time (μ s)	D Wire feed (m/min)	E Reinforcement (wt%)	MRR (mm ³ /min)	SR (μ m)	S/N for MRR	S/N for SR
1	30	2	2	4	3	25.514	3.38	28.14	-10.58
2	30	2	6	6	6	21.423	3.06	26.62	-9.71
3	30	2	10	8	9	17.262	3.57	24.74	-11.05
4	30	6	2	6	9	33.112	3.97	30.40	-11.98
5	30	6	6	8	3	26.104	3.3	28.33	-10.37
6	30	6	10	4	6	25.705	3.51	28.20	-10.91
7	30	10	2	8	6	39.086	3.98	31.84	-12.00
8	30	10	6	4	9	31.122	3.74	29.86	-11.46
9	30	10	10	6	3	25.689	3.59	28.19	-11.10
10	50	2	2	4	3	21.058	3.3	26.47	-10.37
11	50	2	6	6	6	16.457	3.43	24.33	-10.71
12	50	2	10	8	9	13.54	4.02	22.63	-12.08
13	50	6	2	6	9	26.772	3.4	28.55	-10.63
14	50	6	6	8	3	20.165	3.66	26.09	-11.27
15	50	6	10	4	6	19.543	3.07	25.82	-9.74
16	50	10	2	8	6	31.742	3.45	30.03	-10.76
17	50	10	6	4	9	22.764	3.57	27.15	-11.05
18	50	10	10	6	3	20.549	3.59	26.26	-11.10
19	70	2	2	4	3	12.321	3.24	21.81	-10.21
20	70	2	6	6	6	9.995	3.86	20.00	-11.73
21	70	2	10	8	9	8.378	4.21	18.46	-12.49
22	70	6	2	6	9	16.365	3.97	24.28	-11.98
23	70	6	6	8	3	12.339	3.4	21.83	-10.63
24	70	6	10	4	6	11.429	3.45	21.16	-10.76
25	70	10	2	8	6	18.475	3.49	25.33	-10.86
26	70	10	6	4	9	14.489	3.65	23.22	-11.25
27	70	10	10	6	3	12.719	3.29	22.09	-10.34

2.6.1. Taguchi Method. The Taguchi method is used in product design and quality improvement. It presents the design engineer with a quick and easy way to determine near-optimal design parameters. To analyze as many variables as possible with a small number of experiments, the Taguchi technique employs OA from the DoE theory. Selecting the most relevant OA and assigning the parameters and their interactions to the proper columns are the first step in designing an experiment. The Taguchi approach maximizes the S/N ratio, a statistical measure of performance that is used to find the best parametric combination. The three most common signal-to-noise ratios are the lower the better, the higher the better, and nominal-the-best. The Taguchi experimental design, which heavily relies on orthogonal arrays, is a powerful method for increasing process/product quality with a small number of trials. The method can improve performance characteristics by determining the appropriate parameter settings and lowering the system's susceptibility to sources of variation. For high productivity and low cost components, manufacturers optimise process parameters. The Taguchi approach is aimed at improving a

specific response characteristic. Table 3 shows the machining input parameters and their levels.

3. Results and Discussion

3.1. Microstructure. Metallographic analyses are an important-to-investigative technique as well as a potent quality control tool. Samples were cut from each composite and finely polished to achieve a mirror-like surface. The fundamental goal of microstructural analysis is to ensure that reinforcement particles are dispersed uniformly throughout the matrix. The optical microscope examines the composite specimens [19]. Figures 5(a)–5(c) show the optical micrographs demonstrating the matrix's homogenous dispersion of reinforcing particles (boron carbide and fly ash).

Figure 5(a) depicts the distribution of the 3 percent hybrid (B₄C and fly ash) composite. The eutectic elements of the Al-Si alloy Al-Si12 are lengthy, acicular, script-like, and unaltered. The micrographs of hybrid metal matrix composites of Al-Si12 alloys with 6% addition of hybrid (B₄C and fly ash) composites are shown in Figure 5(b). In

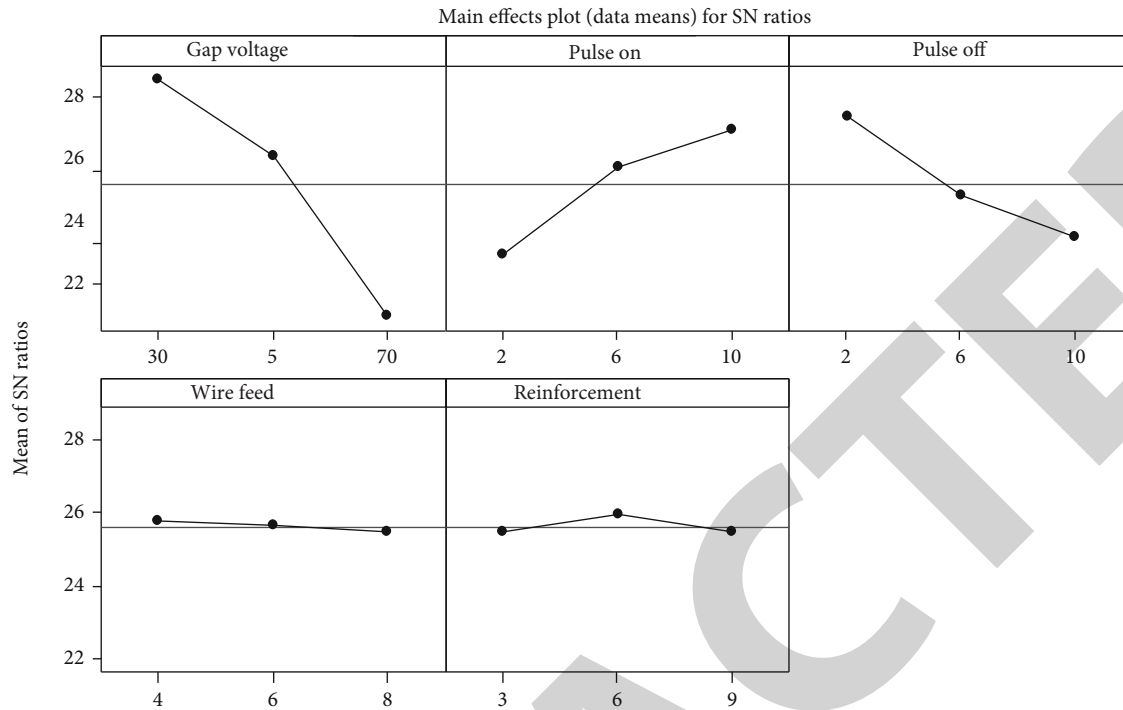


FIGURE 8: MRR (Al-Si12/boron carbide/fly ash) response graphs.

Al-Si12, the Al-Si eutectics are big, script-like, and have sharp angles. On the other hand, composite dispersion is even, and Al-Si is finer. Figure 5(c) depicts micrographs of 9 percent hybrid (B_4C and fly ash) aluminium matrix composites. The distribution of Al-Si12 alloys is uniform. Due to the increased silicon content in Al-Si12 alloys, this distinctive homogeneous distribution tendency is preserved.

3.2. Density. The density is a physical attribute that replicates the properties of composites. It is determined experimentally by utilising displacement techniques [20] and an ASTM D 792-66 test procedure. The standard formula that is used to calculate the density is given in Equation (1).

$$\text{Density} = \frac{\text{Mass}}{\text{Volume}} \quad (1)$$

The mass is determined using an electronic weighing system with a precision of 0.001 grams. The volume of specimens was determined by a graduated cylinder from the displacement of water. Figure 6 shows the effect of reinforcement (RF) on the density of the composites. The densities of all the composites are observed to be lower than the parent metal. It is because the densities of reinforcements are lower than the matrix material.

3.3. Hardness. Resistance to scratching, indentation, distortion, and abrasion are all examples of hardness. The Rockwell test compares the depth of indenter penetration under a huge load to the depth of preload penetration to assess hardness. There are many scales that employ various loads or indenters. The samples were initially polished, and at least five different measurements were taken in each sample at

TABLE 5: MRR (Al-Si12/boron carbide/fly ash) response table.

Level	Gap voltage	Pulse on time	Pulse off time	Wire feed	Reinforcement
1	28.48	23.69	27.43	25.76	25.47
2	26.37	26.07	25.27	25.63	25.93
3	22.02	27.11	24.17	25.48	25.48
Delta	6.46	3.42	3.26	0.28	0.46
Rank	1	2	3	5	4

TABLE 6: MRR (Al-Si12/boron carbide/fly ash) ANOVA.

Source	DOF	Sum of squares	Mean sum of squares	F	Contribution (%)
A	2	195.37	97.69	849.43	64.60%
B	2	55.37	27.69	64.09	18.31%
C	2	49.38	24.69	57.15	16.33%
Error (pooled)	20	2.3	0.115		0.76%
Total	26	302.42			100%

random and averaged to determine the specimen's exact hardness [21]. Figure 7 shows the effect of reinforcement on the hardness of the composites.

The hardness of composites was found to be greater than that of the base alloy. The addition of hard particles (B_4C and fly ash) increases the hardness of composites by increasing their resistance to plastic deformation. When reinforcement particles are added to composites, the surface area of the reinforcement is raised and the grain size of the matrix is reduced. The presence of such strong reinforcing particles

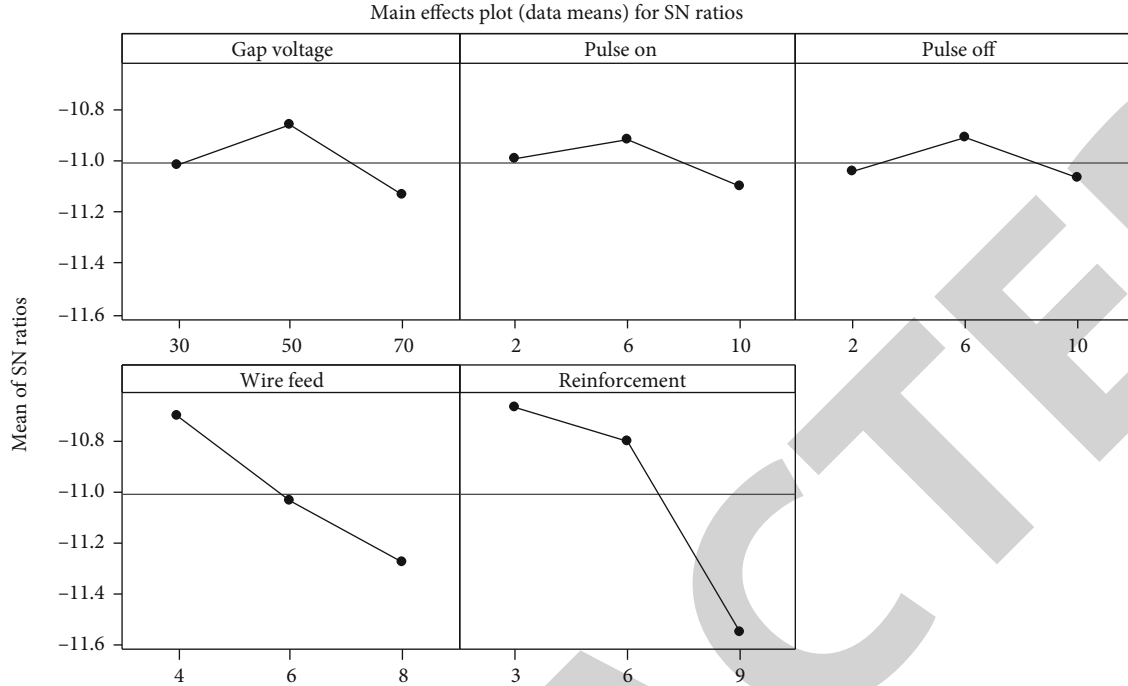


FIGURE 9: Response graphs for SR (Al-Si12/boron carbide/fly ash).

on the surface prevents the material from deforming due to plastic deformation. By raising the weight percentage of reinforcement, the strength of the grain boundaries is enhanced to its extreme level, and the displacement of atoms is reduced, resulting in higher matrix strength and composite hardness.

3.4. WEDM of Hybrid Composites. The experimental results on WEDM of hybrid Al-Si12/B₄C/fly ash AMCs are presented in this section. The MRR and SR were the focus of the analysis [22]. An S/N ratio analysis was utilized to select optimal process parameters.

3.4.1. Experimental Results. The purpose of the WEDM experiments was to test the influence of process factors on output responses. Experimental results for MRR, SR, and S/N ratios are presented in Table 4.

3.4.2. Analysis of MRR. The S/N ratio of each variable at various values was calculated using experimental data. The special effects of S/N data process factors were displayed. Analyzing the response graphs and ANOVA tables yields the most favourable values of process variables in terms of the average performance parameters. The effect of process parameters on MRR was investigated using L₂₇ OA experiments. As seen in Figure 8, MRR increases with increasing reinforcement and pulse on time.

It decreases as the gap voltage, wire feed, and pulse off time increases. The discharge energy rises as the pulse lengthens, resulting in a quicker rate of material removal. The frequency of discharges during a given period increases as the pulse off time decreases, resulting in a greater MRR. The average discharge gap widens as the gap voltage rises,

resulting in a decreased MRR [23, 24]. Wire feed and reinforcement have no major effects on MRR. MRR is, likewise, evidently lowest at the low level of pulse on time and highest at the low level of pulse off time.

3.4.3. Optimal Levels for MRR. Table 5 shows the response table S/N statistics for each factor level. The significance of each element in the response is indicated by the ranks. As shown by the rankings and delta values, gap voltage has the most effect on MRR, followed by other process variables. Figure 8 depicts the maximum MRR in the WEDM process for the level 1 of gap voltage, level 3 of pulse on time, level 1 of pulse off time, and wire feed, and the level 2 of reinforcement. $F_{0.05,2,20} = 3.49$ as can be shown in ANOVA Table 6, gap voltage, pulse on time, and pulse off time are all significant. The error term included the percentage reinforcement, wire feed, and the interactions of gap voltage with other process variables.

3.4.4. MRR-Confirmation Experiments. The optimal parameters are employed in the confirmation experiments as well as in estimating the MRR. The outcomes of the experiments are examined in order to determine the optimal parameters. The factors at level A₁, B₃, C₁, D₁, and E₂ are shown in Figure 8 and response Table 5. The optimal parameters for getting maximum MRR are 30 V gap voltage, 10 μs pulse on time, 2 μs pulse off time, 4 m/min wire feed, and 6% reinforcement. MRR is expected to be 36.12 mm³/min, whereas the experimental measurement is 38.01 mm³/min.

3.4.5. Analysis of SR. Experiments using L₂₇ OA were carried out to examine the influence of process factors on surface roughness. Table 4 displays the experimental results of SR.

TABLE 7: Response table for SR (Al-Si12/boron carbide/fly ash).

Level	Gap voltage	Pulse on time	Pulse off time	Wire feed	Reinforcement
1	-11.02	-10.99	-11.04	-10.70	-10.66
2	-10.86	-10.92	-10.91	-11.03	-10.80
3	-11.14	-11.10	-11.06	-11.28	-11.55
Delta	0.28	0.18	0.15	0.58	0.89
Rank	3	4	5	2	1

TABLE 8: ANOVA for SR (Al-Si12/boron carbide/fly ash).

Source	DOF	Sum of squares	Mean sum of squares	F	Contribution (%)
D	2	1.502	0.751	5.48	11.60%
E	2	4.123	2.062	15.05	31.85%
AB	4	2.682	0.671	4.89	20.72%
AC	4	1.787	0.447	3.26	13.81%
AE	4	1.481	0.370	2.70	11.44%
Error (pooled)	10	1.370	0.137		10.58%
Total	26	12.945			100%

For S/N data, Figure 9 illustrates the SR for all parameters at levels 1, 2, and 3. The SR is increased by increasing the gap voltage, pulse on time, pulse off time, wire feed, and reinforcing. As the pulse lengthens, the discharge energy (DE) increases, and a larger DE produces a larger crater, resulting in higher work piece surface roughness. The frequency of discharges decreases as the pulse off time increases, resulting in an improved surface finish due to stable machining.

3.4.6. Selection of Optimal Levels for SR. The S/N data of each factor at each level is shown in Table 7. The outcomes of the experiments are examined to determine the best parameters. Figure 9 shows that in the WEDM process, the second level of gap voltage, pulse on time, and pulse off time, first level of wire feed, and first level of reinforcement offer the lowest SR [25]. ANOVA was used to investigate the importance of the process factors in relation to SR. $F_{0.05,2,10} = 4.10$ and $F_{0.05,4,10} = 3.48$ are the F values from the table at the 5% significance level. So, according to ANOVA Table 8, wire feed and reinforcement and the interaction of gap voltage with pulse on time are the effective parameters. The error term was made up of the gap voltage, pulse on time, pulse off time, and the interactions of gap voltage with wire feed.

3.4.7. Confirmation Experiments-SR. The optimal parameters are employed in the confirmation tests as well as in estimating the SR. The outcomes of the experiments are examined in order to determine the optimal parameters. The factors at level $A_2, B_2, C_2, D_1,$ and E_1 are shown in Figure 9 and Table 7. The following settings produce the lowest SR: gap voltage of 50 V, pulse on time of 6 μ s, pulse off time of 6 μ s, wire feed of 4 m/min, and reinforcement

of 3%. The predicted SR is 3.15 μ m, while the experimental SR is 3.24 μ m.

4. Conclusions

In this study, the effects of control parameters on material removal rate and surface roughness in WEDM of Al-Si12/B₄C/fly ash composites were investigated, with the following findings:

- (1) The optimal factors and their levels for the maximum MRR and minimal Ra were defined. $A_1, B_3, C_1, D_1,$ and E_2 (gap voltage 30 V, pulse on time: 10 μ s and pulse off time: 2 μ s, wire feed: 4 m/min, and reinforcement percentage 6%) and $A_2, B_2, C_2, D_1,$ and E_1 (gap voltage 50 V, pulse on time: 6 μ s, pulse off time 6 μ s: wire speed: 4 m/min, and reinforcement percentage 3%)
- (2) The most significant parameter on MRR was gap voltage (64.60%), followed by pulse on time (18.31%). The MRR increased as the pulse on time increased
- (3) The reinforcement percentage is the most significant factor in surface roughness, with a contribution of 31.85%, whereas the other machining parameters have no effect. Furthermore, the Ra increased as the wire feed and pulse on time values increased; the lowest Ra values were recorded at a pulse off time of 6 μ s
- (4) The predicted MRR was determined to be 36.12 mm³/min, compared to 38.01 mm³/min in the experimental measurements
- (5) In the WEDM of the Al-Si12/B₄C/fly ash composite in the interval of the specified machining circumstances, the predicted surface roughness is 3.15 μ m, whereas the experimental measurement is 3.24 μ m
- (6) The Taguchi approach could be effectively utilized for optimizing machining parameters in WEDM operations

Data Availability

The data used to support the findings of this study are included within the article.

Conflicts of Interest

The authors declare that they have no conflicts of interest regarding the publication of this paper.

References

- [1] M. K. Surappa, "Aluminium matrix composites: challenges and opportunities," *Sadhana*, vol. 28, Parts 1 & 2, pp. 319–334, 2003.
- [2] M. K. Surappa, "Microstructure evolution during solidification of DRMMCs (discontinuously reinforced metal matrix

Retraction

Retracted: Environmental Emission Analysis of Biodiesel with Al₂O₃ Nanometal Additives as Fuel in a Diesel Engine

Journal of Nanomaterials

Received 11 July 2023; Accepted 11 July 2023; Published 12 July 2023

Copyright © 2023 Journal of Nanomaterials. This is an open access article distributed under the Creative Commons Attribution License, which permits unrestricted use, distribution, and reproduction in any medium, provided the original work is properly cited.

This article has been retracted by Hindawi following an investigation undertaken by the publisher [1]. This investigation has uncovered evidence of one or more of the following indicators of systematic manipulation of the publication process:

- (1) Discrepancies in scope
- (2) Discrepancies in the description of the research reported
- (3) Discrepancies between the availability of data and the research described
- (4) Inappropriate citations
- (5) Incoherent, meaningless and/or irrelevant content included in the article
- (6) Peer-review manipulation

The presence of these indicators undermines our confidence in the integrity of the article's content and we cannot, therefore, vouch for its reliability. Please note that this notice is intended solely to alert readers that the content of this article is unreliable. We have not investigated whether authors were aware of or involved in the systematic manipulation of the publication process.

Wiley and Hindawi regrets that the usual quality checks did not identify these issues before publication and have since put additional measures in place to safeguard research integrity.

We wish to credit our own Research Integrity and Research Publishing teams and anonymous and named external researchers and research integrity experts for contributing to this investigation.

The corresponding author, as the representative of all authors, has been given the opportunity to register their agreement or disagreement to this retraction. We have kept a record of any response received.

References

- [1] M. I. A. M. Alghamdi, I. Colak, M. M. A. Zahra, and T. Bothichandar, "Environmental Emission Analysis of Biodiesel with Al₂O₃ Nanometal Additives as Fuel in a Diesel Engine," *Journal of Nanomaterials*, vol. 2021, Article ID 2544098, 7 pages, 2021.

Research Article

Environmental Emission Analysis of Biodiesel with Al₂O₃ Nanometal Additives as Fuel in a Diesel Engine

Mohammad Ibrahim Al Mishlah Alghamdi,¹ Ilhami Colak,²
Musaddak Maher Abdul Zahra,^{3,4} and T. Bothichandar⁵ 

¹Department of Computer Science, Al Baha University, Al Baha, Saudi Arabia

²Department of Electrical & Electronics, Nisantasi University, Istanbul, Turkey

³Computer Techniques Engineering Department, Al-Mustaqbal University College, Hillah, Iraq

⁴Electrical Engineering Department, College of Engineering, University of Babylon, Hillah, Babil, Iraq

⁵Department of Industrial Engineering, Ambo University, Ambo, Ethiopia

Correspondence should be addressed to T. Bothichandar; bothi.chandar@ambou.edu.et

Received 19 July 2021; Revised 7 August 2021; Accepted 28 September 2021; Published 21 October 2021

Academic Editor: Karthikeyan Sathasivam

Copyright © 2021 Mohammad Ibrahim Al Mishlah Alghamdi et al. This is an open access article distributed under the Creative Commons Attribution License, which permits unrestricted use, distribution, and reproduction in any medium, provided the original work is properly cited.

The exploitation of fossil fuels has fueled the modern world's development since the industrial revolution. Other energy sources, such as wood, charcoal, and animal power, were displaced by these fuels, which were relatively easy to obtain, had low cost of production, and were easily transportable. The possibility of these fossil reserves being depleted in the medium term, combined with an increase in environmental awareness and the reality of environmental degradation, has changed the situation, reactivating the search for alternative fuels. Biofuels such as bioethanol, biomethanol, and biodiesel are among the alternative fuels gaining popularity due to their environmental benefits. This research investigates the behaviour of a diesel engine that runs on biodiesel (a fuel made from new and unrefined algae oil), ethanol (an essential raw nanomaterial that is readily available in India), and nanometal additives.

1. Introduction

Plant products have long been used at the heart of engines; for example, Rudolf Diesel, the inventor of the compression ignition engine or diesel engine, used peanut oil to power his engine [1]. According to one of his creations at the 1900 Paris exhibition, the origins of the use of nonfossil fuels can be traced back more than a century [2]. Throughout these one hundred years, and especially in the second half of the twentieth century, an endless number of investigations and experiences took place, all under the banner of “cooking oil will be the fuel of the future,” a phrase that has gotten a lot of attention in recent years [3]. Nonetheless, due to world-limited conventional fuel reserves, it is necessary to seek viable energy alternatives in the short and medium term to obtain the necessary energy from renewable sources. Biodiesel, a renewable fuel made from vegetable oils derived

from seeds, plants, or oleaginous algae, deserves special attention in this regard because of its properties, which allow it to replace fossil diesel in internal combustion engines without modification [4]. They have properties similar to petroleum-derived diesel fuel and can be mixed in any proportion with conventional diesel. Due to the ability to combine several phases of its production, in this case, the obtaining phase, and the possibility of self-sufficiency in the essential input for obtaining it, oil, this fuel, which can be applied to any sector, can be very feasible, particularly for the agricultural sector. Low-cost alternatives include seed, oil extraction, and biofuel processing [5]. The addition of ethanol and nanoparticles to biodiesel blends is primarily to improve fuel combustion in the cylinder. The complete combustion of the fuel in the cylinder generates a large amount of combustion pressure on the piston's head. Furthermore, biodiesel is an oxygenated fuel with ethanol

additives [6]. It produces more heat energy and aids in complete combustion. With the addition of additives and nanoparticles, the heat release rate of biodiesel fuel increases. Many scientists and researchers have reported the engine's combustion characteristics when using biodiesel blends with additives and nanoparticles [7]. Researchers have investigated cerium oxide 30 ppm in a neat biodiesel blend and investigated a 5 to 6% increase in brake thermal efficiency, a 3% decrease in BSFC, and a 1% increase in BP. Researchers have used 50 ppm graphene nanoparticles as an additive in Honge oil methyl ester. It was found that the graphene-based additive biodiesel fuel improved brake thermal efficiency, reduced BSFC, and improved brake power compared to conventional biodiesel without additives [8]. Adding ethanol, DEE, methanol, and n-butanol to biodiesel reduces the fuel's overall calorific value, lowers engine performance, and increases fuel consumption. As a result, adding nanoparticles to the blends is the most innovative way to improve the blends' properties, thereby improving performance and lowering fuel consumption. Only a few researchers have experimented with nanoparticles containing ethanol as an additive. The high thermal conductivity of graphene improves fuel properties, combustion, and engine performance. There is very little information available about graphene nanoparticles as a biodiesel additive [9]. Cooler combustion, cleaner lubricating oil, lower octane requirements, and lower emissions are all advantages of having a clean combustion chamber. Minor fuel droplets vaporize entirely, leaving no unburned residue. As a result, there is complete combustion, which increases power and mileage. Many experimental studies using a wide range of metal additives to improve fuel properties and engine performance and reduce emissions have been reported. Many experimental studies have been published that use various metal additives to improve fuel properties and engine performance while also lowering emissions [10]. Experiments have shown that bimetallic platinum and cerium diesel fuel-borne catalysts reduce engine emissions and improve the performance of the diesel particulate filter and that particulate matter emissions decrease while NO_x emissions increase as oxygenate content in the fuels increases. Because of their large surface area per unit volume, CeO₂ nanoparticles may have high catalytic activity, resulting in increased fuel efficiency and lower pollution emissions. ZnO powder has a wide range of applications. With this background in mind, the current research project focuses on biodiesel's performance, emissions, and physicochemical properties with the addition of a pure Al₂O₃ nanopowder additive for the fuel using an ultrasonic shaking process [11]. Based on the literature review findings, it is concluded that using diesel-biodiesel with Al₂O₃ metal oxide nanoparticles as additives to improve performance and reduce exhaust emissions is a viable solution.

2. Characteristics of Biodiesel Used as Fuel

Biodiesel is a diesel engine fuel that is made from renewable raw materials such as vegetable oils [3]. When a vegetable oil or animal fat undergoes a transesterification reaction, this is what happens. Reacting with alcohol (methanol or ethanol)

TABLE 1: Results of the tests carried out on biodiesel and nanometal fuel.

Properties	B20	B20 + Al ₂ O ₃
Viscosity 40°C (cSt)	12.1	12.3
Flash point (°C)	190	210
Flash point (°C)	134	143
Density (g/cm ³)	0.905	0.925
Viscosity index	229	234

in the presence of a catalyst produces biodiesel and glycerol (NaOH or KOH). During transesterification, the catalyst and the alcohol combine to form a very strong polar chemical compound that breaks down the triglycerides in glycerin (glycerol) and forms ester chains with alcohol (biodiesel). Unsold and unrefined algae oil extracted from seeds using an endless screw machine were the raw materials used to make biodiesel in this case [12]. The oil was sieved and allowed to settle for 24 hours to remove impurities and suspended solids before drawing clean oil from the container's top. Due to cost concerns, it was decided to use ethanol, which, despite being rarely recommended, is used in most of the literature reviews [13]. According to some reports, the water content allows for a 96% transesterification reaction with ethanol. When ethanol is used, potassium hydroxide is the most commonly recommended catalyst for initiating and speeding up transesterification [14]. The biodiesel characterization tests were carried out in the Fuels and Lubricants Laboratory of the Division Center, where this type of test is usually carried out. Table 1 summarises the findings of the research. It should be noted that algae oil has a viscosity of 35 cSt, which has been reduced to some extent but not completely. The flashpoint value was higher than average in about 40% of the cases. The rest of the variables investigated are within the biodiesel standard's range [15].

3. Engine Test Setup

The experimental setup consists of a 4-stroke, single-cylinder engine with a variable loading dynamometer. The setup includes the equipment required to measure the crank angle, combustion pressure, airflow, temperature, and load and fuel flow. All of these devices are linked to your computer. The configuration consists of an individual panel box comprising a fuel tank, an airbox, a manometer, fuel, an airflow measurement transmitter, a fuel-measuring unit, an engine indicator, and a process indicator. Rotational speeds are provided to measure the cooling water flow rate, and a rotameter is provided to measure the calorimeter water flow rate. Engine emissions are measured by the type 5 gas analyzer AVL DITEST Gas 1000 BL. An analysis of engine combustion, performance, and emission characteristics is possible through the experimental arrangement. The engine display includes instant pressure measurement, TDC position recording, and CA at the same instant. These measurements are necessary for engine combustion analysis and the calculation of the work indicated. The apparent

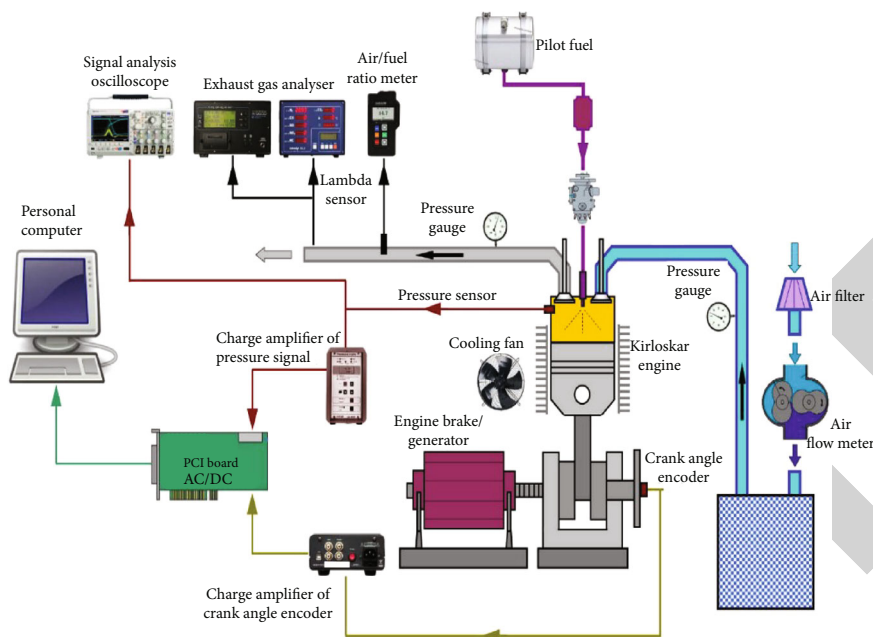


FIGURE 1: Block diagram of the experimental installation.

HRR and the burning process's extent are the most significantly useful quantities accessible from the engine combustion analysis's recorded engine data. In optical systems, HR research is complex. Its use as an analytical tool covers a wide range of objectives, including the advancement of modern combustion engines; the investigation of optional fuel combustion; statistical simulation substantiation; and the study of engine geometry, isolation, and modern injection techniques. The explanation of an advanced engine with a measurement system is given here, considering the importance of representing measurements for engine development and research. The investigator must monitor and obtain the most valuable outputs from recorded data to carry out proper experimentation. For mechanical engineers, observing burned-gas pressure is important as the engine starts; the Watt indicator has been installed. While the IC engine becomes the main extensive heat machine, pressure value measurement and old-time measurement are required for its investigations and enhancement and carried out using different indicator mechanisms. Piezoelectric crystals were designed as a pressure-sensing element for phenomena occurring in the engine. At the end of the 1960s, complex analog instruments capable of performing signal processing became available. Such tools have been used initially for specific applications, such as IP assessment, IMEP, and engine misfire and knock investigation. The interface displayed voltage relative to the IMEP throughout a voltmeter or using an electromechanical device that reflected cycles in which misfire or knock occurred. When ADC was introduced into the systems at the beginning of the seventies, flexible and low-complexity investigative sets were developed. The analog signal from the amplifiers was digitally converted and stored in computer memory, allowing additional software manipulation. Therefore, higher storage capacity and suit-

ability were assured in information investigation, retaining an appropriate accuracy level. The block diagram of the experimental installation is shown in Figure 1.

4. Speed Characteristics

A Kirloskar four-stroke engine with prechamber injection is connected to a load-transmitting cup dynamometer on the test bench. The technical characteristics of the engine and the dynamometer are shown in Table 2.

4.1. Injection Advance Angle. Biodiesel fuel increased engine temperature above typical working values in the first stage of the experiment, reaching 98°C . This is due to the fact that, under the same conditions, the combustion delay time for gasoline increases when compared to diesel [16]. This is due to gasoline's higher flashpoint. The injection angle was increased from 10 to 20° , and the temperatures returned to normal, ranging from 50 to 72° . The atmospheric conditions in which the experiment was carried out were as follows: atmospheric pressure, $1,017$ bar; dry bulb temperature, 30°C ; wet-bulb temperature, 26°C ; relative humidity, 75% . The torque curves in the upper part of Figure 2 correspond to torque values with differences of 5 to 12% . The smallest differences occur at the lowest rotational speeds, and as the motor revolutions increase, the differences become larger [17]. The specific fuel consumption is shown in Figure 3. It can be seen that for low revolutions, these curves almost overlap, resulting in similar consumptions per unit of power [18]. The differences are more pronounced in the middle zone of rotation speed, increasing proportionally with the motor rotation speed. These are observed slopes and similar behaviour characteristics, except that diesel is slightly higher than biodiesel, and the point where they differ in their

TABLE 2: Engine and dynamometer characteristics.

Engine type	Make Kirloskar 1-cylinder, 4-stroke, water-cooled, diesel (computerized), modified-to-VCR engine
Model	TV1
Bore diameter	87.50 mm
Stroke	110.00 mm
Combustion principle	Compression ignition
Engine capacity	661 cc
Peak pressure	77.5 kg/cm ²
Power	3.5 kW at 1500 rpm
Dynamometer	Eddy current dynamometer cooled by water includes a loading unit
Airbox	Fabricated by MS including an orifice meter and U-tube manometer
Fuel tank	Maximum capacity of 15 liters including metering column
Piezoelectric sensor	Range 345 bar, including no noise cable
Encoder	1-degree resolution, 5500 rpm speed including TDC pulse
Data acquisition system	NI USB-6210, 250 kb/s, 16 bit
Digital voltmeter	0-200 mV range mounted on panel
Temperature detector	RTD-type, K-type thermocouple, and PT100
Load indicator	0-50 kg range, digital type
Load sensor	Strain gauge with 0-50 kg range
Direction of rotation	Clockwise (looking from flywheel end side)
Idle speed range	750 rpm to 2000 rpm
Min. running speed	1200 rpm
Fuel timing for the engine	23° BTDC
Valve clearance	At inlet: 0.18 mm
Valve clearance	At exhaust: 0.20 mm
Bumping clearance	0.046 inches to 0.052 inches
BMEP at 1500 rpm	6.35 kg/cm ²
Lubricating oil pump	Gear type
Lub. oil pump	6.50 l/min
Sump capacity	2.70 liters
Lub. oil consumption	1.5% normally exceed fuel
Connecting rod length	234 mm
Overall dimensions	617 × 504 × 877 mm
Weight	160 kg
Software	“EnginesoftLV” engine performance analysis

highest value, about 10%, is at 1460 rpm. The behaviour of hourly consumption (Figure 4) is depicted by the last pair of curves at the bottom of the graph. As the engine revolutions increase, these curves trend upward [19]. It should be noted that the hourly consumption of biodiesel is approximately 12% higher than that of diesel. The behaviour of engine parameters when using diesel and biodiesel is at a rotational speed of 1450 rpm, the point at which the differences are most significant [20]. The torque, which is 9.45% lower when using biodiesel, is represented by the first pair of bars from the left to the right, followed by the bars of effective power. When using biodiesel, this decreases by 9.76%. The third set of bars shows the consumption schedule, which shows that biodiesel consumption is 11.95% higher than diesel [21]. The fourth set of bars, which represents specific consumption, shows that biodiesel consump-

tion is 24.25% higher than diesel consumption. Finally, the last bars show engine performance, which is 18.99% lower than diesel when using biodiesel [3].

4.2. Exhaust Gas Emissions in the External Speed Test. The measurement of gas emissions was carried out for three points, similar for both fuels, to achieve a reference for comparison between them [22]. Figures 5 and 6 show the behaviour of gas emissions, paying particular attention to NO_x and SO₂ emissions for three different engine rotation speeds. The first component of the exhaust gases to be analyzed is SO₂ which, as can be seen in the case of diesel at 1000 rpm, is at a concentration of 420 ppm; at 1250 rpm, it is at a concentration of 368 ppm; and at 1500 rpm it is at a concentration of 240 ppm. For those same points using biodiesel, the SO₂ concentration was 0 ppm, which shows that

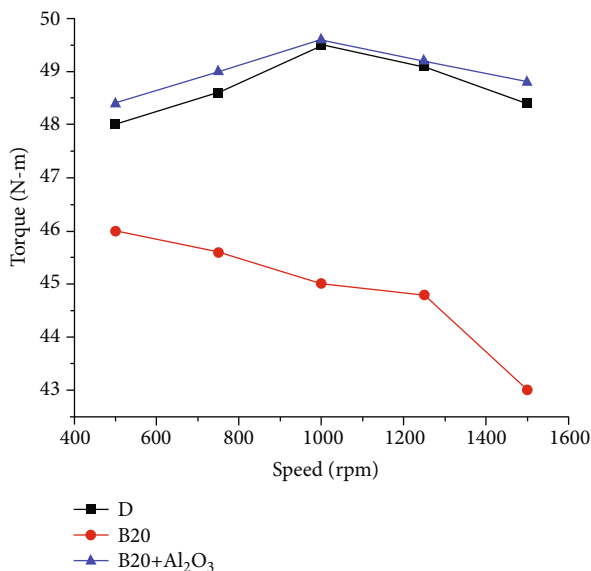


FIGURE 2: Torque vs. speed.

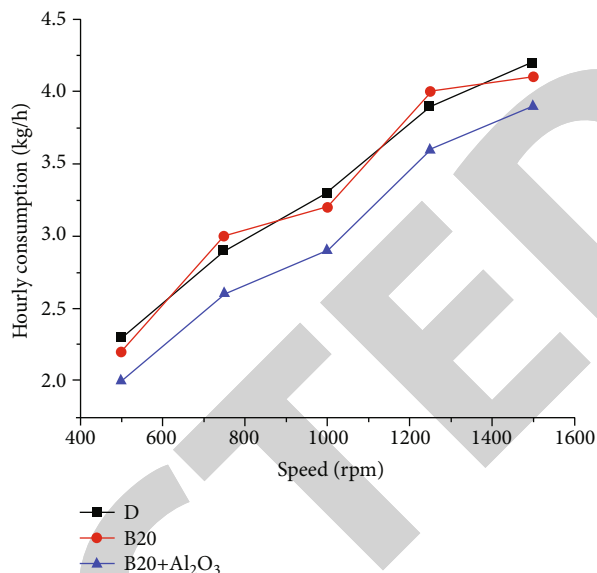


FIGURE 4: Hourly consumption vs. speed.

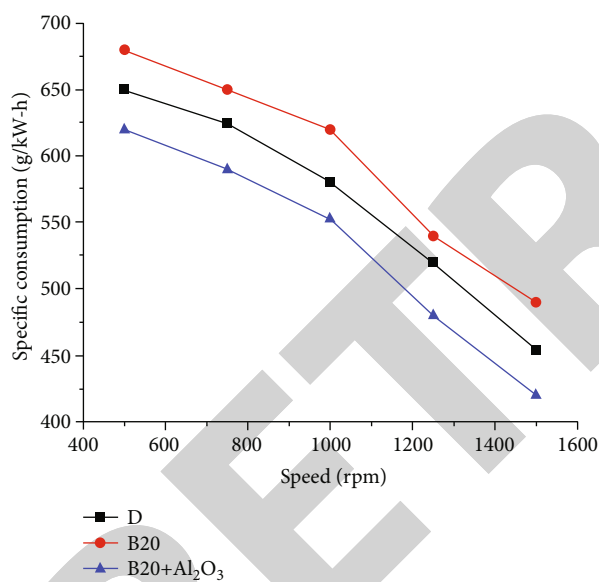


FIGURE 3: Specific consumption vs. speed.

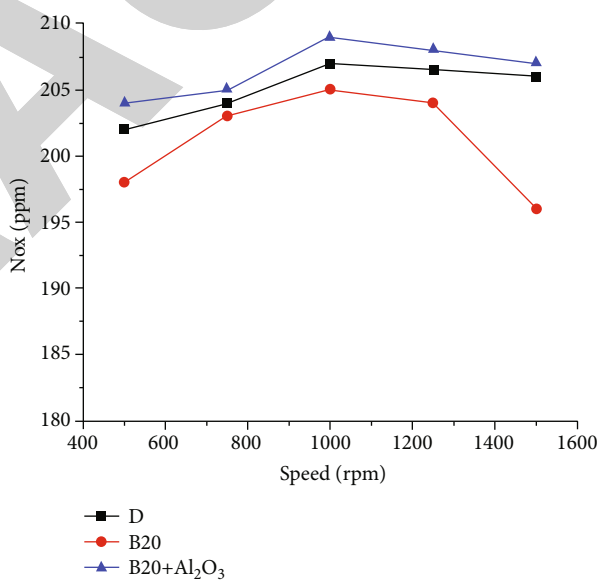
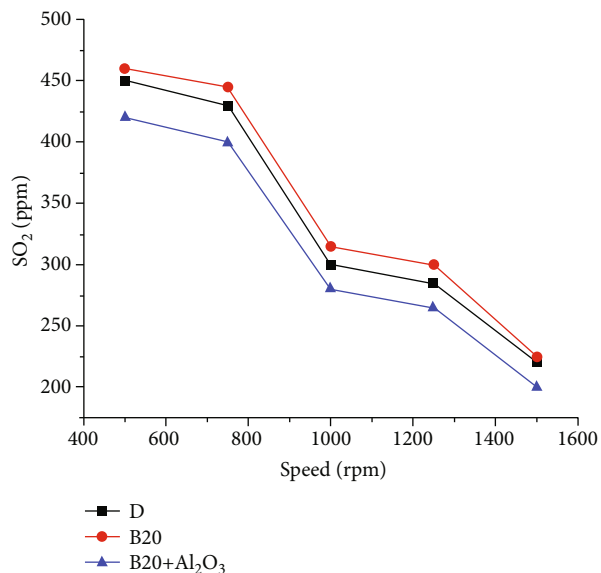
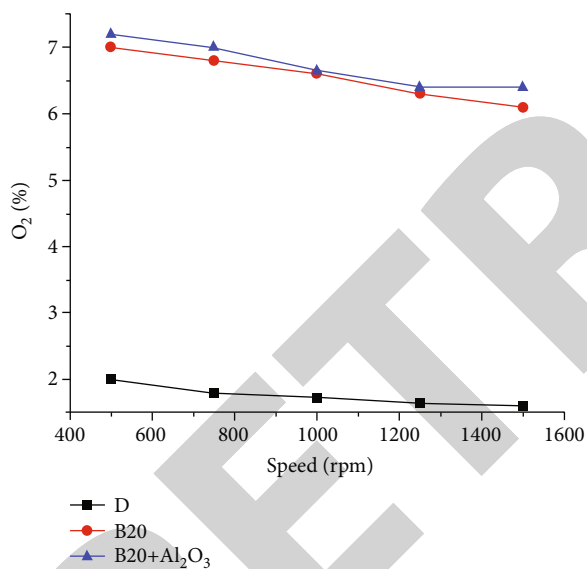


FIGURE 5: NOx vs. speed.

the sulfur content of biodiesel is zero [23]. The exhaust gas temperature parameter is higher when using diesel fuel; these curves are similar, with a tendency to increase as the rpm increases. For the case of diesel, the higher temperature is due to the higher calorific power of this fuel compared to biodiesel, and the percentages of temperature increases at each point are 5.4%, 10.8%, and 12.8%, respectively [24]. The maximum temperature values in diesel reach up to 399°C, while they reach up to 353°C when using biodiesel. The nitrogen oxide emissions in the engine are given by the maximum temperature reached in combustion. As in this case, diesel is higher, and then the emission of nitrogen oxides will be higher. These curves have similar behaviour. However, that corresponding to diesel is higher and reaches

a maximum value of 215 ppm [25]. In comparison, for biodiesel, the maximum value is 115 ppm, representing an almost double reduction of this pollutant. Figure 7 shows the behaviour of excess air and the remaining free O₂ in the exhaust gases [18]. The O₂ found present in the exhaust gases using biodiesel is higher than that recorded when using diesel. In biodiesel, a certain amount of oxygen is present, higher than that found in diesel, and participates in the combustion reaction [26]. Part of the oxygen enters with the intake air and leaves without reacting with the exhaust gases. These differences are even more accentuated when working at low rotation speeds, reaching a difference of 65%. Therefore, the excess air for biodiesel is higher than that for diesel, and the minimum point is at approximately 1250 rpm [27].

FIGURE 6: SO₂ vs. speed.FIGURE 7: O₂ vs. speed.

5. Conclusions

The experiments in the diesel engine using biodiesel made from algae oil and as raw materials are similar to those reported in the literature. The viscosity of the biodiesel used was acceptable for use in the motor used, even though it was still higher than that specified in the ASTM standard. The sulfur dioxide emissions are reduced to zero, and nitrogen oxides are reduced by half when biodiesel is used. Carbon monoxide emissions are also reduced. The differences in engine parameters when using diesel and biodiesel fuels increase as the engine revolutions increase. The torque, power, hourly consumption, and specific consumption differences for the engine are highly recordable.

Data Availability

The data used to support the findings of this study are included in the article.

Conflicts of Interest

The authors declare that they have no conflicts of interest regarding the publication of this paper. This study was performed as part of the employment of the authors at Ambo University, Ethiopia.

References

- [1] A. S. Adekunle, J. A. O. Oyekunle, A. I. Oduwale et al., "Biodiesel potential of used vegetable oils transesterified with biological catalysts," *Energy Reports*, vol. 6, pp. 2861–2871, 2020.
- [2] U. Rajak and T. N. Verma, "Effect of emission from ethylic biodiesel of edible and non-edible vegetable oil, animal fats, waste oil and alcohol in CI engine," *Energy Conversion and Management*, vol. 166, pp. 704–718, 2018.
- [3] S. S. Hoseini, G. Najafi, B. Ghobadian, M. T. Ebadi, R. Mamat, and T. Yusaf, "Performance and emission characteristics of a CI engine using graphene oxide (GO) nano-particles additives in biodiesel-diesel blends," *Renewable Energy*, vol. 145, pp. 458–465, 2020.
- [4] O. Ogunkunle and N. A. Ahmed, "Exhaust emissions and engine performance analysis of a marine diesel engine fuelled with *Parinari polyandra* biodiesel—diesel blends," *Energy Reports*, vol. 6, pp. 2999–3007, 2020.
- [5] M. A. Asokan, S. Senthur Prabu, P. K. K. Bade, V. M. Nekkanti, and S. S. G. Gutta, "Performance, combustion and emission characteristics of juliflora biodiesel fuelled DI diesel engine," *Energy*, vol. 173, pp. 883–892, 2019.
- [6] A. T. Hoang, T. H. Nguyen, and H. P. Nguyen, "Scrap tire pyrolysis as a potential strategy for waste management pathway: a review," *Energy Sources, Part A: Recovery, Utilization, and Environmental Effects*, vol. 1–18, pp. 1–18, 2020.
- [7] P. S. Ranjit and V. Chintala, "Impact of liquid fuel injection timings on gaseous hydrogen supplemented-preheated straight vegetable oil (SVO) operated compression ignition engine," *Energy Sources, Part A: Recovery, Utilization, and Environmental Effects*, vol. 1–22, pp. 1–22, 2020.
- [8] D. N. Cao, A. T. Hoang, H. Q. Luu, V. G. Bui, and T. T. H. Tran, "Effects of injection pressure on the NOx and PM emission control of diesel engine: a review under the aspect of PCCI combustion condition," *Energy Sources, Part A: Recovery, Utilization, and Environmental Effects*, pp. 1–18, 2020.
- [9] K. Kalaimurugan, S. Karthikeyan, M. Periyasamy, and G. Mahendran, "Experimental investigations on the performance characteristics of CI engine fuelled with cerium oxide nanoparticle added biodiesel-diesel blends," *Materials Today: Proceedings*, vol. 33, no. 7, pp. 2882–2885, 2020.
- [10] S. Karthikeyan, A. Prathima, M. Periyasamy, and G. Mahendran, "Emission analysis of the diesel engine using *Stoehospermum marginatum*, brown marine algae with Al₂O₃ nano fluid," *Materials Today: Proceedings*, vol. 33, no. 7, pp. 4047–4053, 2020.
- [11] A. K. Hussein, "Applications of nanotechnology in renewable energies—a comprehensive overview and understanding," *Renewable and Sustainable Energy Reviews*, vol. 42, pp. 460–476, 2015.

Retraction

Retracted: Tribological Behavior and Surface Characterization of Gray Cast Iron-EN31 Steel under Lubricated Sliding Conditions

Journal of Nanomaterials

Received 11 July 2023; Accepted 11 July 2023; Published 12 July 2023

Copyright © 2023 Journal of Nanomaterials. This is an open access article distributed under the Creative Commons Attribution License, which permits unrestricted use, distribution, and reproduction in any medium, provided the original work is properly cited.

This article has been retracted by Hindawi following an investigation undertaken by the publisher [1]. This investigation has uncovered evidence of one or more of the following indicators of systematic manipulation of the publication process:

- (1) Discrepancies in scope
- (2) Discrepancies in the description of the research reported
- (3) Discrepancies between the availability of data and the research described
- (4) Inappropriate citations
- (5) Incoherent, meaningless and/or irrelevant content included in the article
- (6) Peer-review manipulation

The presence of these indicators undermines our confidence in the integrity of the article's content and we cannot, therefore, vouch for its reliability. Please note that this notice is intended solely to alert readers that the content of this article is unreliable. We have not investigated whether authors were aware of or involved in the systematic manipulation of the publication process.

Wiley and Hindawi regrets that the usual quality checks did not identify these issues before publication and have since put additional measures in place to safeguard research integrity.

We wish to credit our own Research Integrity and Research Publishing teams and anonymous and named external researchers and research integrity experts for contributing to this investigation.

The corresponding author, as the representative of all authors, has been given the opportunity to register their agreement or disagreement to this retraction. We have kept a record of any response received.

References

- [1] S. Ananth, P. Sivaprakasam, J. Udaya Prakash, P. Maheandera Prabu, V. Perumal, and G. Kalusuraman, "Tribological Behavior and Surface Characterization of Gray Cast Iron-EN31 Steel under Lubricated Sliding Conditions," *Journal of Nanomaterials*, vol. 2021, Article ID 7725959, 9 pages, 2021.

Research Article

Tribological Behavior and Surface Characterization of Gray Cast Iron-EN31 Steel under Lubricated Sliding Conditions

S. Ananth ¹, P. Sivaprakasam ², J. Udaya Prakash ³, P. Maheandera Prabu ⁴,
Varatharaju Perumal ⁵ and G. Kalusuraman ⁶

¹Department of Mechanical Engineering, Shri Ram Murti Smarak College of Engineering & Technology, Bareilly, India

²Department of Mechanical Engineering, Center of Excellence-Nano Technology, College of Electrical and Mechanical Engineering, Addis Ababa Science and Technology University, Addis Ababa, Ethiopia

³Department of Mechanical Engineering, Vel Tech Rangarajan Dr. Sagunthala R&D Institute of Science and Technology, Chennai, India

⁴Department of Ocean Engineering, Indian Institute of Technology Madras, Chennai, Tamil Nadu, India

⁵Department of Automotive Technology, Ethiopian Technical University, Addis Ababa, Ethiopia

⁶Department of Agricultural Engineering, Kalasalingam Academy of Research and Education, Krishnankoil, Tamil Nadu, India

Correspondence should be addressed to P. Sivaprakasam; shiva@aastu.edu.et

Received 10 July 2021; Accepted 28 September 2021; Published 14 October 2021

Academic Editor: Karthikeyan Sathasivam

Copyright © 2021 S. Ananth et al. This is an open access article distributed under the Creative Commons Attribution License, which permits unrestricted use, distribution, and reproduction in any medium, provided the original work is properly cited.

This research investigates the tribological behavior of gray cast iron against EN31 steel under lubricated conditions. The most typical lubricated sliding phenomena are the reduction of wear on both the sliding surfaces and any one of the critical surfaces. Static and hydrodynamic wear can be reduced based on fluid properties or the accessibility of fluid between the surfaces. The oil's viscosity or content of the hydrocarbon and additives present in the oil plays a major role in controlling the wear of reciprocating surfaces. Therefore, this research work focused on metal-to-metal contact wear under the influence of lubricating oil (40 pride oil). The Taguchi method was used to select the sliding parameter combinations. Lubricated sliding resulted in a relatively reduced order of friction coefficient, attributable to better load distribution due to the formation of the lubricant film.

1. Introduction

Gray cast iron (GCI), used in the manufacturing of industrial components, is more accessible to machines and requires less lubricant than other cast irons [1]. This study deals with the sliding wear behavior of GCI-steel (EN31) contact pair under lubricated conditions over a range of load, sliding speed, and sliding distance. A solid-solid contact/solid-fluid contact pair is the most common type of contact pair. Solid-solid contact could be expected corrosion, adhesion, abrasion, and diffusion wear [2]. Tribological characteristics such as friction and adhesion wear are considered in the current study of solid-solid contact. GCI exhibits the essential microstructure and is commonly used in wear-resistant products such as cylinder liners, piston rings, clutches, and disc brakes [3].

Prasad [4] examined the sliding wear behavior of GCI in dry and lubricated conditions (SAE 40) over a range of sliding speeds and pressure. It was found that the cast iron wear rate increased with sliding speed and applied pressure. The temperature increased initially at a high rate in the specimen's surface after reducing the later stages of sliding at low pressures. Adhesion plays a significant role in causing oil and oil content loss plus graphite-lubricated state. Oil wear rate is lower than dry wear rate [4]. Grabon et al. [5] measured the tribological quality of honed cylinder liners made from GCI on the plateau. The selected counterpart material consisted of piston rings of GCI.

A reciprocating test was used for comparing the honed cylinder liner with or without additional oil pockets (SAE 40 diesel engine oil) created by the burnishing method. In addition, dimples were prepared on the surface of the honed

cylinder liner, which shows a reduction of half of the friction coefficient as in the usual surface. Each grade of industrial lubricant usually comes with several additives that are physically or chemically absorbed on the surface to avoid aggressive wear conditions under the boundary lubrication regime. Lubricants are primarily used to separate two sliding surfaces to reduce friction and wear. It also serves other purposes, including removing heat and pollutants from the contact. Lubricants are typically made up of oil plus compounds called additives that assist oils in performing specific roles successfully [6].

Flake Graphite Iron (FGI) is highly suggested for wear resistance applications among the GCI due to its flaky graphite structure [7]. GCI is generally used in automotive applications, particularly cylinder liners. According to the literature, the best wear-resistant microstructure is a pearlitic matrix with a tiny quantity of free ferrite. GCI includes such a matrix, and its use for a range of tribological applications has been seen in the past, particularly in sliding contact systems [8, 9].

The wear map for ASTM A30 GCI was created with a pearlitic matrix, which summarized the wear rate and its mechanisms into ultramild, mild, and severe wear regimes by Riahi and Alpas [10]. There was no palpable evidence of plastic deformation in ultra and mild wear formation of oxide layers covering contacting surfaces. The material was transferred on the surface of the AISI 52100 steel as a counter face because surface roughness increased from $0.12\ \mu\text{m}$ to $4.0\ \mu\text{m}$. The hardness, temperature, and surface roughness increased during the severe wear regime due to surface deformation on the cast iron and welded on the EN31 steel with a maximum height of $10\ \mu\text{m}$. The severe wear appeared when oxide layer formation was unstable due to delaminating of tribo oxides. The author has referred to the formation of graphite flakes under low loading conditions during dry sliding which reveals excellent wear resistance of GCI [10].

The wear behavior of different compositions of alloyed gray cast iron tested against hardened steel (62 HRC) was analyzed [11]. The results show that the alloyed hypereutectic cast iron has three times lower wear rate than the elemental iron, owing to the larger graphite content and strong carbides in the matrix. Also, tensile strength and specific wear rate decrease with increasing graphite volume. Simultaneously, due to three-body abrasion, the hard carbide particle present in debris generation started along the wear track, preventing material loss during sliding. Chawla et al. [12] investigated the GCI wear mechanism, using the pin-on-disc wear tests under dry sliding conditions. The results show greater wear in stainless steel 304 with an increase in sliding speed at normal load and getting softened with an increase in the load parameter. But the wear ratio of GCI has been low with increasing load due to graphite (ferrite) matrix and decohesion observed. Masuda et al. [13] conducted sliding wear experiments under lubrication using gray cast iron AISI NO.35B. Wear surface and sliding wear mechanism was observed during the sliding wear process. The aluminium-modified cast iron (Fe-C-Al) has lower wear resistance and friction

TABLE 1: Chemical composition of grade GCI specimen (BS 1452).

Material	C	Si	Mn	S	Cr	P	Cu	Fe
Weight%	3.2	2.1	0.7	0.06	0.3	0.25	1.5	Remainder

TABLE 2: Process parameter and their levels.

Levels	Parameters		
	Load (N)	Sliding speed (m/s)	Sliding distance (m)
1	15	0.5	300
2	30	1.0	600
3	45	1.5	900

when compared to conventional (Fe-C-Si) cast iron [14]. Singh and Bhowmick [15] investigated the tribological behavior of hybrid AMMC sliding against steel and cast iron with MWCNT-oil lubrication; the inclusion of lubricants permits the creation of tribo layers which controls the relevant antifriction and antiwear processes.

Prasad [16] investigated the wear characteristics of GCI in both dry and oil-lubricated environments. It was found that the wear rate of cast iron increased with the sliding speed and pressure. At the initial stage due to adhesion, the temperature near the specimen surface increased, whereas at later stages the temperature decreased at low pressure. In practice, GCI-steel contact pair finds wide application. The base GCI has superior mechanical properties like good vibration damping, low coefficient of friction, good toughness, and excellent wear resistance. Gray cast iron type consists of predominantly pearlitic/ferrite matrix or both with graphite flakes. Even though it has good properties, it must withstand the application environments such as dry and lubricated sliding, which has exposed positive and negative wear. Many researches attempted wear behavior of gray cast iron under wet conditions, but limited studies reported on positive and negative behavior of GCI. Therefore, this research describes the lubricated environment conditions under the contact pair of GCI-EN31 steel.

2. Experimental Procedure

2.1. Selection of Material. Cast iron (200-250/BS 1452, also called GCI) is a popular material used in modern industrial applications. The price is so low (20-40%) than the steel, and it has a wide variety of mechanical properties. High carbon and chromium-containing low alloy steel EN31 (AISI 52100) was selected as a counter face specimen for this experiment. The chemical composition of GCI is tabulated in Table 1.

2.2. Test Parameters. Table 2 shows the wear test parameters such as load, sliding speed, and sliding distance. Wear study was carried out under dry and lubricated (40 pride oil) conditions using pin-on-disc tester shown in Figure 1. A combination of test parameters was selected and experimented based on the Taguchi design of experiments (DOE) principle with orthogonal array (OA) of L_{27} . The contact surface comprises stationary pins made of EN31 steel against a rotating

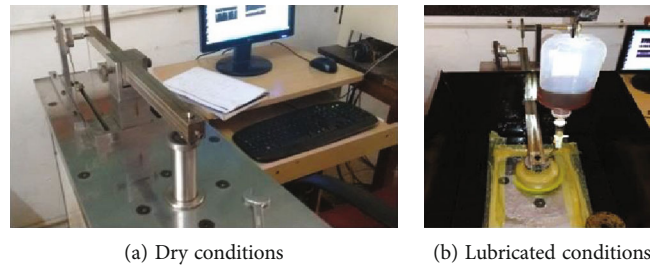


FIGURE 1: Photograph of pin-on-disc wear tester.

TABLE 3: Experimental results.

S. no.	Load (N)	Sliding speed (m/s)	Sliding distance (m)	COF	Disc wt. loss (g)	Pin wt. loss (g)
1	15	0.5	300	0.1066	0.0028	0.052
2	15	0.5	600	0.0847	-0.0018	0.009
3	15	0.5	900	0.1146	-0.008	-0.006
4	15	1.0	300	0.0808	0.0041	0.006
5	15	1.0	600	0.0973	-0.0058	0.009
6	15	1.0	900	0.1081	-0.0012	0.016
7	15	1.5	300	0.1084	0.0012	-0.001
8	15	1.5	600	0.0901	-0.0018	-0.009
9	15	1.5	900	0.0901	-0.0037	-0.021
10	30	0.5	300	0.124	-0.007	-0.004
11	30	0.5	600	0.1034	-0.0011	-0.016
12	30	0.5	900	0.1095	-0.002	-0.003
13	30	1.0	300	0.1258	0.0004	-0.002
14	30	1.0	600	0.1258	0.003	0.001
15	30	1.0	900	0.0902	0.001	-0.002
16	30	1.5	300	0.1167	-0.0005	-0.024
17	30	1.5	600	0.1033	0.0013	-0.003
18	30	1.5	900	0.1313	0.0021	0.004
19	45	0.5	300	0.1443	-0.0003	0.017
20	45	0.5	600	0.1257	-0.0002	-0.019
21	45	0.5	900	0.1262	0.0005	0.022
22	45	1.0	300	0.1227	-0.0004	-0.005
23	45	1.0	600	0.0948	-0.0014	-0.001
24	45	1.0	900	0.0976	0.0031	-0.083
25	45	1.5	300	0.0861	0.0037	-0.011
26	45	1.5	600	0.1125	-0.0028	0.001
27	45	1.5	900	0.11	0.0004	0.005

cast-iron disc under the standard testing condition of ASTM G99 [17–19]. The test conditions are chosen based on the literature review and experience gained through earlier tests.

2.3. Sample Preparation. GCI discs of outer diameter 55 mm, inner diameter 6 mm, and 10 mm thickness were machined to conduct the experiments. The surface hardness of GCI is 28 HRC.

The counter specimen pin EN31 was machined from BS 970 grade with 6 mm diameter and length 60 mm and hardened to 58 to 60 HRC.

3. Results and Discussion

3.1. Observation on Lubricated Sliding. The GCI disc and pin are examined with 40 pride oils (additive oil), and the results are tabulated in Table 3. Sliding wear tests were conducted under a lubricated environment using 40 pride oil. It is seen that the wear of GCI on the counter pin varies only marginally with 40 pride oil during sliding; it could be because additive oil does not affect low load and speed conditions. Figure 2(a) illustrates the variation of wear with increasing sliding speed under the load of 15 N for the GCI disc with various sliding distance. Figure 2(b) shows the variation of

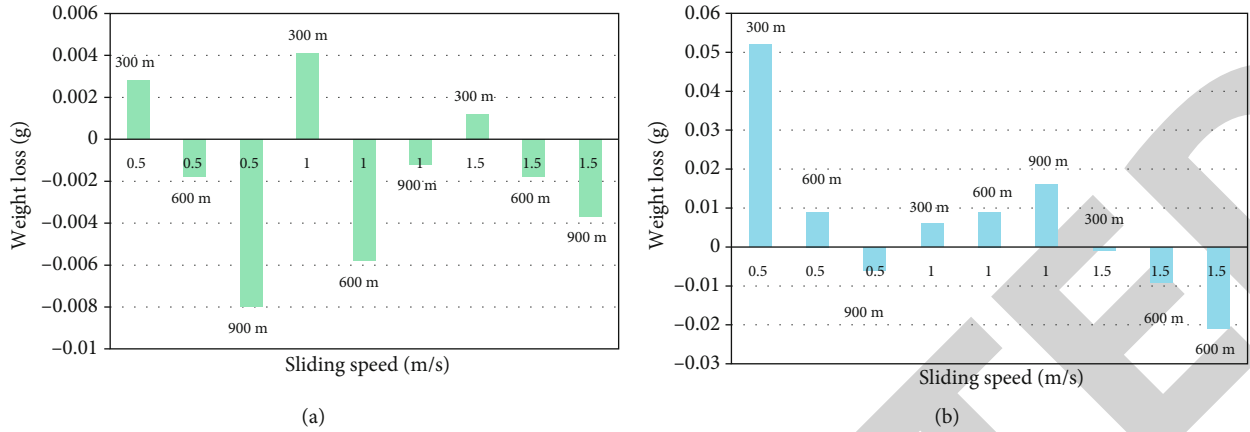


FIGURE 2: (a) Disc weight loss at 15 N load. (b) Pin weight loss at 15 N load.

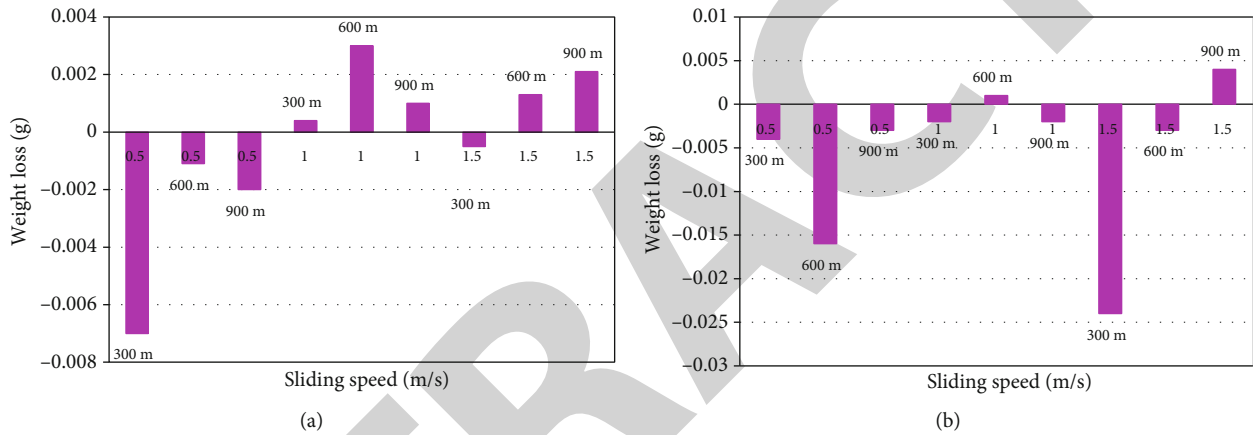


FIGURE 3: (a) Disc weight loss at 30 N load. (b) Pin weight loss at 30 N load.

wear with increasing sliding rate under the load of 15 N for EN31 steel pin with lubricated condition (40 pride oil).

From Figure 2(a), at 15 N load, it is seen that with 40 pride oil, the disc exhibits smaller order of wear and predominantly negative mode. With a lower speed of 0.5 m/s, sliding wear tends to drop down from positive to negative mode with the sliding distance. The change of wear mode could be attributed to the presence of transferred wear debris from the counter surface.

With increasing sliding speed (1 m/s), the disc encounters positive to negative mode of wear (marginally varying magnitude). With the higher speed of 1.5 m/s, an overall reduction in wear can be seen; the mode of wear changes from positive to negative mode. Typically monitored variation of wear of counter steel surface is illustrated in Figure 2(b). It is seen that with increasing speed and sliding distance, a gradual reduction in wear changing from positive to negative mode occurs. Sliding under 15 N load with a sliding speed of 1 m/s is seen.

At the same time, the counter steel surface exhibits a marginally increasing positive mode of wear; the GCI disc shows a fluctuating mode of wear, i.e., unlike the case of dry sliding. With 40 pride oil, under increasing speed (associated interface/contact temperature), likely, oil film factor on steel surface attributes to the reduction in wear; also,

the occurrence of negative mode on both the contact surfaces could be due to effective transport of material between contact surfaces by the lubricant.

Figure 3(a) illustrates the variation of wear with increasing sliding speed under the load of 30 N for GCI disc. Figure 3(b) illustrates the variation of wear with increasing sliding rate under the load of 30 N for EN31 steel pin, in lubricated condition (40 pride oil). From Figure 3(a), GCI exhibits native wear at low sliding speed, whereas in increasing speed, it tends to rise to positive mode. The counter steel pin materials exhibit mostly negative wear. However, compared to 15 N loading, the counter steel pin surface exhibits a mainly negative mode of wear of relatively smaller magnitude. Also, it is seen that around 1 m/s sliding speed, a trend change can be observed. A similar observation is found, when wear losses increase as wear time, rotating speed, and applied pressure increase [20].

Figure 4(a) illustrates the variation of wear with increasing sliding speed under the load of 45 N for the GCI disc. Figure 4(b) shows the variation of wear with increasing sliding speed under the load of 45 N for EN31 steel pin, in lubricated condition (40 pride oil).

Unlike in the case of 15 N load (sliding), GCI disc exhibits mostly reduced order of wear; as observed in the trials, with this test condition (45 N), CI exhibits a visible rise

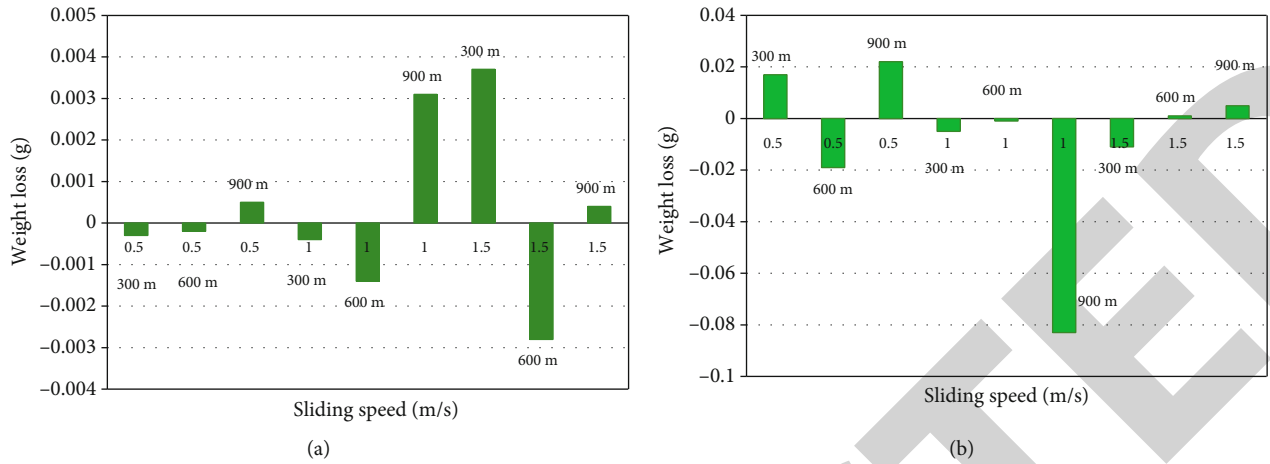


FIGURE 4: (a) Disc weight loss at 45 N load. (b) Pin weight loss at 45 N load.

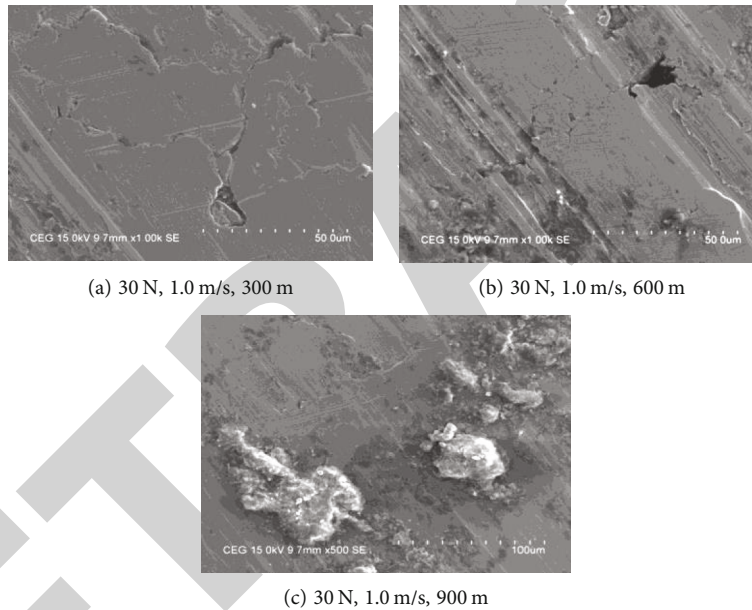


FIGURE 5: (a–c) Micrograph with 40 pride oil.

in wear (from -0.0014 to 0.0031 gms) at a sliding speed of 1 m/s and sliding distance of 900 m, thus indicating the dependency of adhesion wears on the PVT factor. Applied pressure may have the opposite effect by causing induced surface hardening, which in turn improves wear resistance [20].

Also, it is seen that a drop in adhesion wear can be seen with a higher speed of 1.5 m/s. This could be attributed to better film formation of this additive oil with increasing speed. Under the lubricated condition, it is known that the thickness of the lubricating film “*h*” is given in

$$h \propto (\eta u)^{1/2}, \tag{1}$$

where η is the kinematic viscosity and u is the sliding velocity.

It is also known that when the film thickness exceeds the composite surface roughness of contacting surface, the Dow-

son ratio is calculated by using

$$D = \frac{h}{(V_{a1} + V_{a2})} \text{ (Dowson ratio)}. \tag{2}$$

V_{a1} is the roughness of CI; V_{a2} is the roughness of steel pin.

When “*D*” ratio is greater than 1-1.4, there will be effective separation of contacting surfaces, resulting in less interaction and wear.

Typical monitored variation of wear of counter steel surface at 45 N normal load is illustrated in Figure 4(b); with a lower sliding speed of 0.5 m/s, the pin exhibits relatively higher wear (0.017 mg-0.022 mg); with increasing sliding speed, 1 to 1.5 m/s, a reduction in wear (mostly negative mode) can be seen. With increasing sliding speed, better film formation results in enhanced wetting/absorption, causing a reduction in wear with the lower speed of 0.5 m/s, associated

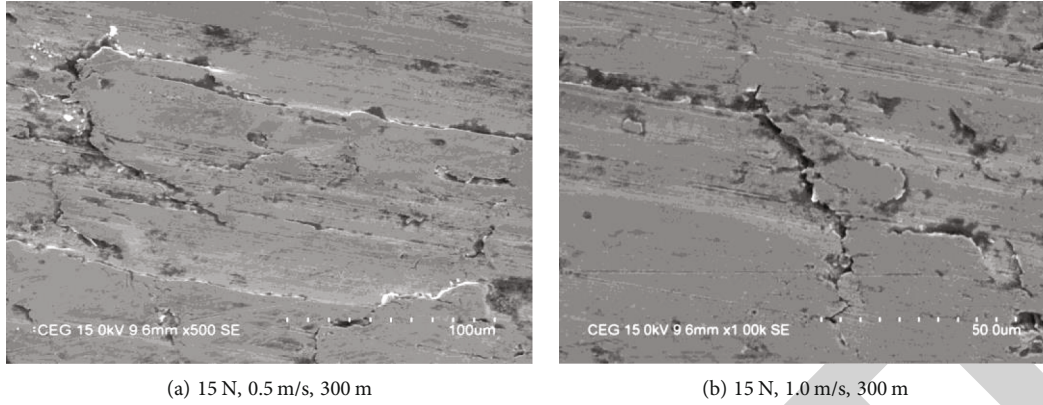


FIGURE 6: (a, b) Micrograph with 40 pride oil sliding.

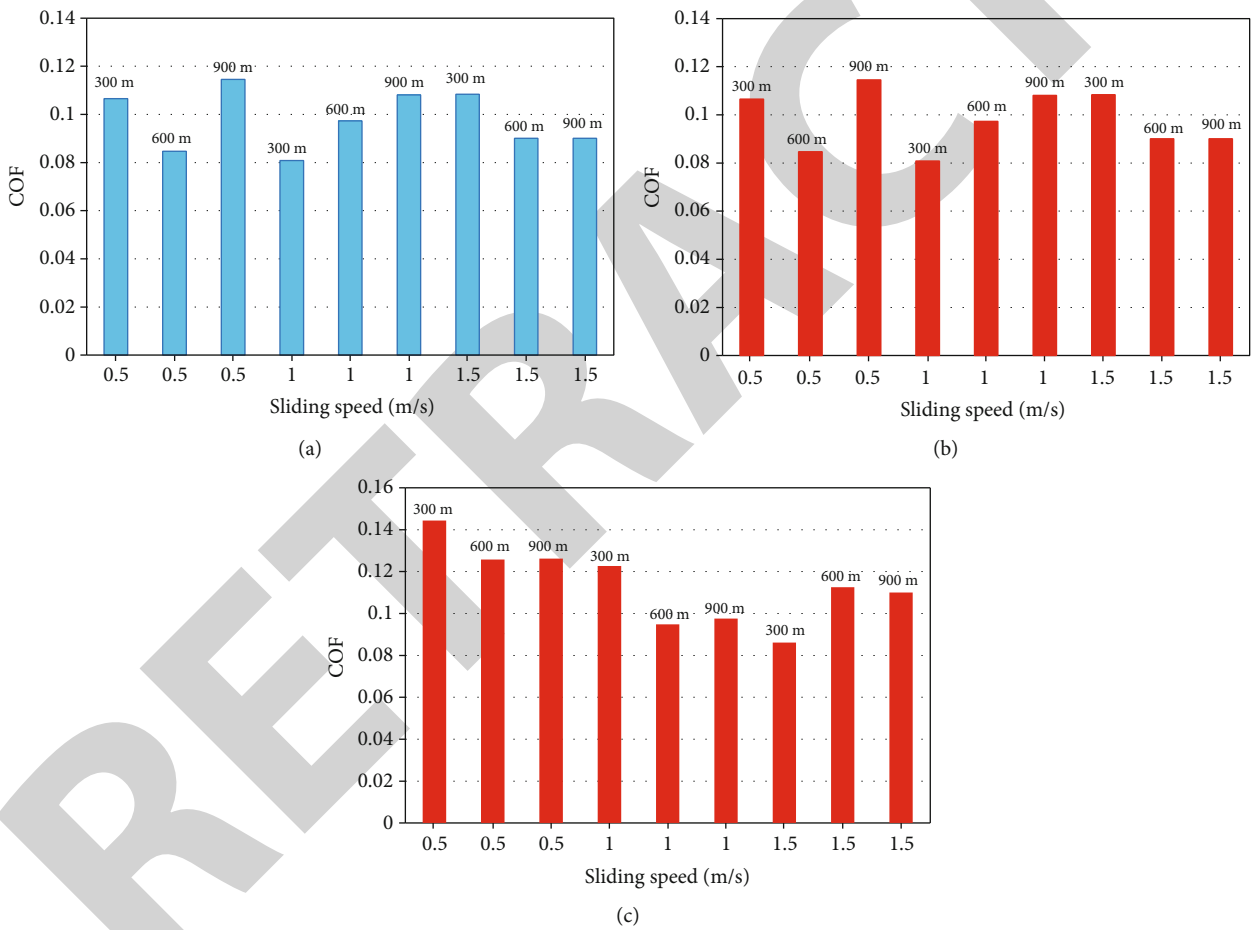


FIGURE 7: (a) COF at 15 N load. (b) COF at 30 N load. (c) COF at 45 N load.

with inadequate film formation, effectively a dry contact occurs, tending to enhanced wear. The observed higher order wear negative wear with 1 m/s sliding speed and sliding distance of 900 m could be attributed to the enhanced wear of GCI disc (at the same condition) and transfer.

3.2. *Micrograph of Lubricated Sliding Conditions.* A micrograph of worn-out sliding track on CI disc tested with 40 pride oil is shown in Figure 5(a). The positive mode of wear

is associated with a worn-out micrograph showing surface cracking and discrete pits at the crack tip. Micrograph of worn-out surface on the sliding track of GCI disc presents partially glazed texture with discrete pull out of material shown in Figure 5(b). A typical micrograph in Figure 5(c) shows partially glazed texture, with discrete spots of transferred debris from the counter steel surface.

A micrograph of worn-out sliding track on GCI disc exposed to sliding contact with steel surface is shown in

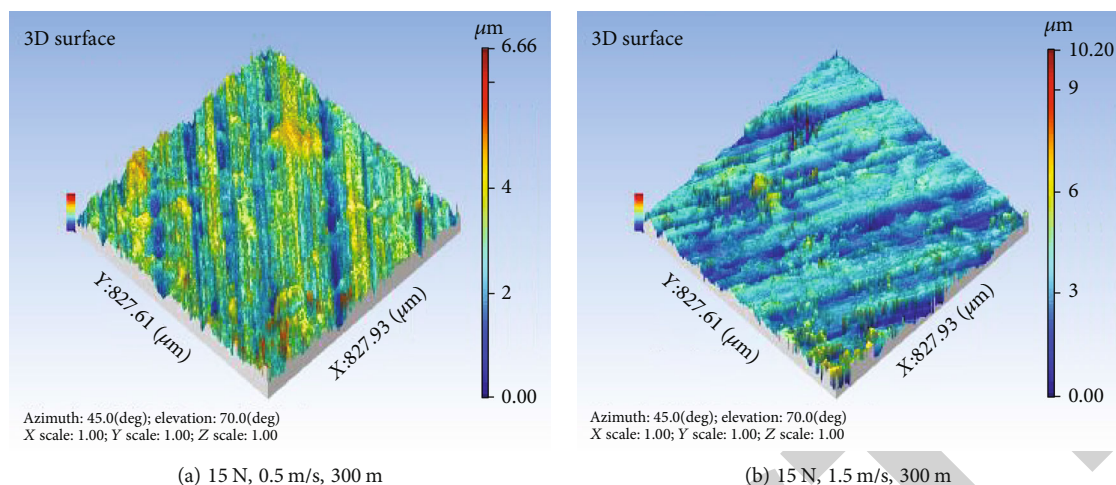


FIGURE 8: (a, b) 3D surface texture views.

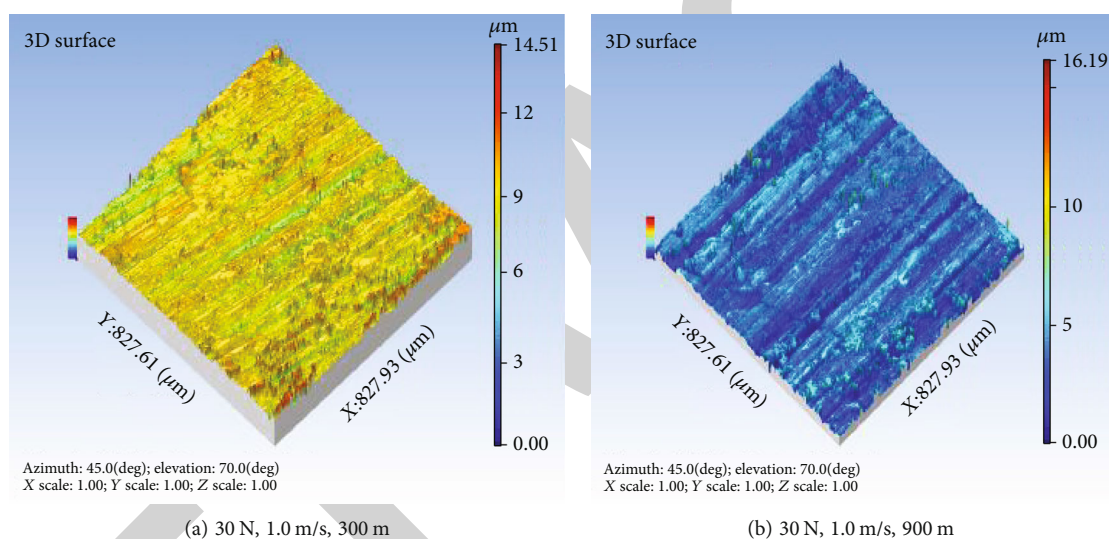


FIGURE 9: (a, b) 3D surface texture views.

Figure 6(a) at 15 N load, 0.5 m/s, and 300 m. As presented earlier, the GCI disc encountered positive mode of wear, supplemented by the surface distress exhibited by the micrograph. Severe ridging and spalling of graphite can be seen. With additive oil such as 40 pride oil, under the low sliding condition of 15 N, 1.0 m/s, and 300 m, the contact would be dominating stick-slip in nature. The micrograph of worn-out track shown in Figure 6(b) pertains to a region of the track, exhibiting severe sliding spalling of graphite and discrete dents on the surface.

3.3. COF under Lubricated Contact. From Figure 7(a), the lower-order COF can be seen, with increasing load (30 N). COF marginally rises and is fluctuating around 0.1 to 0.123 with a higher load (45 N); a steady reduction in COF can be seen. The COF decreases and increases marginally with increased speed, indicating a slow improvement in wetting by the oil. The decrease part may be attributable to the wear of oxide film. At higher speeds, an almost steady state of COF occurs due to better film formation.

From Figure 7(b), the COF variation with increasing speed for 40 pride oil at 30 N load is very similar to 40 pride oil at 15 N. However, at most speeds, the COF value is marginally higher, which is attributable to higher load and lubricant inaccessible on the surface. It is seen that while the COF tends to rise with one m/s parametric combination, at 15 N, it tends to drop down for 45 N loading shown in Figure 7(c). This could be attributed to the increased surface interaction due to the accessibility of the additive oil to lubricate the interface at a low load. With increasing load, i.e., 45 N, possibly due to increasing contact temperature, better (lubricant) film formation occurs, tending to a reduction in COF.

3.4. 3D Surface Textures. Figure 8(a) shows the 3D surface texture which contains discontinuous sliding track/texture with transferred wear debris. A typical recorded surface profile is shown in Figure 8(a) and the following features: Ra $-0.415 \mu\text{m}$, Rt $3.77 \mu\text{m}$, and Rz $2.72 \mu\text{m}$ relatively higher order Rt/Ra ratio (≈ 9); associated with a wavy texture,

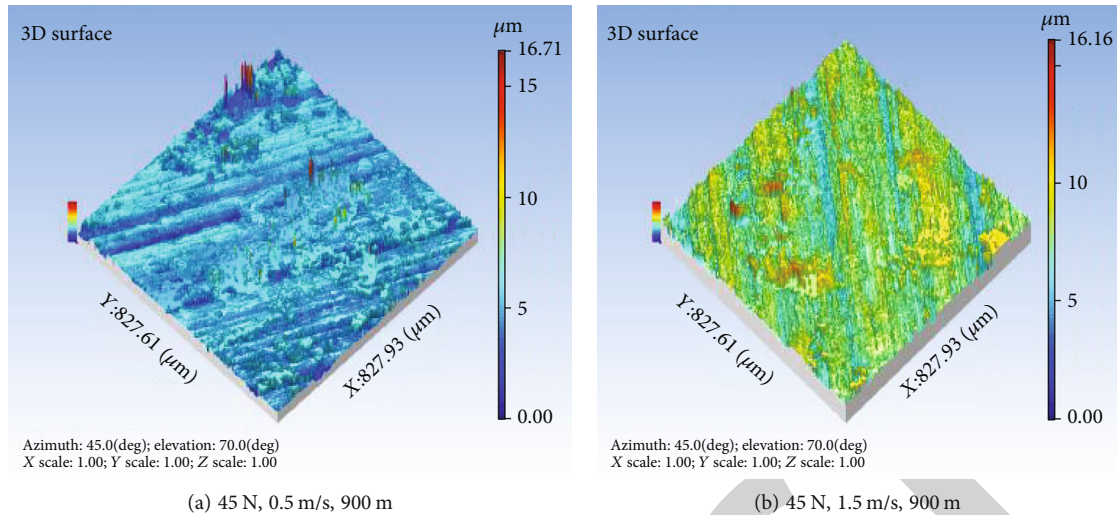


FIGURE 10: (a, b) 3D surface texture views.

maximum peak height R_p $1.42 \mu\text{m}$ and maximum valley depth R_v $-1.29 \mu\text{m}$.

Under the severe test condition, relatively smoother texture observed is illustrated in Figure 8(b), higher speed, absence of stick-slip contact, hence resulting in the less wavy profile, with reduced R_t/R_a ratio R_a $-0.386 \mu\text{m}$, R_t $-1.87 \mu\text{m}$ ($R_t/R_a \approx 5$), R_p $-0.746 \mu\text{m}$, and R_v $-1.03 \mu\text{m}$. Reduction of R_p and R_v indicates mild crest flattening due to sliding. Kurtosis of 3.13 (typically 3) displaying reasonably uniform texture, also supplemented by the minor order skewness (Figure 8(b)), shows better texture R_a -0.386 , R_v -1.87 , $R_t/R_a \approx 5$, kurtosis 3.17, and skewness 3.34 (left center texture).

Figure 9(a) presents a relatively smoother texture of distributed layer under medium load conditions (30 N, 1 m/s, 300 m) in mostly positive mode of wear. Profile indicates mild wavy texture, R_a $-0.236 \mu\text{m}$, R_t 1.9, and $R_t/R_a \approx 8$. The kurtosis (4.68) indicates wavy texture, skewness 0.266 left centric (nonuniform). In Figure 9(b), the 3D surface shows uniform texture with ridges, locally distributed layer R_a $0.18 \mu\text{m}$, R_t $3.07 \mu\text{m}$, and $R_t/R_a > 10$. The kurtosis is 3.18 and skewness is 0.224, wavy texture left centric (non-uniform texture).

Figure 10(a) depicts the surface texture feats of the worn-out track surface exposed to 45 N, 0.5 m/s, 900 m. The mild positive wear 3D texture, distributed pattern, locally crumbled surface and surface profile is right centric, R_a $-0.682 \mu\text{m}$, R_t 5.97, and $R_t/R_a \approx 8$. The kurtosis is 10.3 and skewness is 0.37. Wavy texture is presented (due to crumbling of material). In another region from Figure 10(b) 3D surface with distributed layer, R_a $-0.325 \mu\text{m}$, R_t $-4.5 \mu\text{m}$, and $R_t/R_a > 10$. Kurtosis 4.39 and skewness 0.058 indicate that the surface comprises a wavy texture mostly centric.

4. Conclusions

- (i) A gray cast iron/steel sliding contact pair, with contact pressure of 0.6 MPa to 1.7 MPa, exhibits stick-slip contact wear, which has a predominance of

ploughing behavior. Positive as well as a negative wear mode was shown depending on the contact pressure and sliding velocity

- (ii) With 40 pride oil, an additive oil, the counter steel pin surface exhibits mostly negative wear, while GCI disc exhibits mostly positive wear, while GCI disc exhibits fluctuating wear with a rise in wear for higher contact speeds. At relatively lower contact pressure and temperature, the effectiveness of oil addition could not be realized
- (iii) Micrograph of GCI disc tested with 40 pride oil exhibits +ve mode of wear with the worn-out surface exhibiting surface cracking and discrete pits
- (iv) The higher surface roughness values R_a $-0.682 \mu\text{m}$ were obtained at 45 N, 0.5 m/s, 900 m and lower surface roughness values (R_a $0.18 \mu\text{m}$) were obtained at 30 N, 1.0 m/s, 900 m
- (v) Lubricated sliding results in relatively reduced order of coefficient of friction, attributable to better load distribution due to formation of lubricant film

Data Availability

The data used to support the findings of this study are included within the article.

Conflicts of Interest

The authors declare that they have no conflicts of interest regarding the publication of this paper.

References

- [1] R. Evans, *Metalworking Fluids (MWFs) for Cutting and Grinding*, Woodhead Publishing, 2012.
- [2] S. Ananth, J. Udaya Prakash, R. Krishna Murthy, K. V. Arun Pillai, and T. V. Moorthy, "Tribological behaviour of grey cast

Retraction

Retracted: Experimental Study on Surface Roughness and Flank Wear in Turning of Nimonic C263 under Dry Cutting Conditions

Journal of Nanomaterials

Received 11 July 2023; Accepted 11 July 2023; Published 12 July 2023

Copyright © 2023 Journal of Nanomaterials. This is an open access article distributed under the Creative Commons Attribution License, which permits unrestricted use, distribution, and reproduction in any medium, provided the original work is properly cited.

This article has been retracted by Hindawi following an investigation undertaken by the publisher [1]. This investigation has uncovered evidence of one or more of the following indicators of systematic manipulation of the publication process:

- (1) Discrepancies in scope
- (2) Discrepancies in the description of the research reported
- (3) Discrepancies between the availability of data and the research described
- (4) Inappropriate citations
- (5) Incoherent, meaningless and/or irrelevant content included in the article
- (6) Peer-review manipulation

The presence of these indicators undermines our confidence in the integrity of the article's content and we cannot, therefore, vouch for its reliability. Please note that this notice is intended solely to alert readers that the content of this article is unreliable. We have not investigated whether authors were aware of or involved in the systematic manipulation of the publication process.

Wiley and Hindawi regrets that the usual quality checks did not identify these issues before publication and have since put additional measures in place to safeguard research integrity.

We wish to credit our own Research Integrity and Research Publishing teams and anonymous and named external researchers and research integrity experts for contributing to this investigation.

The corresponding author, as the representative of all authors, has been given the opportunity to register their agreement or disagreement to this retraction. We have kept a record of any response received.

References

- [1] J. F. Xavier, B. Ravi, D. Jayabalakrishnan, C. Ezilarasan, V. Jayaseelan, and G. Elias, "Experimental Study on Surface Roughness and Flank Wear in Turning of Nimonic C263 under Dry Cutting Conditions," *Journal of Nanomaterials*, vol. 2021, Article ID 2054399, 11 pages, 2021.

Research Article

Experimental Study on Surface Roughness and Flank Wear in Turning of Nimonic C263 under Dry Cutting Conditions

J. Francis Xavier ¹, B. Ravi,² D. Jayabalakrishnan ³, Chakaravarthy Ezilarasan ⁴,
V. Jayaseelan ⁵ and G. Elias ⁶

¹School of Mechanical Engineering, VIT Bhopal University, Bhopal, India

²Department of Mechanical Engineering, Swarna Bharathi Institute of Science and Technology Khammam, Telangana, India

³Department of Mechanical Engineering, Sriram Engineering College, Chennai, India

⁴Center for Materials Research, Chennai Institute of Technology, Chennai, India

⁵Department of Mechanical Engineering, Prathyusha Engineering College, Chennai, India

⁶Department of Mechanical Engineering, College of Electrical and Mechanical Engineering, Addis Ababa Science and Technology University, Addis Ababa, Ethiopia

Correspondence should be addressed to G. Elias; elias.gmichael@aastu.edu.et

Received 2 September 2021; Revised 21 September 2021; Accepted 27 September 2021; Published 12 October 2021

Academic Editor: Karthikeyan Sathasivam

Copyright © 2021 J. Francis Xavier et al. This is an open access article distributed under the Creative Commons Attribution License, which permits unrestricted use, distribution, and reproduction in any medium, provided the original work is properly cited.

Aircraft component manufacturing sector is looking for high precision machining in aircraft components. The present work explores the operability of green manufacturing of Nimonic C263 using dry turning. Nimonic C263 is tough to turn owing to its inherent quality like low conductivity and more work hardening. Therefore, in order to improve this machined surface/integrity, the controlling factors were optimized based on desirability approach for minimum of surface roughness and flank wear during turning of this alloy using CBN insert. L27 orthogonal array was chosen to carry out the experiment. The effects of controlling factors, such as cutting speed (V), feed rate (S), and cut penetration/depth of cut (a_p) on the outputs, were also explored. The feed rate was a major impact to affect surface finish and flank wear. The average error percentage between the experimental and RSM models for surface finish was 4.76 percent and 2.79 percent for flank wear.

1. Introduction

High strength alloy Nimonic C263 has been extensively used in many decisive parts of aircraft. Due to the excellent mechanical properties, fatigue strength, and creep properties, this alloy is used in a high-temperature environment. However, FCC structure, gamma precipitates presence in this alloy cascades into the group of difficulty-to-cut materials as of its lower thermal conductivity and higher work hardening rate, which would damage the tool. Therefore, the machining of this hardened alloy is considered an important one for aircraft part manufacturers to ensure the quality of the parts. These factors depend on process parameters such as cutting swiftness, feed rate, and penetration of cut.

Ti-6Al 4V-ELI alloy was machined by Kechagias and colleagues [1] to determine the cutting force and surface roughness and the properties of machining aspects such as cutting speed, feed rate, and depth of cut on machining performances. For the experimental trials, L27 was used as a full factorial design. There is a consensus among experts that cutting speed should be set at 600 revolutions per minute, the feed rate should be 0.10 mm/rev, and the cut depth should be 0.50 mm. PCBN inserts with enhanced high toughness were used to finish turn the difficult to cut metal Inconel 716, and the machining attributes were evaluated. The PCBN insert was found to be the best to get quality surface finish. PCBN inserts with enhanced high toughness were used to finish turn the difficult to cut metal Inconel 716, and the machining attributes were

evaluated. The PCBN insert was found to be the best to get quality surface finish [2].

Ramesh et al. [3] investigated the machinability of titanium-based metal matrix composite during turning using CBN inserts. They have reported that the wear zones on the flank face were identified in turning this material at high cutting speed using CBN such as black and white zones. Debonding of attached materials from the tool was caused by abrasion and oxidation mechanisms that were discovered. Ren et al. [4] conducted dry machining experiments on Ti-6Al-0.6Cr-0.4Fe-0.4Si-0.01B (TC7) utilizing PCD and PCBN tools. They have investigated the machining performance of TC7 and the wear mechanism of PCD and PCBN tools. The wear of PCBN was more serious than PCD insert, and the adhesion-dissolution-diffusion mechanisms were also reported.

Das et al. [5] used an experimental trial on AISI 4340 steel that was conducted utilizing a multilayer-coated CVD (TiN/TiCN/Al₂O₃/TiN) carbide tool using a three-level factorial design employing Taguchi's L9 orthogonal array (OA). At varying levels of machine settings, they have noticed changes in surface shape and insert wear. They discovered that feed rate influenced surface roughness and flank wear more than other parameters, and that abrasion wear due to rubbing was the most common type of wear. Further, they have concluded that this coated tool can be effectively used in place of CBN and ceramic tools. Padhan et al. [6] have evaluated the machining performance in turning austenitic stainless steel Nitronic 60 under dry, compresses-air cooled machining environment, flooded, and minimum quantity lubrication. As SiAlON turned the steel, the cutting force, tool wear, cutting temperature, and surface roughness were evaluated. They came to the conclusion that the MQL technique increased and enhanced the machining performance of their machines. Cutting force and surface roughness decreased as cutting speed increased, while a force, roughness, and temperature increased when feed rate increased; yet, tool wear decreased.

CBN tool hard turning of maraging steel was optimized by [7], and they have used L27 orthogonal array to conduct experimental trails and reported that surface roughness and flank wear were affected by feed rate compared to other parameters. Further, DEFORM 3D software was used to simulate the temperature distribution at optimal machining condition, and 885°C was observed. Vinothkumar et al. [8] have reported the machining attributes in turning Inconel 718 alloy under dry and atomic spray cutting fluid using PVD coated carbide insert. They have concluded that the ASCF technique has an improved surface finish and reduced tool wear by about 17-34% compared to dry. These reductions were reported owing to the lubrication effect in the tool interface. Singh et al. [9] conducted turning trails on AISI 316L in a dry turning environment. Several process factors were selected for study: cutting speed, feed rate, cutting depth, and tool nose radius. Outputs included cutting force, tool flank wear, and surface roughness. To decrease tool wear and surface roughness, the process parameters were modified based on a desirability approach. According to them, the workpiece and tool develop contact at high nose radius levels, resulting in flank wear proportionate to the depth of cut. Rebecka et al. [10] have studied the wear mech-

anisms in turning difficult-to-cut alloy using PCBN and PCD insert, and it was observed that the fracture on the flank face was caused owing to deterioration mechanism. It is further found that PCD performed well compared to PCBN in view of life of the tool.

Volodymyr Bushlya et al. [11] conducted turning process at high speed on Inconel 718 using CBN insert, and they have reported that diffusion with boron and nitrogen wear mechanisms was found on the rake [11]. Wei Fan [12] reviewed the performance of carbide, ceramics, and CBN inserts on machining aeroalloys in terms of cutting tool failure, cutting tool material, cutting tool geometry, and chip morphology. PCBN insert retains its hardness at high temperature; however, it possesses two major limitations such as crack in insert and difficult in chip breaking. Lubin et al. [13] stated that tool wear and worst chip break are the two limitations of the PCBN inserts. Turning experimental trails were carried out on super alloy GH4169 using PCBN at supplying various pressure ranges cooling and machining attributes such as flank wear and cutting force were observed. The flank wear and cutting force were controlled by supplying high pressure cooling. Owing to great hardness, CBN inserts are recommended to machine the difficult-cut alloys; however, the control over flank wear was found to be major challenges. The abrasive wear mechanism was found to be major compare to addison and diffusion in turning process using CBN inserts. No scratches and marks were found on the machined surface during machining at high speed owing to high-temperature generation in the cut zone [14]. The properties and characteristics of inserts are main factors in the machining processes to get reliability. In view of machining performance, the CBN insert showed good results compared to ceramic during machining of super alloys, and the cutting temperature was more as the level of sped and depth of cut increases followed by feed rate [15].

Pardeep Kumar et al. [16] conducted turning experiment on AISI H13 using various CBN grades, and the parameters like work material hardness, cutting speed, and feed were found to be predominant factor on surface roughness and cutting forces. Further, it has been found that the CBN-10 grade found to be best than CBN-600 grade and CBN BNC-300 grade.

From the state of the art, it was identified that rapid tool wear during machining of any alloy would affect severely on the outputs, which also affects the integrity of the machined surface. There is also an inadequate research in dry tuning of Nimonic C263 using CBN insert. Therefore, appropriate tool material and geometry should be explored to get minimum of flank wear and enhanced the integrity. Therefore, strive is taken to study experimentally the effects of the factors on surface finish and flank wear in dry turning of Nimonic C263 using CBN. RSM was used to make a model to predict the machining attributes, and that model would also be benefited to predict the values of these attributes before the actual experiments.

2. Materials and Methods

The workpiece was made of Nimonic C263 alloy. The diameter of the work piece was 70 millimeters. The weight percentage of the chemical composition of Nimonic C263 and

TABLE 1: Chemical composition of Nimonic C263 and nomenclature of insert CBN.

S.no	Composition	Weight %	Nomenclature of CBN insert	
1	Ni	52.49	Back rake angle	-6°
2	Si	0.19	Side rake angle	-6°
3	Mn	0.46	End relief angle	-6°
4	Cr	20	Side relief angle	-6°
5	Mo	6.29	End cutting edge angle	5°
6	Cu	0.07	Side cutting angle	-5°
7	Fe	1.0	Nose radius	0.8 mm
8	Co	16.7	Tool holder	PCLNR 2020 K12
9	Ti	1.94		
10	Al	0.48		
11	Nb	0.04		
12	W	0.15		
13	V	0.02	CBN insert	Sandvik CNGA 120 408S01030A, 7025 grade
14	C	0.02		
15	S	0.001		
16	Ta	0.007		

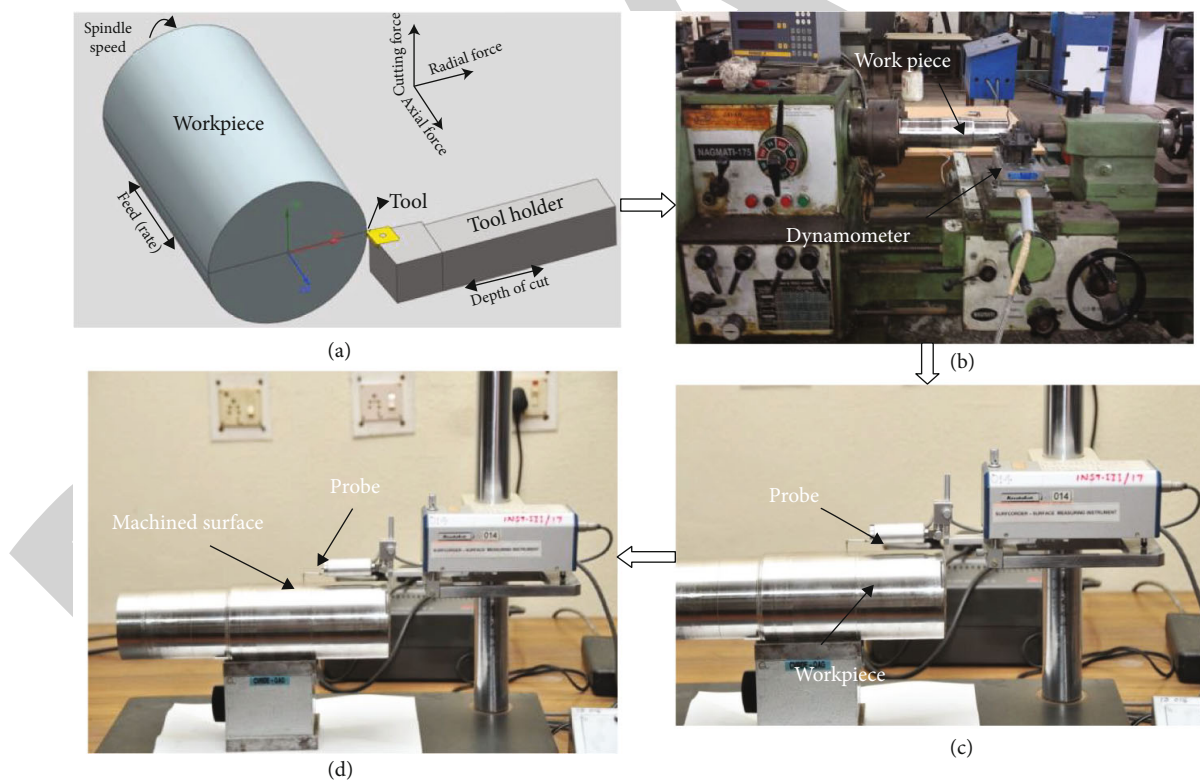


FIGURE 1: Experimental details: (a) turning setup, (b) experimental setup, (c) surf coder, and (d) tool maker microscope.

insert details of CBN are shown in the Table 1. According to a recent study, nickel-based alloys can be machined using materials such as CBN. Tools made from CBN have better thermal conductivity than carbide and ceramic cutting tools, allowing them to maintain their cutting wedge for longer

periods, function at faster cutting speeds, and produce superior surface finish [16].

The schematic view of the turning process, the experimental set-up, surface finish, and tool wear measurement are shown in Figure 1. The surface roughness and flank wear

TABLE 2: Parameters for machining.

S. No.	Control constraints	Units	Levels		
			L-1	L-2	L-3
1	V	m/min	80	125	190
2	S	mm/rev	0.055	0.096	0.159
3	a_p	mm	0.25	0.50	0.75

TABLE 3: Results from both experimental and RSM-modeled studies.

S. No.	Controlling factors			Experimental values		RSM values		% age error expt. vs. RSM	
	V	S	a_p	R_a (μm)	VB (mm)	R_a (μm)	VB (mm)	R_a (μm)	VB (mm)
1	80	0.055	0.25	2.55	0.30	2.51	0.301	1.56	0.33
2	80	0.055	0.50	2.2	0.32	2.34	0.317	5.98	0.93
3	80	0.055	0.75	2.35	0.34	2.18	0.338	7.23	0.58
4	80	0.096	0.25	2.8	0.33	2.88	0.329	3.04	0.30
5	80	0.096	0.50	2.6	0.35	2.71	0.348	4.05	0.57
6	80	0.096	0.75	2.4	0.36	2.56	0.372	6.25	3.22
7	80	0.159	0.25	3.1	0.38	3.02	0.362	0.33	4.73
8	80	0.159	0.50	3	0.39	2.87	0.385	4.33	1.28
9	80	0.159	0.75	2.8	0.40	2.73	0.413	2.50	3.14
10	125	0.055	0.25	2.25	0.29	2.18	0.291	3.11	0.34
11	125	0.055	0.50	2.1	0.31	2.00	0.306	4.76	1.29
12	125	0.055	0.75	1.7	0.33	1.85	0.326	8.10	1.21
13	125	0.096	0.25	2.65	0.30	2.67	0.315	0	4.76
14	125	0.096	0.50	2.55	0.345	2.49	0.333	0.74	3.47
15	125	0.096	0.75	2.65	0.365	2.34	0.356	11	2.46
16	125	0.159	0.25	2.93	0.32	2.96	0.342	1.01	6.43
17	125	0.159	0.50	2.6	0.36	2.80	0.364	7.14	1.09
18	125	0.159	0.75	2.5	0.41	2.66	0.391	6.05	4.63
19	190	0.055	0.25	1.6	0.42	1.76	0.393	9.09	6.42
20	190	0.055	0.50	1.65	0.38	1.58	0.407	4.24	6.63
21	190	0.055	0.75	1.45	0.42	1.41	0.426	2.75	1.40
22	190	0.096	0.25	2.65	0.39	2.43	0.412	8.30	5.33
23	190	0.096	0.50	2.15	0.45	2.25	0.429	4.44	4.66
24	190	0.096	0.75	1.9	0.46	2.09	0.451	9	1.95
25	190	0.159	0.25	2.8	0.45	2.94	0.430	4.7	4.44
26	190	0.159	0.50	2.95	0.44	2.77	0.451	6.10	2.43
27	190	0.159	0.75	2.7	0.47	2.62	0.477	2.96	1.46

were measured by surf coder and universal measuring microscope (UMM).

A factorial three-factor-three-level design was used in the experiment. The cutting speed, feed rate, and cut depth were all taken into account as controlling factors. The turning environment was dry during the experiment. In this experiment, L27 OA was arranged in an orthogonal array. These parameters are stated in sequence in Table 2. A software package called Design Expert was used to model and analysis the impact of parameters.

3. Modeling of Machining Parameters

3.1. Regression Analysis. Table 3 presents experimental results and RSM-modeled values for surface irregularities and wear of the flank. The regression model was developed to evaluate the surface roughness and flank wear as given in equations (1) and (2). Tables 4 and 5 show the results of the ANOVA for surface roughness and flank wear. From the ANOVA, roughness is influenced most by feed rate, followed by other parameters. However, the speed was the

TABLE 4: Surface irregularity: an analysis of variance (R_a - μm).

S. No.	Source	DOF	Seq-SOS	Adj MS	F	% contribution
1	Model	9	4.86	0.54	18.24	
2	V	1	0.79	0.79	26.71	14.71
3	S	1	3.14	3.14	106	58.47
4	a_p	1	0.46	0.46	15.43	8.56
5	$V \times S$	1	0.34	0.34	11.55	6.33
6	$V \times a_p$	1	7.654E-004	7.654E-004	0.026	0.014
7	$S \times a_p$	1	5.402E-004	5.402E-004	0.018	0.00010
8	V^2	1	4.730E-003	4.730E-003	0.16	0.088
9	S^2	1	0.066	0.066	2.23	1.22
10	a_p^2	1	6.000E-004	6.000E-004	0.020	0.0111
11	Residual	17	0.50	0.030		9.31
12	Total	26	5.37			100%

R-sq-97%

TABLE 5: Wear flank (VB-mm).

S. No.	Source	DOF	Seq SOF	Adj MQ	F	% contribution
1	Model	9	0.069	7.675E-003	25.70	
2	V	1	0.027	0.027	91.84	36.48
3	S	1	0.014	0.014	46.59	18.91
4	a_p	1	7.852E-003	7.852E-003	26.29	10.61
5	$V \times S$	1	3.971E-004	3.971E-004	1.33	0.536
6	$V \times a_p$	1	1.335E-005	1.335E-005	0.045	0.018
7	$S \times a_p$	1	1.900E-004	1.900E-004	0.64	0.25
8	V^2	1	0.014	0.014	45.45	18.91
9	S^2	1	5.139E-008	5.139E-008	1.721E-004	0.00006944
10	a_p^2	1	3.750E-005	3.750E-005	0.13	0.050
11	Residual	17	5.077E-003	2.987E-004		6.86
12	Total	26	0.074			100%

R-sq-95%

TABLE 6: Optimization goals and limits.

S. No.	Parameter and Result	Goal	Minor limit	Greater limit	Inferior weight	Superior weight	Significance
1	V-m/min	Is in variety	80	190	1	1	3
2	S-mm/rev	Is in choice	0.055	0.159	1	1	3
3	a_p -mm	Is in choice	0.25	0.75	1	1	3
5	R_a - μm	Minimalize	1.45	3.1	1	1	3
6	VB-mm	Minimalize	0.29	0.47	1	1	3

TABLE 7: Greatest global solutions for optimization.

Solution No.	V-m/min	S-mm/rev	a_p -mm	R_a - μm	VB-mm	D value
1	135	0.055	0.597	1.867	0.321	0.787
2	135	0.055	0.598	2.16	0.299	0.787
3	135	0.055	0.590	2.15	0.301	0.787

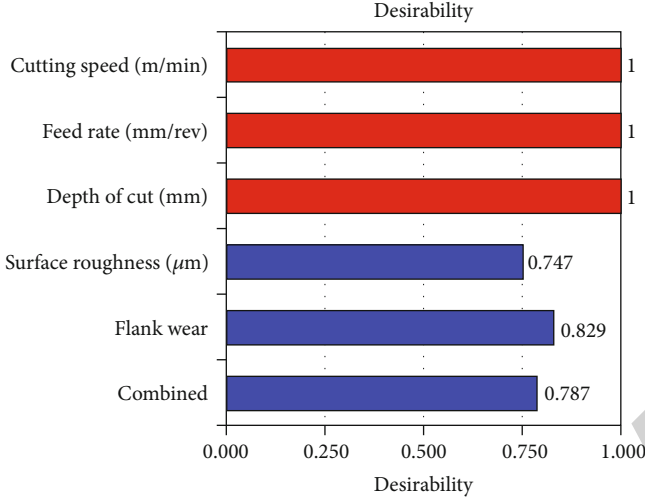
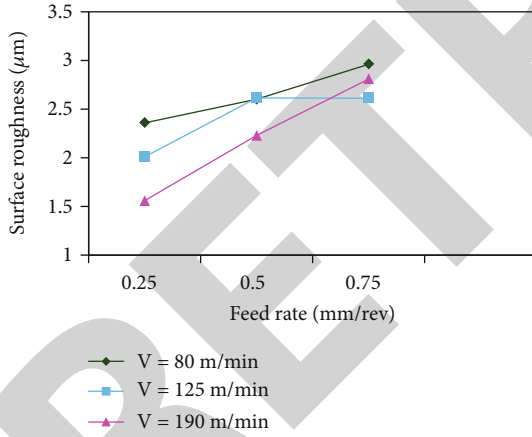
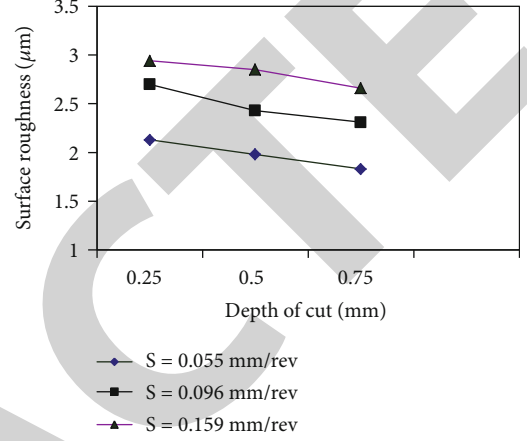


FIGURE 2: Desirability histogram.

FIGURE 3: Impact of "V," Vs, and "S" on R_a .

most predominant factor in spoiling status of the flank wear, followed by other factors.

$$\begin{aligned} \text{Surface roughness } R_a, (\mu\text{m}) = & +3.09 - 0.01 \times V + 7.63 \times S - 0.77 \\ & \times ap + 0.05 \times V \times S - 5.77657E \\ & - 004 \times V \times ap + 0.49 \times S \times ap \\ & + 9.65208E - 006 \times V^2 - 36.08 \\ & \times S^2 + 0.16 \times ap^2, \end{aligned} \quad (1)$$

FIGURE 4: Impact of " a_p ," Vs, and "S" on R_a .

$$\begin{aligned} \text{Flank wear VB, (mm)} = & +0.43971 - 3.45937E - 003 \\ & \times V + 0.62419 \times S + 0.02 \times ap \\ & - 1.92528E - 003 \times V \times S \\ & - 7.62943E - 005 \times V \times ap \\ & + 0.29 \times S \times ap + 1.63515E \\ & - 005 \times V^2 + 0.03 \times S^2 + 0.04 \times ap^2. \end{aligned} \quad (2)$$

4. Parametric Optimization

For the multiresponse optimization, the RSM-based desirability was utilized to optimize the factors for minimum of flank wear and surface roughness in turning of this alloy. When optimizing, a variety of goals are taken into consideration. A goal, lower and upper limits, and weights and importance of components are listed in Table 6. These three elements and reactions are included in the goals. "Minimize" aims to surface roughness and flank wear. "Within range" is the goal when it comes to all other aspects. A goal's desirability function could be adjusted by assigning it a weight. Table 7 shows the five best solutions to the multiresponse optimization problem using cubic boron nitride. Figure 2 shows the desirability histogram for the best choice. Causes and responses are treated independently when calculating the desirability score. There are three bars for the input parameters and four to five bars for required surface roughness and flank wear values. Three bars indicate the input parameters. Last but not least, the eighth bar represents the aggregate desirability value.

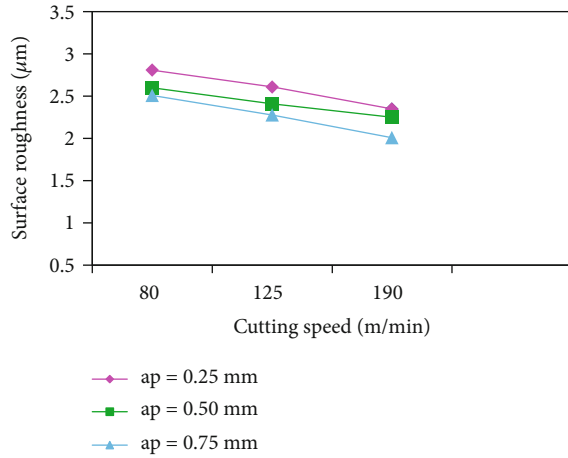


FIGURE 5: Impact of "V"-Vs-" a_p " on R_a .

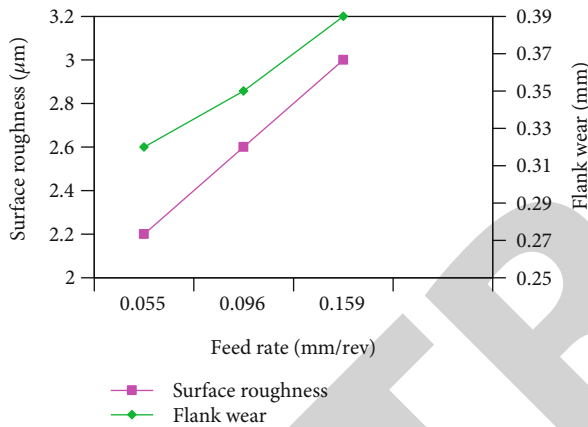


FIGURE 6: Impact of "S" at V=80 m/min and a_p 0.50 mm on VB and R_a .

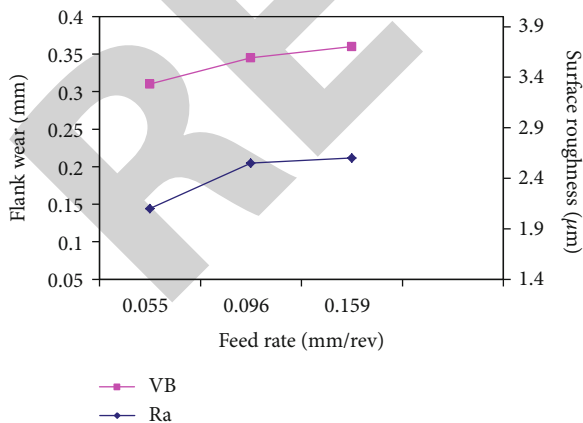


FIGURE 7: Impact of "S" at V=125 m/min and a_p 0.50 mm on VB and R_a .

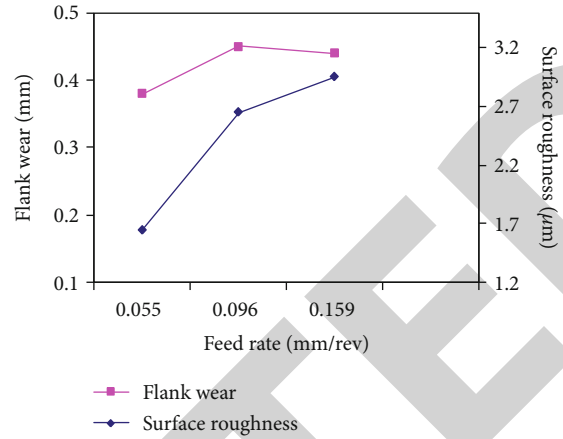


FIGURE 8: Impact of "S" at V=190 m/min and a_p 0.50 mm on VB and R_a .

5. Consequence of Progression Parameters on Machining Attributes

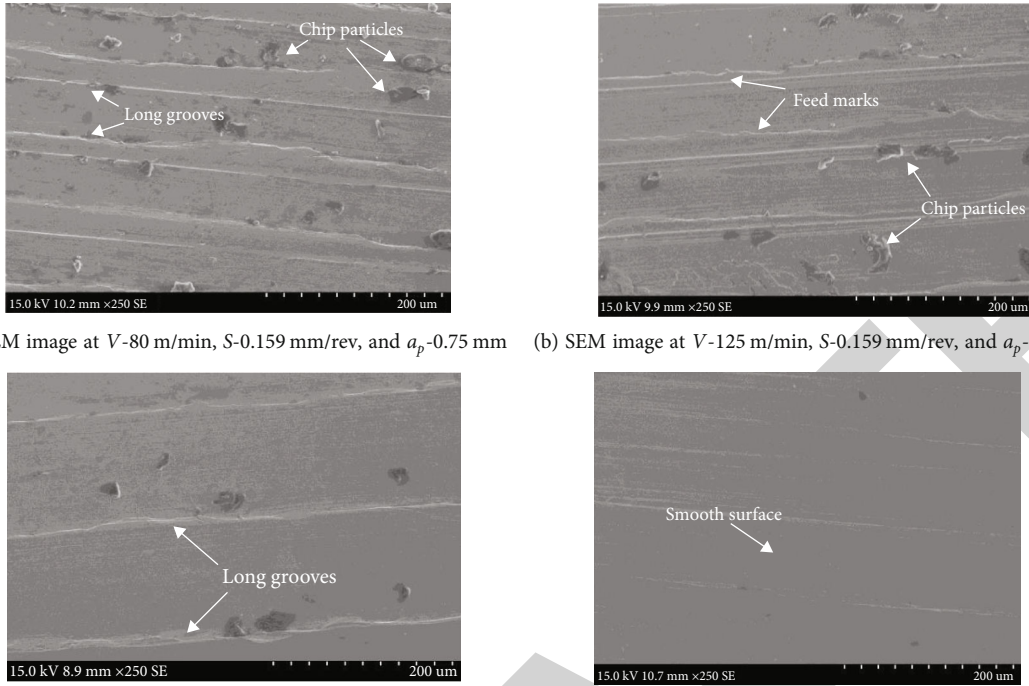
The consequence of process limitations on retorts such as surface irregularities and wear of flank was estimated and appraised when Nimonic C-263 alloy was turned using cubic boron nitride.

5.1. Surface Roughness Analysis. At varying speeds and feed rate, Figure 3 shows the change in the rate of surface roughness, and it is evident that the surface finish reduces with increasing feed rate. The surface finish is improved as the speed level increase at low feed rate, and the same findings were reported by [17]. Figure 4 shows that both feed rate and depth of cut affect surface roughness. If feed rate increases, surface roughness increases, but if cut depth is increased and feed rate decreases, surface irregularity is significantly reduced. As the depth of the incision increased, the surface roughness decreased.

A reduction in surface roughness can be expected due to work hardening the layer surface at a deeper cut. As increasing the cut depth and speed improves the surface finish and is shown in Figure 5, at high cut depth and speed, the roughness is lower than the roughness observed at low speed and cut depth. The feed rate is a critical aspect that requires more consideration than cutting speed and depth of cut, because at high feed, the worn flank is rubbed, and the roughness changes dramatically.

At all cutting speeds, surface roughness tends to grow. Enroute the limited thermal conduction of the Nimonic C-263 alloy causes heat to be generated at points where the tool and work are in contact. The higher import of the feed rate followed by speed and cut depth designates the rubbing action on flank face, and the surface irregularities are associated on the machined surface. The roughness seems to increase when the level of flank wear increases at all range of the speed, and it is evidently illustrated in Figures 6–8; also, the heat at tool-work contact zone is generated more owing to low thermal conductivity of Nimonic C263.

The micrograph of the machining shallow under different cutting settings is shown in Figure 9(a)–9(d). There is a



(a) SEM image at $V=80$ m/min, $S=0.159$ mm/rev, and $a_p=0.75$ mm (b) SEM image at $V=125$ m/min, $S=0.159$ mm/rev, and $a_p=0.75$ mm
 (c) SEM image $V=190$ m/min, $S=0.096$ mm/rev, and $a_p=0.75$ mm (d) SEM image $V=190$ m/min, $S=0.159$ mm/rev, and $a_p=0.75$ mm

FIGURE 9: (a)–(d) SEM micrographs of machined surface at different cutting conditions using CBN insert.

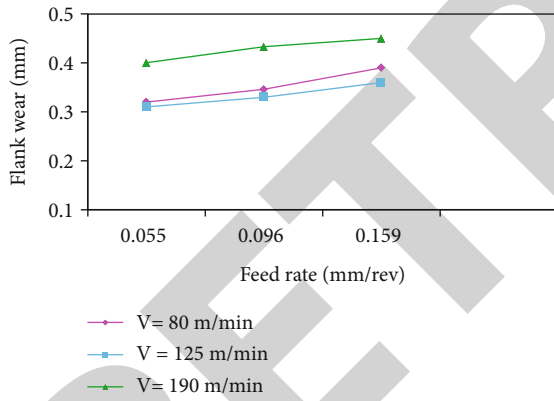


FIGURE 10: Impact of “S,” Vs, and “V” on “VB”-mm.

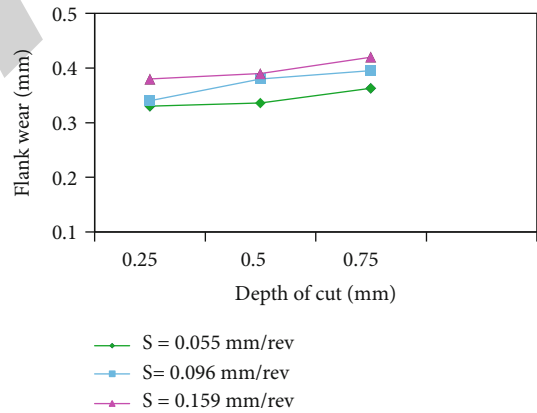


FIGURE 12: Impact of “ a_p ,” Vs, and “S” on “VB”-mm.

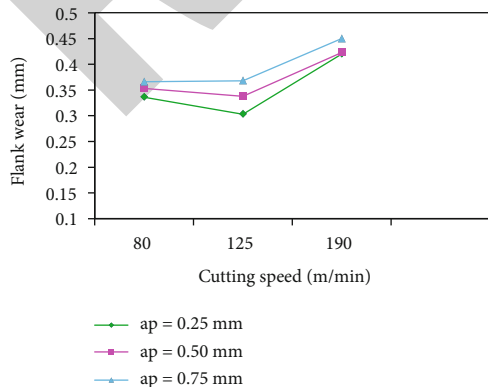


FIGURE 11: Impact of “V,” Vs, and “ a_p ” on “VB”-mm.

smeared surface as well as feed marks and chip particles. Many of these surface conditions are related to stresses, and temperature increases in the cutting zone, as well as distortion on the flank face and observance of the work portion substantial to its surface as a whole. Owing to the pressure weld between the tool and the chip, which may erratically resolve and scrape the machined surface, the chip may attach to the tool surface at lower cutting speeds. Another possibility is that the tool material was periodically removed, resulting in an increase in wear and the resulting degrading of the machined surface, as seen in Figure 9(a)–9(d). The metal is easier to remove when it is heated up at a high cutting speed [14]. This is accredited to the fact that increasing the speed, causing rise in temperature in the cutting zone, thereby dropping the surface

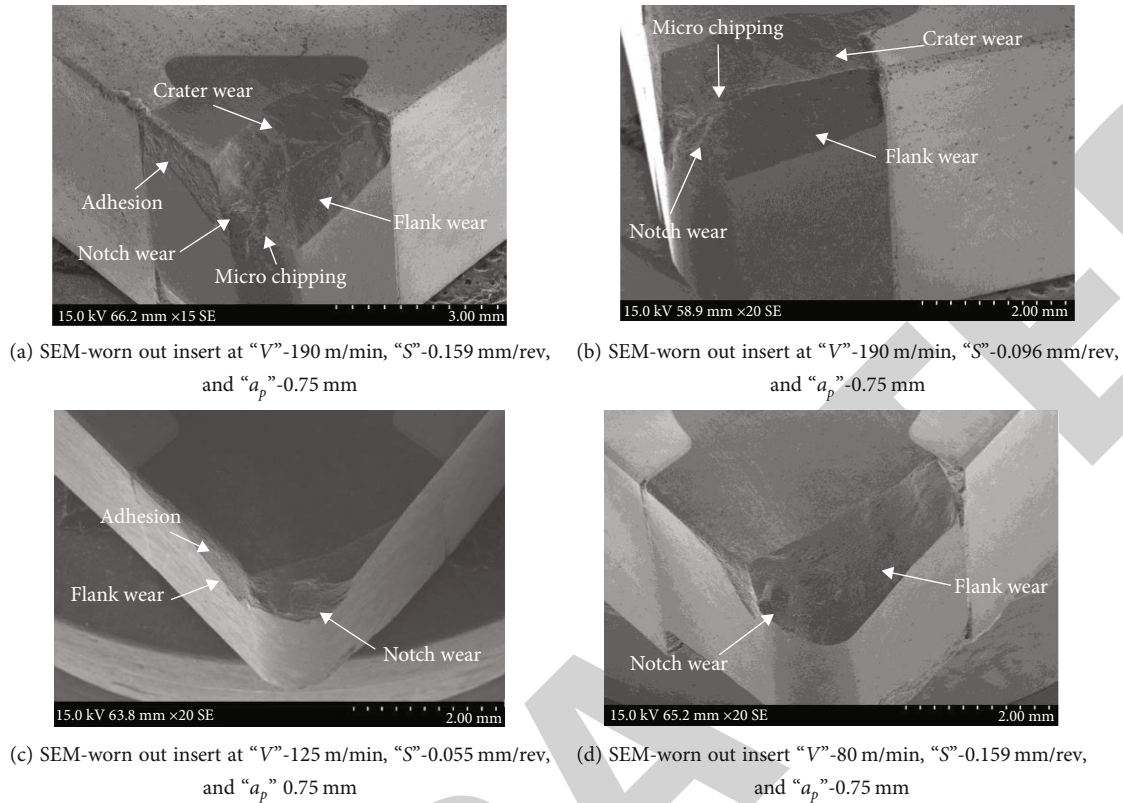


FIGURE 13: (a)–(d) SEM-worn out cutting edge observed at various levels of parameters while turning Nimonic C263 using CBN.

TABLE 8: Plan of the confirmation experiments and results for cubic boron nitride insert.

Sol.No	V-m/min	S-mm/rev	a_p -mm	Predicted	R_a - μ m		VB-mm	
					Experimental values	Predicted	Experimental values	
1	135	0.055	0.597	1.867	1.75	0.321	0.315	
2	135	0.055	0.598	2.16	2.25	0.299	0.290	
3	135	0.055	0.590	2.15	2.05	0.301	0.310	

roughness, and improving exterior texture, as seen from the micrograph given in Figure 9(a)–9(d).

5.2. Consequence of Machining Restrictions on Flank Wear.

Figure 10 shows how feeding rate influences flank wear at dissimilar cutting rates. Feed rate has a bigger effect on flank wear than cutting speed, as shown in the graph. The least amount of flank wear is produced by low feed rates and moderate cutting speeds. In comparison to cutting depth, flank wear increases much more slowly with cumulative cutting speed. The gradual degradation to the cutting edge and the resulting upsurge in interaction area among the cutting edge and the machined work surface could be responsible for the increased flank wear with higher penetration of cut. Cut speeds in the middle range and depths of cut in the lower range result in decreased flank wear as shown in Figure 11. With reference to Figure 12, the rates of flank wear increase as level of feed rate and depth of cut increases. However, the rate of increase of the flank wear is affected lot by feed compare to cut depth.

The observed flank wear at high feed and cut depth is 0.42 mm; it is remarkable more than the flank wear of 0.33 mm, which is seen at a minimum level of feed and cut depth. Therefore, it is found that, during turning Nimonic C-263 alloy with a cubic boron nitride, cutting speed and feed rate significantly impact and the impact of the parameters on flank wear can be seen in SEM images as shown in Figure 13(a)–13(d). The buildup edge and wear of the flank are treated as major pattern of failure in machining the alloys using CBN insert [12]. Adhesion, abrasion, diffusion, and microchipping [11, 12] are the primary wear processes identified in machining Nimonic C-263 with a cubic boron nitride insert, as evident in Figure 13(a)–13(d).

6. Confirmation Experiment for Optimal Solution Using Cubic Boron Nitride Insert

CBN inserts were utilized to confirm the optimal solutions provided by the desirability technique in dry turning the Nimonic C263 alloy. The optimal experimental condition is set as 135 m/min cutting speed, and 0.055 mm/rev feed rate,

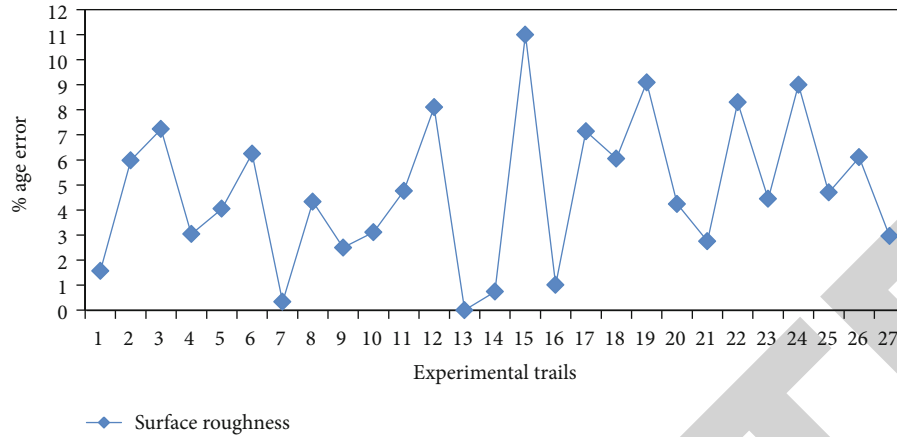


FIGURE 14: % age error: expt. vs. RSM- R_a (μm).

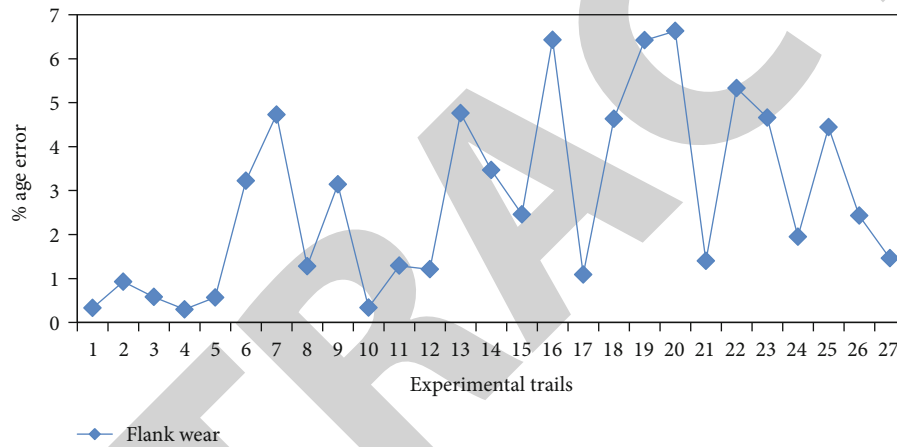


FIGURE 15: % age error: expt. vs. RSM-VB (mm).

and 0.597 mm cutting depth. The predicted values of surface roughness and flank wear obtained from the optimal condition are shown in the Table 8, and the forecasted values were found to be close to the experimental trail values.

The % age error among the experimental and RSM predicted values of surface roughness and flank wear is shown in Figures 14 and 15, respectively. The average percentage error for surface finish and wear of the flank was found to be 4.76 percent and 2.79 percent, respectively. As a result, using the RSM model, roughness and flank wear can all be forecasted with 95 percent confidence.

7. Conclusion

The following findings have been drawn based on experimental work and analysis performed on Nimonic C 263 alloy utilizing CBN inserts.

- (i) The developed RSM model was verified, which is close to the value experimental trail values. It shows the average % age error 4.76% and 2.79% for roughness and wear of the flank, respectively

- (ii) Optimum of surface finish and wear of the flank was obtained as multiresponse optimization at V -135 m/min, S -0.055 mm/rev, and a_p -0.597, and the predicted values were validated

- (iii) Adhesion, abrasion, and microchipping were found to be wear mechanism while turning Nimonic C263 with CBN

- (iv) Feed rate badly affects the cutting edge of the insert followed by speed and depth of cut

- (v) High feed rate and low speed badly affect the surface regularity. However, the roughness is reduced at high cut depth, high level of speed, and low feed rate in turning Nimonic C263 with CBN

- (vi) The surface roughness observed at low speed and high feed rate was found to be 47% higher than the surface roughness observed at high cutting speed and low feed rate

- (vii) The flank wear observed at high cutting speed and high feed rate was found to be 31% more than the

Retraction

Retracted: Analysis of Ethanol to Reduce Solid Particle Pollution in SI Engines

Journal of Nanomaterials

Received 11 July 2023; Accepted 11 July 2023; Published 12 July 2023

Copyright © 2023 Journal of Nanomaterials. This is an open access article distributed under the Creative Commons Attribution License, which permits unrestricted use, distribution, and reproduction in any medium, provided the original work is properly cited.

This article has been retracted by Hindawi following an investigation undertaken by the publisher [1]. This investigation has uncovered evidence of one or more of the following indicators of systematic manipulation of the publication process:

- (1) Discrepancies in scope
- (2) Discrepancies in the description of the research reported
- (3) Discrepancies between the availability of data and the research described
- (4) Inappropriate citations
- (5) Incoherent, meaningless and/or irrelevant content included in the article
- (6) Peer-review manipulation

The presence of these indicators undermines our confidence in the integrity of the article's content and we cannot, therefore, vouch for its reliability. Please note that this notice is intended solely to alert readers that the content of this article is unreliable. We have not investigated whether authors were aware of or involved in the systematic manipulation of the publication process.

Wiley and Hindawi regrets that the usual quality checks did not identify these issues before publication and have since put additional measures in place to safeguard research integrity.

We wish to credit our own Research Integrity and Research Publishing teams and anonymous and named external researchers and research integrity experts for contributing to this investigation.

The corresponding author, as the representative of all authors, has been given the opportunity to register their agreement or disagreement to this retraction. We have kept a record of any response received.

References

- [1] P. Sivaprakasam, P. M. Prabu, M. Srinivasan, S. Balakrishnan, V. S. Karthikeyan, and M. C. P. Selvan, "Analysis of Ethanol to Reduce Solid Particle Pollution in SI Engines," *Journal of Nanomaterials*, vol. 2021, Article ID 2726645, 11 pages, 2021.

Research Article

Analysis of Ethanol to Reduce Solid Particle Pollution in SI Engines

P. Sivaprakasam ¹, **P. Maheendera Prabu** ², **M. Srinivasan** ³, **S. Balakrishnan** ⁴,
V. S. Karthikeyan ⁵ and **M. Chithirai Pon Selvan** ⁶

¹Department of Mechanical Engineering, College of Electrical and Mechanical Engineering, Center of Excellence-Nano Technology, Addis Ababa Science and Technology University, Addis Ababa, Ethiopia

²Department of Ocean Engineering, Indian Institute of Technology Madras, Chennai, 600036 Tamil Nadu, India

³Department of Mechanical and Mechatronics, College of Engineering, Dhofar University, Salalah 211, PO Box 2509, Oman

⁴Department of Chemical Engineering, College of Biological and Chemical Engineering, Addis Ababa Science and Technology University, Addis Ababa, Ethiopia

⁵Department of Mechanical Engineering, Christian College of Engineering and Technology, Oddanchatram, 624619 Tamil Nadu, India

⁶School of Science and Engineering, Curtin University Dubai, Dubai International Academic City, Dubai, UAE

Correspondence should be addressed to P. Sivaprakasam; shiva@aastu.edu.et

Received 3 August 2021; Revised 29 August 2021; Accepted 1 September 2021; Published 28 September 2021

Academic Editor: Karthikeyan Sathasivam

Copyright © 2021 P. Sivaprakasam et al. This is an open access article distributed under the Creative Commons Attribution License, which permits unrestricted use, distribution, and reproduction in any medium, provided the original work is properly cited.

The present work carries out an experimental comparative analysis of the performance and emission of exhaust gases of the Otto cycle with four automotive times. The comparison was made between alternative fuels such as E10, E15, and E20, with both 90 and 95 octane each the commercialized fuel. The experimental tests were carried out with an engine load corresponding to 25% of the maximum load. After carrying out the tests, the following conclusions can be reached: on the performance and effective parameters of the engine, the obtained best indicator, and as expected, was the case E10 (90 octane). Also, the E15 (90 octane) showed a slight difference compared to the reference fuel E10 (90 octane). About emissions, it was found that these decrease as the concentration of ethanol in the fuel increases.

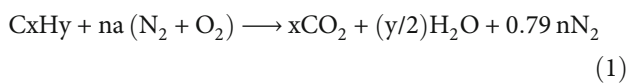
1. Introduction

Gasoline is a liquid, volatile, and flammable compound consisting of carbon and hydrogen atoms (hydrocarbons), boiling temperatures ranging from 40°C to 200°C, and various forms of paraffin (aliphatic hydrocarbons). Gasoline is obtained from petroleum; a nonrenewable natural resource is a compound of organic origin formed by a complex non-homogeneous mixture of hydrocarbons. Also, it is the result of fossil remains. The hydrocarbon molecules that compose it are from the simplest and smallest CH₄- methane, to elaborate and extensive with more than 50 carbon atoms [1, 2]. A considerable variation in parameters was found, such as colour, density, gravity, viscosity, heat capacity, contami-

nants etc. [3]. These variations are due to the different proportions of different hydrocarbons present. Octane number becomes the most relevant property of gasoline since it is highly related to the performance of the vehicle's engine. It is the measure of antiknock quality, meaning the ability to burn without causing detonation. Gasoline has an octane number between 85 and 100 depending on the type of gasoline [4, 5]. The volatility property of gasoline has been measured by vapor pressure and the values from 0.7 to 0.85 mmHg. Gasoline is very volatile, and it indirectly represents the content of volatile components that provide safety for gasoline, transportation, and storage [6]. The distillation curve property has related to the composition of gasoline, its volatility, and its vapor pressure. Therefore, 10% distillation,

with a boiling temperature below 70°C, was considered. The presence of volatile components has ensured easy cold starting. At 50% distillation, with a boiling temperature below 140°C, correct volatility and maximum power are provided during engine acceleration. For the case, 90% the endpoint of distillation, boiling temperature ranges between 190°C and 225°C. If this amount occurs in large proportions, gasoline can have corrosive effects on the engine's metal parts and exhaust pipes. It is also related to the harmful impacts on the environment and is an important factor in creating acid rain [7, 8]. Ethanol, also known as ethyl alcohol, is an organic compound (produced from renewable sources) with the chemical formula C₂H₅-OH (carbon, hydrogen, and hydroxyls). Under normal conditions, it appears as a liquid, colourless, clean, pleasant, but highly penetrating odour, caustic, and burning flavour; likewise, it is miscible in all proportions, flammable, and volatile. It has classified into two products: hydrated and anhydrous, and it depends on the volume of water they contain [9–11]. The main environmental advantage of these fuels lies in their origin. Biofuels come mainly from biomass, which has extracted part of the carbon dioxide (CO₂) released into the atmosphere. Therefore, biofuels as fuels do not lead to a net increase in carbon dioxide from the atmosphere, thus helping to minimize the effect of greenhouse gases [12, 13]. Gasohol is the mixture of gasoline and alcohol in different proportions as fuel in explosion engines designed to burn petroleum derivatives. Gasohol can be mixed with ethyl alcohol (ethanol) or methyl alcohol (methanol), although ethanol is the type of alcohol used for commercial purposes. Methanol has been used in a more limited way because it is toxic [14]. The ratio between the two fuels is indicated by the percentage of ethanol preceded by a capital E. In this way, E10 gasohol comprises 10% ethanol and 90% gasoline, and E85 contains by mixing 85% ethanol and 15% gasoline (Calam et al. [15]). For experimental investigations, E10, E15, and E20 were considered. The stoichiometric air-fuel ratio (A/F) is a dimensionless parameter necessary to describe the air sufficient for the complete combustion of used fuel, so the air is much higher than the amount of fuel for the chemical reaction [16]. The ideal or stoichiometric value of the AF ratio for most commercial gasoline is very close to 15:1. Injection systems or carburetors serve to regulate the fuel content for any airflow. Gasoline engines typically have an AF range from 12:1 to 18:1, depending on operating conditions. Stoichiometric combustion is defined as complete combustion carried out with a strict amount of oxygen; the air used in combustion is the minimum necessary to contain the amount of oxygen corresponding to the complete oxidation of all the components of the fuel [17].

The expression of this combustion is



There are two scenarios of carbon combustion such as complete and incomplete carbon combustion. When complete carbon burning produces CO₂, which is the main con-

tributor to the greenhouse effect, this component is an inevitable consequence of combustion. The incomplete carbon combustion creates CO toxic gas that, in high concentrations, can even cause death [18]. The minimum fuel required is consumed, thus producing the least CO₂ [19]. The presence of sulfur in fuels gives in variable proportions; oxidation of sulfur can produce SO₃. At high flame temperatures, the nitrogen in the fuel and the nitrogen in the oxidizing air can combine with oxygen to form NO. This product in the atmosphere slowly combines with oxygen in the air to form NO₂ [20]. Sulfur contact with combustion or atmospheric water can give rise to condensed sulfuric acid (H₂SO₄) that accompanies raindrops, giving rise to what is known as "Acid rain." At high flame temperatures, the nitrogen in the fuel and the nitrogen in the oxidizing air can combine with oxygen to form NO; this product in the atmosphere slowly combines with oxygen in the air to create NO₂ [20]. The present investigation deals with the method to reduce polluting gas emissions using alternative fuels, such as gasohol in concentrations E10, E15, and E20. Also, it is not enough to modify the engine without this concentration of ethanol.

2. Materials and Methods

The ethanol and commercial gasohol were mixed to obtain the E10, E15, and E20 gasohols, experimental methodology, the experimental test protocol, standardization of the turning regimes for each fuel, and finally the equations necessary for the calculation of some important parameters. The E15 and E20 gasohol involved in the experimental tests [21]. To make the necessary measurements for the mixtures, graduated cylinders and a conical funnel were used. Measurements were made based on one litre (maximum capacity of the cylinder). Then, they were poured into a container [22]. The procedure was performed for each of the six fuels. The mixtures were made from the commercial gasohol E10 (90% gasoline and 10% ethanol). The amounts of absolute ethanol were added to obtain the volumetric concentrations [23, 24]. The calculations of the quantities of fuel required were made based on 1000 mL (1 litre), and volumetric concentrations of the fuels involved in the tests are given in Table 1. The physicochemical properties of gasoline and anhydrous ethanol are presented in Table 2.

3. Experimental Methodology

The main characteristics of the engine used in the tests with specifications are given in Table 3. The engine is connected to a direct current dynamometric brake with a maximum revolution speed of 3000 rpm; the engine's testing was restricted to that speed. The referred dynamometric brake has a reader camry force analog in charge of taking a reading of the force demanded by the load to which the motor is subjected, expressed in kgf, and can test engines with a maximum load of 50 kg for a torque of 147 Nm with a resolution of ±1.

Equation (2) is used to calculate torque. An induction sensor (±1 rpm) is installed on the axis of said brake to have

TABLE 1: Physicochemical properties of gasoline and anhydrous ethanol.

S. no	Parameters	Obtained measurement
Gasoline		
1	Boiling temperature (°C)	38.8
2	Flash temperature (°C)	21
3	Auto-ignition temperature (°C)	250
4	Water solubility	Insoluble
5	Vapor pressure (kPa)	6.5-7.8
6	Lower calorific power (kJ/kg)	44,000
7	Superior calorific power (kJ/kg)	47 300
8	Octane number (RON, MON)	91/80
9	Stoichiometric ratio (A/F)	14.7-15
Anhydrous ethanol		
1	Boiling temperature (°C)	78.5
2	Flash temperature (°C)	13
3	Auto-ignition temperature (°C)	363
4	Water solubility	Miscible
5	Vapor pressure (mmHg at ambient T °)	43
6	Lower calorific power (kJ/kg)	26800
7	Superior calorific power (kJ/kg)	29600
8	Octane number (RON, MON)	109/98
9	Stoichiometric ratio (A/F)	9

a detailed and instantaneous record of engine revolutions, data evidenced in the test bench control panel. Regarding the measurement of fuel consumption, a volumetric measurement system was implemented between one plate and another in the measurement tank. A measurement reading was taken at stabilizing engine speed to consume the volume differential of 29.5 cm³.

At atmospheric conditions, a digital thermo hygrometer was used to measure temperature (±1°C) and relative humidity (±1%). Two thermometers (2°C) were installed, one at the refrigerant inlet and the other at the refrigerant exit. These thermometers were installed in the refrigerant transport ducts, thus ensuring a constant and instantaneous reading of engine coolant temperature for each proposed speed. The barometric pressure data, measured twice a day before starting and ending the tests, is due to its invariance of reading as it is a single location. U-shaped inclined water manometer (±1 cm H₂O) in the test bench was used, necessary for measuring differential pressure through the nozzle of the buffer tank in the air intake process. After completing the relevant derivation, the system was already prepared for measuring gasses, and the measurements were initiated using a Bosch type emission analyzer. It is necessary to modify the exhaust pipe, which extends outside the roof, to measure combustion gases. As a result, the analyzer probe had to be inserted through a bypass above the exhaust pipe silencer. Insert the probe into the tube and wait approximately 0.5 minutes for the analyzer to record the data for CO, CO₂, NO, O₂, HC, lambda factor, temperature, and engine oil. It is necessary to modify the exhaust pipe, which extends out-

side the roof, to measure combustion gases. As a result, the analyzer probe needed to be inserted through a bypass above the exhaust pipe silencer. The various engine parameters are calculated using Equations (2)–(10).

The following is the calculation of parameters:

Effective torque

$$Me = F_d \times g \times l, \quad (2)$$

where Me is the effective torque (Nm), F_d is the force (kgf), g is the gravity (m/s²), and l is the length of dynamometric brake arm (m).

Effective power

$$Ne = Me \times \eta \times \pi 30000, \quad (3)$$

where Ne is the effective power (kW) and η is the rate of turn (RPM).

Mass flow of fuel

$$\dot{m}c = \dot{V} \times \rho c. \quad (4)$$

Where:

$\dot{m}c$: Mass flow [Kg / s]

\dot{V} : Volumetric flow [cm³ / s]

ρc : Fuel density [Kg / cm³]

In the case of E10, E15 and E20 gasohol:

$$\dot{m}c = V_e \times \rho_e + \dot{V}_{gas} \times \rho_{gas}. \quad (5)$$

Where:

V_e : Volumetric flow of ethanol in the mixture (cm³ / s)

ρ_e : Density of ethanol [Kg / cm³]

\dot{V}_{gas} : Volumetric flow of commercial gasohol in the mixture (cm³ / s)

ρ_{gas} : Density of gasohol in the mixture [Kg / cm³]

Mass air flow

$$\lambda = (AF)_R / (AF)_t \quad (6)$$

Where:

$(AF)_t$: Theoretical air fuel ratio.

$(AF)_R$: Real air fuel ratio.

$$(AF)_R = \dot{m}a \cdot \dot{m}c \longrightarrow \dot{m}a = (AF)_R \times \dot{m}c. \quad (7)$$

Where:

$\dot{m}a$: Mass air flow [g / h]

Specific fuel consumption

$$SFC = [\dot{m}_{gas} + (PC.PCI_{gas})\dot{m}c]360 \quad (8)$$

Where:

SFC : Specific fuel consumption [g / KW - h]

PCI_e : Lower calorific value of ethanol [KJ / Kg]

PCI_{gas} : Lower calorific value of gasoline [KJ / Kg]

TABLE 2: Volumetric concentrations of the fuels involved in the tests.

Mix (1000 mL)	Ethanol percentage (%)	E10 gasohol volume (mL)	Initial volume of ethanol (mL)	Volume of ethanol added (mL)	Volume of ethanol in the mixture (mL)
E10	10	1000	78	—	78
E15	15	867.7	67.7	132.3	200
E20	20	813.4	63.4	186.6	250

TABLE 3: Main characteristics of the engine used in the tests.

S.no	Specification	Value
1	Power	40 kW at 5500 rpm
2	Torque	76.5 Nm at 2800 rpm
3	Number of cylinders	3
4	Displacement	993 cc
5	Cylinder diameter	76 mm
6	Piston race	73 mm
7	Compression ratio	9:1
8	Fuel injection	Carburetor
9	Ignition type	Spark
10	Ignition order	1-2-3

Average effective pressure.

$$p_{me} = W_e V_T \quad (9)$$

Where:

p_{me} : Effective mean pressure [KPa]

W_e : Work done by the Engine [KJ]

V_T : Displacement [m^3]

Effective performance.

$$\eta_e = (N_e \dot{m}_{gas} PCI_{gas} + \dot{m}_e PCI_e) 100 \quad (10)$$

Where:

PCI_{gas} =44000KJ/Kg

PCI_e =26800KJ/Kg

η_e : Effective return [%]

4. Results and Discussion

The characteristic curves of the calculated variables are presented using dispersion graphs in this result: effective torque (T_e), effective power (P_e), specific fuel consumption (SFC), fuel mass flow (\dot{m}_c), mass airflow (\dot{m}_a), and effective return (η_e), and the emissions are as follows: carbon monoxide (CO), carbon dioxide (CO_2), and nitrogen oxides (NO). The comparisons were made for E10, E15, and E20 by taking an average of all measurement regimens between the two fuels while keeping the corresponding octane level (OC).

4.1. Engine Performance

4.1.1. Torque. Figure 1 presents the results of torque produced by various biofuels with respect to speed. The E10 (90) octanes made the highest torque, with a maximum peak

of 51 Nm for a 2000 rpm regime, while the E10 (95) had the lowest torque, with a value of 22 Nm. This may be due to the mechanical operating design of the main engine components and their responsiveness to different octane numbers. Hence, the manufacturer recommends using 90 octane fuel and not 95 or other octane levels. The results obtained from torque for 90 octane fuels, in which the average torque of the E10 DE (90) amounts to 47 Nm. At the same time, the E15 presents an average torque of 40, representing a decrease in this last to commercial gasohol of 7.5%; likewise, for the E20, an average torque of 31 Nm was obtained, representing a reduction of 34% compared to E10. In 95 octane fuels, the E10 obtained values were an average torque of 35 Nm, compared to the E15 average torque of 34. The latter represents a 3% decrease to E10, and on the other hand, E20 increase of 0.09% compared to E10, an insignificant increase [25].

4.1.2. Effective Power. Figure 2 shows that the values obtained power for different speeds (rpm) with varying conditions of fuel. It shows that the power directly depends on the engine's speed; as the speed increases, the sufficient power delivered by the engine also increases. Also, the highest point was offered by the E10 (90) octane with adequate power of 13.04 kW at 3000 rpm. On the other hand, the 90 octanes E20 offered the lowest point with a value of 6.85 kW. The effective power results for 90 octane fuels; the E10 presented an average sufficient power of 12.08 kW. Compared to the 10.50 kW of the E15, the latter represents a decrease corresponding to 15.28%. The results for 95 octane fuels, commercial gasohol E10 provided an average sufficient power rising to 9.16 kW, while E15 showed a power of 8.99 kW, which compared to E10 represents a decrease of 3.09%. On the other hand, the E20 provided an average power of 8.36 kW, representing 34.7% less than the E10. Then, the E20 delivered a brake power of 9.17 kW, which compared to the E10 leads, considering the values of their respective standard deviations, to a negligible variation [26].

4.1.3. Specific Fuel Consumption. Figure 3 shows the results obtained for the specific fuel consumption with speed. The figure shows that the 90 octane E20 presents remarkable supremacy over other fuels, whose maximum value of 700.73 g/kW-h at 2400 rpm. The minimum value obtained by the 95 octane E20 was 232.65 g/kW-h at 1500 rpm. The results for 90 octane fuels, commercial gasohol E10 provided a specific fuel consumption of 269.24 g/kW-h. At the same time, E15 showed a specific consumption of 293.14 g/kW-h, which, compared to E10, represents an increase of 9.0%. Then, the E20 delivered a specific consumption of 575.78 g/kW-h, which,

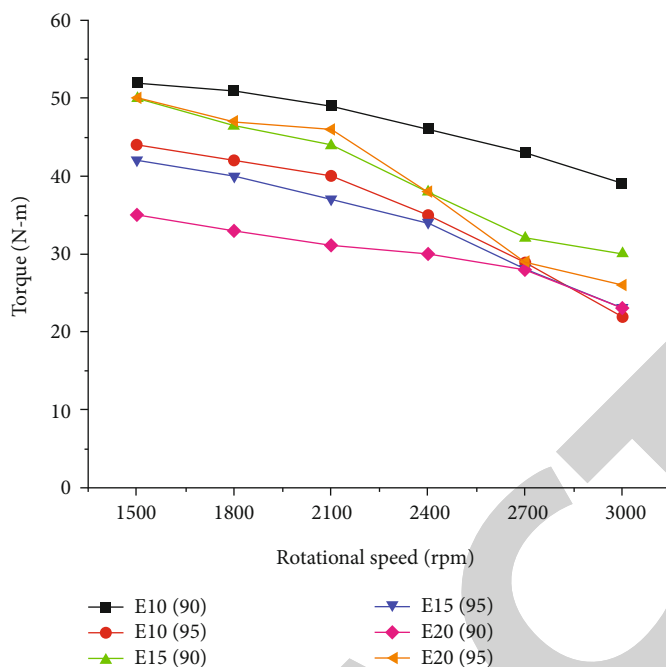


FIGURE 1: Effective torque vs. RPM for different ethanol-gasoline blends and octane levels.

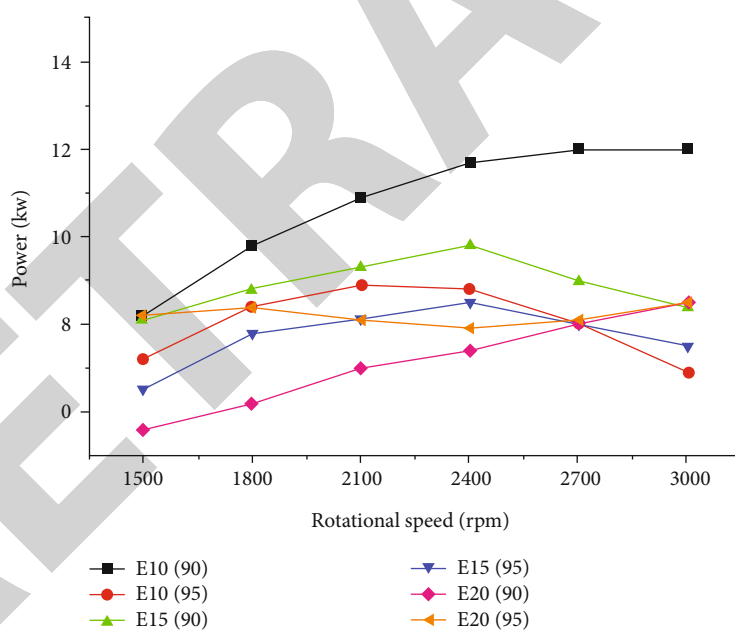


FIGURE 2: Effective power vs. RPM for various ethanol-gasoline blends and octane levels.

compared to the E10, implies an increase of 115.29%. The results of the 95 octane fuels are that the commercial gasohol E10 presented a specific fuel consumption of 356.26 g/kW-h. The E15 had a specific consumption of 354.42 g/kW-h compared to E10, representing a decrease of 0.52%. Next, the E20 presented a specific consumption of 328.18 g/kW-h, representing a decrease of 8.95% compared to the E10 [27].

4.1.4. Fuel Mass Flow. Figure 4 depicts the mass flow of fuel sustained in it. From the figure, the mass flow of fuel

increases as the rotational speed increases. The 90 octane E20 exhibits a substantial difference when compared to other fuels, with a maximum value of 0.00159 kg/s acquired at 2700 rpm and a lowest value of 0.000562 kg/s obtained at 1500 rpm for the 95 octane E20. The results obtained from the fuel mass flow only for 90 octane fuels showed that the E15 presents an average mass fuel flow of 0.00082 kg/s compared to the 0.00083 Kg/s obtained by the E10 represents a decrease of 1.63%. E20 had an average mass fuel flow of 0.001268 kg/s, representing an increase of 53.22%. About

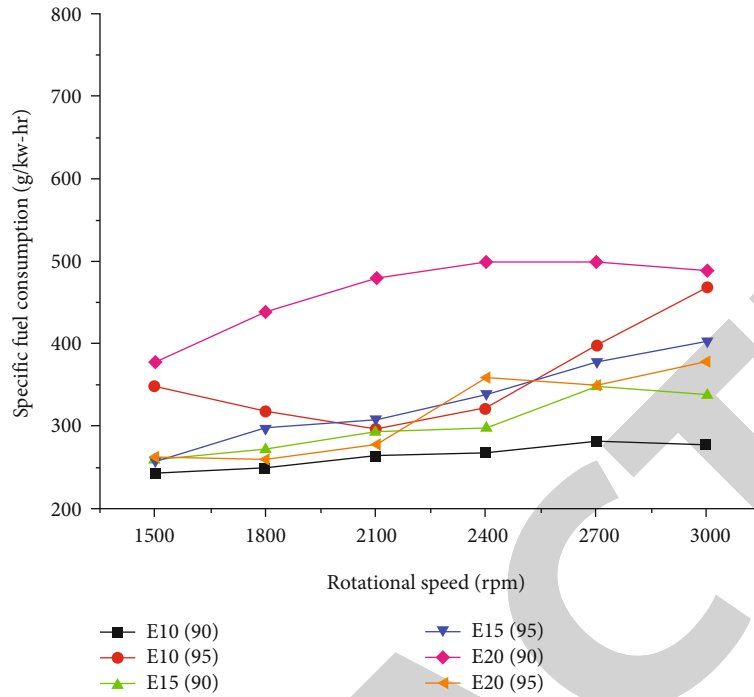


FIGURE 3: Specific consumption vs. RPM for various gasoline-ethanol blends and octane levels.

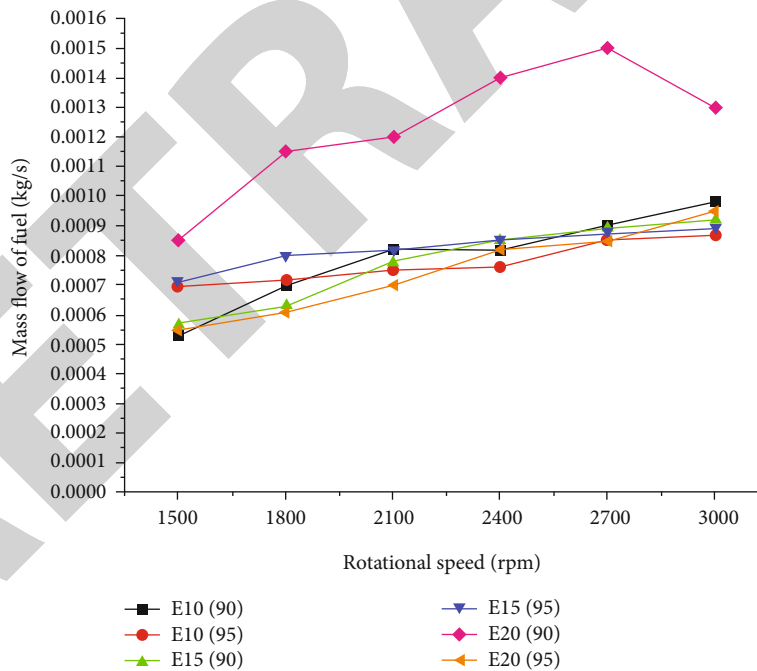


FIGURE 4: Mass flow of fuel vs. RPM for different ethanol-gasoline blends and octane levels.

95 octane fuels, it follows that the average mass flow of fuel corresponding to E15 amounts to a value of 0.000825 kg/s, compared to E10, which obtained a value of 0.000796 kg/s represents an increase of 3.83%. In contrast, E20 obtained a value of 0.000796 kg/s, which compared to E10 represents a decrease of 3.6%.

4.1.5. *Mass Airflow.* Figure 5 depicts the air mass flow and the effects of this parameter. The test results show that this parameter does not have a proportional relationship with the speed of rotation. In the same, it is evidenced that, analogously to the results of the maximum fuel flow, the E20 (90) octane shows notorious supremacy over the other fuels,

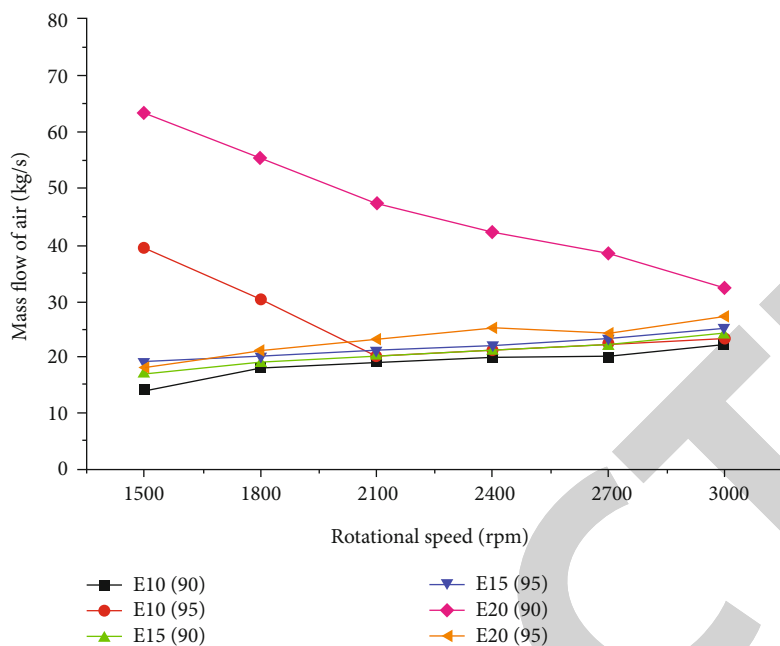


FIGURE 5: Mass air flow vs. RPM for different ethanol-gasoline blends and octane levels.

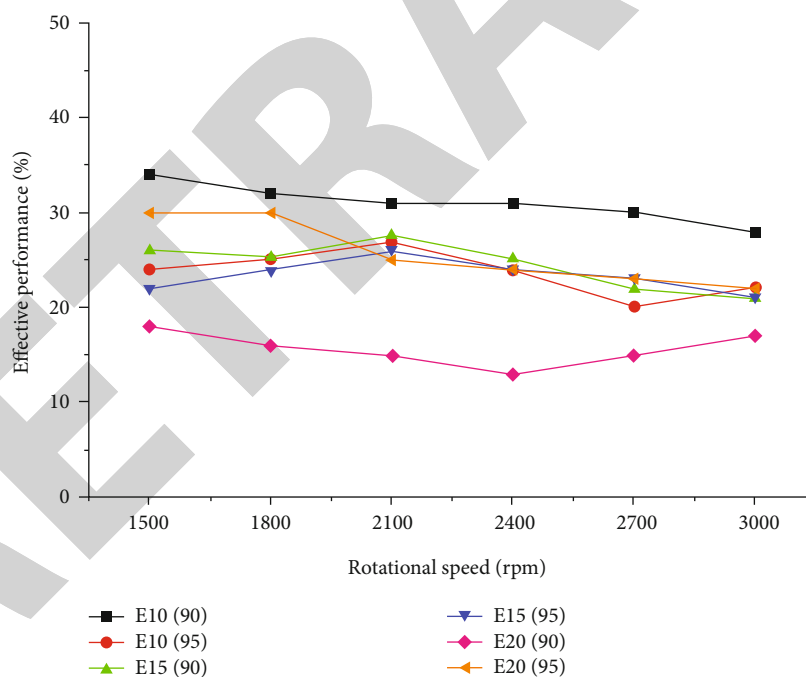


FIGURE 6: Effective performance vs. RPM for different ethanol-gasoline blends.

reaching a maximum peak at 1500 rpm of 61.14 kg/s. Likewise, the minimum value corresponds to the E20 of 95 octanes at 1500 rpm, which amounts to 14.38 kg/s. The mass flows of air corresponding to 90 octane fuels were found to be 19.82 kg/s and 20.4 kg/s for E10 and E15, respectively. E20 showed an average mass airflow of 44.74 kg/s, which, compared to the value obtained by E10, offers a 133% increase. The results obtained for 95 octane fuels, the average

mass airflow of 24.24 kg/s that corresponds to E10 can be deduced, and the E15 showed an average value of 20.37 kg/s compared to E10 that shows a decrease of 17.67%. Likewise, E20 obtained an average value of 20.57 kg/s and 16.9% less than E10.

4.1.6. *Effective Performance.* Figure 6 shows the results obtained corresponding to the adequate performance of

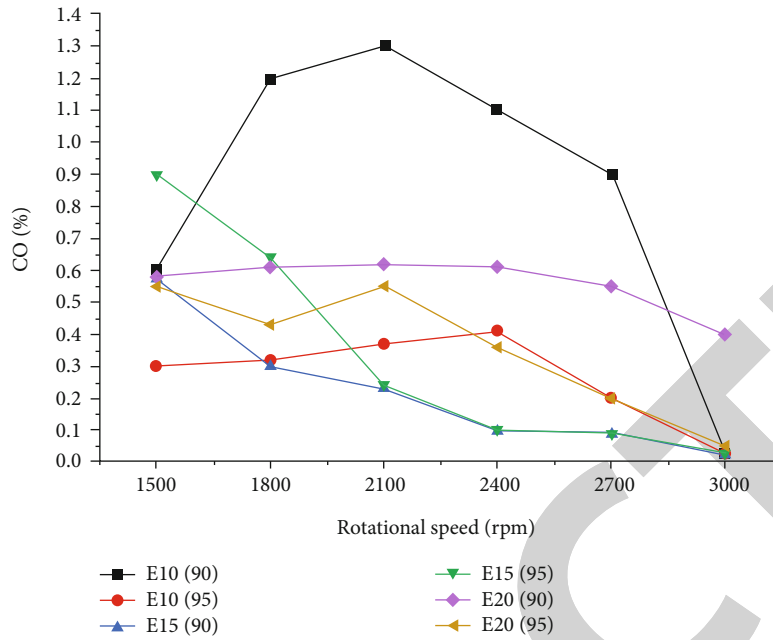


FIGURE 7: Carbon monoxide vs. RPM for different concentrations of ethanol-gasoline and octane levels.

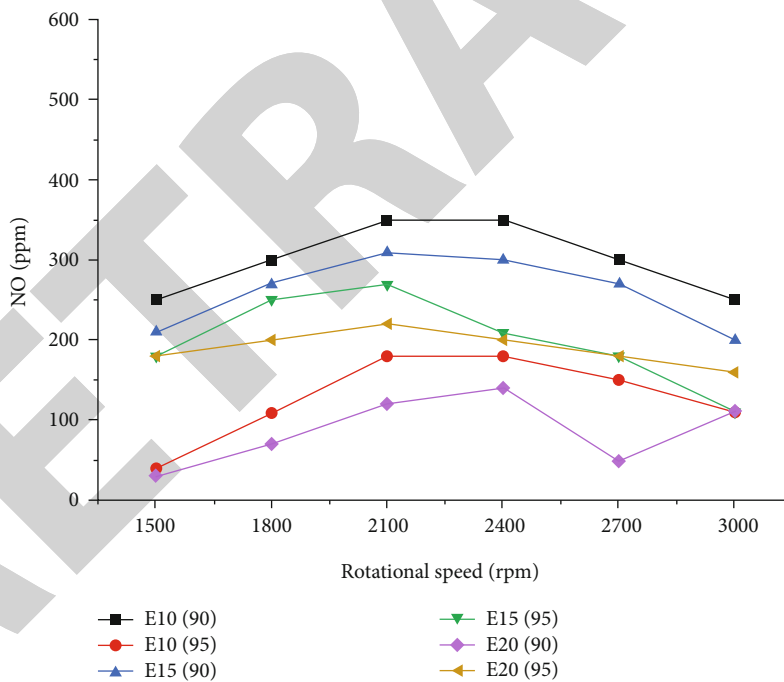


FIGURE 8: Nitrogen oxides vs. RPM for different ethanol-gasoline blends and octane levels.

the engine operating with different fuels. The highest engine performance was observed with E20 (95) octane at 1500 rpm with a value of 37.4 percent, as shown in the figure. The E20 at 1500 revolutions is data obtained through theoretical calculations (interpolation) and not experimental, hence its high standard deviation. At 1500 rpm with a value of 33.5%, the 90 octane E10 obtains immediately lower noninterpolated data. The test analysis and comparison was per-

formed with datasets equal to E20 with their respective standard deviation. The better performance results were obtained by using E10 (90 octane). The specific results for 90 octane fuels deduced an average effective yield for the E15 of 29.27%. Compared to the value obtained by the E10, an average yield of 31.58% represents a decrease of 8.56%. The E20 obtained an average return of 15.44%, representing a decrease of 53.9% compared to E10. The results for

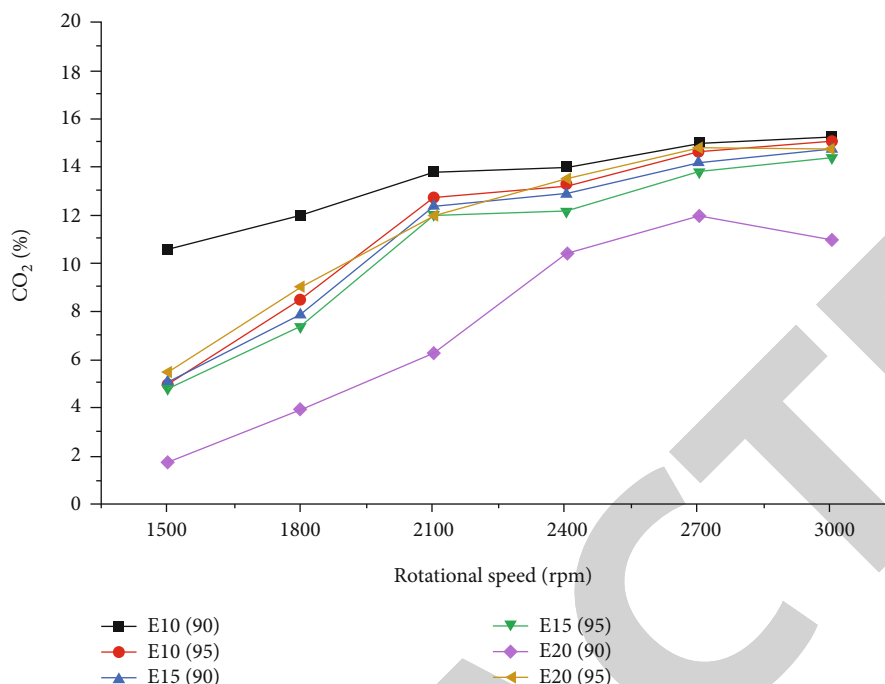


FIGURE 9: Carbon dioxide vs. RPM for different ethanol-gasoline blends and octane levels.

95 octane fuels show average effective rates of 24.4%, equal to E15, which are not significantly different compared with 24.53% produced from E10. For its part, the E20 obtained a performance of 26.87%, which represents an increase of 10.96% to the E10 [28].

4.2. Emission Characteristics

4.2.1. Carbon Monoxide Emissions (CO). Figure 7 shows the level of the variable CO for all different concentrations of ethanol in the fuel and octane levels. In this, one can notice a high dispersion of the data, and it does not have a proportional relationship to the speed of rotation. Similarly, the E10 of 90 octanes with a value of 4.2% at 2100 rpm achieved the highest value. E15 (95) octane, with a rating of 0.02%, was the lowest value. To the specific results for 90 octane fuels, an average CO emission of 0.19% corresponding to E15 can be deduced, which, compared to the 0.93% that the E10 showed, represents a decrease of 81.44%. E20 led to an average CO concentration of 0.58%, which means a decrease corresponding to 36.9% to that obtained by E10. The complete results for 95 octane fuels, an average CO emission of 0.27% deduced for E15, compared to 0.25% shown by E10, an increase of 9.4%. For its part, E20 showed an average CO concentration of 0.25%, which leads to a null variation of data obtained for both fuels (E15 and E10) [29, 30].

4.2.2. Nitrogen Monoxide Emissions (NO). Figure 8 shows the results obtained for the variable NO for each of the six fuels involved in the tests. The figure depicts the data's specific dispersion. Results found for 90 octane fuels solely, where average 276.7 ppm emissions of this gas are equivalent to E15, representing an 11.7% drop compared to the 309.4 ppm of the E10. Similarly, the E20 of 95 octanes

with a value of 511 ppm obtained the highest value at 1500 rpm, while the E10 (95) octane with a value of 7 ppm obtained the lowest value. The E20 presented an average emission of nitrogen oxides of 98.58 ppm, which, compared to the value of E10, represents a corresponding decrease of 69.36%. For the 95 octane fuels, an average NO emission corresponding to the E15 of 224.2 ppm can be seen, compared to 151.72 ppm of E10, representing an increase of 49%. Likewise, in the case of E20, it presents a value of 256.6 ppm, representing an increase of 70.6% to E10 [29].

4.2.3. Carbon Dioxide Emissions (CO₂). Figure 9 presents the results obtained for the CO₂ variable for each of the six fuels involved in the tests. In this case, the E10's rate of rotation of 90 octane at 3000 rpm is proportionally increasing at 16.02%, while the E20 (90) octane at a value of 2.55% at 1500 rpm was the lowest value. The test results show that for 90 octane fuels, the CO₂ emissions are 13.3% at E15 and 16% at E10. The E20 presented an average emission of carbon dioxide of 8.39%, which, compared to the value of E10, represents a corresponding decrease of 46.9%. For the results of the 95 octane fuels, it can see an average carbon dioxide emission corresponding to E15 of 14.05%, which, compared to 13.05% of E10, represents an increase of 9.4%. Likewise, E20 presents a value of 13.23%, representing an invaluable variability to E10.

5. Conclusions

When gasohol was used in higher ethanol concentrations than the commercial one, E15 and E20, the engine had complications to stabilize it at low revolutions due to the need to modify the engine. The power loss of engine was found at

2100 rpm in the E15 and 2400 rpm in the E20 fuel compositions. The experimental tests concluded that the E10 achieved the maximum effective performance for the various fuels evaluated (90). The E15 of 90 octanes would be an excellent alternative fuel option for engine performance because there is a minimal difference between fuel and another. CO₂ emissions were connected with octane level and ethanol concentration, which was confirmed by the present investigation, which stated that as ethanol concentration increases, CO₂ emissions decrease. The CO has found that when the concentration of ethanol increases. This is owing to the increased concentration of oxygen atoms in ethanol. A larger amount of oxygen is required to burn the fuel, demonstrating more notoriety between the E10 and E15, reducing up to 100%. In terms of emissions, fuels with a higher ethanol concentration have a considerable advantage over traditional fuels. However, the difference between the E15 and the E20 is not as noticeable. Based on the above results, it is concluded that the 90 octane E15 is the fuel with which it is possible to reduce the emissions of a 4-stroke engine for automotive use without this significantly affecting its performance.

Data Availability

The data used to support the findings of this study are included within the article.

Disclosure

It was performed as a part of the employment of Addis Ababa Science and Technology University, Ethiopia.

Conflicts of Interest

The authors declare that they have no conflicts of interest regarding the publication of this paper.

References

- [1] Y. İcingür and A. Calam, "The effects of the blends of fusel oil and gasoline on performance and emissions in a spark ignition engine," *Journal of the Faculty of Engineering and Architecture of Gazi University*, vol. 27, pp. 143–159, 2012.
- [2] O. I. Awad, O. M. Ali, R. Mamat et al., "Using fusel oil as a blend in gasoline to improve SI engine efficiencies: a comprehensive review," *Renewable and Sustainable Energy Reviews*, vol. 69, pp. 1232–1242, 2017.
- [3] E. Vanzela, W. C. Nadaleti, R. A. Bariccatti et al., "Physico-chemical properties of ethanol with the addition of biodiesel for use in Otto cycle internal combustion engines: results and revision," *Renewable Sustainable Energy Reviews*, vol. 74, pp. 1181–1188, 2017.
- [4] S. Li, W. Li, M. Xu, X. Wang, H. Li, and Q. Lu, "The experimental study on nitrogen oxides and SO₂ emission for oxy-fuel circulation fluidized bed combustion with high oxygen concentration," *Fuel*, vol. 146, pp. 81–87, 2015.
- [5] B. M. Masum, H. H. Masjuki, M. A. Kalam, S. M. Palash, and M. Habibullah, "Effect of alcohol-gasoline blends optimization on fuel properties, performance and emissions of a SI engine," *Journal of Cleaner Production*, vol. 86, pp. 230–237, 2015.
- [6] J. M. Bergthorson and M. J. Thomson, "A review of the combustion and emissions properties of advanced transportation biofuels and their impact on existing and future engines," *Renewable & Sustainable Energy Reviews*, vol. 42, pp. 1397–1417, 2015.
- [7] M. C. Ferreira, A. J. Meirelles, and E. A. Batista, "Study of the fusel oil distillation process," *Industrial & Engineering Chemistry Research*, vol. 52, no. 6, pp. 2336–2351, 2013.
- [8] W. N. M. W. Ghazali, R. Mamat, H. Masjuki, and G. Najafi, "Effects of biodiesel from different feedstocks on engine performance and emissions: a review," *Renewable & Sustainable Energy Reviews*, vol. 51, pp. 585–602, 2015.
- [9] A. K. Agarwal, H. Karare, and A. Dhar, "Combustion, performance, emissions and particulate characterization of a methanol-gasoline blend (gasohol) fuelled medium duty spark ignition transportation engine," *Fuel Processing Technology*, vol. 121, pp. 16–24, 2014.
- [10] O. M. Ali, R. Mamat, N. R. Abdullah, and A. A. Abdullah, "Effects of blending ethanol with palm oil methyl esters on low temperature flow properties and fuel characteristics," *International Journal of Advanced Science and Technology*, vol. 59, pp. 85–96, 2013.
- [11] L. G. Anderson, "Effects of using renewable fuels on vehicle emissions," *Renewable & Sustainable Energy Reviews*, vol. 47, pp. 162–172, 2015.
- [12] C. Ji, C. Liang, Y. Zhu, X. Liu, and B. Gao, "Investigation on idle performance of a spark-ignited ethanol engine with dimethyl ether addition," *Fuel Processing Technology*, vol. 94, no. 1, pp. 94–100, 2012.
- [13] S. M. Sangeeta, M. Pande, M. Rani et al., "Alternative fuels: an overview of current trends and scope for future," *Renewable Sustainable Energy Reviews*, vol. 32, pp. 697–712, 2014.
- [14] E. Rajasekar, A. Murugesan, R. Subramanian, and N. Nedunchezian, "Review of NO_x reduction technologies in CI engines fuelled with oxygenated biomass fuels," *Renewable Sustainable Energy Reviews*, vol. 14, no. 7, pp. 2113–2121, 2010.
- [15] A. Calam, Y. İcingür, H. Solmaz, and H. Yamık, "A comparison of engine performance and the Emission of fusel oil and gasoline mixtures at different ignition timings," *International Journal of Green Energy*, vol. 12, no. 8, pp. 767–772, 2015.
- [16] S. Kumar, J. H. Cho, J. Park, and I. Moon, "Advances in diesel-alcohol blends and their effects on the performance and emissions of diesel engines," *Renewable Sustainable Energy Reviews*, vol. 22, pp. 46–72, 2013.
- [17] F. D. Mayer, L. A. Feris, N. R. Marcilio, and R. Hoffmann, "Why small-scale fuel ethanol production in Brazil does not take off?," *Renewable Sustainable Energy Reviews*, vol. 43, pp. 687–701, 2015.
- [18] J. E. Anderson, D. M. DiCicco, J. M. Ginder et al., "High octane number ethanol-gasoline blends: Quantifying the potential benefits in the United States," *Fuel*, vol. 97, pp. 585–594, 2012.
- [19] R. H. Chen, L. B. Chiang, M. H. Wu, and T. H. Lin, "Gasoline displacement and NO_x reduction in an SI engine by aqueous alcohol injection," *Fuel*, vol. 89, no. 3, pp. 604–610, 2010.
- [20] B. M. Masum, H. H. Masjuki, M. A. Kalam, I. M. Rizwanul Fattah, S. M. Palash, and M. J. Abedin, "Effect of ethanol-gasoline blend on NO_x emission in SI engine," *Renewable Sustainable Energy Reviews*, vol. 24, pp. 209–222, 2013.

Retraction

Retracted: Emission Measurement Analysis of Sapodilla Seed Oil Blending Fueled IC Engine

Journal of Nanomaterials

Received 11 July 2023; Accepted 11 July 2023; Published 12 July 2023

Copyright © 2023 Journal of Nanomaterials. This is an open access article distributed under the Creative Commons Attribution License, which permits unrestricted use, distribution, and reproduction in any medium, provided the original work is properly cited.

This article has been retracted by Hindawi following an investigation undertaken by the publisher [1]. This investigation has uncovered evidence of one or more of the following indicators of systematic manipulation of the publication process:

- (1) Discrepancies in scope
- (2) Discrepancies in the description of the research reported
- (3) Discrepancies between the availability of data and the research described
- (4) Inappropriate citations
- (5) Incoherent, meaningless and/or irrelevant content included in the article
- (6) Peer-review manipulation

The presence of these indicators undermines our confidence in the integrity of the article's content and we cannot, therefore, vouch for its reliability. Please note that this notice is intended solely to alert readers that the content of this article is unreliable. We have not investigated whether authors were aware of or involved in the systematic manipulation of the publication process.

Wiley and Hindawi regrets that the usual quality checks did not identify these issues before publication and have since put additional measures in place to safeguard research integrity.

We wish to credit our own Research Integrity and Research Publishing teams and anonymous and named external researchers and research integrity experts for contributing to this investigation.

The corresponding author, as the representative of all authors, has been given the opportunity to register their agreement or disagreement to this retraction. We have kept a record of any response received.

References

- [1] P. M. Prabu, P. Sivaprakasam, V. Perumal, S. C. Kim, P. Balasubramani, and S. S. Kumar, "Emission Measurement Analysis of Sapodilla Seed Oil Blending Fueled IC Engine," *Journal of Nanomaterials*, vol. 2021, Article ID 2385356, 8 pages, 2021.

Research Article

Emission Measurement Analysis of Sapodilla Seed Oil Blending Fueled IC Engine

P. Maheandera Prabu ¹, P. Sivaprakasam ², Varatharaju Perumal ³, Sung Chul Kim,⁴
P. Balasubramani ⁵ and S. Santosh Kumar ⁶

¹Department of Ocean Engineering, Indian Institute of Technology Madras, Chennai, 600036 Tamil Nadu, India

²Department of Mechanical Engineering, College of Electrical and Mechanical Engineering, Center of Excellence-Nano Technology, Addis Ababa Science and Technology University, Addis Ababa, Ethiopia

³Department of Automotive Technology, Ethiopian Technical University, Addis Ababa, Ethiopia

⁴School of Mechanical Engineering, Yeungnam University, Gyeongsan, Gyeongbuk 712-749, Republic of Korea

⁵Department of Mechanical Engineering, Sona College of Technology, Salem, India

⁶Department of Mechanical Engineering, Indian Institute of Technology Indore, Indore, 453552 Madhya Pradesh, India

Correspondence should be addressed to P. Sivaprakasam; shiva@aastu.edu.et

Received 8 July 2021; Accepted 3 August 2021; Published 14 August 2021

Academic Editor: Karthikeyan Sathasivam

Copyright © 2021 P. Maheandera Prabu et al. This is an open access article distributed under the Creative Commons Attribution License, which permits unrestricted use, distribution, and reproduction in any medium, provided the original work is properly cited.

This present work focused on investigating the thermal behavior and emission level of sapodilla oil mixed with diesel to an internal combustion (IC) engine. The behavior of the engine is measured via brake thermal efficiency (BTE), brake-specific energy consumption (BSEC), heat release rate (HRR), cylinder pressure, and cumulative heat release rate (CHRR). The test results were evaluated with diesel fuel. Carbon deposits were low in sapodilla seed oil with slight variation of calorific value than standard diesel fuel. BTE value for case B20 is found to equal diesel fuel. For lower and higher blends, the cylinder pressures are lower than the diesel fuel. HRR decreased as increased of the blend ratio. Inferior blends of sapodilla are emitted lower HC and CO. The BTE of B100 works 88.13% efficiently, similar to diesel for low load conditions. When compared to diesel, a maximum NO_x reduction of up to 30% was achieved while using the sapodilla blend. It is found that the oil derived from the sapodilla seed kernels will be the promising additive for fossil fuels for a greener environment.

1. Introduction

The world towards the substitute renewable ecological resource fuels from natural resources due to global oil supply production will be attained [1]. Researchers from several countries have conducted numerous experiments in an internal combustion (IC) engine using vegetable oils. They found the thermal efficiency of different oil cerates is considerably experienced with the mineral diesel. In vegetable oil, the particulate emissions are higher, and the CO, NO_x, PAH, and SO_x values are lesser when compared with diesel. The minor variation in the fuel system, vegetable oil is suitable as a substitute for conventional fuel. On the other side, the imperfect combustion effect, the minor atomization, and the lower vol-

atility lead to higher emission formation and the gum deposit in the cylinder cavity. As a result, pure vegetable oil has inefficient effectiveness while using fuel in IC engines [2].

Animal fats and vegetable oils are renewable sources from nature, which are low emission properties and ecological. It has better probability to reduce the pollution [3]. Numerical and experimental methods examined the fuel injection angle on the delivery system for diesel [4]. Low bioethanol fraction mbwazirume used as fuel in the engine [5] and found E15 gives low CO and CO₂ emission. The soya bean blend performance with emission behavior was analyzed on diesel engine (DE) by numerical and experimental technique [6]. The engine performance results significantly increased when the mahua was used as the additive [7]. The



(a) (b)

FIGURE 1: (a, b) Sapodilla broken seeds and seed kernel.



FIGURE 2: Oil extraction machine with sapodilla inner seed kernels.

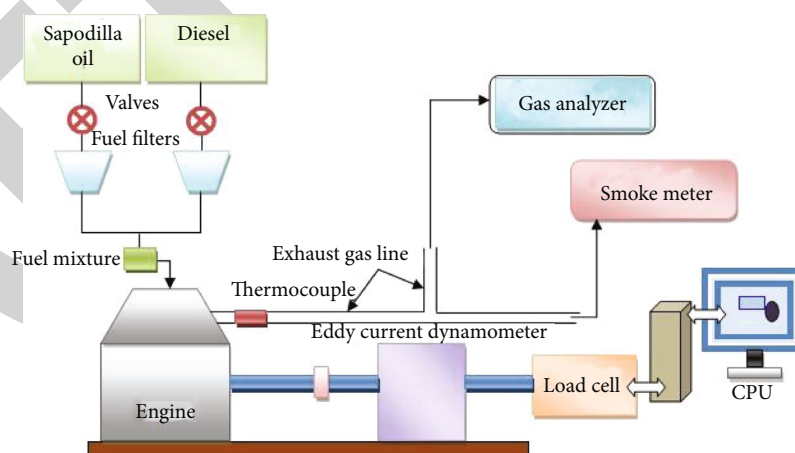


FIGURE 3: Experimental setup—schematic diagram.

energy level and emission outcome of *Moringa oleifera* and palm oils utilized as fuel for diesel engines with percentages of MB5, MB10, PB5, and PB10 were compared to diesel [8]. In addition, the DE (single cylinder) behavior and smoke level of karanja oil [9], free fatty acid neem oil [10], *Jatropha* oil [2, 3], and mixes were investigated. The detailed energy

production from various waste biomass and biochar are given [11, 12]. *Camelina sativa* oil performed effectively in an IC engine with minor fuel system modifications [1]. Food and fuel are the most important factors and raises even for the next-generation biofuel when cultivation pattern may have direct and indirect effects on fuel supply cost [13].

TABLE 1: Types of blends (sapodilla oil with diesel).

Sl.No	Sapodilla oil-diesel percentage	Name
1	0% + 100%	Mineral diesel only
2	10% + 90%	B10
3	20% + 80%	B20
4	50% + 50%	B50
5	75% + 25%	B75
6	100% + 0%	B100 (pure sapodilla oil)

Jaikumar et al. [14] studied about the performance of Niger seed oil with methyl ester on diesel engine and reported the smoke opacity decreased by 5.09%. The lesser ignition delay for neat rapeseed oil with its blend on DE and the combustion character closely followed the diesel [15]. Properties of soap nut oil blend (SNO) 10% were given better IC engine performance [16]. The CO, HC, and smoke emissions were deduced, and then, the NO_x emission somewhat increased when the load at partial and higher condition on IC engine using diesel bioethanol as fuel [17]. The jojoba oil (B20) and sunflower oil (S100) were found to be the promising substitute fuel for DE with no engine alteration [18].

The methyl esters and the apricot seed-kernel oil with lesser concentration significantly accelerated engine performance with exhaust emissions [19]. The analysis carried about emission behavior by preheated raw rapeseed oil with the diesel mix at IC engine [20]. The highest engine performance was observed at the injection pressure 250 bar, BTHE enhanced in 8.9%, and the BFSC improved in 10% [1]. The brake thermal efficiency was determined to be 2.4% percent when the brakes were fully loaded, and the combustion character was comparatively similar with diesel fuel for Eu50 (eucalyptus oil blends) with Me50 mix (methyl ester of paradise oil) [21]. The relatively estimated performance characteristics of the karanja, polanga, and Jatropha using the tractor engine [22]. The turpentine diesel blend is used as alternate fuel in the duel fuel engine with slight modification [23]. The Jatropha oil was used as fuel and found that the fuels 97.4%/2.6% mix given the highest cetane number [24]. The slight alters in DE for raw vegetable oil and the higher emission induced [25] when NO_x reduced. Recently, researchers concentrate on biofuel extraction from various natural resources such as Jatropha seeds [26], cashew nut [27], and deoxygenated vegetable oils [28]. Also, the researchers used several vegetable seeds for producing biodiesel and carried out their research experiments on that fuel. Based on the comprehensive literature survey, it is found that less concentration focused on the sapodilla oil. This work deals with sapodilla oil's thermal energy and emission levels among its blends in DE.

2. Experimental Procedure

2.1. Extraction of Sapodilla Oil. From the fruit, the seeds are removed, and the seeds are dried for one or two days at room temperature. The hard outer cover of seeds is broken (Figure 1(a)), and the inner seed kernels (Figure 1(b)) are

separated manually. These seed kernels are then grounded in the electric-driven oil expeller, and pure brown, clear high viscous sapodilla oil is extracted (Figure 2).

2.2. Engine Setup. Experimental work is conducted at the 4-stroke diesel engine (single cylinder) combined with an eddy current dynamometer. The experimental setup is illustrated schematically in Figure 3.

The data acquisition system is coupled with the engine via an interface, and signals are recorded in the connected computer. The signals from the engine, a slight engine warm-up is needed for few cases of blends. The Kirloskar, TV-1, single cylinder, 4-stroke, DE is utilized for analysis, and it is a water-cooled system. DE have a rated power of 5.2 kW (7 hp) with 1500 rpm of speed, and the compression ratio is 17.5:1. Nozzle opening pressure is between 200 and 205 bar, and the brake mean effective pressure (BMEP) value is 6.34 kg/cm³ for the bore and stroke length 102 and 116 mm. The displacement volume is 0.9481.

2.3. Emission Measurements. The exhaust gas is passed through the portable multigas analyzer (AVL) to the exhaust pipeline. The AVL is used to measure CO, HC, CO₂, and NO_x. The experiments are conducted for several blends of varying concentrations of sapodilla oil (Table 1).

3. Results and Discussions

3.1. Physical and Chemical Concentration. A physical and chemical concentration of raw sapodilla oil with ASTM standard is specified in Table 2. From the results, the cloud point, density, and pour point of the sapodilla oil are high compared to mineral diesel. Therefore, sapodilla oil is unsuitable for colder climates. Sapodilla oil has high flash and fire points, and it is safe to handle. It is found that the ash content is higher for sapodilla oil when compared to diesel fuel.

From the results, the calorific values of diesel and sapodilla oils are 41.536 kcal/kg and 45.343 kcal/kg, respectively. It is visible that new sapodilla oil has 90.16% of calorific energy when compared to diesel. The combustion delay of sapodilla oil (48.1) was found to be lesser as evaluated with diesel, according to cetane number measurements (diesel, 47). The sulfur level is lower for sapodilla oil. The blends of sapodilla oil-diesel considered for the present investigation are B10, B20, B50, B75, and B100, and it is subject to the following rated load variations such as 20%, 40%, 60%, 80%, and 100%.

3.2. Combustion Characteristics

3.2.1. BSEC Value of Sapodilla Blends. Figure 4 depicts the BSEC value of diesel, B100, B75, B50, B20, and B10 for different load conditions. As two different fuels with different density properties are used as fuel in the IC engine, the BSEC may be suitable for brake-specific fuel consumption [21]. From the results, the BSEC value decreased with load increases for all the blends. B100 pure sapodilla oil is having the highest BSEC than diesel.

It occurs because of higher volatility, dense, and density along with lower heat content capability. These natures are

TABLE 2: Raw sapodilla properties.

Properties	Raw sapodilla oil	Mineral diesel
API gravity	22.9	36.95
Density @ 15°C	915.5 kg/m ³	840 kg/m ³
Kinematic viscosity @ 40°C	42.3 C St	2.44 C St
Flash point	295° ± 1°C	71° ± 3
Fire point	310° ± 3°C	103° ± 3
Cloud point	14° ± 1°C	3° ± 1°C
Pour point	Bel + 2°C	-6° ± 1°C
Ash point	0.43 wt%	0.01 wt%
Total sulfur	0.023% S wt%	0.25
Specific gravity @ 15/15°C	0.9163	0.838
Total acid number	0.087 mg of KOH/gm	0.2 mg of KOH/gm
Cross calorific value	41.536 kcal/kg	45.343 kcal/kg
Cetane no.	48.1	47
Carbon (%w/w)	84.37	80.33
Hydrogen (%w/w)	13.52	12.36
Nitrogen (%w/w)	0.21	1.76
Oxygen (%w/w)	1.88	1.19
Sulfur (%w/w)	0.018	0.25
Conradson carbon residue	0.71%	0.1 ± 0.0%

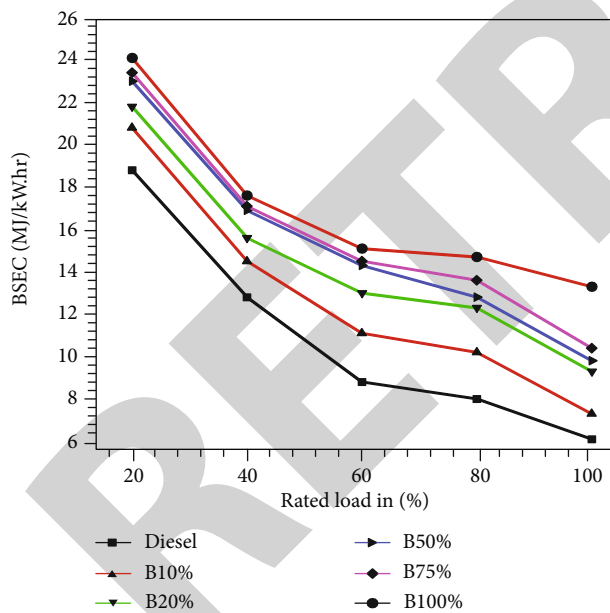


FIGURE 4: BSEC of sapodilla oil and diesel.

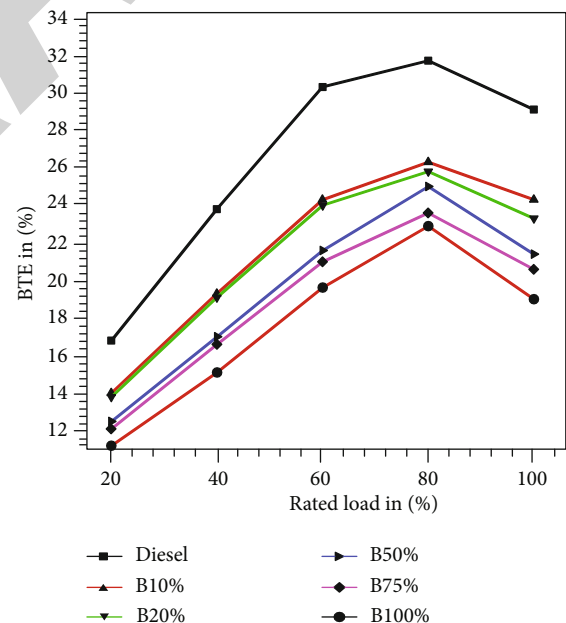


FIGURE 5: BTE of sapodilla oil and diesel.

lead to incomplete combustion and results in unburnt fuel. Hence, the usage of pure sapodilla oil leads to additional fuel to meet the engine's requirement for the same load. For any particular load, when blend decreases, the BSEC approaches towards convectional mineral diesel. However, this trend follows a nonlinear trend.

3.2.2. BTE of Sapodilla Blends. Figure 5 denotes the influence of rated load in connection with BTE for sapodilla and diesel.

BTE is increased with the rated load up to 80% and further decreased gradually with an increase in load. When adding sapodilla oil to diesel as a blend, the BTE decreases for all the cases. Similar BTE trends are noticed for B10 and B20 BTE up to 60% load, and it denotes the lesser effect on BTE when incrementing the blend by 10%. Due to the calorific value effect, the BTE value decreases for the remaining cases. The maximum BTE of 27.05% is noticed for B10 with the

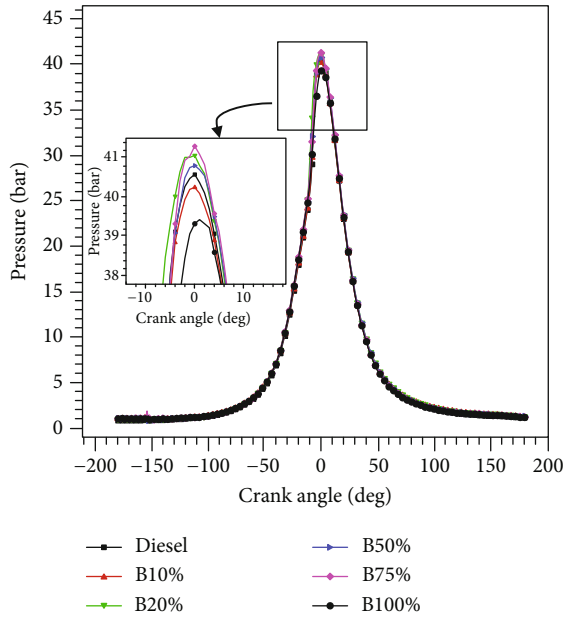


FIGURE 6: Cylinder pressure of sapodilla oil, diesel, and various blends.

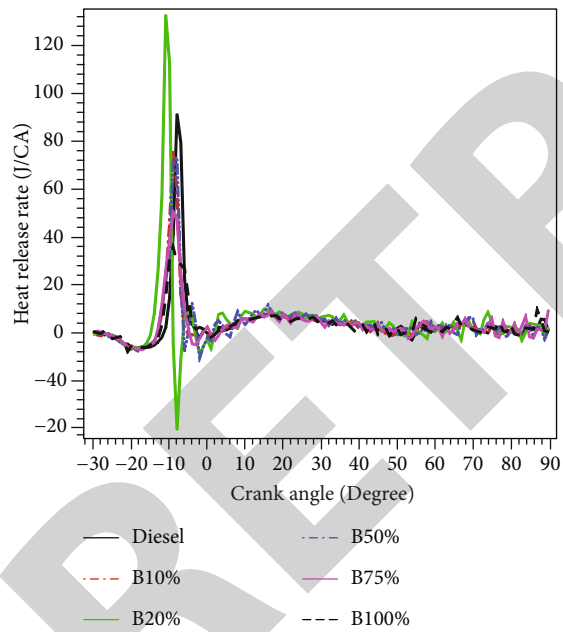


FIGURE 7: HRR of sapodilla oil and diesel.

rated load of 80%, and also, the 80% rated load gives the maximum BTE for all the cases considered. The BTE of B100 works 88.13% efficiently, similar to diesel for low load conditions.

3.2.3. Variations of Cylinder Pressure with Crank Angles. Figure 6 depicts the cylinder pressure for sapodilla oil mixes and diesel at various crank angles. First, the peak pressure 41.3 bar occurs, corresponding to B75. Then, the peak pressure is 40.5, 40.24, 41.06, 40.80, 41.25, and 39.43, corresponding to diesel, B10, B20, B50, B75, and B100, respectively, and

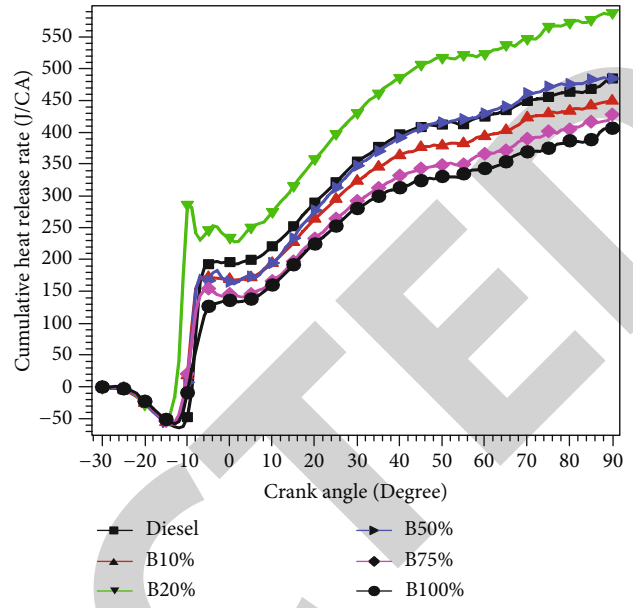


FIGURE 8: CHRR of sapodilla oil and diesel.

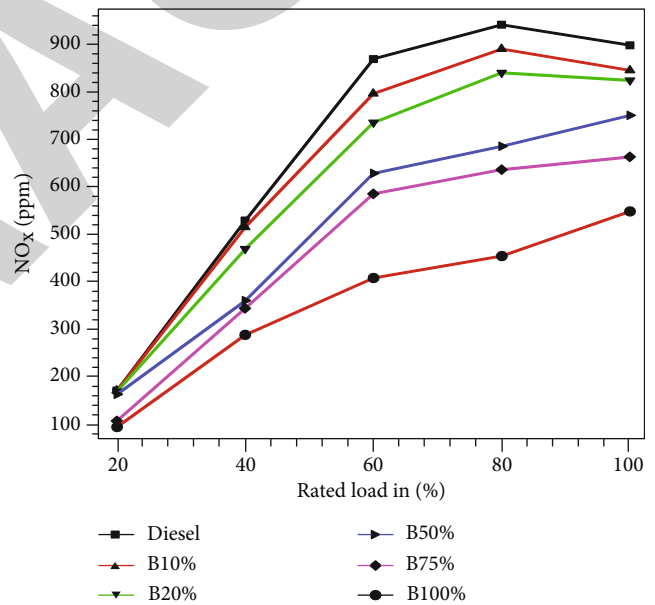


FIGURE 9: NO_x emission of sapodilla oil, diesel, and various blends (biodiesel) with respect to loads.

it happens by the consequence of cetane number, which is higher and very close to diesel, so that the blends B20, B50, and B75 showed higher cylinder pressure. Devan and Mahalakshmi [21] and Gad et al. [26] noticed a similar kind of cylinder pressure behavior.

3.2.4. HRR of Sapodilla Blends. The changes in HRR with crank angle higher rated load, 100% (maximum load), are shown in Figure 7. The fluctuations in HRR of sapodilla blends with crank angle are observed from the diagram, and the B20 sapodilla blend provides high heat releases. When the blending ratio increases, the HRR tends to

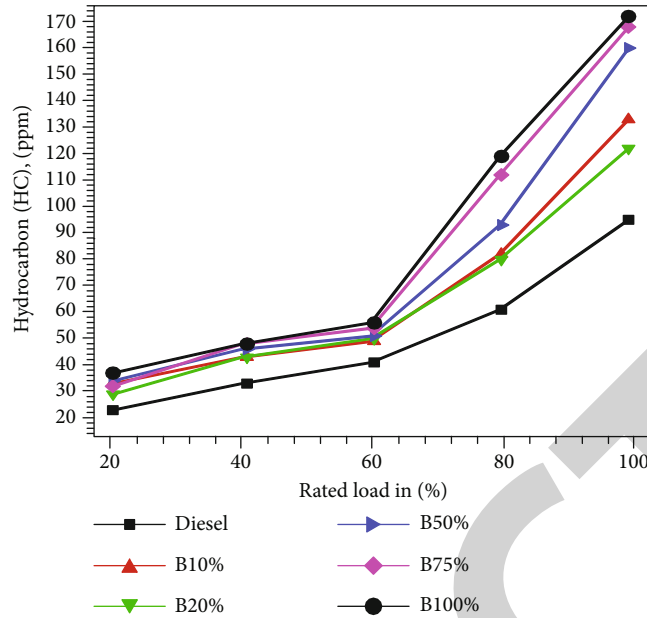


FIGURE 10: Hydrocarbon emissions of sapodilla oil and blends and diesel with respect to loads.

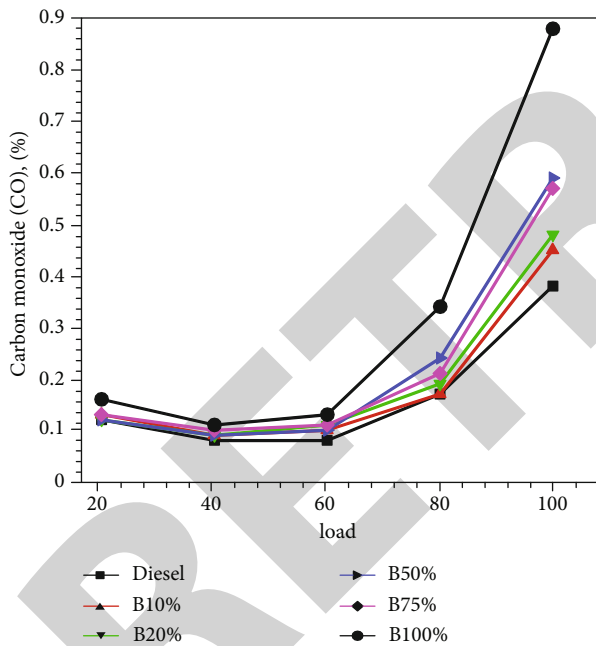


FIGURE 11: CO emission of sapodilla oil, diesel, and various blends (biodiesel) with respect to loads.

decrease. The atomization is affected when the blend quantity is increased, which results in a decrease in HRR.

3.2.5. Fluctuations in Cumulative HRR with Different Crank Angle. Figure 8 shows the CHRR in connection through crank angle for various blends. Initially, CHRR is negative because of ignition delay, which affects fuel evaporation accumulation, and afterward, the CHRR value increased with a nonlinear trend. B20 produces the higher CHRR for all the crank angles. This occurring due to more oxygen particles in the blended oil results higher CHRR value than diesel [29].

3.3. Emission Characteristics. Emission characteristics such as NO_x , HC, CO, and CO_2 are observed (Figures 9–12) for sapodilla oil and its blends.

3.3.1. Oxides of Nitrogen (NO_x). In general, due to absolute and higher burning temperatures, NO_x emissions are high. This can be oxygen content present in sapodilla fuel and mixtures, and it helps the better combustion process. The maximum combustion temperature is targeted by this efficient combustion. When the higher temperature occurs in the burning, the NO_x reaches its maximum [17]. The NO_x emission for various blends of sapodilla oil and diesel used for different load conditions is presented in Figure 9. NO_x emission for B10 acts similar to diesel for the corresponding load of 20%. Reduction in NO_x has been identified when adding sapodilla oil to diesel from B10 to B100 for all rated loads. B100 blends for the 20% rated load resulted in 44.8% less NO_x emission than diesel. Shi et al. [30] observed the same trends on their analysis. When compared to diesel, the maximum NO_x reduction up to 30% was achieved while using sapodilla blend.

3.3.2. Hydrocarbon Emissions (HC). Figure 10 depicts the HC values for various sapodilla blends and diesel for various load conditions. At 40% of the rated load, the hydrocarbon emissions of B50 and B75 are almost equal to diesel. However, for all rated loads, the HC emissions are higher for various blends due to sapodilla oil present when evaluating with diesel. Occurring of this incident, perhaps, the influence of higher viscosity and carbon content value is present in sapodilla. Hence, these properties react to the lower dispersion at the combustion chamber. Also, similar behavior was noticed by Barabas et al. [17]. In all the blends and loads, HC values were lower than the diesel value and the same tendency was noticed by Balakumar et al. [31].

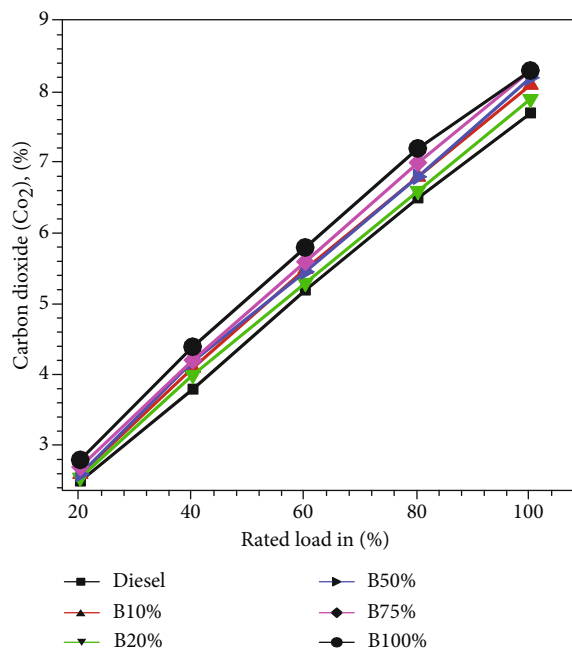


FIGURE 12: CO₂ emission of sapodilla oil, diesel, and various blends (biodiesel) with respect to loads.

3.3.3. Carbon Monoxide Emissions (CO). The CO emissions for various sapodilla blends are compared with mineral diesel, shown in Figure 11. The CO emission value of sapodilla oil blends at lesser load condition is close to the mineral diesel. For example, the B20 and B50 CO emissions are equal to diesel emission for a rated load of 20% [32]. For a rated load of 80%, the B10 blend showed a closer CO emission than that of mineral diesel. A similar trend is observed by [10, 33]. The CO emissions of B10, B20, and B50 at the rated load of 40% increased, and CO values little higher than diesel. CO will be higher for blended oil due to reduced oxygen during ignition delay inside the cylinder at full load conditions.

3.3.4. Carbon Dioxide Emissions (CO₂). Figure 12 describes the CO₂ for various sapodilla blends. The rated load of 80%, B20, and B50 blend shows lesser CO₂ emissions, and for the rated load of 20%, B20, B50, B75, and B100, the CO₂ emissions are comparatively equal as evaluated with diesel fuel. The B75 is given the exact value of the CO₂ emission of diesel for a rated load of 80%. The CO₂ emissions are gradually increased with the increase of load from 20% to 100%. Lower emission of CO₂ is noticed caused by the higher viscosity of the sapodilla blend. Here, the complete combustion is indicated the more emission of CO₂. Hence, higher CO₂ emissions in all mixes indicate efficient combustion due to oxygen, resulting in complete fuel combustion. The CO₂ values were increased from 1% to 11% when evaluated with diesel. From the properties of fuel, sapodilla is having an oxygen value of 1.88 and diesel is having an oxygen value of 1.19; based on this variation, it acts a virtual role on CO₂ emission.

4. Conclusions

The thermal behavior and emission levels of sapodilla blends with a diesel mix are studied in unmodified DE. The viscosity of the mixture is lowered in this test by combining it with diesel. The properties of sapodilla oil and diesel are investigated in terms of their physical, chemical, and thermal properties. The BSEC decreases with increasing loads for all the blends, and BTE increased with load up to 80% rated load and after that decreased gradually with an increase in loads.

- (i) The BTE of B100 works 88.13% efficiently, similar to diesel for low load conditions
- (ii) The variations in-cylinder pressures are nearer to diesel, and as the blend ratio increased, the heat release rate decreased
- (iii) The sapodilla oil blends showed lower NO_x emission than diesel
- (iv) The higher percentage of sapodilla blends had given the higher level of HC emissions in every load condition
- (v) The emission level of CO for the sapodilla is close to diesel at lower and medium load conditions
- (vi) The CO₂ emissions increase when the load increases. When compared to diesel, the maximum NO_x reduction up to 30% was achieved while using sapodilla blend

Data Availability

The data used to support the findings of this study are included within the article.

Conflicts of Interest

The authors declare that they have no conflicts of interest regarding the publication of this paper.

References

- [1] S. W. Kruczynski, "Performance and emission of CI engine fuelled with camelina sativa oil," *Energy Conversion and Management*, vol. 65, pp. 1–6, 2013.
- [2] D. Agarwal and A. K. Agarwal, "Performance and emissions characteristics of Jatropa oil (preheated and blends) in a direct injection compression ignition engine," *Applied Thermal Engineering*, vol. 27, no. 13, pp. 2314–2323, 2007.
- [3] B. S. Chauhan, N. Kumar, H. M. Cho, and H. C. Lim, "A study on the performance and emission of a diesel engine fueled with Karanja biodiesel and its blends," *Energy*, vol. 56, pp. 1–7, 2013.
- [4] L. Lesnik, J. Iljaz, A. Hribernik, and B. Kegl, "Numerical and experimental study of combustion, performance and emission characteristics of a heavy-duty DI diesel engine running on diesel, biodiesel and their blends," *Energy Conversion and Management*, vol. 81, pp. 534–546, 2014.